Dynamic characteristics and leakage performance of liquid annular seals in centrifugal pumps

by

Eskild Storteig

Thesis submitted in partial fulfillment
of the requirements for the degree

Doktor Ingeniør

Department of Marine Engineering
Norwegian University of Science and Technology, NTNU

Submitted 30.11.1999

Acknowledgement

This thesis was made possible thanks to the sponsors of the project, Statoil, Frank Mohn Flatøy A/S, who was the project leader, Dept. of Marine Engineering-NTNU, and the Research Council of Norway, contract NFR 31791/211.

I am especially grateful to my advisor Prof. Maurice F. White, who helped me progress in a defined direction when decisions were hard to make.

Thanks to the Department of Marine Engineering and in particular my friend and colleague on the project, Erik Torbergsen for all fruitful discussions, the review and suggestions regarding the thesis, and for a place to stay during the experimental tests in Bergen.

I would also like to thank the Technical Director Oddbjørn H. Jacobsen at Frank Mohn Flatøy A/S who helped to start the project and Terje Vedeler, Terje Hollingsæter and Håkon Grimstad for all help in seeing the project through.

Further I would like to thank those at Frank Mohn Fusa A/S who made the test-rig materialize. Erik Dalen, for organization and creative solutions, Alf T. Heggland and Gorm Færevåg, for detailed drawings, Ulv K. Hjellestad for electrical components, Ole Vik for roughness measurements, and a special thanks to Jon Alfheim for test-rig assembly and great team-work.

I was also very pleased with the excellent CFX support desk at AEA Technology UK, and the help from Prof. Dara Childs at Texas A&M University for superb feedback on all questions, and the willingness to share information.

I am also grateful to Jan Christian Anker and David T. Zemer at ANKER - ZEMER Engineering A/S for final proof reading of this thesis.

Finally, my warmest thanks to Mona for all support and understanding.

Abstract

In centrifugal pumps the leakage and dynamic characteristics of annular seals are important factors for pump performance. Both seal leakage and dynamics are greatly affected by the relationship between fluid flow and wall friction. In this thesis explicit friction factors were developed which relate the turbulent fluid flow in the seal to wall friction for seals with rectangular grooves. Computational Fluid Dynamics (CFD) was used to study a range of groove width to depth ratios between 1 and 16 and groove depth to clearance ratios between 0.2 and 25.8. In this range an optimal groove geometry for leakage reduction was found which may increase the volumetric efficiency of pumps considerably. Based on a similarity assumption for grooves and hole patterns a friction factor was proposed for hole pattern seals.

Based on the developed friction factors extensions were made to a theory for predicting dynamic characteristics of plain seals to deal with grooved and hole-patterned seals or a combination of both. The method does not require calibration to experiments in order to give useful results. A parameter study indicated that for certain stator hole patterns the cross-coupled stiffness could be greatly reduced compared to that of a smooth seal. This means that self excited vibrations from the seal may be prevented, and the range of stable operation of the pump may be increased. Another extension of the theory accounts for angular stiffness, damping, and added mass moment of inertia for tapered seals. A previously published isotropic friction factor based on pipe flow in the transition between laminar and fully turbulent flow was also included in the theory for predicting dynamic coefficients. Results compared well to previously published theoretical results, however, comparisons to experimental results indicate that this friction factor is of limited use for seals.

Inlet and exit conditions of seals affect both seal leakage and rotordynamic coefficients to some extent. An experimental study of inlet and exit losses for seals with sharp, chamfer, and protruding edge inlet and exit geometries was carried out for a range of axial and tangential flow velocities. The inlet loss was sensitive to geometry changes, while the exit loss was not. The commonly used assumptions of no rotational speed dependency for entrance and exit losses holds well when the average tangential flow is less than or equal to the axial flow. However, as the tangential flow became much larger than the axial flow this assumption did not hold well. In the same study leakage for seals with shallow grooves was studied. Experimental leakage results for shallow grooves on the rotor corresponded well with theoretical predictions based on the friction factor developed in this thesis.

Contents

Nomenclature

Sub- and superscripts

$\square_0$	Zeroth order variables
$\square_1$	First order variables
$\square_z$	Axial direction
$\square_\theta$	Tangential direction
$\bar{\square}$	Average or complex parameter
$\dot{\square}$	Total derivative with respect to time
$\tilde{\square}$	Non-dimensional description of rotordynamic coefficients
$\ddot{\square}$	Total double derivative with respect to time
$\square_g$	Groove portion
$\square_h$	Hole portion
$\square_l$	Land zone
$\square_{r,s}$	Denotes two expressions, one for rotor and one for stator respectively

Roman letters

$\bar{C}_r$	Average minimum clearance for tapered seal
$\bar{L}_{lr,s}$	Average land zone lengths for groove and hole pattern surfaces
$\bar{r}$	Average pipe radius
$\bar{W}$	Average axial bulk velocity for tapered seals
a_1, b_2, b_3	Moody friction factor constants $a_1 = 1.375 \cdot 10^{-3}$, $b_2 = 20000$, $b_3 = 10^6$
$a_{2\theta gr,s}$	Roughness parameters for the tangential friction factor for grooves
$a_{2gr,s}$	Roughness parameters for the tangential friction factor for grooves
$a_{2hr,s}$	Roughness parameters for the isotropic friction factor for hole patterns
$a_{2r,s}$	Roughness parameters used for the Moody friction factor
$a_{2zgr,s}$	Roughness parameters for the axial friction factor for grooves
A_3, A_4	Constants for the transition to turbulence model, $A_3 = 2000$, $A_4 = 4000$
$a_{r,s}, b_{r,s}$	Friction factor parameters used for grooves and holes
b	Ratio between tangential rotor surface speed and the average axial bulk velocity
C	Minimum seal clearance (no taper) or direct translational damping coefficient
c	Cross-coupled translational damping coefficients
$C_{\alpha\epsilon}$	Cross-coupled translational velocity to angular damping coefficient
$c_{\alpha\epsilon}$	Cross-coupled translational velocity to angular damping coefficient
C_α	Direct angular damping coefficient
c_α	Cross-coupled angular damping coefficient
$C_{\epsilon\alpha}$	Cross-coupled angular velocity to translational damping coefficient
$c_{\epsilon\alpha}$	Cross-coupled angular velocity to translational damping coefficient
C_d	Total pressure drop coefficient
C_{ef}	Effective damping

C_{in}, C_{ex}	Clearance at inlet and exit of seal respectievly
D_h	Hydraulic diameter
$d_{hr,s}$	Hole diameters for hole pattern surfaces
$e_{\theta gr,s}$	Equivalent tangential roughnesses for the grooves
e	Absolute pipe surface roughness used with the Moody friction factor
$e_{gr,s}$	Rectangular groove depths
$e_{hr,s}$	Hole depths
$e_{r,s}$	Absolute surface roughnesses
$f_{\theta gs}$	Tangential friction factors for grooves (excludes land portion)
$f_{\theta r,s}$	Average tangential friction factors for grooved surfaces
$f_{hr,s}$	Friction factors for the part of the seal surface covered by holes
$f_{lr,s}$	Friction factors for the groove surface land zone
$F_{r,\theta}$	Radial and tangential force action on rotor
$f_{r,s}$	Isotropic friction factors
$f_{r,s}^{lamin}$	Laminar friction factor contribution to transition to turbulence model
$f_{r,s}^{moody}$	Moody friction factor contribution to transition to turbulence model
$F_{X,Y}$	Reaction force from the fluid on the rotor in the X- and Y-directions
$f_{zgr,s}$	Axial friction factors for the grooves (excludes land portion)
$f_{zr,s}$	Average axial friction factors for a grooved surface
H, h	Local film thickness for tapered seal (excludes groove depth) and corresponding dimensionless variable
H^*, h^*	Local film thickness for tapered seals (includes grooves) and corresponding dimensionless variable
H^+, h^+	Total added film thickness for grooves ($H^+ = H_s^+ + H_r^+$) and corresponding dimensionless variable
$H_{r,s}^+$, $h_{r,s}^+$	Added film thicknesses for grooves and corresponding dimensionless variables
K	Direct translational stiffness coefficient
k	Turbulent kinetic energy or cross-coupled translational stiffness coefficient
k_m	Roughness multiplier
$K_{\alpha\epsilon}$	Cross-coupled translational displacement to angular stiffness coefficient
$k_{\alpha\epsilon}$	Cross-coupled translational displacement to angular stiffness coefficient
K_α	Direct angular stiffness coefficient
k_α	Cross-coupled angular stiffness coefficient
$K_{\epsilon\alpha}$	Cross-coupled angular displacement to translational stiffness coefficient
$k_{\epsilon\alpha}$	Cross-coupled angular displacement to translational stiffness coefficient
K_{ef}	Effective stiffness
$L_{er,s}$	Groove width to depth ratio and hole diameter to depth ratio
$L_{gr,s}$	Width of grooves
$L_{lr,s}$	Width of land zones for groove and hole pattern surfaces
$Lex_{r,s}$	Exit land zone lengths

$Lin_{r,s}$	Entrance land zone lengths
M	Direct translational added mass
m	Cross-coupled translational added mass
$M_{\alpha\epsilon}$	Cross-coupled translational acceleration to added inertia coefficient
$m_{\alpha\epsilon}$	Cross-coupled translational acceleration to added inertia coefficient
M_{α}	Direct added mass moment of inertia coefficient
m_{α}	Cross-coupled added mass moment of inertia coefficient
$M_{\epsilon\alpha}$	Cross-coupled angular acceleration to translational added mass coefficient
$m_{\epsilon\alpha}$	Cross-coupled angular acceleration to translational added mass coefficient
M_{ef}	Effective added mass
$m_{r,s}$, $n_{r,s}$	Hirs' friction factor parameters
$M_{X,Y}$	Reaction moment from the fluid on the rotor about the X- and Y-axes
$N_{gr,s}$	Number of grooves
P, p	Pressure and dimensionless pressure
P_e, p_e	Seal exit chamber pressure and corresponding dimensionless pressure
P_s, p_s	Supply pressure at seal inlet chamber and corresponding dimensionless pressure
P_{ex}, p_{ex}	Pressure at the seal exit and corresponding dimensionless pressure
P_{in}, p_{in}	Pressure at the seal inlet and corresponding dimensionless pressure
Q	Volumetric flow rate
q	Dimensionless seal taper angle
R_O	Radius of rotor orbit
r_{min}, r_{max}	Minimum and maximum pipe radius
$R_{r,s}$	Rotor and stator radius at respective land surfaces
Ra	Mean machining surface roughness
Re_z	Axial Reynolds number
$Re_{r,s}$	Reynolds number relative to rotor and stator $= \frac{2\rho U_{r,s} C}{\mu}$
T	Fluid transition time through seal
U, u	Tangential bulk velocity (swirl) and dimensionless swirl $= \frac{U}{\omega R_r}$
u_∞	Fully developed tangential bulk velocity relative to the stator
$u_{r,s\infty}$	Fully developed total bulk flow velocities
$U_{r,s}$, $u_{r,s}$	Average total fluid velocities and corresponding dimensionless velocities
W, w	Axial bulk velocity and the corresponding dimensionless velocity
WFR	Whirl frequency ratio $= \frac{\omega_d}{\omega}$
x, y	Dimensionless cartesian coordinates
y^+	Non-dimensional wall distance to the near wall cell in CFD solutions
Z, z	Axial position and dimensionless axial position
Z_p, z_p	Axial location of pivot point for angular perturbation and corresponding dimensionless location

Greek letters

α	Seal taper angle
$\alpha_X, \alpha_Y, \alpha_x, \alpha_y$	Angular amplitudes for rotation about the $X-$ and $Y-$axis and dimensionless versions of the same angles
$\chi_{\theta lr,s}$	Land portions of grooved surfaces used for the tangential friction factor
$\chi_{gr,s}$	Relative portions of seal surfaces covered by grooves
$\chi_{hr,s}$	Relative portions of seal surfaces covered by holes
$\chi_{lr,s}$	Relative land portions of groove or hole pattern surface
$\chi_{zlr,s}$	Land portions of grooved surfaces used for the axial friction factor
$\boldsymbol{F}$	Dimensionless whirl frequency
ϵ	Dissipation rate of turbulent kinetic energy
$\epsilon_{\theta gr,s}$	Effective relative tangential surface roughnesses for grooves
$\epsilon_{r,s}$	Relative roughnesses
$\gamma_{r,s}$	Fraction of surface areas covered by holes
μ	Dynamic viscosity
Ω	Angular speed of rotor orbital motion
ω	Rotational speed of rotor
ω_d	Angular speed of the rotor for which tangential fluid forces become destabilizing
ρ	Density
$\sigma_{\theta r,s}$	Tangential friction parameters
$\sigma_{zr,s}$	Axial friction parameters
τ	Dimensionless time
$\tau_{\theta gr,s}$	Tangential shear stress in jet at radii $R_{r,s}$ in the grooves
$\tau_{\theta r,s}$	Average tangential shear stresses for groove/land
$\tau_{r,s}$	Wall shear stresses
τ_{ra}, τ_{sa}	Pseudo shear stresseses in the directions of $U_{r,s}$ respectively
τ_{rb}, τ_{sb}	Pseudo shear stresseses in the directions of $U_{r,s}$ respectively
$\tau_{zr,s}$	Average axial shear stresses for groove/land
θ	Angular coordinate
ξ, ξ_e	Viscous entrance- and exit loss coefficient respectively
ξ_O	Entrance loss coefficient at zero swirl
$\xi_{r,s}$	Weighting parameters used in the transition to turbulence model
ζ	Ratio between minimum and average clearance friction factor

Abbrevations

avg	Average value
CFD	Computational Fluid Dynamics
Exp	Experimental result
SD	Standard deviation
Th	Theoretical results

Chapter 1

Introduction

In the oil exploitation industry high speed water injection pumps are used to maintain oil well pressures in order to increase oil production rate and the total amount of oil drawn from a well. Some centrifugal pumps operate at 300 bar pressure, rotational speeds in excess of 15000 rpm, and with an energy consumption up to several megawatts. Important aspects in the design of such pumps are efficiency, dynamic stability, and compactness.

1.1 Pump efficiency

The pump efficiency is defined as the ratio of pump energy output to the energy input applied to the pump rotor. Many centrifugal pumps can achieve an efficiency in excess of 90% at the best design point and considerably less at off design operation. Significant cost savings to be made if one can increase this efficiency. The main causes for pump efficiency loss are:

- Mechanical losses due to friction between the rotating and stationary parts, for example at ball- and journal-bearings, seals, shrouds, and impellers
- Leakage losses due to back flow of fluid in for example seals and bleed offs
- Hydraulic losses made up of circulation losses, friction losses in the blade passage, and by losses at the inlet due to imperfect match of the inlet and impeller cross sections

The total efficiency is the product of the individual mechanical, volumetric, and hydraulic efficiency. Generally all three items have to be considered to improve pump performance.

The most important factor for seal leakage reduction is to reduce the clearance between the rotating and stationary parts. However, clearance is restricted by machining

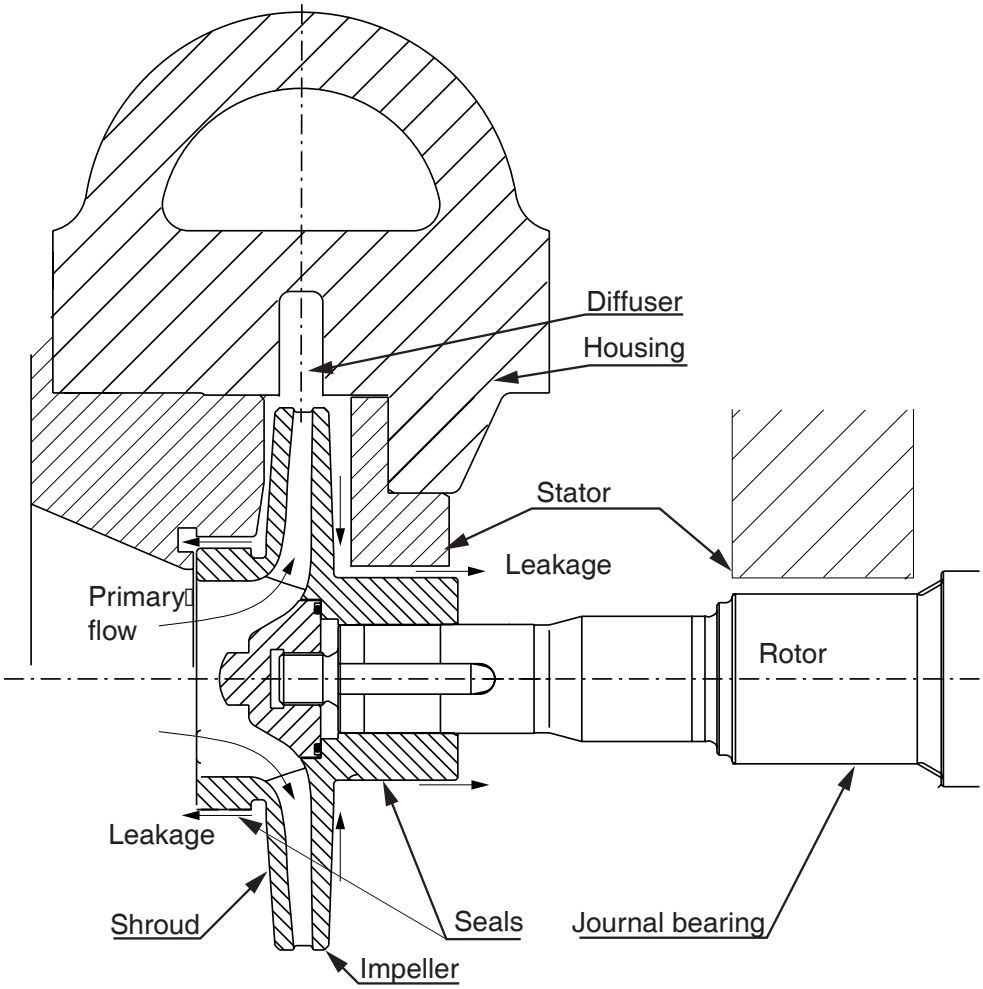

Figure 1.1: High speed centrifugal pump, main flow, and leakage paths.

and assembly tolerances. Another way of decreasing leakage through the seals is to make the seals longer, but this method has its limitations since it increases the total length of the rotor, influences the dynamic behaviour of the pump, and puts greater demands on tolerances. Previous research, reviewed in Chapter 2, has shown that leakage reduction also is possible by introducing circumferential or helical grooves, hole-, diamond-, or honeycomb-patterns to the seal surfaces. Since so many variations exist of surface patterns there is limited knowledge regarding which patterns give optimal leakage reduction. By reducing the seal leakage the pumps volumetric loss decreases. However, a reduction in leakage may be accompanied with an increase in mechanical loss, or increased rotor eccentricity so these effects must be considered in order to verify that the overall pump performance can be improved.

1.2 Dynamic stability

For given requirements of mass flow rate and pressure for a centrifugal pump it is often desirable to keep the dimensions of the pump as small as possible. To achieve this, the industry is trying to design pumps running at increased rotational speeds.

In this search for higher power density it is essential to quantify the forces acting on the rotor and housing during operation and to predict the rotor's dynamic behaviour. An example of compact pump design is shown in Fig. 1.1. Some industrial pumps are designed to run below the pumps first natural frequency in order to suppress destructive vibrations due to resonance. Others may be designed to run above their first natural frequency. For the latter type there has to be enough damping of the rotor to suppress vibrations at the natural frequencies, or the pump can be accelerated quickly past the critical speed(s), and operate between two natural frequencies. For either type of pump it is essential to accurately predict the natural frequencies of the rotor so that a safe range of operation can be determined. The current challenge in predicting the natural frequencies and stability of the rotor is to master the interaction between the rotating parts and the surrounding fluid. Due to the overall complexity of the problem it is common to consider the fluid structure interactions at seals, bearings, shrouds, and impellers/diffusers separately.

In this thesis the focus will be on fluid structure interaction in liquid annular seals. Previous studies have shown that the force on the rotor rotating around its own axis at a rotational speed ω and at the same time precessing at a speed Ω about the seal axis at a radius R_O can be expressed as a quadratic function of the whirling speed Ω (see Fig. 1.2). The coefficients of the quadratic equation relating force to displacement, velocity, and acceleration are termed stiffness, damping, and added mass respectively. Collectively these coefficients are referred to as rotordynamic coefficients. The coefficients relating a perturbation and force of the same direction are called direct coefficients while those relating a perturbation in one direction and force in another are called cross-coupled coefficients.

Although the complete dynamic characteristics of the rotor is needed for stability considerations, some general statements can be made regarding the seal's positive and negative effects on the dynamics of the rotor. Consider Fig. 1.2 which shows an axial section of a rotating and whirling rotor. If the orbit radius is less than half the clearance the coefficients relating rotor motion to F_X and F_Y forces are nearly symmetric. This means that $K_{XX} = K_{YY} = K$ etc. The equation relating rotor reaction force and motion is then (Childs, 1993)

$$-\begin{bmatrix} F_X \\ F_Y \end{bmatrix} = \begin{bmatrix} K & k \\ -k & K \end{bmatrix} \begin{bmatrix} X \\ Y \end{bmatrix} + \begin{bmatrix} C & c \\ -c & C \end{bmatrix} \begin{bmatrix} \dot{X} \\ \dot{Y} \end{bmatrix} + \begin{bmatrix} M & m \\ -m & M \end{bmatrix} \begin{bmatrix} \ddot{X} \\ \ddot{Y} \end{bmatrix} \quad (1.1)$$

The cross-coupled mass is often close to zero and hence often neglected. The force in the cartesian direction which varies with time can be transformed into a steady radial and tangential force acting on the rotor in the coordinate system fixed to the rotor. The radial and tangential reaction force from the fluid on the rotor are

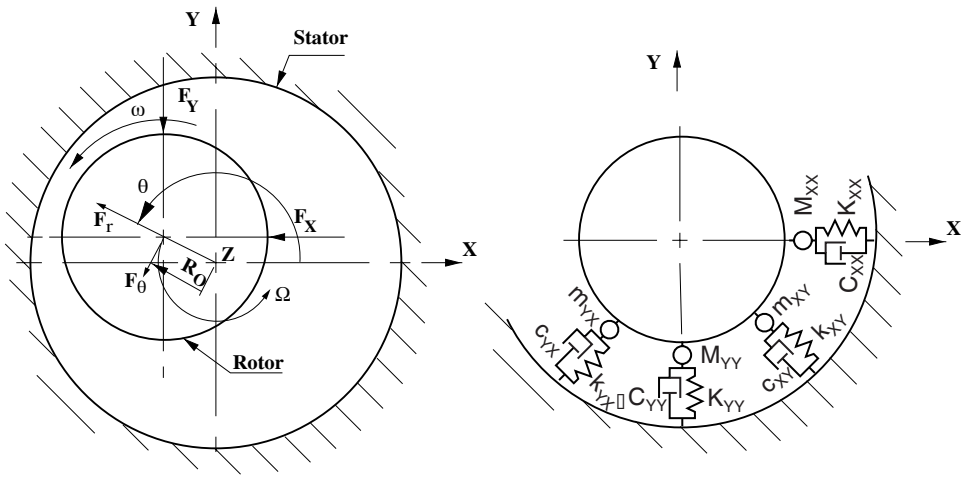

Figure 1.2: Whirling rotor motion, forces, and dynamic coefficients.

$$F_r = (-K + c\Omega + M\Omega^2)R_O \tag{1.2}$$

$$F_\theta = (k - C\Omega + m\Omega^2)R_O \tag{1.3}$$

The expression for radial force shows that a positive direct stiffness will act to centre the rotor when it is perturbed radially. Typically seals with a much higher axial- than tangential bulk flow velocity will have a positive stiffness while those that have a high tangential bulk velocity relative to the axial will have a negative direct stiffness which acts to increase the eccentricity of the rotor. Hence, one may expect for a given pump that a seal leakage reduction which has a positive effect on the pump efficiency may have the negative side effect of reducing direct stiffness which may be destructive to the seal.

From the expression of tangential force and Fig. 1.2 it can be seen that a positive cross-coupled stiffness creates a force acting in the same direction as the whirling orbital motion and will act destabilizing. By doing a linear stability analysis similar to the one by (Lund, 1966) for journal bearings the frequency ω_d of the self excited destabilizing force can be expressed by the whirl frequency ratio, WFR.

$$\omega_d = WFR \cdot \omega = \frac{k}{C} \tag{1.4}$$

The cross-coupled stiffness, k, is a function of the tangential bulk flow (mass flow average) velocity in the seal and usually it increases linearly with rotational speed, while the direct damping C is approximately constant, and this implies a constant value for the whirl frequency ratio.

Usually the cross-coupled stiffness is the coefficient which is altered in order to modify the WFR, and to reduce vibration levels. Typically the cross-coupled stiffness, k, is positive for a tangential bulk flow, U, in the same direction as the tangential rotor velocity (positive U). Zero U gives a near zero value for k and negative U gives a negative k-value. Up until the early 1980's no one had introduced special measures to control the tangential velocity. Usually the ratio $U/(\omega R)$, where ω is the rotational speed, and R is the rotor radius, was assumed to be 0.5. This typically resulted in a WFR near 0.5 and self excited vibrations from the seal at two times the first natural frequency of the pump. Since then, various designs have been suggested to reduce the tangential velocity (also called swirl) of the seal using swirl brakes or by injecting fluid with negative swirl velocity at the seal inlet. Another way of reducing swirl (von Pragenau, 1982) is to introduce a rough stator surface which increase the fluid friction at the stator compared to the rotor and hence reduced the average swirl velocity. Only a limited number of stator roughnesses have been studied in the literature, and little is known about optimal surface patterns for swirl reduction.

In general there are forces and moments developed due to tilting motion of the rotor as well which yield 4 by 4 matrices for stiffness, damping, and added mass. When these coefficients are known, the seal's contribution to the overall rotordynamic behaviour can be determined and optimized based on variations in seal geometry and surface treatment.

1.3 Scope of work

As indicated in this introduction there are knowledge gaps regarding surface roughness effects on leakage, dynamic characteristics, and mechanical losses. This lead to the scope of work for this thesis.

- By using Computational Fluid dynamics, CFD, friction factors will be developed for turbulent flow in liquid annular seals with a wide range of rectangular grooves, and by using a similarity assumption a friction factor for hole pattern surfaces is suggested. This is the topic of Chapter 3.
- Based on the developed friction factors the rotordynamic coefficients of seals can be calculated by using a theoretical approach similar to the one by other authors for smooth and machining roughness seals. Chapter 4 concerns this theory and comparisons to experimental results.
- An experimental study on seal entrance and exit losses, which influence both leakage and dynamic characteristics, is carried out in Chapter 5. Leakage is also studied in the transition to turbulent flow for plain and shallow groove seals. Results are compared to those from CFD and the analytical friction factors developed in Chapter 3.

The literature survey in Chapter 2 gives more in depth reasons for choices made, and final conclusions of the outcome are found in Chapter 6.

Chapter 2

Literature survey

2.1 Background

A multistage centrifugal pump with three typical annular seals, is shown in the cross section drawing, Fig. 2.1. In this Chapter the focus will be on the previous research related to the prediction of leakage, mechanical loss, and dynamic characteristics of liquid annular seals.

The categories of literature which will be covered are:

- Primary and secondary flow patterns of seals
- Leakage predictions
- Bulk flow model
- Dynamic characteristics of seals
- Computational Fluid Dynamics (CFD)

2.2 Primary and secondary flow fields in seals

The primary fluid flow pattern and possible secondary flow patterns in a seal with a rotating rotor are shown in Fig. 2.2. The radial velocity profiles for the primary flow in the laminar and turbulent regime are also shown in Fig. 2.2.

(Taylor, 1923) was the first to mathematically predict the onset of toroidal vortices (now known as Taylor vortices) for laminar flow between two concentric cylinders where the inner cylinder is rotating and there is no axial flow (see Fig. 2.2). (Kaye & Elgar, 1958) discuss Taylor vortices in turbulent flow including swirl and maps

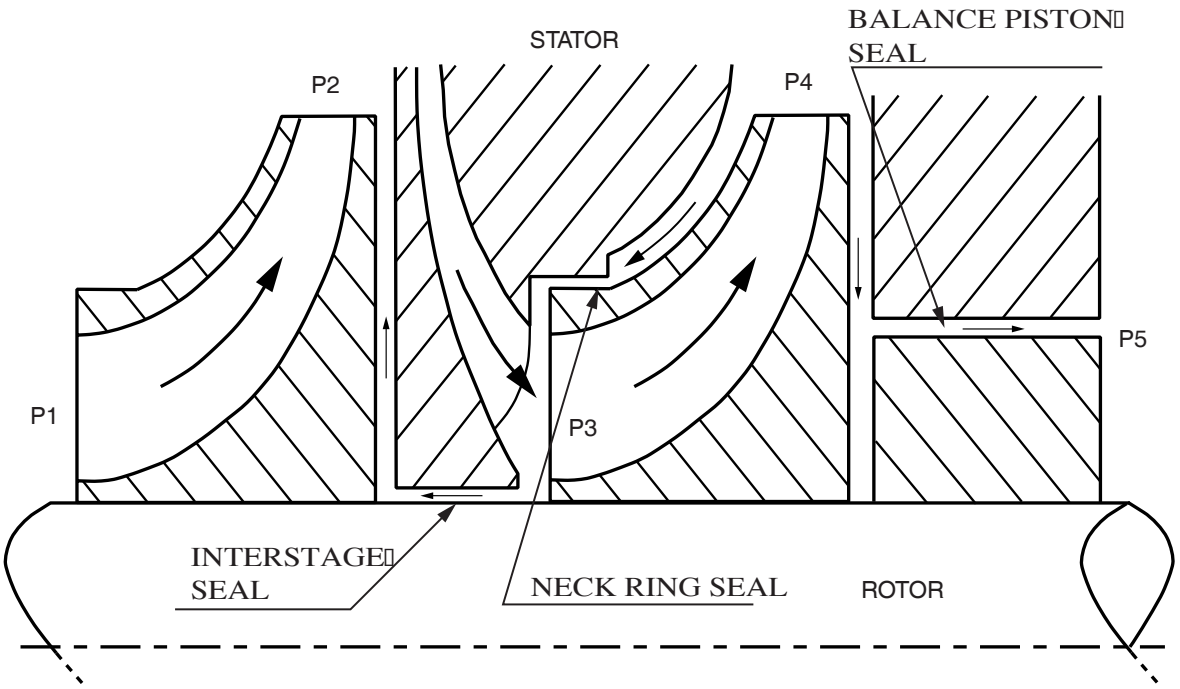

Figure 2.1: Annular neck-ring, interstage, and balance piston seals.

the flow characteristics in four regions as a function of the axial Reynolds number (0-2500) versus tangential Taylor number (0-700).

The of regions of flow are:

- Laminar flow
- Laminar flow plus vortices
- Turbulent flow plus vortices
- Turbulent flow

In the literature regarding liquid annular seals Taylor vortices are rarely an issue. This is because the small clearance, large axial flow and eccentricity usually suppress the formation of the vortices. This type of secondary flow pattern will not be treated in this thesis since the operating conditions for typical industrial seals are of interest.

At low axial flow rates other secondary flow patterns may exist as documented by (Tam *et al.*, 1988) who found that the flow may re-circulate in the tangential direction (see Fig. 2.2). This type of flow pattern, which is common for journal bearings with an eccentric rotor relative to the stator annulus, is rarely considered in seal analysis since the eccentricity for seals usually is significantly less, and the dominating axial flow suppresses this type of secondary flow as well. Since the clearances in modern

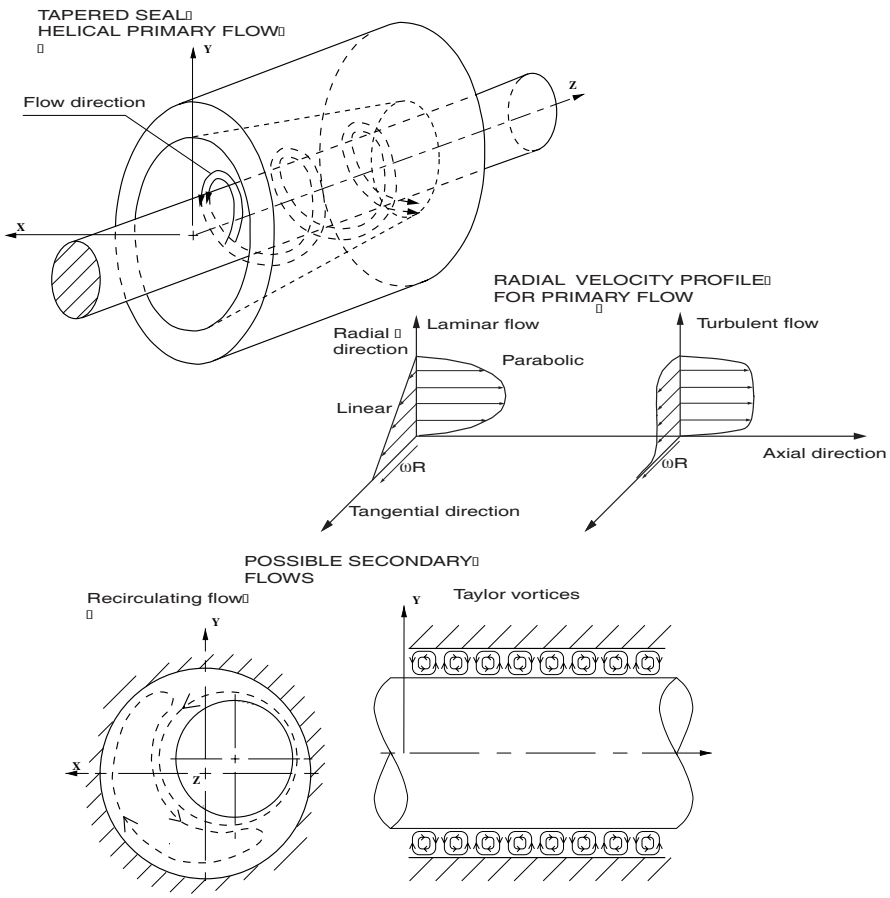

Figure 2.2: Top: Tapered seal with no secondary flow effects. Middle: The corresponding radial velocity distribution. Bottom: Eccentric seal with possible recirculating flow, Taylor vortices for concentric cylinders.

seals are approaching those of journal bearings, this secondary flow pattern may be worth considering in future research. However, this will not be dealt with in this thesis since there are still lacking knowledge about primary flow which was considered more important.

2.3 Leakage predictions

This section primarily considers how leakage can be predicted for a seal for a given pressure difference across the seal. In Fig. 2.1 the fluid enters the first stage of the pump at a pressure P1, and the pressure is increased through each impeller up to the pressure P4. One primary function of the seal is to reduce the leakage caused by the pressure differences, P3-P2, P4-P3, and P4-P5. A typical pressure distribution along the rotor past for example in the interstage seal in Fig. 2.1 is shown in Fig. 2.3.

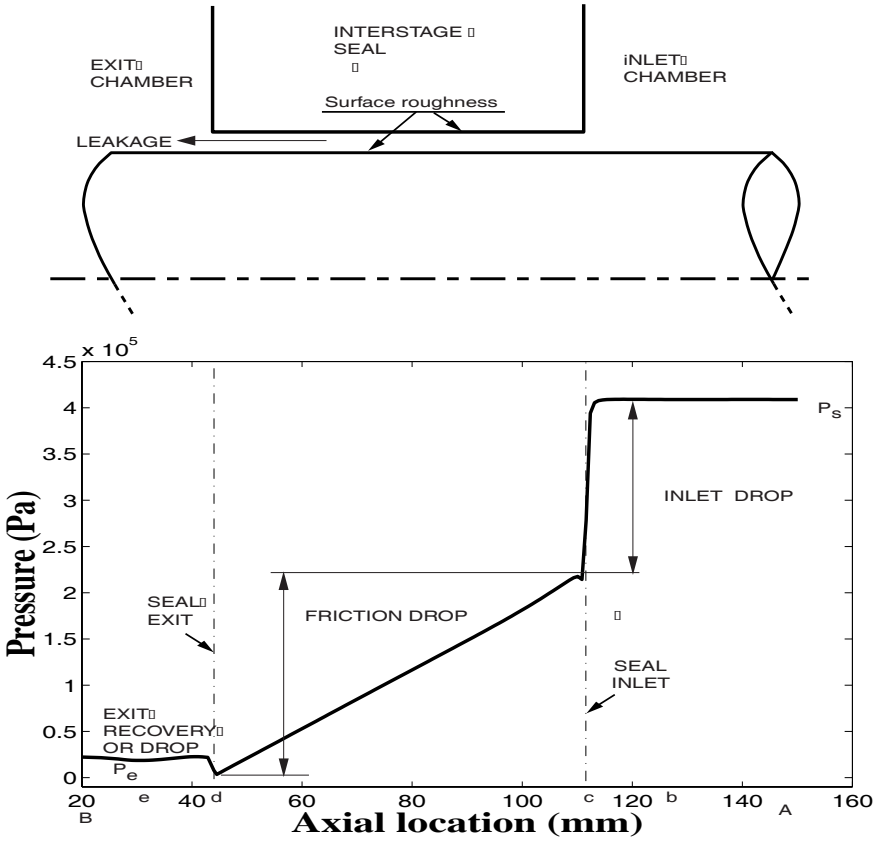

Figure 2.3: Pressure distribution across an interstage seal.

As shown in Fig. 2.3 the pressure drop across the seal can be divided into three separate parts which are inlet-, seal-, and exit pressure drop. The literature concerning experimental and theoretical predictions of the three parts will be discussed in turn. First an example is given, based on Eq. 2.1 (Childs, 1993), of how the typical total pressure drop, ΔP, from the seal inlet chamber to the exit chamber is calculated.

$$P_s - P_e = (\xi + \xi_e + 4f\frac{L}{2C})\rho\frac{W^2}{2} \tag{2.1}$$

where ξ is the inlet loss coefficient, ξ_e the exit loss, f the friction factor, L the seal length, C the seal clearance, ρ the fluid density and W the average axial fluid velocity. Typical seal designs for a rotor of 50 mm radius have a clearance in the order of 0.1 mm, a length of 50 mm, and a friction factor for a machined surface and fully turbulent flow in the order of 0.01. The inlet- and exit loss coefficients are typically in the range 0.5 to 1.0 and 0.1 to 0.5 respectively depending on inlet and exit geometries and flow. This means that the friction loss term, $f\frac{2L}{C} = 10$, in the seal is one order of magnitude greater than the entrance and exit loss and that it in this

case would completely dominate leakage predictions. Since inlet and exit losses may have a significant contribution on dynamic characteristics of the seal, (Childs, 1993), this means that for many practical seal designs the detailed geometry of seal inlet and outlet can be optimized for dynamic characteristics without having a significant influence on leakage. If one excludes inlet and exit losses from the leakage predictions, the leakage can be expressed as:

$$Q = 2\pi R\sqrt{\frac{(P_s - P_e)C^3}{f\rho L}} \tag{2.2}$$

where R is the average seal radius and Q is the volumetric flow rate.

From Eq. 2.2 it is clear that for a given pressure difference across the seal, the seal clearance is the dominating factor for the leakage Q, since halving the clearance has the same effect as increasing the length of the seal, L, or the friction factor, f, by a factor eight.

2.3.1 Friction factor

Fig. 2.2 illustrates the radial velocity profiles expected in an annular seal at laminar and turbulent Poiseuille flow (pressure driven axial flow) and Couette flow (shear driven tangential flow). The friction factor relates the average axial and tangential fluid velocity to shear stress at the wall, which determines pressure drop (or leakage) and mechanical losses for the seal. In addition, the friction factor is essential for predicting how the tangential flow develops and for predicting dynamic seal characteristics. As discussed in (Hirs, 1973) the friction factor for pure Couette turbulent flow is about 20% lower than that for pure Poiseuille flow. However, in his theory the pressure distribution on a seal rotor was predicted well for a combination of Couette and Poiseuille flow only based on the knowledge about the Poiseuille flow friction factor. Hence, this section will focus primarily on pressure driven turbulent flow.

Since the pressure drop due to fluid friction in seals is similar to the pressure drops found in fully developed flow in various types of long channels the theory developed from experiments made on pressure drops in pipelines, or between parallel plates have been used extensively for predicting pressure drops in seals. In order to apply the results from other cross sections than that for an annular seal one can use the procedure from for example (White, 1994). He defines the friction factor for predicting pressure drops in pipes as a function of axial Reynolds number and relative roughness, and how the corresponding Reynolds numbers and relative roughnesses should be calculated for other cross sections based on an equivalent hydraulic diameter. For seals the equivalent hydraulic diameter is two times the clearance, and this is used throughout this thesis. According to (White, 1994), the accuracy in the conversion of pipe friction factors to ducts of arbitrary cross section is within $\pm 15\%$.

Early studies on the friction factor were performed by (Nikuradse, 1933) who studied the influence on friction drop for laminar, transition to turbulence, and fully turbulent

flow for a range of random-like sand grain roughnesses and (Schlichting, 1936) who studied the influence from numerous surface patterns. For industrial pipes, (Colebrook, 1939) introduced an implicit formula for pressure drop predictions that was later simplified to an explicit formula by (Moody, 1944). His formula, Eq. 2.3, became an industrial standard for pipes.

$$f = 5.5 \cdot 10^{-3} \left[1 + \left(\frac{2 \cdot 10^4 e}{D_h} + \frac{10^6}{Re_z} \right)^{\frac{1}{3}} \right] \tag{2.3}$$

for a range of Reynolds numbers, $Re_z = \frac{\rho W D_h}{\mu}$ from 4000 to 10^7 and a relative roughness $\frac{e}{D_h}$ of 0 to 0.05. D_h is the hydraulic diameter, e the absolute roughness, ρ the density, μ the dynamic viscosity, and W the average fluid velocity. In the literature of seals it is customary to use the Fanning format of the friction factor for which the above friction factor is divided by a factor four. The Fanning format will be used throughout this thesis except for the comparisons made between results for pipes and seals in this section where direct comparisons to the Moody diagram can be made. A weakness of the Moody formula is that it does not take into account the distribution of surface roughnesses. Other experiments, for example those by (Schlichting, 1936), have shown that the friction factor can change by a great amount for by varying the distribution and form of the roughnesses.

An issue rarely discussed in text books regarding the Moody and other friction formulas for pipes is how the diameter D_h was measured for the experimental data to which the formula was fitted. In (H.Möbius, 1940) it is explicitly stated that a volume average diameter was measured which included the grooves, and from the dimensions stated in (Nikuradse, 1933), (Schlichting, 1936) it appears that an average diameter was used. This becomes important when studying roughness profiles which are about 2% of the hydraulic diameter or greater, which is often the case for roughness profiles used in seal studies. In this thesis the minimum clearance is used throughout for determining the friction factor. This choice was made for convenience since one can immediately compare leakage performance for two seals with the same minimum clearance by comparing their friction factor.

Some experiments in the past which show particularly high values for the friction factor will now be discussed since they indicate what surface patterns reduce leakage the most. Fig. 2.4 and Table 2.1 show the roughnesses studied and Fig. 2.5 shows the friction factors achieved.

To relate results to the minimum hydraulic diameter a pipe friction factor f based on a diameter D correspond to an equivalent friction factor $\bar{f}$ based on a diameter $\bar{D}$ by Eq. 2.4. The corresponding Reynolds number conversion from Re_z to $\bar{Re}_z$ is given by Eq. 2.5. How these equations were derived is shown in Appedix D.

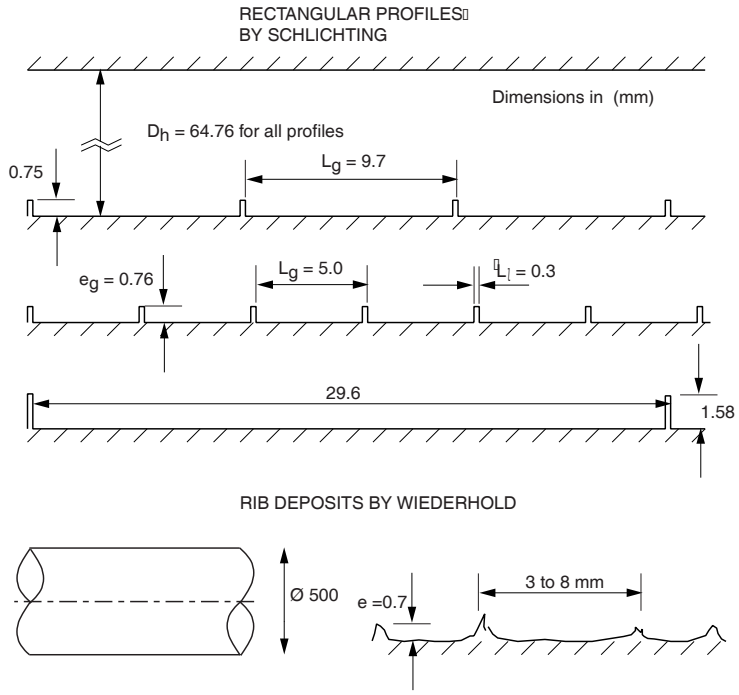

Figure 2.4: Various roughness profiles by Schlichting and rib deposits documented by Wiederhold.

$$f = \bar{f}\left(\frac{D}{\bar{D}}\right)^5 \tag{2.4}$$

$$Re_z = \bar{Re}_z \frac{\bar{D}}{D} \tag{2.5}$$

Based on this conversion formula the results from (Nikuradse, 1933), (Wiederhold, 1949), (Schlichting, 1936) will not depend much on whether the minimum or average hydraulic diameter are used. Hence, no conversion was made for these results. However, for the experiment of (H.Möbius, 1940) conversion becomes important, and all his results were converted to the minimum diameter, by using Equations 2.4 and 2.5. The definition of an average radius, $\bar{r}$, used by (H.Möbius, 1940) is

$$\bar{r} = \sqrt{\frac{r_{min}^2 L_l + r_{max}^2 L_g}{L_l + L_g}} \tag{2.6}$$

where r_{min} is the minimum pipe radius and r_{max} is the maximum, L_l and L_g are the length of land and groove portions respectively of the grooved surface (see Fig. 2.4).

Table 2.1: Roughness profiles studied by various authors, all dimensions in millimeters. e_g denotes groove depth, e means average roughness height.

Profile No.	D_h	L_l	L_g	e	e_g	$\frac{e,e_g}{D_h}$	$\frac{L_g}{e_g}$
(Nikuradse, 1933), sand grain roughness in pipe							
1	N/A	N/A	N/A	0.0	N/A	0.0	N/A
2	99.4	N/A	N/A	0.1	N/A	0.00101	N/A
3	49.4	N/A	N/A	0.1	N/A	0.00202	N/A
4	99.2	N/A	N/A	0.4	N/A	0.00403	N/A
5	24.34	N/A	N/A	0.2	N/A	0.00822	N/A
6	24.34	N/A	N/A	0.4	N/A	0.01643	N/A
7	24.12	N/A	N/A	0.8	N/A	0.03317	N/A
(H.Möbius, 1940), rectangular profiles in pipe							
8	48.514	2.5	45.0	N/A	0.742	0.0153	60.65
9	47.020	2.5	45.0	N/A	1.489	0.0317	30.22
10	44.996	2.5	90.0	N/A	2.501	0.0556	35.99
11	46.978	1.5	27.0	N/A	1.499	0.0319	18.01
12	44.996	2.5	45.0	N/A	2.501	0.0556	17.99
13	44.996	2.5	22.5	N/A	2.501	0.0556	8.996
14	39.016	2.5	45.0	N/A	5.491	0.1407	8.195
(Wiederhold, 1949), wavy deposits in pipe							
15	500	N/A	N/A	0.005	N/A	0.0001	N/A
16	499.3	~ 0	~ 5	~ 0.7	N/A	~ 0.0014	~ 7.1
(Schlichting, 1936) rectangular profiles and a 40x170 rectangular channel							
17	64.76	0.3	29.6	N/A	1.58	0.0244	18.73
18	64.76	0.3	9.7	N/A	0.75	0.0116	12.93
19	64.76	0.3	5.0	N/A	0.76	0.0117	6.57

To get a comparison of the friction factors achieved in pipe experiments and those reported for annular seal Table 2.2 gives a summary of the maximum axial friction factors reported (minimum leakage for a given clearance). The references studied are (Yamada, 1962a), (Nordmann *et al.*, 1987), (Florancic, 1990), (Marquette *et al.*, 1997), (H.Möbius, 1940), (Black & Cochrane, 1973), and (Kim, 1985). By using Equations 3.13 and 3.17, the friction factors in the Table 2.2 are calculated based on the minimum clearance. In addition Yamada's axial Reynolds number has to be multiplied by two to fit the definition used by the other authors. (H.Möbius, 1940) is the only reference that is based on pipe flow. The other reference on seals use a plain rotor - grooved stator configuration. For those tests made in the low Reynolds number regime the friction factor at maximum Reynolds number is reported.

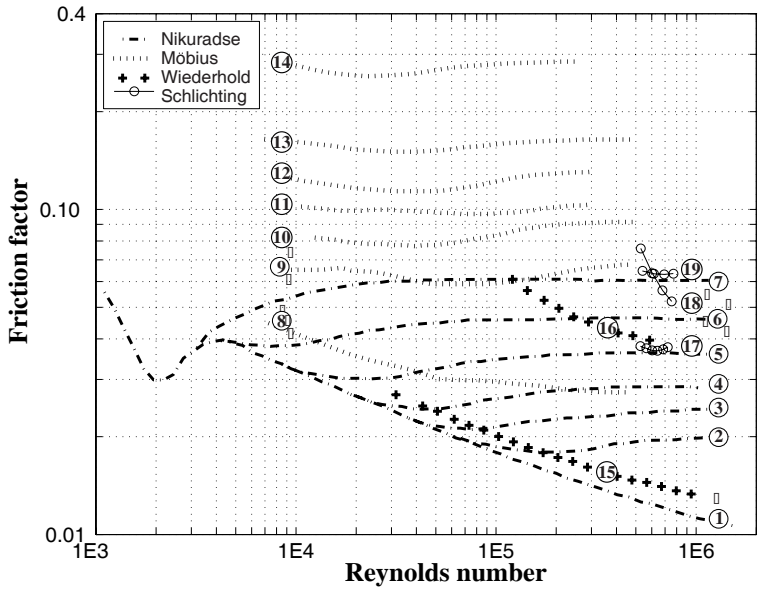

Figure 2.5: Friction factors as a function of Reynolds number and roughness from various experiments.

Table 2.2: Comparison of maximum friction factors f in Moody diagram format and corresponding test geometry and Reynolds number.

Reference	f_{max}	D_h(mm)	L_l(mm)	L_g (mm)	$\frac{Re_z}{1000}$	$\frac{e_g}{D_h}$	$\frac{L_g}{e_g}$
Yamada	0.13	1.85	1.0	19.0	0.1-8	2.7	3.8
Nordmann	0.055	0.4	1.5	0.7	5-9	1.25	1.4
Florancic	0.11	0.74	1.0	1.0	22-300	0.47	2.9
Marquette	0.075	0.2210	1.587	1.587	10-14	1.0	7.2
Möbius	0.27	39.02	2.5	45	7-250	0.14	8.2
Black	0.11	0.36	1.76	1.76	4-14	0.35	13.9
Kim	0.11	1.05	1.6	1.6	90-250	0.36	4.2

Discussion of friction factor experiments

None of the friction factors in Table 2.2 or Fig. 2.5 come close to the one obtained by (H.Möbius, 1940), and it is also remarkable that the result of (H.Möbius, 1940), was achieved when the groove depth was 0.11 times the diameter and the groove width to depth ratio was 8.1 Some conclusions that can be made from his findings are:

- The friction factor varies less than $\pm$ 10 percent about a mean value in the whole Reynolds number range when the relative roughness is greater than 0.03.
- The highest friction factor was found for a groove width to depth ratio in the range 6-8.
- The friction factor scales very well with geometry. Two pipes with different diameters but the same $\frac{e_{gs}}{D_h}$ and $\frac{L_{gs}}{e_{gs}}$ ratios gave friction factors that varied less than 5 percent over the entire Reynolds number range.
- The sharpness of corners has a significant influence on the friction factor. If scaling of the geometry should work one would also have to pay close attention to the scaling of corner roundness.
- Regarding leakage the results show a maximum friction factor of about 0.27 at a Reynolds number of 10000 giving a flow rate of about 1/3 of that from a smooth pipe of the same hydraulic diameter.

For the seals in Table 2.2 the $e_g/(D_h)$ ratio is higher than the ratio tested by (H.Möbius, 1940) while the $L_g/(e_g)$ ratio is smaller. On the other hand the results of (H.Möbius, 1940) did not go beyond the relative roughness of 0.14 so no conclusion could be made whether an increased groove depth would increase the friction factor even further.

In the results by (Wiederhold, 1949) a peculiar type of surface roughness caused by deposits on the pipe wall gave a much higher pressure drop than anticipated. In a 0.5 m diameter pipe used for water transport a rib like structure with the "ribs" perpendicular to the flow direction and average rib peaks of 0.7 mm gave a pressure drop corresponding to an equivalent sand grain roughness of 14.6 mm at a Reynolds number of $1.38 \cdot 10^5$. The radial velocity profile was also measured and found to be very similar to that of the corresponding sand grain roughness, which indicates that it is unlikely that secondary flow patterns could be the cause of the unexpected large pressure drop. For the pipeline the reduction in maximum flow rate due to rib like wall deposits was about 57% compared to the new pipe. The trend in the friction factor above is also supported by the profile number 18, Table 2.1, in the experiment of (Schlichting, 1936). Both profiles indicate that for low relative groove roughnesses the friction factor may vary a lot more with Reynolds number than for the relative roughnesses greater than 0.03 reported by (H.Möbius, 1940). (Wiederhold, 1949) suggested that the cause of the large pressure drop experienced for the particular type of roughness in the pipe line could be due to a resonance effect in boundary layer vortices, but to the author's knowledge the proof of such an effect has not been given to date.

Regarding the low friction factors achieved for annular seals in Table 2.2 in comparison to the maximum achieved by (H.Möbius, 1940), some explanation can be given based on the results and conclusions of (Yamada, 1962a)

- The value of the friction factor becomes maximum when the land width, L_l, (Fig. 2.4) approaches zero. Hence, the relatively long land widths for the seal studies in Table 2.2 contribute to a low value for the friction factor.

- The maximum value of the friction factor is achieved when the seal groove depth is small compared to the clearance. Hence, seal grooves of the same order or greater than the seal clearance give low values for the friction factor.

Since all the groove seal experiments involve a smooth rotor or stator the smooth surface contributes to reduce the total friction factor for the seals. By putting grooves on both rotor and stator and keeping the land zone as small as possible the friction factor might increase considerably, but more experimental/numerical results are needed to determine the amount of increase.

The main focus of the studies by (Nordmann *et al.*, 1987), (Florancic, 1990), (Marquette *et al.*, 1997), (Black & Cochrane, 1973),and (Kim, 1985) was rotordynamic coefficients and a limited number of geometries were studied. However, from (Black & Cochrane, 1973) one can conclude that:

- For the given seal clearance, groove spacing and width the friction factor increases when groove depth/hydraulic diameter goes from 0 to .35 while it decreases thereafter as groove depth is increased.

Another conclusion of (Yamada, 1962a) is that:

- A large value of the axial friction factor can be achieved without increasing the friction torque significantly.

This indicates that the friction factor for grooved seals is highly anisotropic and that mechanical pump losses may be kept relatively constant while leakage is reduced significantly.

Similarly in pipe flow (Weiss, 1993) the effect of longitudinal riblets parallel to the axial flow have been shown under optimal conditions to give 5-10% reduction in wall friction relative to hydraulically smooth surfaces. A great deal of research has been put into the field of drag reduction during the last two decades for many application (see for example (Hirschel *et al.*, 1988)), and it turns out that drag reduction only occurs around the relative roughness range studied by (Wiederhold, 1949) for transverse ribs. For seals, however, this type of micro-grooves will possibly be of little benefit due to wear of the surfaces.

2.3.2 Entrance loss

The definition commonly used for the entrance- (ξ) and exit loss (ξ_e) coefficients (Childs, 1993) for a seal is given by:

$$P_s - P_{in} = \frac{\rho}{2}(1+\xi)W^2 \tag{2.7}$$

$$P_{ex} + \frac{\rho}{2}(1+\xi_e)W^2 = P_e \tag{2.8}$$

where P_s is the inlet chamber pressure, P_{in} and P_{ex} are the pressures just inside the seal at the entrance and exit respectively, ρ the fluid density, W the axial fluid velocity, and P_e is the exit chamber pressure.

For pipe flow (White, 1994) documents pipe entrance losses from a "infinite" reservoir into a pipe with various entrance geometries (see Fig. 2.6). For seals (Kündig, 1993) has documented a similar trend in results for a finite inlet chamber as one can see from Fig. 2.6. The results of (Kündig, 1993) are given as a function of Reynolds number, and a variation is found with a mean value that is close to the single coefficient documented for pipe flow. For seals a significant inlet chamfer may easily occur due to the machining process or wear. Such chamfers will reduce the entrance loss, increase leakage slightly, and change the direct stiffness of the seal. (Kündig, 1993) argues that the entrance should be made as sharp as possible to get maximum entrance loss. However, considering Fig. 2.6 for a reentrant pipe the entrance loss indicates that there might be even more to gain by a protruding inlet. To the author's knowledge protruding inlets have not been tested for seals.

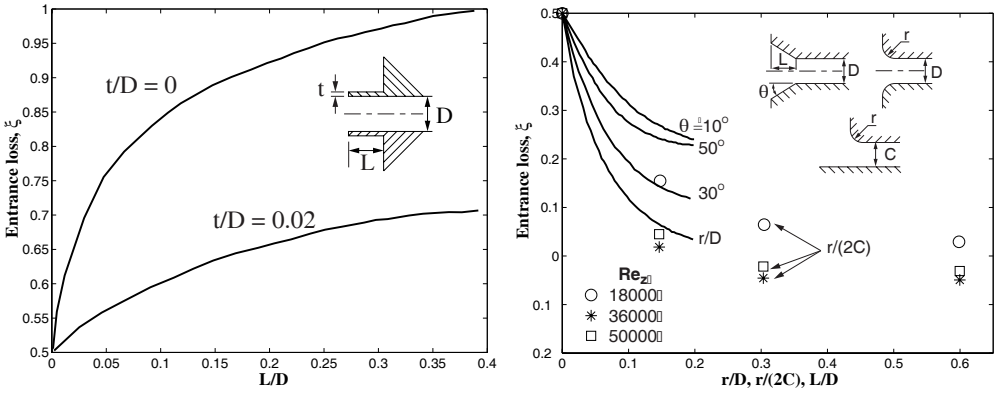

Figure 2.6: Left figure: Entrance loss coefficient from an infinite reservoir to a reentrant pipe for turbulent flow, (White, 1994). Right figure: Infinite reservoir entrance loss coefficient for pipes with turbulent flow from (White, 1994) and finite reservoir coefficients for an annular liquid seal from (Kündig, 1993) for three different Reynolds numbers and zero swirl.

An important finding by (Kündig, 1993) was that the entrance loss was dependent

on the ratio of the circumferential- to axial flow, and he suggests the formula.

$$\xi = \xi_O 10^{\frac{U}{12W}} \tag{2.9}$$

where ξ_O is the entrance loss at zero swirl and U, W are the tangential and axial bulk velocities. There are, however, several points regarding this formula that need further clarification:

- Since the formula was derived for a finite chamber of width and height just one order of magnitude greater than the seal clearance, the flow field in the chamber itself might affect the coefficient.
- For the large clearance studied, 1.8 mm, there will be a radial pressure gradient at the inlet for high U/W ratios. This means that it might be necessary to resort to a two-dimensional mass flow average definition of pressure and kinetic energy, instead of Equations 2.7 and 2.9.
- Since only two clearances were considered it is uncertain whether Eq. 2.9 is independent of the C/R ratio.

(Athavale *et al.*, 1993) document similar trends to Eq. 2.9 by a CFD code while in some experiments on seals, for example in (Childs *et al.*, 1988), the trend in results for the inlet coefficient are mixed. Some seals show an increased inlet loss coefficient as the ratio of tangential to axial bulk velocity increases while others show a decrease. Related experiments by (Florancic, 1990) and (Kilgore & Childs, 1990) on coarsely grooved seals, which theoretically can be treated as a succession of inlet and exit losses for each groove, show a marked increase in leakage for high rotational speeds. This is the opposite effect of the formula by (Kündig, 1993). So there appears to be an inconsistency in results and further investigations are needed.

For Eq. 2.7 fully developed friction factor models are usually applied from the seal entrance while there in fact will be a flow development. For pipe flow this effect has been studied by (Barbin & Jones, 1963) who also studied the friction factor variation for flow between flat plates. In (White, 1994) it is shown that for a pipe the maximum development length for laminar flow is $138 \cdot diameter$ at the critical Reynolds (maximum Reynolds number before onset of turbulence = 2300). For Reynolds numbers in the range $4000 - 10^8$ the corresponding development lengths are $18 - 95$ times the pipe diameter. (Elrod, 1988) included this entrance effect in gas seal analysis and measured the friction factor variation along the seal experimentally. Both experimental and theoretical results showed a much larger friction factor at the seal entrance than the one for fully developed flow. By including the entrance effect in the theoretical model for predicting rotordynamic coefficients better agreement with experimental data were found. For liquid annular seal the developing flow does not appear to have a great influence for seals where the length is two orders of magnitude greater than the clearance. However, as seal length is decreased, this effect might be more pronounced. In this thesis this entrance effect will not be considered since very short seals were not in focus.

2.3.3 Exit losses

For a sharp corner pipe exit into an infinite chamber it is stated in (White, 1994) that there will be no pressure recovery at the exit and hence the exit coefficient is 1. For seals this is the most commonly assumed value for predicting rotordynamic coefficients. In the literature on seals there are relatively few references to this subject. (Stampa, 1971) documents exit coefficients between 0.5 and 1.0 as a function of axial Reynolds number for liquid annular seals for a finite exit chamber, but there were large margins of uncertainty and the number of geometries studied was limited. (Florancic, 1990) documents that when predicting rotordynamic coefficients the best fit to experimental data was achieved when the exit coefficient was set to 0.85 and to 0.7 for two different seals, where the second had twice the clearance of the first. However, the exit coefficient were not measured directly which means that the value is somewhat uncertain. The measurements by (Weber, 1971) show that the exit coefficient will vary as a function of the ratio between round off radius and seal clearance similar to a diffuser. From (White, 1994) fully developed turbulent flow into a conical diffuser of 5°, 20° and 40° cone angle gives an exit loss coefficient $\xi_e = 0.3$, 0.5 and 1.0 respectively. According to the theoretical calculations of (Childs, 1993) a change in the exit loss coefficient from 1.0 to 0.5 approximately doubled the direct stiffness of a specific seal, but to the author's knowledge no experiments have been carried out to study dynamic coefficients as a function of exit cone angle of the seal. Since a swirling flow will be present at the seal exit this will also influence the "diffuser"-performance. According to (Schetz & Fuhs, 1996) swirl suppresses flow separation, and in (McDonald *et al.*, 1971) it was found that diffuser performance could be increased by up to 40% for those diffusers that had flow separation for pure axial flow. Also it is mentioned in (Schetz & Fuhs, 1996) that for swirling flow the simple relationship for diffuser performance which is similar to that given by Eq. 2.7 no longer holds and that an integral relationship which involves the mass average value of pressures and inlet kinetic energy should be used. Since it is very tedious to achieve mass average values experimentally, (Schetz & Fuhs, 1996) conclude that the data available are not extensive and in many cases only qualitative.

More studies are needed to quantify the exit coefficient as a function of swirl and the seal exit and exit chamber geometry. Also experiments on dynamic characteristics are needed to verify whether the theoretical predictions for a given exit coefficient hold.

2.4 Bulk flow model

An important contribution to the theory of turbulent thin films in journal bearings and seals is found in (Hirs, 1973) who introduced the "Bulk-Flow Theory", which does not consider fluctuations in local velocities due to turbulence or the shape of the velocity profiles when relating average fluid velocity to wall shear stresses. This simplified mathematical modelling of seals compared to previous models since radial effects were eliminated without significant loss in accuracy. In order to calculate the pressure distribution for a seal or journal bearing with turbulent flow it is important to consider the combined effect of Couette and Poiseuille flow, since the flow usually

is both shear and pressure driven. By the theory of (Hirs, 1973) the wall shear stress that contribute to pressure changes are calculated based on the knowledge of the average flow velocity vector relative to the wall and friction factors developed for Poiseuille flow. For an isotropic rotor surface roughness the wall shear stress, τ_r, that contributes to the pressure gradient in the direction of the bulk flow direction is according to (Hirs, 1973)

$$\tau_r = \rho f_r \frac{U_r^2}{2} \tag{2.10}$$

where U_r is the total Poiseuille/Couette bulk velocity relative to the rotor surface. Similarly for the stator surface

$$\tau_s = \rho f_s \frac{U_s^2}{2} \tag{2.11}$$

Both friction factors f_s and f_r are based on Poiseuille flow only. Although (Hirs, 1973) pointed out that the actual shear stress on the surface, which is needed for mechanical loss calculation, is slightly different when a Couette flow component is present, this fact appears to have been neglected in later implementations for liquid annular seals.

Consider a seal that has no axial flow. If one uses the formulation directly the rotor shear stress is due to Couette flow only, and the above formulation gives a shear stress which is overestimated by approximately 20% due to the difference in friction factors for Poiseuille and Couette flow, according to (Hirs, 1973). Since this is likely to be the extreme case, and since an overestimate of the mechanical loss would be conservative for pump design this fact is not elaborated on in this thesis.

2.5 Dynamic characteristics

The fluid friction model in (Yamada, 1962b) was later adopted by (Black, 1969) in his theoretical prediction of dynamic characteristics of liquid annular seals. In (Black, 1969) the effect of the seal entrance loss factor which particularly contributes to seal direct stiffness was also taken into account. (Lomakin, 1958) documented the self centering ability of high pressure seals today usually referred to as the "Lomakin" effect due to axial flow in an eccentric seal. It counteracts the radial outward force that is obtained when the Bernoulli equation is applied to the circumferential flow. The two effects are shown in separate idealised versions in Fig. 2.7. For most seals the rotor will orbit around the seal centre at a small eccentricity ratio (typically less than 0.5), and there is no cavitation or recirculation present. The theoretical solution to seal dynamic coefficients differs from that of journal bearings due to a several factors. Journal bearings usually have little axial flow which means that the

Lomakin effect is negligible. They operate at lower pressures and usually cavitate, and the large eccentricity introduces a wedge that influence the pressure gradient. Added mass effects are normally negligible which means that the inertial terms in the Navier Stokes momentum-equations can be omitted. Viscous heating must normally be included which means that a coupled solution between the Reynolds equation and the energy equation must be carried out.

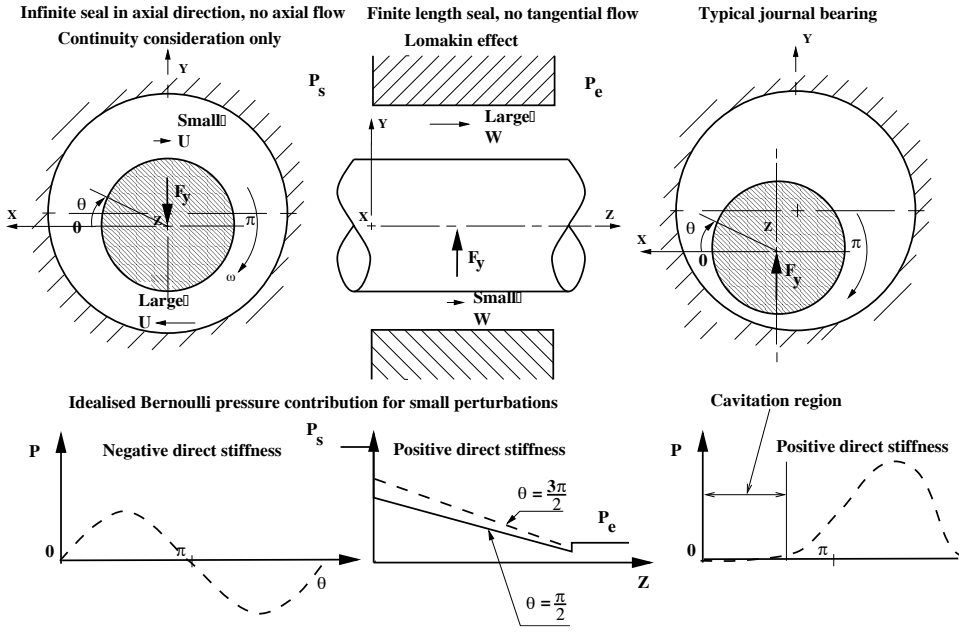

Figure 2.7: Idealised Bernoulli and Lomakin effects, and typical journal bearing pressure distribution.

(Black & Murray, 1969) solved the one-dimensional flow problem for a concentric rotor and made a perturbation solution that yielded analytical expressions for stiffness, damping, and added mass coefficients for the seal. Their solution covers laminar, transition, and turbulent flow for smooth rotors and stators. Main weaknesses of the theory by (Black & Murray, 1969) are that the tangential velocity is assumed to be fully developed Couette flow and that surface roughness effects are not considered.

In (Black *et al.*, 1981) the swirl development within the seal was predicted to some degree of accuracy and shown to have a significant influence on cross-coupled stiffness.

Based on the bulk flow theory of (Hirs, 1973) an improved solution was given by (Childs, 1983) which included swirl calculations and the possibility to deal with surfaces of different roughness. Also procedures for calculating moment coefficients by the same method were presented in (Childs, 1982). In (Childs, 1993) it is suggested that moment coefficients should be included for seals with length to diameter ratios of 1 and greater, which would be typical for balance piston seals. The main weakness

of the solution based on the Hirs friction factor was that for rough seals the friction factor had to be calibrated to experiment.

An important discovery by (von Pragenau, 1982) was that a greater surface roughness on the stator relative to the rotor reduced the average tangential fluid velocity in the seal. This in turn reduces both cross-coupled stiffness and the onset speed for self excited vibrations from the seal.

To directly take into account surface roughness the Moody based solution is attractive due to its simplicity and a comparison between the Moody and Hirs solution for dynamic seal coefficients is made in (Nelson & Nguyen, 1986). The implementation of the two models for seal analysis is described in detail in (Childs, 1993). (Scharrer & Nelson, 1991) also documents the effect of partial roughened seal surfaces on incompressible liquid seal characteristics.

An extension to the one-dimensional model by Childs was made by (San Andres, 1991) who solves the bulk flow in both axial and tangential directions. This model makes it possible to include variations in fluid properties and film thickness in the tangential direction. A further development was made by (Zirkelback & San Andres, 1996) who include surface roughness effects in the transition regime between laminar and fully turbulent flow. In the publication of (Zirkelback & San Andres, 1996) there are, however, no comparisons to experimental solutions to verify the applicability of the theoretical results.

Although the Moody friction factor includes a parameter for the absolute roughness height it does not take into account the shape or distribution of the roughnesses, and it is limited to roughness heights 0.05 times the hydraulic diameter. In (Childs & Fayolle, 1998) where deep round hole pattern stator surfaces are studied for a liquid annular seal it is concluded that the friction factor by (Moody, 1944) would not be valid.

Some attempts to deal with grove and hole pattern seals have been made by using a Hirs based solution. (Nordmann *et al.*, 1987) made extensions to the model by (Childs, 1983) to include the extra circumferential flow of grooved seals, and (Childs *et al.*, 1990) and (Childs & Fayolle, 1998) used the Hirs solution for hole pattern seals. These and later experiments by (Kilgore & Childs, 1990) for grooved seals show unexplained large differences between some of the predicted and measured dynamic coefficients. Since experiments were needed to predict the effect of a given surface pattern, the Hirs based method does not make it possible to predict what groove and hole pattern would be best for a particular seal.

An improved three volume method for predicting leakage and dynamic coefficients for circumferentially grooved seals was suggested by (Florancic, 1990) and later modified by (Marquette *et al.*, 1997). These models include approximations of the flow field inside the grooves, and by calibration of a small number of coefficients very good correspondence with experimental results was found.

At present no similar model for hole pattern seals has been suggested, and the current models for circumferentially grooved seals need calibration to experimental data for every groove width to depth ratio, groove depth to seal clearance ratio, and rotational speed.

2.5.1 Gas- and two-phase seals

A wide range of gas seals and models have been discussed in the literature and an extensive summary of these with some detailed derivations are given in (Childs, 1993). Here some of the main references on this topic are given.

In gas seals the fluid should generally be treated as compressible and for seals containing water-steam or water-air the different phases and their interaction should be treated in order to predict seal characteristics. (Nelson, 1985) extended the incompressible tapered annular seal model by (Childs & Dressman, 1985) to include a compressible perfect gas formulation. For a labyrinth seal a one-control-volume model was suggested by (Iwatsubo, 1980), and (Iwatsubo *et al.*, 1982) and later expanded to a more physically correct two-control-volume model by (Wyssman *et al.*, 1984). (Nordmann & Weiser, 1990) have made a three-control-volume model following the method of (Florancic, 1990). (Dietzen & Nordmann, 1987) solve the Navier-Stokes equation for labyrinth seals including a first order perturbation to find dynamic coefficients. The Navier Stokes solution offers an alternative attractive approach but the computational time is several orders of magnitude above that of bulk flow models. Recent detailed measurements of the flow field in a labyrinth seal (Morrison & Johnson, 1996) could serve as verification cases for future CFD simulations.

Two-phase flows in seals and the effects on rotordynamics has rarely been discussed in the literature. (Iwatsubo & Nishino, 1994) report theoretical results for homogeneous two-phase air/water seals that match qualitatively with measurements. Thermodynamic analysis of water/steam seals have been studied by (Beeler, 1985), (Beatty & Hughes, 1987) and stratified flow analyses were performed by (Beatty & Hughes, 1990). However, dynamic coefficients were not an issue in the water/steam analyses. For journal bearings (Braun *et al.*, 1987) offer a homogeneous two-phase solution to the generalized Reynolds Equation for thin film lubrication which is not directly applicable to seals. One reason why so few data are available for two-phase dynamic coefficient may be that pump manufacturers design two-phase pumps so that they can deal with 100% gas and 100% liquid and assume that these cases will be the limiting ones for the design. The results of (Iwatsubo & Nishino, 1994) support this assumption. This means that if the seal forces are destabilizing on the system the pure liquid seal will excite the system with a greater force than the pure gas seal and if the seal forces are stabilizing on the system behaviour the gas seal will have a smaller stabilizing force than the liquid seal. However, in (Iwatsubo & Nishino, 1994) where this conclusion was made, shock waves were not considered. Hence, one cannot conclude in general that the single phase gas and liquid calculations will give the limiting factors for design.

Since liquid annular seals were of main interest to the industrial partners of this project, gas- and two-phase seals will not be considered further in this thesis.

2.6 Detailed Navier Stokes solutions

Computational Fluid Dynamics, CFD, has in addition to experimental and purely theoretical research become "a new third approach in the philosophical study and development of the whole discipline of fluid dynamics" (Anderson Jr., 1995). With CFD the fundamental equations for fluid flow can be solved by dividing an arbitrarily shaped volume of fluid into a discrete number of points at which unknown variables like velocity, pressure, etc. can be computed. In theory the fundamental Navier-Stokes equations (see for example the derivation in (White, 1994)) can be used to solve all the details of a flow field, but in practice the computational effort in doing so is too great. One major challenge is to deal with turbulence (see definitions in (Tennekes & Lumley, 1972)).

2.6.1 Turbulence models

Since the length scales of turbulent flow typically are several orders of magnitude smaller than a practical computational grid approximate models have been suggested. The Reynolds-Averaged Navier-Stokes (RANS) for incompressible flows, as derived in for example (White, 1994), provide a starting point for turbulence modeling and practical turbulent flow computations.

The fluctuating velocities due to turbulence introduce six unknowns in the RANS equations and many turbulence models that attempt to calculate these have been proposed. None of them have proved to be superior to the others for all types of flow. It is therefore up to the user of a CFD program to chose the method which is most appropriate for a given problem (see for example the discussion in (Rodi, 1993)).

Although the detailed solutions of the Navier - Stokes equations offer new insight into effects like secondary flow pattern Taylor vortices, new questions arise about the turbulence and wall models used. The much used $k-\epsilon$ turbulence model, for which two partial differential equations are solved for turbulent kinetic energy production (k) and dissipation (ϵ), does not include the boundary layer development from the seal entrance or arbitrary wall roughness effects. Also authors like (Launder & Spalding, 1974) and (Rodi, 1993) question the applicability of the $k-\epsilon$ turbulence model for swirling flows and comment that some of the constants in the model need to be calibrated to the specific flow in order to yield good results.

(Rodi, 1993) discusses a range of available turbulence models and their applicability. Apparently a Reynolds Stress differential turbulence model may offer an interesting solution to fluid flow in seals since it allows for anisotropic turbulence effects. No results for whirling seals with this type of turbulence model where found in the literature survey.

2.6.2 CFD solutions to whirling seals

The early work by (Dietzen & Nordmann, 1986) describes a quasi 3-D Finite-Difference based technique for solution of the Navier Stokes equation for incompressible flow in

polar coordinates and includes turbulence by the $k-\epsilon$ model. First order perturbation equations were also solved and rotordynamic coefficients compared well to the bulk flow solution of (Childs, 1983). Later (Dietzen & Nordmann, 1988) gives a full 3-D solution to the Navier Stokes equations in a rotating frame of reference. This solution permits finite perturbations which enable studies of eccentricity effects. A limitation of the solution is the assumptions of inlet and exit conditions which are not accurately known. (Nordmann & Weiser, 1988) showed similar solutions to Labyrinth Seals and got good agreement with experimental data for rotordynamic coefficients.

For liquid annular seals (Baskharone, 1994) and (Athavale *et al.*, 1995) compared the theoretical solutions of the detailed three-dimensional flow field based on the $k-\epsilon$ turbulence model and laser anemometer measurements by (Morrison *et al.*, 1992) and (Thames III, 1992). (Athavale *et al.*, 1995) conclude that the agreement between the theoretical solution and the experimental is fair to good but they comment that the measurements show that the turbulence in the seal is clearly anisotropic, which means that the isotropic $k-\epsilon$ model has limited applicability.

(Baskharone, 1994) concludes that the theoretical solution obtained by his perturbation approach to a whirling seal yields good results in the downstream half of the seal where admission losses have dissipated. He also makes the important note that the pressure field which is needed to obtain rotordynamic coefficients is among the least sensitive thermophysical quantities. Hence, it is quite possible to get reasonable results for rotordynamic coefficients although other details of the flow field have been poorly solved. Since the flow field inside a seal has a clearly identifiable length scale it is also possible to use simpler turbulence models than the $k-\epsilon$ and still get good result for fluid dynamic force. For example (Tam *et al.*, 1988) use a mixing length concept described in (Launder & Spalding, 1974) and a lumped model of fluid dynamic force (from (Muszynska, 1986b) - (Muszynska, 1986a)) based on the average circumferential velocity ratio.

In order to handle complex geometries in an easy manner (Baskharone & Hensel, 1991a) and (Baskharone & Hensel, 1991b) used a Finite Element based Navier Stokes solution that includes a perturbation solution that stems from the discrete finite-element form rather than the differential form used by for example (Dietzen & Nordmann, 1986). (Baskharone & Hensel, 1991a) compare results for radial velocity profiles in the seal to measurements done by (Morrison *et al.*, 1988) and does numerical studies on grid refinement to get an optimal grid that has negligible numerical errors and gives minimum calculation time.

(Athavale *et al.*, 1993) and (Athavale *et al.*, 1994) describe a three-dimensional CFD code based on the Finite Volume method to predict fluid flows and fluid forces accurately in seals. In (Athavale *et al.*, 1993) a low Reynolds Number $k-\epsilon$ turbulence model was used to simulate the transition regime between laminar and fully turbulent flow. Very good correlations between theoretical and experimental results by (Kanemori & Iwatsubo, 1992) were presented.

As discussed above, surface roughness effects can contribute significantly to leakage and seal rotordynamics. (Tam *et al.*, 1988) used different multipliers to smooth friction factors for axial and circumferential flow based on a calibration to experiment. Another approach to surface roughness treatment was made by (Lucas *et al.*, 1994)

and (Lucas *et al.*, 1996) who used an algebraic turbulent coefficient model derived from generalized Couette flow. Their model was limited in protrusion height and no relevant experimental data were available to determine whether their model was superior to the bulk flow model in (Childs, 1993). In a series of publications (Arghir & Frêne, 1997c), (Arghir & Frêne, 1997a) a Navier-Stokes, $k-\epsilon$ solution to seals is outlined, and in (Arghir & Frêne, 1997b) wall roughness effects are introduced based on the work by (Koh, 1992). (Koh, 1992) implements a wall law that is adjustable to several types of surface roughness distributions in addition to the usual sand-grain roughness treatment, and the law is made general enough so that there are no apparent limitations to the size of the roughness protrusions. However, as surface roughness geometry becomes so large that the fluid flow in the voids or protrusions become important CFD is currently not used due to the large computational efforts needed. Examples of such roughness geometries are hole-, diamond-, and honeycomb-pattern seals where the pattern has depths similar to the seal clearance.

2.6.3 Advantages and disadvantages of CFD

CFD- offers an alternative approach to bulk-flow models and has certain advantages and disadvantages which are listed below.

Advantages:

- Effects from secondary flow fields may be studied.
- Model geometry can be extended beyond seal entrance and exit.
- Details of the seal flow may be studied and increase the understanding of the physical phenomena.
- Transient solutions including the seal whirling motion with a defined eccentricity may be performed.
- One may potentially increase accuracy of solution compared to bulk-flow models.

Disadvantages:

- Long computational time, possibly hours or days instead of seconds which is common for bulk-flow solutions.
- The accuracy of turbulence models is limited.
- Discrete types of roughnesses in three dimensions like hole-, diamond-, and honeycomb patterns are difficult to approach with this method due to the large computational efforts needed.

In this project it was desired to produce a fast and easy to use tool for predicting seal characteristics. Hence, it was decided not to use a full CFD approach. Also the approach in this thesis allows the analysis of hole-pattern seals which is currently beyond the capabilities of CFD solutions.

However, it was decided to use a commercial CFD-program, CFX, developed by AEA-Technology, UK, for detailed studies of seal surface profiles and inlet/outlet geometry effects that could be applied in a bulk-flow formulation.

2.7 Conclusions from the literature survey

Based on the literature survey it was concluded that circumferentially grooved surfaces show good potential for leakage reduction while keeping mechanical losses close to those for smooth seals. Although a some groove width and depths relative to seal clearance or pipe diameter have been studied in the past no analytical friction factor exists that cover a wide range rectangular groove geometries. Since studies using CFD had proved to yield good results for leakage predictions for numerous grooved seals it was decided to use CFD to study a range of groove geometries not covered in the literature. The goal being to derive an analytical friction factor for engineering use. This is the topic of Chapter 3 where also a friction factor for hole pattern seals will be proposed.

Although seal bulk flow models predict dynamic coefficients well for plain seals and seals with a machining type roughness, the methods lack accuracy when dealing with groove and hole pattern seals. It has been concluded in the literature that lack of an accurate friction factors may be a major reason for discrepancies in results. Hence, it was decided to use the friction factor developed in Chapter 3 in a bulk flow theory approach described in (Childs, 1993) and (Nordmann *et al.*, 1987), for predicting rotordynamic coefficients. Chapter 4 covers this theory and comparisons to experimental result.

Since future research might produce new friction factors for other types of surface roughnesses it was decided to modify the theory development so that inclusion of new friction factors would be simplified. It was also found in (Childs, 1993) and (Nordmann *et al.*, 1987) that moment coefficients for tapered annular seals where missing in their bulk flow approach, so their theory was modified to include these coefficients in Chapter 4.

Since the attractive friction factor for the transition to turbulent flow by (Zirkelback & San Andres, 1996) had not been implemented in the approach by (Childs, 1993) it was decided to do so in this thesis, and to compare the result to those by (Iwatsubo & Sheng, 1990) to verify if this friction factor would improve the results for rotordynamic coefficients in the transition to turbulence region.

Regarding seal exit loss the knowledge regarding what factors influence it seemed to be weak. Since the inlet loss coefficients dependency on swirl is inconclusive in previous research a test-rig was proposed to investigate both inlet- and exit coefficients. It was also decided to study the friction factor for turbulent flow in shallow grooved seals, and to do comparisons of transition to turbulence friction factors for machine roughened seals. From the experiment, comparisons to the theoretical friction factors used in this thesis could also be made. Chapter 5 concerns this experiment.

Chapter 3

Seal leakage predictions by CFD

3.1 Introduction

In this chapter a friction factor will be developed for seals with rectangular grooves and a friction factor for hole pattern seals is proposed based on a similarity assumption. By deriving explicit analytical formulas for predicting friction factors for grooves and hole patterns the leakage and tangential friction of seals that have any of the 16 rotor stator combinations below can be studied:

Table 3.1: Stator and rotor roughness combinations.

ROTOR	STATOR
Smooth	Smooth
Machining Roughness	Machining roughness
Grooved	Grooved
Hole pattern	Hole pattern

It is known from the literature on grooved seals that the friction factor in the axial direction is significantly smaller than than the tangential for the same bulk flow velocity. The first part of this chapter deals with axial friction and the second part with tangential friction. It was decided to study a test matrix of 88 different groove geometries by using Computational Fluid Dynamics (CFD). The purpose of the proposed study was to:

- Find suitable groove patterns for leakage reductions.
- Derive analytical expressions for the groove friction factors which can be used in mathematical models for predicting rotordynamic characteristics.

- Suggest a friction factor for hole pattern seals based on an assumption of similar flows in grooves and holes.

With CFD only a fraction of the seal needs to be analyzed in order to extract the friction factor needed for computationally fast and easy to use bulk flow models. Although there are several limitations in CFD such as the accuracy of turbulence models, limits to discretisation, and the accuracy of boundary conditions it has proved to give useful results for grooved seals in the past, see for example (Nordmann & Weiser, 1988). The software used for the computations are described in Appendix A.

3.2 Description of numerical study

Fig. 3.1 shows a seal with grossly exaggerated clearance and taper. The friction factor may be given in different formats, and the one used here is the so called Fanning format which was used for seals by (Black, 1969). For a seal with constant clearance it is given by

$$P_{in} - P_{ex} = 4f\left(\frac{L}{2C}\right)\frac{\rho W^2}{2} \tag{3.1}$$

where P_{in} and P_{ex} are the pressures at the seal inlet and exit respectively, f is the friction factor, L is the seal length, $C_{in} = C_{ex} = C$ is the minimum film thickness, W is the bulk axial velocity ρ is the fluid density.

In order to find the average friction factor given by Eq. 3.1 for a grooved seal the hypothesis was that one can split the grooved surface into three different control volumes as shown in Fig. 3.2 and calculate the friction factor for rotor-stator and groove-land separately. When the shear stress on each surface is known the combined average shear can be calculated. Control volume I in Fig. 3.2 can be treated as regular plain seal and the wall friction can be calculated when bulk velocities are known. For control volume II the only unknown shear stresses are τ_{zgs} and $\tau_{\theta gs}$. So the objective in the CFD analyses sections was to determine explicit formulae for these shear stresses. For a concentric seal there will be no net radial flow in control volume III so this volume was not considered.

In the numerical study the minimum clearance is constant, but at the end of the chapter tapered seals will be taken into account by including the local minimum see through film thickness H (see Fig. 3.1) in the formulation.

The test matrix of groove geometries proposed is shown in Table 3.2 and Fig. 3.3.

Experimental studies by (H.Möbius, 1940) discussed in Chapter 2 indicate that the friction factor can be assumed constant over a wide range of Reynolds numbers (6000 - 450000) with an accuracy of about $\pm$ 10 percent. The hypothesis of insignificant Reynolds number dependency was tested for the range $50000 < Re_z < 200000$ for one of the geometries. The hypothesis was found to hold within similar limits as

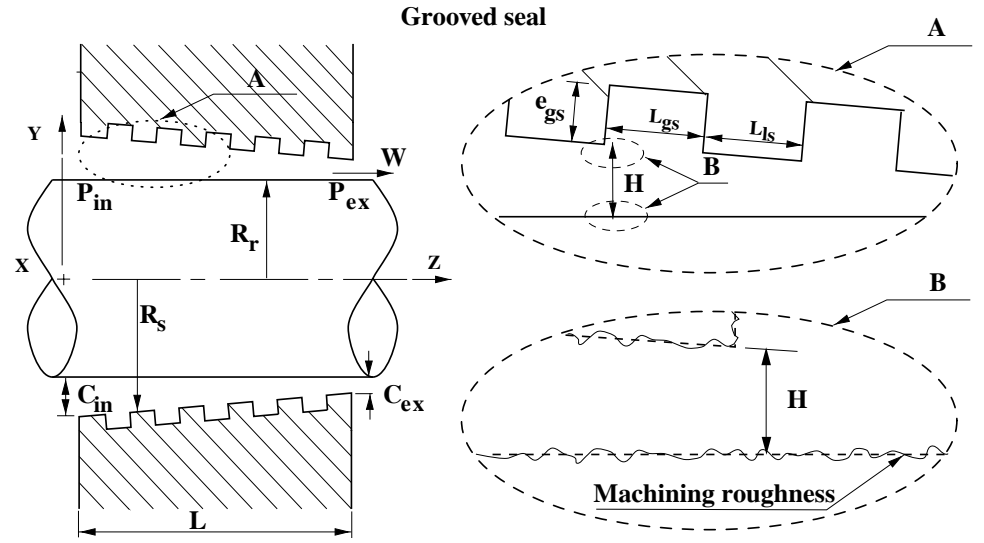

Figure 3.1: Tapered and grooved liquid annular seal with exaggerated clearance and taper. Detail A shows the parameters for the groove patterns to be studied in this chapter. Detail B shows the machining roughness.

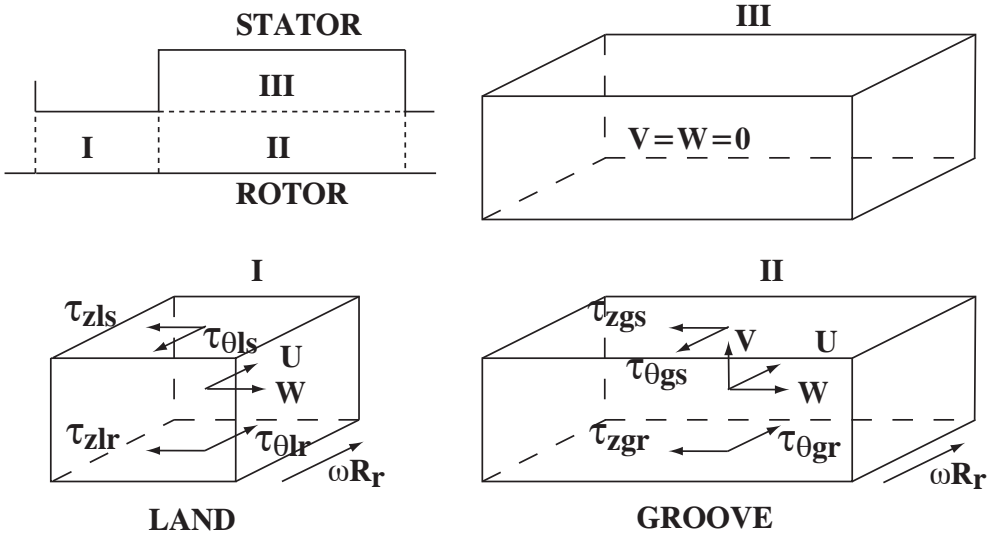

Figure 3.2: Description of shear stresses, wall velocity, bulk flow velocities for groove and land portions of the seal.

Table 3.2: Geometry and fluid properties description.

$\frac{L_{gs}}{e_{gs}} =$	1, 2, 3, 4, 6, 8, 12, 16
$\frac{e_{gs}}{2C} =$	0.10, 0.20, 0.267, 0.40, 0.571, 0.80, 1.067, 1.60, 3.20, 6.40, 12.90
$e_{gs} =$	0.08 mm, is constant throughout
$\rho = 1000\ kg/m^3$, $\mu =$ 1e-4 $Pa \cdot s$, $R_r = 50.0$ mm, $Re_z = 100000$, $\frac{L_{ls}}{L_{gs}} = 0.6$	

the experimental results of (H.Möbius, 1940). Hence the Reynolds number was kept constant at 100000 for the remaining analyses.

For the land-width influence (Florancic, 1990) and (Marquette *et al.*, 1997) used the friction factor by (Moody, 1944) for the land part and a separate treatment for the grooves. An introductory numerical study was carried out, and it supported the validity of this approach. Hence, by deriving a friction factor for the grooves separate from the land (see Fig. 3.2) the total friction factor could be calculated. In this study the land- to groove width ratio was kept at 0.6 throughout.

The axial friction factor dependency on rotational speed is very significant for flow in the transition between laminar and turbulent flow but much less so in the fully turbulent region as found in (Yamada, 1962a). To study the axial friction factor without swirl dependency the test matrix in Figure 3.3 was first studied with no rotational speed. Subsequently swirl was included to calculate the tangential friction and to study how the axial friction factor changes with rotational speed. The tangential

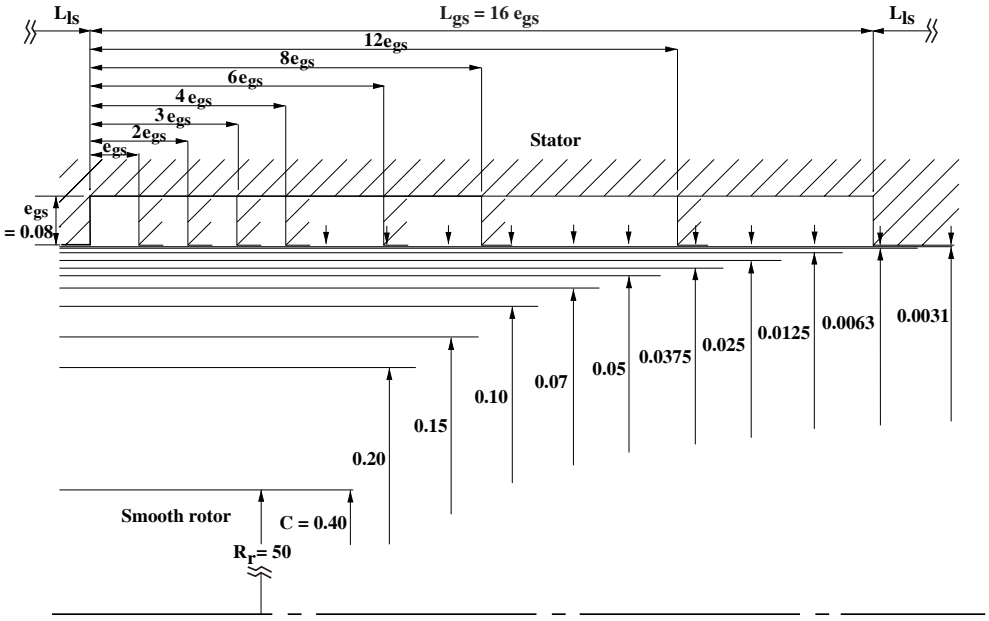

Figure 3.3: Overview of the 88 seal geometries. The land width L_{ls} is $0.6L_{gs}$ for the whole test matrix. Dimensions are in millimeters, R_r is constant.

friction is important to predict swirl development, rotordynamic coefficients, and mechanical loss accurately, and it will be developed at the end of this chapter with the assumption that the axial bulk velocity is in the same order of magnitude or greater than the tangential. The reason for this assumption beeing that most annular seals operate with predominantly axial flow.

The rotor radius to clearance ratio is greater than or equal to 125 for the proposed test matrix, and it is assumed that the friction factor is independent of this ratio. Comparisons between the friction factor developed in this chapter and experimental results by other authors support this assumption.

Although the test matrix for the numerical studies only involves grooves on the stator it is assumed that the friction factor developed is such that grooves can be placed either on rotor or stator or both. The experimental results of (Yamada, 1962a) support this assumption.

3.3 Model description

The geometry modelled for the axial friction factor analyses consists of an inlet section 10 times the clearance and an outlet section that is 30 times the clearance. The length of the rough part varies from model to model with a lower limit of 40 times the minimum clearance (see Fig. 3.4. These choices were made so that the inlet- and outlet boundary conditions would not influence the result significantly in the rough section. The length of the rough section itself was such that a fully developed flow would exist for parts of the section, and from this the friction factor was extracted. Table 3.3 shows a summary of the number of grooves studied for the test matrix.

Table 3.3: Number of grooves modelled for the various analyses, clearance is given in millimeters. $L_{ls} = 0.6L_{gs}$ and $e_{gs} = 0.08mm$ for all analyses.

$\frac{e_{gs}}{2C}$	$\frac{L_{gs}}{e_{gs}}$ 1	2	3	4	6	8	12	16
0.100	256	64	32	32	24	24	12	16
0.200	128	32	24	24	24	24	12	12
0.267	72	24	24	24	12	12	6	12
0.400	48	12	12	12	12	12	6	6
0.571	32	12	12	12	12	12	6	6
0.800	24	12	12	12	12	12	6	6
1.067	12	12	12	12	12	12	6	6
1.600	12	12	12	12	12	12	6	4
3.200	6	6	6	4	4	4	4	4
6.400	6	6	4	4	4	4	4	4
12.90	6	6	4	4	4	4	4	4

An example of the computational grid is shown in Fig. 3.7. Although geometric progression of cell sizes can be used to reduce the computational efforts it increases the numerical truncation error. For a central differencing scheme (Hirsch, 1988), which is used in the CFX-program (see Appendix A), it can be shown that the truncation

error is proportional to the difference in two consecutive mesh lengths. Hence, the mesh progression was kept as low as the computational resources allowed.

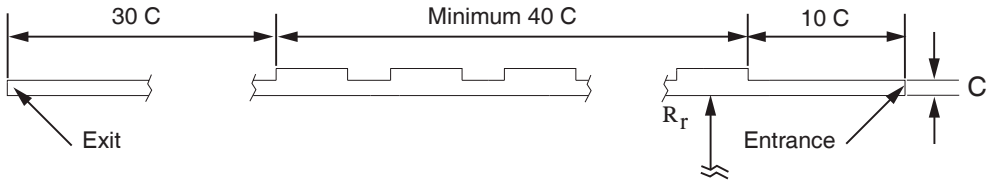

Figure 3.4: Model geometry

3.3.1 Grid details

The computational grid Fig. 3.6 shows a groove geometry modelled with a square grid and Fig. 3.6 shows a geometry where grid stretching was used. For a clearance between 0.0031 and 0.10 mm the number of cells across the minimum clearance was 8. For a clearance of 0.15, 0.20, or 0.40 mm the number of cells across C were 18, 25, and 40 respectively. A grid of square cells was used in the rough section if the total number of cells was below 180000. Otherwise the grid was stretched so that square cells were located at the entrance and exit corners where gradients in the flow field are large. The grid was stretched to maximum cell sizes at the middle of the groove (see Fig. 3.7) where gradients are small. In the inlet and exit regions the grid was stretched in the axial direction as shown in Fig. 3.5.

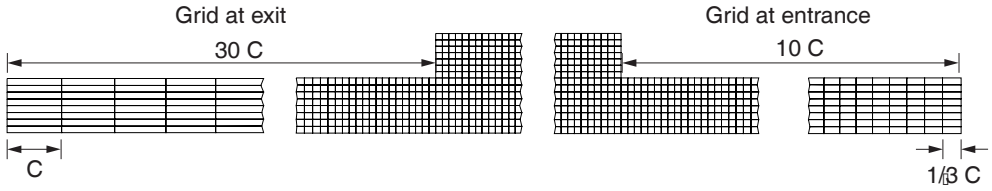

Figure 3.5: Example of grid stretching in entrance and exit portions of the model.

3.3.2 Boundary conditions

Fig. 3.8 describes the boundary conditions applied for the two-dimensional analyses. All the walls were treated as hydraulically smooth (White, 1994), and the default log law velocity profile wall function in CFX was used (CFX, 1997). For the inlet a uniform velocity was described (so called Dirichlet boundary (Hirsch, 1988)). Since the Reynolds number, Re_z, relative to the minimum clearance was constant for all analyses the axial velocity was calculated as shown in Fig. 3.8. Inlet turbulent kinetic energy, k, and the dissipation rate of turbulent kinetic energy, ϵ were specified as shown in 3.8. The expressions for k and ϵ were suggested in (CFX, 1997).

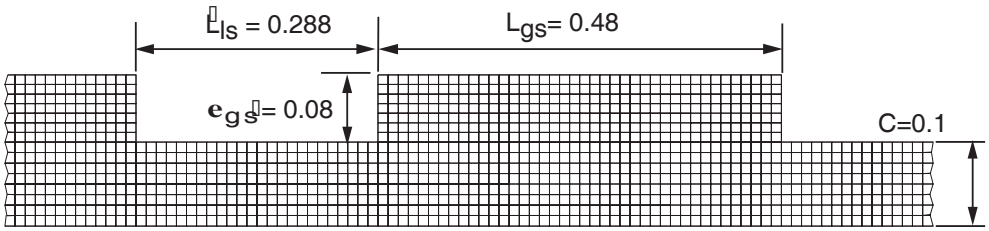

Figure 3.6: Example of geometry were a square grid was used for the grooves.

3.3.3 Program options

User specified options are given in Table 3.4.

The algorithm used to couple the pressure field solution to the momentum equations is the so called SIMPLEC routine (Semi-Implicit Method for Pressure-Linked Equations) by (Doormal & Raithby, 1984).

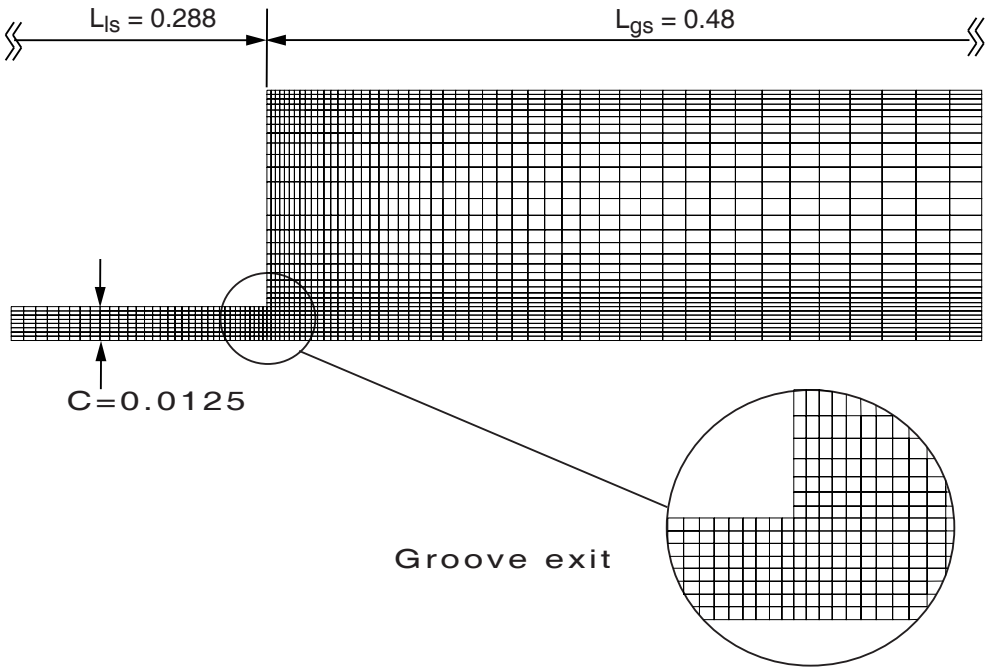

Figure 3.7: Example of grid stretching at grooves for models where square grid would be impossible to compute with the resources available.

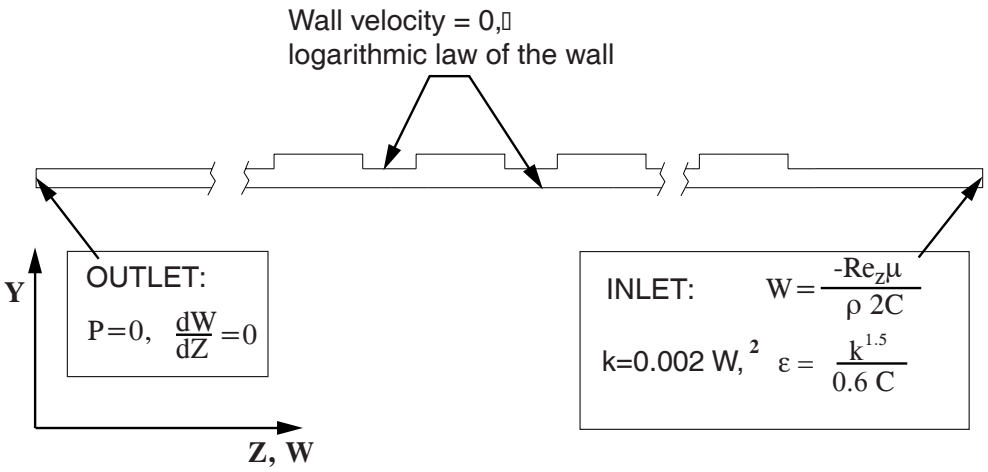

Figure 3.8: Boundary conditions $Re_z = 100000$ for all analyses.

3.4 Results

3.4.1 Sensitivity study

The axial pressure gradient in the rough section is needed in order to calculate the friction factor f. Before the whole matrix of geometries was analysed, a study was made on how the pressure gradient depends on grid refinement, length of inlet and outlet regions, and length of rough section. The results of this study are summarized as follows:

- The sensitivity study showed no significant variations in the pressure drop when the grid was varied to give non-dimensional wall distance, y^+, (White, 1994) in the range 30 to 300. Although an ideal value of y^+ equal to 30 is recommended in (Wakes & Holdœ, 1997), it was decided to accept y^+ values in the range $30 < y^+ < 300$ for the further studies.

Table 3.4: Program options chosen.

Option	Comments
Cylindrical coordinates	Radial- and axial direction
2D solution	No tangential flow
Turbulent flow	Default $k - \epsilon$ model
Isothermal flow	No viscous heating
Incompressible flow	
Steady state solution	Variation in time excluded
Convergence criterion	Residual mass flow less than 0.001 times total flow
Max. 2400 iterations	Typically convergence after 1500 iterations

- Variations in the inlet length showed that an inlet length ten times the minimum clearance or greater gave insignificant change in the pressure profile for the rough section. Hence, the inlet length was kept at 10C for the remaining analyses.
- The outlet boundary condition corresponds to fully developed flow. According to the guidelines from (White, 1994) one would expect fully developed flow to exist after 30 hydraulic diameters. In this study the exit length was finally set to $30C$ which is 15 hydraulic diameters. Exit lengths greater than 30C showed little influence on the pressure profile and increased computer time.
- The length of the grooved portion should ideally be such that fully developed flow can be observed for all quantities in a portion of the seal. However, it was found that the pressure drop pattern develops faster than for example the velocity profile. Although an ideal developed flow was not achievable for all tests due to computational limitations, the loss of accuracy is expected to be negligible.

3.4.2 Examples of numerical results

To illustrate the flow in field in the grooves the result for the example geometries in Figures 3.6 and 3.7 are shown in Figures 3.9 and 3.10. The groove geometry is the same for both models while the clearance is different.

Each vector plot shows a main recirculation vortex. This vortex contributes strongly to viscous dissipation of energy which gives a major contribution to the pressure drop. In Fig. 3.9 the velocity profile at the entrance of the groove does not change much before exit of the groove, while Fig. 3.10 shows a significant diffusion of in the velocity profile throughout the groove. As the clearance approaches zero the flow field is such that the groove viscous losses may be treated as a succession of land exit and entrance losses. This limit was considered when deriving the analytical friction factor in this chapter. By assuming a land entrance and exit loss of 0.5 and 1.0 times the axial kinetic energy ((White, 1994)) good qualitative agreement with the proposed friction factor was found as the seal clearance approached zero.

3.4.3 Axial pressure drop and friction factor

Fig. 3.11 shows the pressure profile along the rotor wall from inlet to outlet for a single groove pattern and the average pressure gradient extracted for friction factor calculations. The graph can be divided in the smooth inlet-, rough intermediate-, and smooth outlet section. Qualitatively one can see that the gradients at the smooth outlet- and inlet, are nearly the same as should be expected for fully developed flow. The total friction factor given by Eq. 3.1 was found by using a least squares curve fit to a straight line for the downstream half of the rough section. The whole rough section was not used since it takes approximately 10 hydraulic diameters before the pressure drop pattern repeats itself.

In the literature (for example in (Childs, 1993)) it has proved to be useful to split the friction factor, f, in Eq. 3.1 in one part for the stator and one for the rotor:

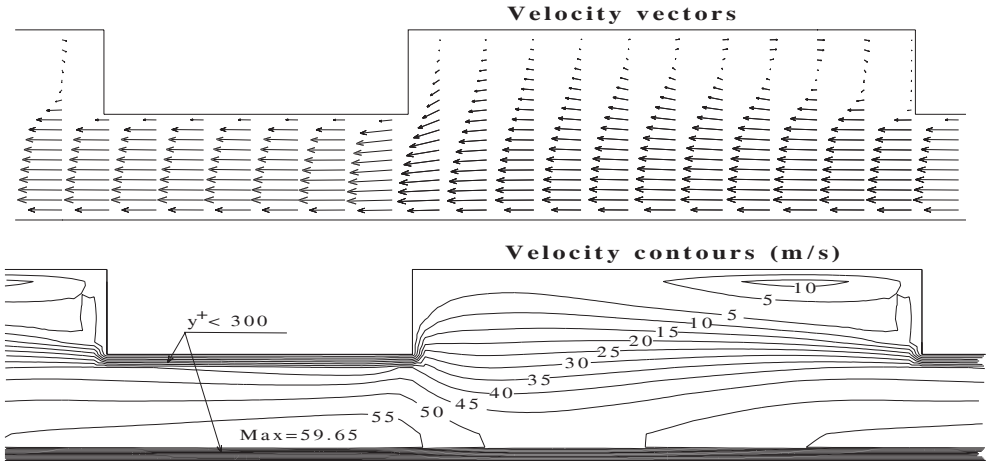

Figure 3.9: Velocity vectors and contours for groove number ten from inlet. $L_{gs} = 0.48$mm, $L_{ls} = 0.0288$mm, $C = 0.1$mm, $e_{gs} = 0.08$mm, $Re_z = 100000$.

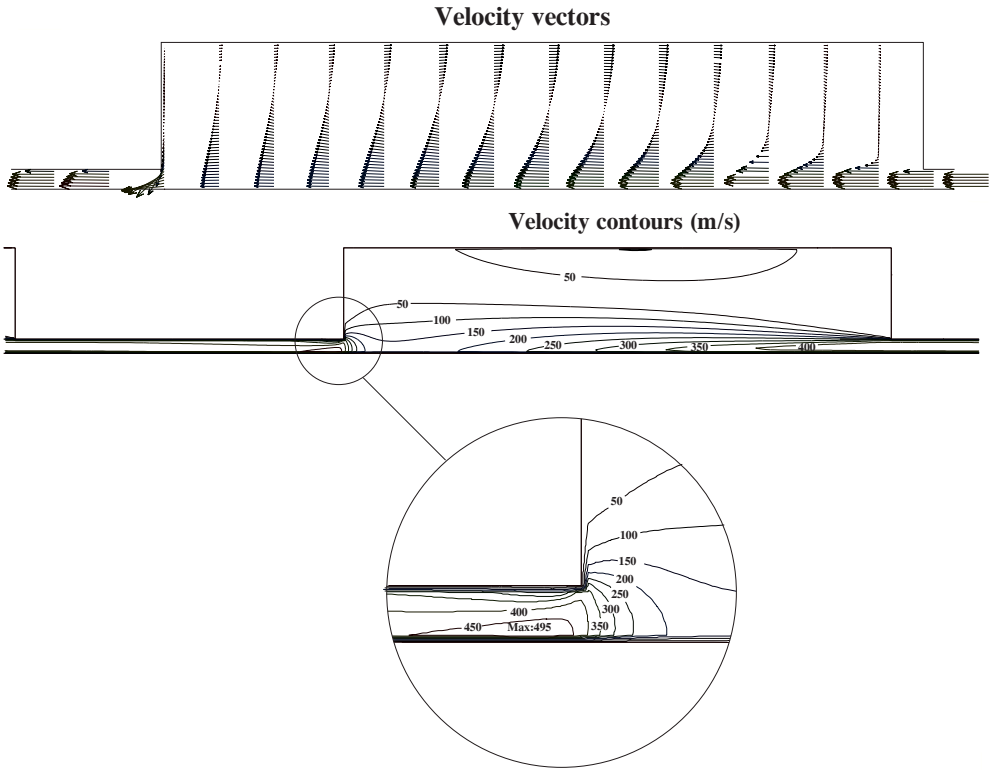

Figure 3.10: Velocity vectors and contours for groove number three from the inlet. $L_{gs} = 0.48$mm, $L_{ls} = 0.0288$mm, $C = 0.0125$mm, $e_{gs} = 0.08$mm, $Re_z = 100000$.

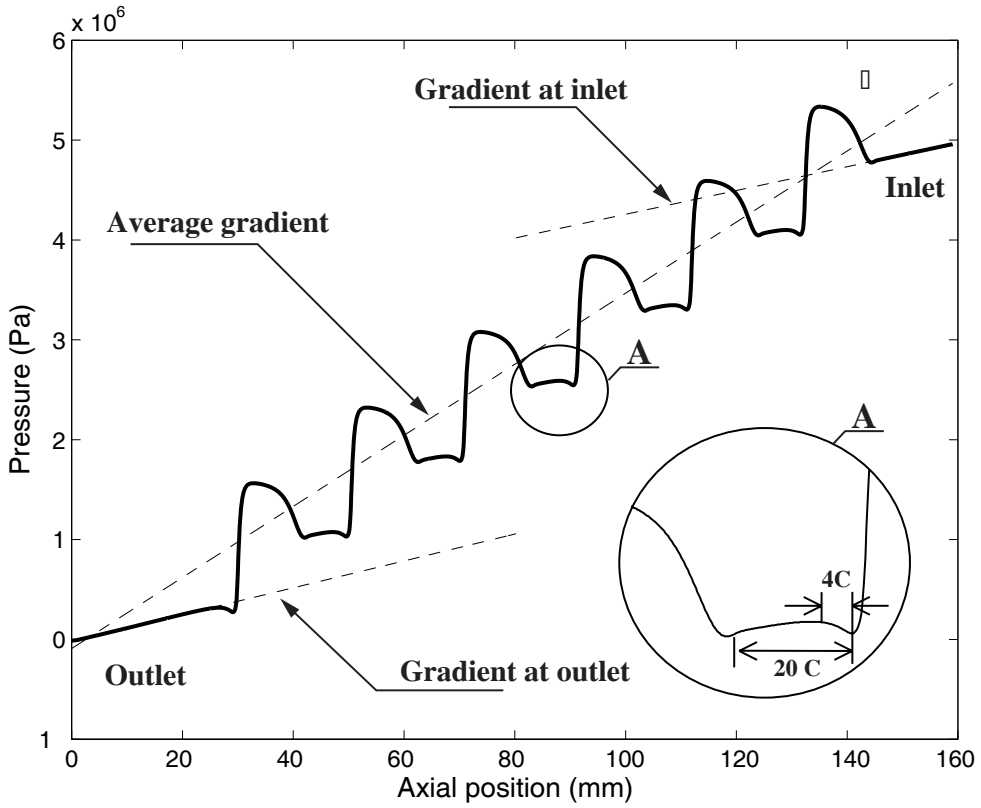

Figure 3.11: Axial pressure plot for $C = 0.1$ mm, $\frac{e_{gs}}{2C} = 0.4$ and $\frac{L_{gs}}{e_{gs}} = 16$, and pressure gradients extracted.

$$f = (f_{zs} + f_r)/2 \tag{3.2}$$

where f_{zs} and f_r stator and rotor friction factors respectively. The reason for introducing the z-subscript for the stator is that for the grooved surface the friction factor is no longer isotropic. Further one may split f_{zs} in one friction factor for the land zone and one for the groove so that

$$f_{zs} = \frac{L_{ls}}{L_{ls} + L_{gs}} f_{ls} + \frac{L_{gs}}{L_{ls} + L_{gs}} f_{zgs} \tag{3.3}$$

where L_{ls} and L_{gs} are the lengths of the land and groove of the stator respectively. f_{ls} and f_{zgs} are the separate friction factors for the land and groove.

From detail A in Fig. 3.11 which shows pressure drop at the inlet of a groove one can see that it takes approximately four minimum clearances, C, from the start of a land section before the pressure gradient becomes approximately constant. This was observed throughout the analyses and a modification to Eq. 3.3 was proposed.

$$f_{zs} = \frac{L_{ls} - 4C}{L_{ls} + L_{gs}} f_{ls} + \frac{L_{gs}}{L_{ls} + L_{gs}} f_{zgs} \tag{3.4}$$

If $L_{ls} - 4C < 0$ it is set equal to zero. Hence, the expression for the groove friction factor becomes

$$f_{zgs} = \left(2f - f_r - \frac{L_{ls} - 4C}{L_{ls} + L_{gs}} f_{ls} \right) \frac{L_{ls} + L_{gs}}{L_{gs}} \tag{3.5}$$

The modification to Eq. 3.3 proposed here has very little significance when the friction factor in the land zone is very small compared to the friction factor for the grooved part. However, when this is not the case, the correlation is better with the modification proposed. By using Eq. 3.5 the friction factor for the grooved portion of the stator was extracted and the results for the complete test matrix are shown in Table 3.5. $f_r = f_l \approx 0.0044$= friction factor for smooth seal at an axial Reynolds number of 100000.

Table 3.5: Axial friction factor for grooved part of stator,f_{zgs}. $L_{ls} = 0.6L_{gs}$, $e_{gs} = 0.08mm$ for all analyses. The entries marked X and XX were not reported due to numerical difficulties.

$\frac{e_{gs}}{2C} \setminus \frac{L_{gs}}{e_{gs}}$	1	2	3	4	6	8	12	16
0.100	X	0.0277	0.0463	0.0596	0.0660	0.0535	0.0477	0.0313
0.200	0.0181	0.0360	0.0502	0.0657	0.0694	0.0643	0.0507	0.0397
0.267	0.0306	0.0378	0.0530	0.0678	**0.0725**	0.0664	0.0483	0.0436
0.400	0.0270	0.0392	0.0570	0.0689	0.0719	0.0635	0.0477	0.0383
0.571	0.0298	0.0441	0.0577	0.0673	0.0684	0.0603	0.0457	0.0364
0.800	0.0330	0.0458	0.0548	0.0619	0.0625	0.0557	0.0423	0.0327
1.067	0.0339	0.0459	0.0528	0.0578	0.0575	0.0514	0.0379	0.0287
1.600	0.0373	0.0441	0.0490	0.0516	0.0507	0.0438	0.0272	0.0216
3.200	0.0363	0.0409	0.0417	0.0403	0.0342	0.0265	0.0213	0.0123
6.400	0.0345	0.0335	0.0299	0.0246	0.0177	0.0129	0.0107	0.0054
12.90	0.0310	0.0234	0.0163	0.0135	0.0086	XX	XX	XX

As shown in Table 3.5 it was not possible to get reliable results for the complete test matrix due to numerical problems. The numerical difficulties that were encountered were of two different types. Those entries labeled XX in Table 3.5 were not obtained due to geometric problems. The single precision pre-processor was not able to produce the desired grid. The entry labeled X was not reported due to convergence difficulties. No great effort was made to try to resolve the two problems above since the trend

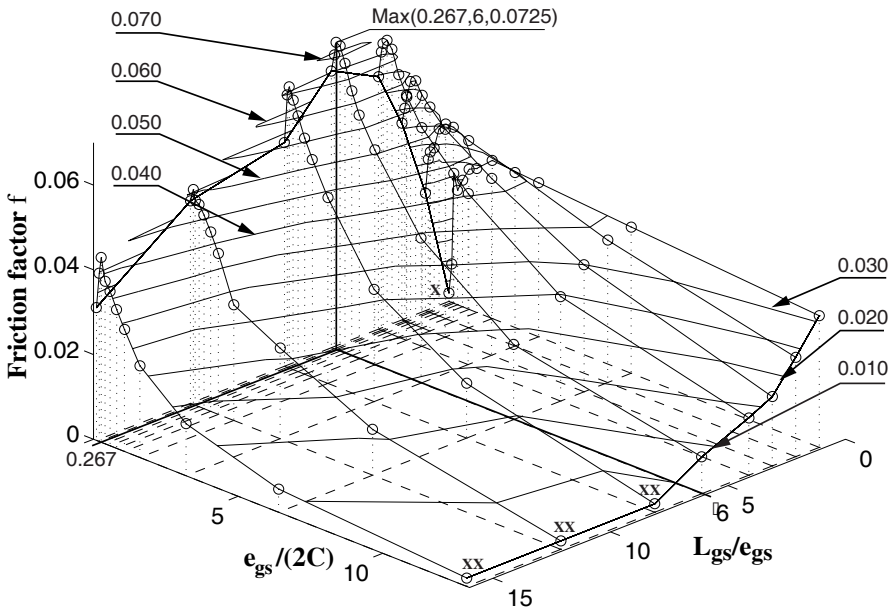

Figure 3.12: Friction factor for grooved part of stator. Entries marked X and XX were extrapolated to smooth seal friction factor values for graphical presentation.

from the surrounding points indicated that the friction factor would approach a very small value, close to that of a smooth seal.

The maximum friction factor found was for $\frac{e_{gs}}{2C} = 0.267$, and $\frac{L_{gs}}{e_{gs}} = 6$. It is highlighted in Table 3.5 and Fig. 3.12. The ratio between the groove friction factor and the hydraulically smooth friction factor for $Re_z = 100000$ is approximately 16. Based on Eq. 3.1 the corresponding groove seal leakage would be only 1/4 of a smooth seal. The steep gradient along the $\frac{e_{gs}}{2C}$ -axis may be significant for dynamic characteristics as is commented by (Childs & Fayolle, 1998). The significance of the friction factor gradient will be investigated further in Chapter 4.

3.5 Analytic axial friction factor for grooved seals

To make more general use of the the friction factor in Table 3.5 an analytic expression was sought by curve fitting. One way to approach the problem is to start out with a known function for a type of roughness and then introduce a roughness height multiplier k_m (see (Schlichting, 1979)). The equation chosen here is Moody's friction factor for commercial pipelines in the format used by (Childs, 1993) for seals:

$$f^{moody} = 0.001375 \left[1 + \left(\frac{20000e}{2C} + \frac{10^6}{Re_z} \right)^{\frac{1}{3}} \right] \tag{3.6}$$

$$Re_z = \frac{2\rho W C}{\mu} \tag{3.7}$$

According to (Moody, 1944) this formula should be accurate to within $\pm 10\%$ for a clean new commercial pipe and Reynolds numbers greater than 4000. In this study completely turbulent flow is considered and the Reynolds number dependency is excluded. By replacing the roughness height e in Moody's formula with the groove depth e_{gs} the proposed friction factor for fully developed turbulent flow over a grooved surface then becomes:

$$f_{zgs} = 0.001375 \left[1 + \left(\frac{20000 e_{gs}}{2C} k_m \right)^{\frac{1}{3}} \right] \tag{3.8}$$

where the unknown roughness multiplier k_m is a function of roughness shape. f_{zgs} is given by Table 3.5 and k_m is readily found. To utilize Eq. 3.8 k_m needs to be expressed as a function of $\frac{e_{gs}}{2C}$ and $\frac{L_{gs}}{e_{gs}}$. Standard curve fitting techniques (polynomial, exponential etc.) as suggested by (Holman, 1994) were tried initially, but no method was found that would give good correlation for the complete region. However, by observing the shape of the curve in the different regions and the number of inflection points the following expression for k_m was proposed:

$$k_m = e^{-(a_s \sqrt{\frac{e_{gs}}{2C}} + b_s)} \tag{3.9}$$

The two unknowns a_s, b_s are constant for a given groove geometry and they were found by graphically comparing the desired k_m values to the results of Eq. 3.9. The values for a_s, b_s where subsequently plotted as a function of the $\frac{L_{gs}}{e_{gs}}$ ratio and curve fit by inspection as well. The resulting expressions are:

$$a_s = 3.8 \cdot tanh(0.16 \cdot (L_{es} + 0.4)) + 0.25\sqrt{L_{es} + 0.4} \tag{3.10}$$

$$b_s = 10.6 \cdot e^{-0.35 \cdot L_{es}} + 0.57 L_{es}^{-0.8} + 1.37 L_{es}^{0.54} - 10 \tag{3.11}$$

where $L_{es} = \frac{L_{gs}}{e_{gs}}$. In addition to the test matrix two limits were considered for Equations 3.10 and 3.11. For $L_{es} \to 0$ there will be no grooves and a minimum

clearance so the multiplier should be zero. For $L_{es} \to \infty$ there will be no grooves and the clearance would be $C + e_{gs}$ and the multiplier, k_m, was set to zero.

The ratio between CFD results from Table 3.5 and curve fit data are given in Table 3.6 and Fig. 3.13. Most curve fit results are within ±10% of the CFD solution, although exceptions exist particularly at the fringes of the test matrix.

Table 3.6: Ratio (CFD-/(Curve fit friction factor) for grooved part of stator. $L_{ls} = 0.6L_{gs}$, $e_{gs} = 0.08mm$ for all analyses.

$\frac{e_{gs}}{2C} \setminus \frac{L_{gs}}{e_{gs}}$	1	2	3	4	6	8	12	16
0.100	X	1.2073	0.9895	0.9279	0.9621	1.1585	1.0431	1.2183
0.200	1.3132	1.0767	1.0350	0.9342	0.9854	1.0163	1.0141	0.9839
0.267	0.8296	1.0808	1.0213	0.9325	0.9563	0.9878	1.0547	0.8842
0.400	1.0246	1.1125	0.9918	0.9407	0.9606	1.0105	1.0277	0.9587
0.571	0.9963	1.0329	1.0021	0.9663	0.9835	1.0165	1.0042	0.9362
0.800	0.9510	1.0241	1.0578	1.0306	1.0228	1.0232	0.9860	0.9385
1.067	0.9651	1.0372	1.0854	1.0670	1.0393	1.0153	0.9864	0.9497
1.600	0.9200	1.0754	1.1175	1.1018	1.0274	1.0036	1.1153	1.0113
3.200	0.9746	1.0749	1.1036	1.0912	1.0433	1.0514	0.8392	1.0260
6.400	0.9832	1.0772	1.1074	1.1485	1.1020	1.0715	0.7681	1.0584
12.90	0.9269	1.0512	1.1477	1.0158	0.8956	XX	XX	XX

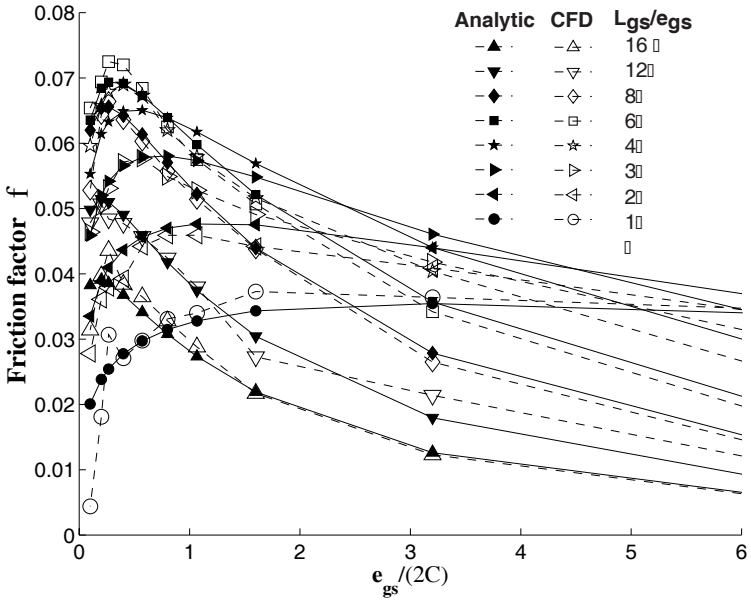

Figure 3.13: Friction factor comparison between CFD solution and proposed analytical formula (filled markers).

3.5.1 Comparison to experimental results

Three references, (Black & Cochrane, 1973), (H.Möbius, 1940), and (Yamada, 1962a) were chosen for comparison of the new analytical friction model and experiments. Figure 3.14 shows an overview of the range of groove geometries that were studied by these authors together with results based on the proposed analytical friction factor.

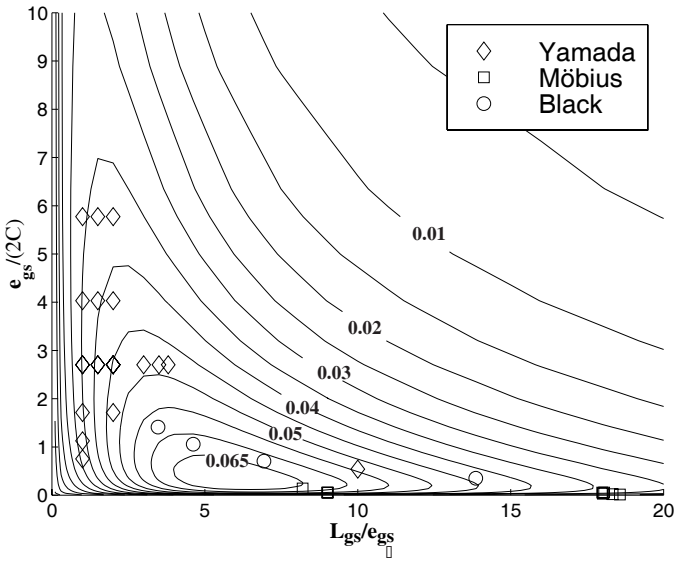

Figure 3.14: Friction factor given by Equations 3.6 to 3.11 and overview of experimental groove geometries.

Yamada

The experiment of (Yamada, 1962a) was carried out in the transition between laminar and turbulent flow with a Reynolds number range of $Re_z = 100$ to 20000. In this comparison only the friction factor at the highest axial Reynolds number recorded by Yamada was used. Yamada also tested a range of tangential Reynolds numbers, but here comparisons were made to his results for zero rotational speed. Table 3.7 shows groove friction factors, f_{gY}, (obtained by setting $f_{gY} = f_{zgs}$ in Eq. 3.5) from Yamada's experiment and comparisons to the analytical friction factor in Eq. 3.8. Equation 3.12 was used to calculate the separate friction factor for rotor and the land part of the stator in Yamada's experiment. The nomenclature used is shown in Fig. 3.1. Since Yamada used the Darcy Weisbach friction factor format his friction factors were divided by four to fit in the Fanning format used here, and the Reynolds number used by Yamada was multiplied by two to fit in the format used in Eq. 3.7. All friction factors from Yamada's results were retrieved at an axial Reynolds number of 10000 apart from the two geometries (C-A1) and (H7) for which $Re_z = 8000$. Note that when the land zone is less than four times the minimum clearance $L_{ls} - 4C$ in Eq. 3.5 is set to zero.

The last column in Table 3.7 shows the ratio between the friction factor f_{gY} for grooved part from the results of Yamada and the analytic friction factor f_{zgs} from Eq. 3.8.

Table 3.7: Yamada's geometry and friction factor comparisons. $e_{gs} = 5$ mm for all geometries apart from I1 for which $e_{gs} = 1$mm The first column is the geometry description used by Yamada.

Geo.	C	L_{gs}	$\frac{L_{ls}}{C}$	$\frac{L_{gs}}{e_{gs}}$	$\frac{e_{gs}}{2C}$	f	f_{gY}	f_{zgs}	$\frac{f_{gY}}{f_{zgs}}$
C-B3	0.925	10	10	2	2.70	0.0150	0.0392	0.0452	1.15
C-A1	0.925	7.5	2.5	1.5	2.70	0.0200	0.0421	0.0412	0.97
A-B1	0.433	5	15	1	5.77	0.0108	0.0334	0.0342	1.02
B-B1	0.620	5	15	1	4.03	0.0110	0.0366	0.0352	0.96
C-B1	0.925	5	15	1	2.70	0.0110	0.0385	0.0353	0.91
D-B1	1.458	5	15	1	1.71	0.0105	0.0379	0.0345	0.91
E-B1	2.218	5	15	1	1.12	0.0103	0.0407	0.0330	0.81
F-B1	3.317	5	15	1	0.75	0.0093	0.0396	0.0311	0.78
A-B3	0.433	10	10	2	5.77	0.0173	0.0466	0.0374	0.80
B-B3	0.620	10	10	2	4.03	0.0150	0.0382	0.0417	1.09
C-B3	0.925	10	10	2	2.70	0.0150	0.0392	0.0452	1.15
D-B3	1.458	10	10	2	1.71	0.0145	0.0389	0.0473	1.21
A-A1	0.433	7.5	2.5	1.5	5.77	0.0200	0.0419	0.0368	0.87
B-A1	0.620	7.5	2.5	1.5	4.03	0.0175	0.0361	0.0394	1.09
C-A1	0.925	7.5	2.5	1.5	2.70	0.0163	0.0328	0.0412	1.25
H1	0.925	5	15	1	2.70	0.0113	0.0405	0.0353	0.87
H3	0.925	10	10	2	2.70	0.0153	0.0402	0.0452	1.12
H5	0.925	15	5	3	2.70	0.0220	0.0474	0.0486	1.02
H6	0.925	17.5	2.5	3.5	2.70	0.0225	0.0424	0.0485	1.14
H7	0.925	19	10	3.8	2.70	0.0325	0.0577	0.0480	0.83
I1	0.925	10	10	10	0.54	0.0170	0.0472	0.0540	1.14

Black & Cochrane

(Black & Cochrane, 1973) did experiments with axial Reynolds numbers from 4000 to 14000 and provided the (Hirs, 1973) formula for the friction factor for the rotor and stator respectively as follows:

$$f_{r,s} = m_{r,s}(Re_{r,s})^{n_{r,s}} \tag{3.12}$$

where Re_s and Re_r are the Reynolds numbers relative to the stator and rotor respectively and the constants m_s, n_s, m_r, and n_r were determined experimentally. To convert Black's reported friction factor f_B for the stator based on the average seal clearance to the friction factor f_{zs} (Eq. 3.4) based on the minimum seal clearance, Eq. 3.13 derived in Appendix D was used.

$$\zeta = \frac{f_{zs}}{f_B} = \left(\frac{R}{R_B}\right)^2 \left(\frac{C}{C_B}\right)^3 \tag{3.13}$$

Average clearance in Black's case is,

$$C_B = C + \frac{L_{gs}}{L_{ls} + L_{gs}} e_{gs} \tag{3.14}$$

and the average radius $R_1 = R_r + C_B/2$ while the average radius based on minimum clearance is $R = R_r + C/2$. The five different geometries studied by Black and the corresponding friction factors for the stator are given in Table. 3.8.

Table 3.8: Black's geometry and friction factor. Constants: $Re_z = 10000$ $R_r = 25.4$mm, $C = 0.18$mm, $\frac{L_{gs}}{L_{ls}+L_{gs}} = 0.5$, $\frac{L_{ls}-4C}{L_{ls}+L_{gs}} = 0.295$, $\frac{L_{ls}}{C} = 9.78$.

Geo.	e_{gs}	$\frac{L_{gs}}{e_{gs}}$	$\frac{e_{gs}}{2C}$	n_s	m_s	f_B	ζ	f_{zs}
A	0.000	0.000	0	-0.22102	0.07959	0.0104	1.0	0.0104
B	0.127	13.85	0.352	-0.29209	0.7292	0.0495	0.4029	0.0199
C	0.254	6.929	0.705	-0.37469	5.5363	0.1755	0.2005	0.0352
D	0.381	4.619	1.058	-0.39314	9.7617	0.2611	0.1138	0.0297
F	0.508	3.464	1.411	-0.39563	16.786	0.4389	0.0706	0.0310

With a known friction factor for the stator f_{zs}, which combines the grooves and the land parts of the grooved surface, Eq. 3.4 was used to determine the friction factor for the grooves only. The friction factor for the land part f_{ls} needed to calculate f_{zgs} was calculated based on Eq. 3.12 and the coefficients m_s and n_s from geometry A in Table 3.8.

Table 3.9: Comparison of the experimental friction factor for the grooved part of stator by Black, and the current theoretical friction factor.

Geo.	f_{zgs} Exp	f_{zgs} $Theory$	Ratio $\frac{Theory}{Exp}$
A	N/A	N/A	N/A
B	0.0337	0.0435	1.29
C	0.0643	0.0627	0.977
D	0.0533	0.0624	1.17
F	0.0559	0.0577	1.03

In Table 3.9 comparisons are made between the groove friction factor obtained from Black's experiment for a Reynolds number of 14000, and the analytical friction factor in Eq. 3.8. Since results for only one Reynolds number are compared and the

comparisons are made for the grooved part only one may ask: How well does the proposed model predict the total friction factor in Eq. 3.2 and leakage for the given geometry in Black's experiment for Reynolds numbers between 4000 and 14000? To answer this question it was assumed that Black's smooth rotor surface has a friction factor given by:

$$f_r = 0.079(Re_z)^{-0.25} \tag{3.15}$$

where the coefficients $mr = 0.079$ and $nr = -0.25$ are from a smooth seal as found by (Yamada, 1962b).

With this assumption one can calculate the total friction factor by using Equations 3.2, 3.6, 3.10, and 3.11 and compare this with the total friction factor from Black's experiment. If one excludes inlet and exit losses for the seal, the ratio between predicted leakage and Black's leakage data are the square root of the inverse friction factor ratio. From Fig. 3.15 it can be seen that the proposed analytical model predicts leakage within ±10% of the experimental for Reynolds numbers greater than 7000 and less than 14000.

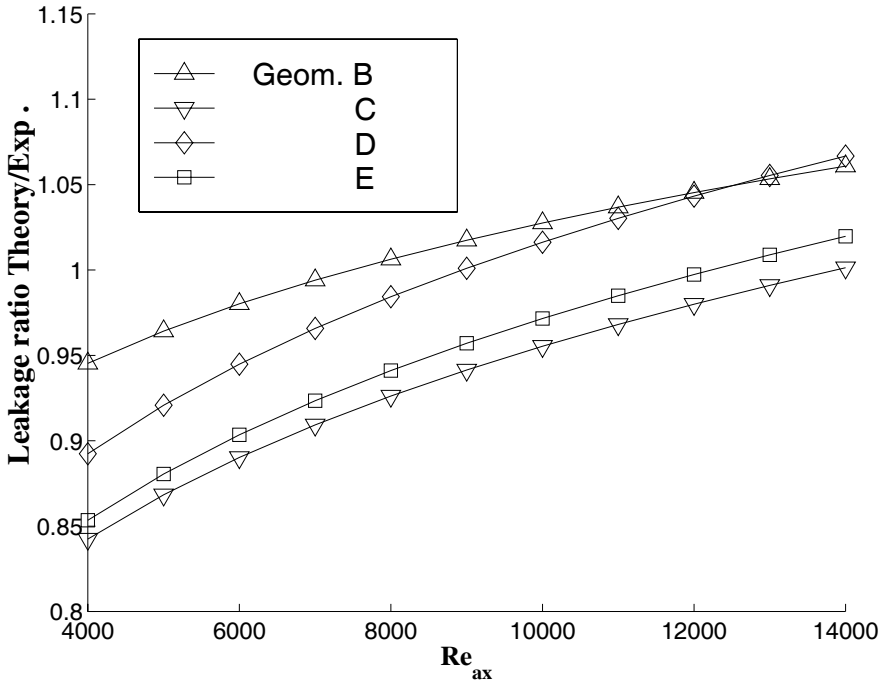

Figure 3.15: Comparison of Black's experimental leakage and theoretical predictions for axial Reynolds numbers from 4000 to 14000.

Möbius

(H.Möbius, 1940) studied the friction factor for water flow in pipes with transverse ribs for axial Reynolds numbers between 6000 and 450000. By comparing Tables 3.10, 3.8, and 3.7 one can see that the relative roughnesses for Möbius' experiment were low compared to the experiments of (Black & Cochrane, 1973) and (Yamada, 1962a). The friction factor in Möbius' experiment varied approximately ±10% over the whole Reynolds number range, and in Table 3.10 the mean value is reported. Only one of the geometries, **ie**, tested by (H.Möbius, 1940) fall within the CFD test matrix so for all the other geometries extrapolations are made by Equations 3.8 to 3.11.

(H.Möbius, 1940) used a volume average radius given by the formula

$$\bar{r} = \sqrt{\frac{r_{min}^2 L_l + r_{max}^2 L_g}{L_{ls} + L_g}} \tag{3.16}$$

where r_{min} is the minimum radius and r_{max} is the maximum, and L_l and L_g are the width of land and groove respectively. The friction factor $\bar{f}$ found for this average radius can be converted to the friction factor f at the minimum radius by means of the conversion factor ζ (see Appendix D for derivation).

$$\zeta = \frac{f}{\bar{f}} = \left(\frac{r}{\bar{r}}\right)^5 \tag{3.17}$$

Table 3.10: Möbius' geometry and friction factor comparisons. The first column is the geometry description used by Möbius.

	D	L_{gs}	$\frac{2L_{ls}}{D}$	$\frac{L_{gs}}{e_{gs}}$	$\frac{e_{gs}}{D}$	f	f_{gM}	f_g	$\frac{f_{gM}}{f_{gs}}$
ia	44.996	22.5	0.1111	8.996	0.0555	0.03896	0.04329	0.05484	1.26
ib	44.996	45	0.1111	17.99	0.0555	0.02982	0.03148	0.03159	1.00
id	47.020	45	0.1063	30.22	0.0316	0.01542	0.01628	0.01490	0.91
ie	39.016	45	0.1281	8.195	0.1407	0.06794	0.07171	0.06364	0.88
ig	43.038	99	0.1626	28.48	0.0807	0.02781	0.02880	0.01826	0.63
ih	46.978	27	0.0638	18.01	0.0319	0.02472	0.02609	0.02889	1.10
ij	48.522	13.5	0.0309	18.56	0.0149	0.01711	0.01806	0.02398	1.32
ik	48.002	18	0.0416	18.32	0.0204	0.03940	0.04159	0.02600	0.62
iia	90.018	45	0.1110	9.027	0.0553	0.03940	0.04378	0.05473	1.25
iib	90.018	90	0.1110	18.05	0.0553	0.02992	0.03158	0.03146	0.99

3.5.2 Discussion of axial friction factor results

The results for the axial friction factor of the CFD analyses show smooth trends for the major part of the test matrix. Numerical difficulties in the CFD software used were experienced for those points named X and XX in Table 3.5. Some of the neighboring points indicate that less accuracy can be expected in these regions. Sources of inaccuracies for deriving the analytical expression for the friction factor by CFD are as follows:

- The groove geometry is sharp edged in theory, not in practice
- The chosen $k-\epsilon$ turbulence model is known to over-predict inlet losses somewhat (Arghir & Frêne, 1995)
- Inaccuracies due to undesirable grid stretching for points labeled XX in Table 3.5
- Convergence difficulties for shallow grooves give larger uncertainties for groove geometries close to the point labeled X in Table 3.5
- Limited accuracy of the law of the wall relating the velocity of the near wall cells to wall shear stresses
- Discretization errors
- Inaccuracies in the curve fitting of CFD results to an analytical expression
- Limited accuracy in the conversion formula for a friction factor dealing with a combined land and groove surface to a friction factor for the grooves only

Experimental inaccuracies may be listed as follows:

- Measurement inaccuracies
- Roundness of groove corners not documented
- Conversion of Black's experimental data to a curve fit

Despite all the uncertainties of the proposed analytic formula the friction factor is predicted within $\pm 20\%$ for a great range of groove geometries and Reynolds numbers. In turn this indicates leakage predictions within $\pm 10\%$. This is similar to results obtained by (Marquette *et al.*, 1997) who studied two geometries experimentally and uses a different theoretical approach. From the comparison to Black's results there is a trend that the proposed friction factor will under-predict the friction factor at low Reynolds numbers (4000 - 7000). One will have to include a Reynolds number dependency in the proposed friction factor to improve results in this region.

The CFD- results show that optimal leakage reduction is given by:

- As short land zone as possible and ribs on both rotor and stator.

- The optimal groove width to depth ratio is about 6 from the CFD and analytical results while the groove depth to hydraulic diameter ratio $\frac{e_{gs}}{2C}$ is 0.267 for the CFD results and 0.333 from the analytic formula. In order to find a more accurate location of this optimal point further studies are needed. Comparing the maximum friction factor for grooves in Fig. 3.12 to a smooth surface friction factor of the same minimum clearance indicates that the leakage for a smooth seal may be reduced by 75.4% at $Re_z = 100000$ and 68% at $Re_z = 10000$ by introducing rectangular grooves.

For dynamic characteristics the friction factor gradient with respect to $\frac{e_{gs}}{2C}$ is important, and it is interesting to observe that near the optimal $\frac{e_{gs}}{2C}$ point for leakage reduction there are steep positive and negative gradients. The significance of the gradient when prediction dynamic characteristics will be studied in Chapter 4.

3.6 Tangential friction factor

In an annular seal for rotordynamic applications the main leakage path is shown in Fig. 2.2. The axial friction factor proposed in the previous section only covers only axial flow while tangential flow is present in practice. The tangential flow has a significant influence on the rotordynamic characteristics of the seal as shown by (von Pragenau, 1982). The method used by (Nordmann *et al.*, 1987) which couples a known axial friction factor to a smooth tangential friction factor does not appear to be accurate as discussed in (Childs *et al.*, 1990). As (Yamada, 1962a) concluded the groove patterns that he studied gave very little change in the tangential friction compared to a smooth seal. For a first approximation it is tempting to treat the grooves as a smooth surface for the tangential friction factor. However, it will be shown by the numerical study carried out in this section that there is a significant increase in tangential friction for certain groove geometries compared to that for a smooth seal.

The tangential shear stress on the rotor and stator walls for a surface with isotropic roughness by (Childs, 1993) and (Hirs, 1973) can be given in a slightly modified form to take into account the anisotropic stator surface used in the numerical analyses for this section.

$$\tau_{\theta s} = \tau_s \cdot \frac{U}{U_s} = \left(f_{\theta s} \rho \frac{U_s^2}{2} \right) \cdot \frac{U}{U_s} \tag{3.18}$$

$$\tau_{\theta r} = \tau_r \cdot \frac{U}{U_r} = \left(f_r \rho \frac{U_r^2}{2} \right) \cdot \frac{U - \omega R}{U_r} \tag{3.19}$$

$\tau_{\theta s}$ is the average tangential shear stress at the grooved stator surface, τ_r is the average tangential shear stress at the smooth rotor surface, τ_r and τ_s are shear stresses in the direction of the total flow velocity relative to the rotor and stator respectively. The difference from the isotropic formulation is that the friction factor for the tangential direction $f_{\theta s}$ differs from the axial f_{zs} developed in the previous section.

The bulk velocities relative to the rotor and stator surfaces are

$$U_s = \sqrt{W^2 + U^2} \tag{3.20}$$

$$U_r = \sqrt{W^2 + (U - R\omega)^2} \tag{3.21}$$

In the the comparison to CFD simulations in this section the average groove/land shear stresses are calculated along a single cylindrical control volume based on the minimum seal clearance. Hence, the tangential friction factor for shear stress calculations can be given as follows:

$$f_{\theta s} = \frac{L_{ls}}{L_{ls} + L_{gs}} f_{ls} + \frac{L_{gs}}{L_{ls} + L_{gs}} f_{\theta gs} \tag{3.22}$$

When no machining roughness is superimposed on the grooved stator, which is the case for the CFD study, f_{ls}, $f_{\theta gs}$, and Re_s are given by

$$f_{ls} = 0.001375 \left[1 + \left(\frac{10^6}{Re_s} \right)^{\frac{1}{3}} \right] \tag{3.23}$$

$$f_{\theta gs} = 0.001375 \left[1 + \left(20000 \epsilon_{\theta gs} + \frac{10^6}{Re_s} \right)^{\frac{1}{3}} \right] \tag{3.24}$$

$$Re_s = \frac{2 \rho U_s C}{\mu} \tag{3.25}$$

$$\epsilon_{\theta gs} = \frac{e_{\theta gs}}{2C} \tag{3.26}$$

The unknown parameter that needs to be determined is $\epsilon_{\theta gs}$, the effective relative tangential surface roughness for stator grooves.

To determine $\epsilon_{\theta gs}$ at the groove part of the control volume surface numerical studies were carried out for the geometries shown in Table 3.11.

Before performing the CFD simulations, it had to be decided what rotational speed(s) should be used for the analyses. If the coupling between axial and tangential friction were strong one would have to solve the test matrix for a range of different rotational speeds to develop a functional relationship. Therefore, an initial test was performed on a subset of geometries where tangential wall speeds were 0.5, 1, 2, and 4 times the axial bulk flow speed. The study showed that the axial pressure drop was virtually independent of rotational speed, and it was decided to neglect this dependency for the friction factor in the grooved section. For the remaining analyses the tangential wall velocity of the rotor was set to two times the axial bulk velocity.

If one could study a fully developed swirling flow one could observe the bulk swirl velocity $\frac{U}{R_r \omega}$ and readily determine the ratio between the friction factor for the smooth

Table 3.11: Number of grooves modelled for the various analyses, clearance is given in millimeters. $L_{ls} = 0.6L_{gs}$ and $e_{gs} = 0.08mm$ for all analyses.

$\frac{e_{gs}}{2C}$	$\frac{L_{gs}}{e_{gs}}$ 1	2	3	4	6	8	12	16
0.100	X	X	X	X	X	X	X	X
0.200	X	X	X	X	X	X	X	X
0.267	72	24	24	24	12	12	X	X
0.400	48	12	12	12	12	12	6	6
0.571	32	12	12	12	12	12	6	6
0.800	24	12	12	12	12	12	6	6
1.067	12	12	12	12	12	12	6	6
1.600	12	12	12	12	12	12	6	4
3.200	X	6	6	4	4	4	4	X
6.400	X	X	X	X	X	X	X	X
12.90	X	X	X	X	X	X	X	X

and grooved surface. However, swirl development was found to be very slow, and to really get fully developed swirling flow one would have to model greater seal lengths than in the study of purely axial flow. This was not possible due to the computational time required. The method chosen to avoid this problem was the following:

- A plug swirl velocity 0.8 times the rotor speed was specified at the inlet.
- A user FORTRAN routine was written in CFX to find the mean tangential flow velocity along the minimum clearance as a function of axial position.
- By using Eq. 3.27 below, derived in Chapter 4, the swirl development by the bulk flow solution was calculated and matched to the CFD solution by graphically finding the best choice of the unknown equivalent relative roughness $\epsilon_{\theta gs}$.
- From the derived value of the relative roughness $\epsilon_{\theta gs}$ the fully developed tangential swirl u_∞ was calculated for $\omega R/W = 2$ when the rotor and internal groove surfaces are smooth and there is no land zone for the stator.
- An analytic function relating u_∞ to the groove geometry was then derived.
- By assuming that an equal machining roughness for the rotor and stator land and internal grooves would yield the same u_∞ value, an expression for the equivalent stator groove roughness was established. This equivalent roughness includes the combined friction do to groove geometry and machining roughness inside the grooves. inside the grooves.

The bulk flow equation for swirl development is given in dimensionless form by (Childs, 1993):

$$\frac{du}{dz} = -\frac{1}{2}\left[u u_s \sigma_{\theta s} + (u-1)\, u_r \sigma_{\theta r}\right] \tag{3.27}$$

$$u_s = \sqrt{1 + b^2 u^2} \tag{3.28}$$

$$u_r = \sqrt{1 + b^2 (u-1)^2} \tag{3.29}$$

$$b = \frac{R_r \omega}{W} \tag{3.30}$$

$$u = \frac{U}{R_r \omega} \tag{3.31}$$

where u is the non-dimensional swirl velocity, u_s and u_r are the non-dimensional total velocity relative to the stator and rotor respectively. The parameters containing the friction factors are $\sigma_{\theta s} = f_{\theta s}\left(\frac{L}{C}\right)$ and $\sigma_{\theta r} = f_r\left(\frac{L}{C}\right)$.

The friction factor for the smooth rotor f_r is given by

$$f_r = 0.001375\left[1 + \left(\frac{10^6}{Re_z u_r}\right)^{\frac{1}{3}}\right] \tag{3.32}$$

$$Re_z = \frac{2\rho W C}{\mu} \tag{3.33}$$

so the only term which is affected by the equivalent relative stator roughness $\epsilon_{\theta gs} = \frac{e_{\theta gs}}{2C}$ is the friction factor $f_{\theta s}$ given by Eq. 3.23. The ordinary differential equation 3.27 was solved in mathematical software, MATLAB version 5.2. By using this procedure the desired value for $\epsilon_{\theta gs}$ which matched the swirl development found by CFD simulations could be established.

3.6.1 CFD model description

The model description options used in the CFX program were the same as described in Section 3.3, with the following exceptions:

- Quasi three dimensional flow field, which means that the computational grid is two-dimensional, but the tangential velocity is computed. The tangential velocity can have gradients in the radial- and axial direction, but it is constant for the tangential direction.
- An initial guess for swirl, $\frac{U(z)}{R\omega} = 0.5$, in the tangential direction was made to speed up convergence.
- The wall velocity in the tangential direction for rotor was twice the axial bulk flow.
- Inlet tangential velocity $\frac{U(0)}{R\omega} = 0.8$

3.6.2 Results

One striking observation based on the CFD solutions was that for each groove width to depth ratio the swirl development was almost independent of the groove depth to clearance ratio. Hence, it was chosen to make the analytic tangential friction factor only a function of the groove width to depth ratio. In Fig. 3.16 the bulk tangential swirl velocity is plotted as function of non-dimensional axial distance from the entrance to the exit for the equivalent relative stator roughness $\epsilon_{\theta gs}$ that best fits the CFD solution. This figure indicates that the tangential friction increases as the ratio of groove width to depth ratio, $\frac{L_{gs}}{e_{gs}}$, decreases. For $\frac{L_{gs}}{=}\frac{e_{gs}}{}6$ which is the optimal for leakage reduction, the swirl development is almost identical to that of a smooth seal, and hence one would expect an insignificant increase in mechanical loss for this groove pattern on the stator compared to that for a smooth stator surface.

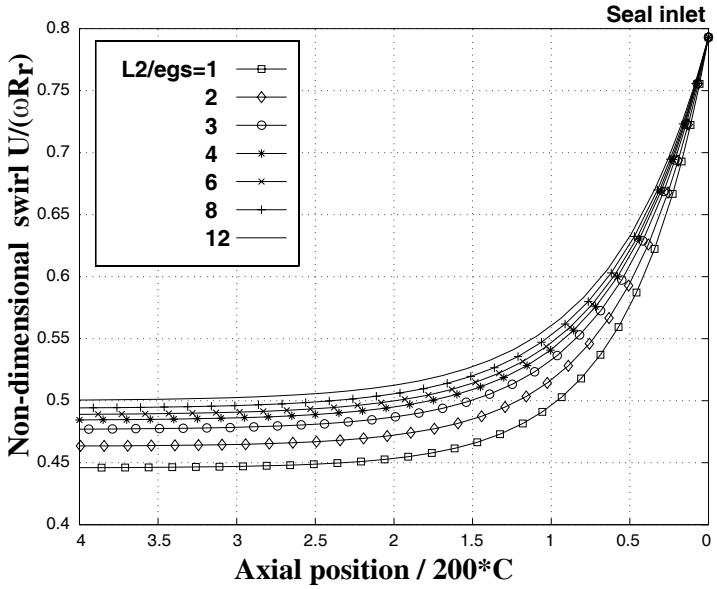

Figure 3.16: Non-dimensional swirl velocity as a function of non-dimensional axial distance for groove width to depth ratios $\frac{L_{gs}}{e_{gs}} = 1$ to 16.

The equivalent relative stator groove roughness $e_{\theta gs}/2C$ and the corresponding fully developed swirl velocity relative to the stator without a land zone on the stator are given in Table 3.12. Note that the relative tangential roughness is very different from the axial relative roughness in Table 3.6. The circumferential grooves give only a small increase in tangential friction compared to a smooth surface. The roughness parameter $e_{\theta gs}$ is the Moody roughness height which gives the equivalent swirl development as the corresponding groove pattern.

u_∞ based on a zero land zone for the grooves was calculated for different values of $\epsilon_{\theta gs}$ based on the equations below. The reason for solving for u_∞ is that $\epsilon_{\theta gs}$ in Table 3.12 only gives the effective roughness for tangential flow at the grooved surface when

Table 3.12: Equivalent relative roughness $e_{\theta gs}/2C$ calculated when $L_{ls} = 0.6L_{gs}$ and $e_{gs} = 0.08mm$ and the corresponding fully developed swirl velocity for grooved stator with zero land zone ($L_{ls} = 0$).

$\frac{L_{gs}}{e_{gs}}$	1	2	3	4	6	8	12	16
$\epsilon_{\theta gs}$	0.0020	0.0010	0.0005	0.0003	0.0002	0.0001	0.0	0.0
u_∞	0.4218	0.4461	0.4656	0.4764	0.4830	0.4907	0.5	0.5

the groove walls are assumed to be hydraulically smooth. In practice there will be a machining roughness present both within the grooves and on the rotor. To be able to find an expression for $\epsilon_{\theta gs}$ which includes the machining roughness inside the grooves the following assumption was made: The fully developed swirl velocity calculated for a smooth rotor and smooth groove walls would be the same as the fully developed swirl for grooves with rough walls if the rotor surface has the same roughness as the groove walls. In order to find the desired expression for $\epsilon_{\theta gs}$ which includes the machining roughness inside the grooves, the fully developed swirl velocity for a smooth rotor surface was calculated by the following shear stress equations:

$$\tau_{\theta gs} = -\tau_{\theta r} \tag{3.34}$$

$$\tau_{\theta gs} = \left(f_{\theta gs} \rho \frac{U_s^2}{2} \right) \cdot \frac{U}{U_s} \tag{3.35}$$

$$\tau_{\theta r} = \left(f_r \rho \frac{U_r^2}{2} \right) \cdot \frac{(U - \omega R)}{U_r} \tag{3.36}$$

$$\frac{f_{\theta gs}}{f_r} = \frac{U_r}{U_s} \frac{(\omega R - U}{U}) \tag{3.37}$$

where f_r and $f_{\theta gs}$ are given by Equations 3.32 and 3.24. Substituting the known values into Eq. 3.37 gives the following equation to be solved for u_∞.

$$\frac{\left[1 + \left(2 \cdot 10^4 \cdot \epsilon_{\theta gs} + \frac{10}{\sqrt{1^2 + 4(u_\infty - 1)^2}} \right)^{\frac{1}{3}} \right]}{\left[1 + \left(\frac{10}{\sqrt{1 + 4(u_\infty - 1)^2}} \right)^{\frac{1}{3}} \right]} = \sqrt{\frac{1 + 4(u_\infty - 1)^2}{1 + 4u_\infty^2}} \left(\frac{1 - u_\infty}{u_\infty} \right) \tag{3.38}$$

The solutions to the equation are given in Table 3.12. A curve fit through the points in the table gave the following expression for u_∞.

$$u_\infty = 0.10(e^{-6L_{es}} - e^{-0.3L_{es}}) + 0.5 \tag{3.39}$$

where L_{es} is the groove width to depth ratio. In the limit $L_{es} \to 0$, the dimensionless swirl $u_\infty = 0.5$. This limit was also used in order to derive Eq. 3.39. The final step needed to calculate $\epsilon_{\theta gs}$ for rough groove walls is to introduce a machining roughness for the grooved surface and the same roughness on the rotor. The non-dimensional velocity relative to the rotor and stator for fully developed flow when $\omega R/W = 2$ is given by.

$$u_{r\infty} = \sqrt{1 + 4(u_\infty - 1)^2} \tag{3.40}$$

$$u_{s\infty} = \sqrt{1 + 4u_\infty^2} \tag{3.41}$$

Now the ratio between the friction factor for the stator and rotor may be written

$$\frac{f_{\theta gs}}{f_r} = \frac{u_{r\infty}}{u_{s\infty}} \frac{(1 - u_\infty)}{u_\infty} \tag{3.42}$$

From Eq.3.42 the expression for $\epsilon_{\theta gs}$ can be expressed explicitly as:

$$\epsilon_{\theta gs} = 2 \cdot 10^4 \left(\left(\frac{u_{r\infty}}{u_{s\infty}} \right) \frac{(1 - u_\infty)}{u_\infty} \cdot \left[1 + \left(a_{2gs} + \frac{a_3}{u_{r\infty}} \right)^{\frac{1}{3}} \right] - 1 \right)^3 - \frac{a_3}{u_{s\infty}} \tag{3.43}$$

where $a_3 = 10^6$, $a_{2gs} = 2 \cdot 10^4 \frac{e_s}{2C}$, and e_s is the absolute roughness superimposed in the grooves.

In order to verify the applicability of the proposed tangential friction factor for swirl prediction no direct comparison to experimental results was made since such results were not available for any of the seal experiments found in the literature survey. Indirectly, however, the validity of the proposed formulation will be verified in Chapter 4 where comparisons between experimentally determined dynamic coefficients for the seal and theoretical predictions based on the proposed model are made.

3.6.3 Summary

In this summary the friction factors developed for a grooved stator (or rotor) are given in their non-dimensional form. To distinguish the friction factor of the rotor from that of the stator the subscript convention r, s was used to indicate two equations, one for the rotor and one for the stator. To extend the formulation to a tapered seal, the local thickness H, which excludes the depth of the grooves, was introduced. In non-dimensional form the film thickness, h, is given by

$$h = \frac{H}{\bar{C}_r} \tag{3.44}$$

$$\bar{C}_r = \frac{C_{in} + C_{ex}}{2} \tag{3.45}$$

where C_{in} and C_{ex} are the clearances at seal inlet and exit respectively.

In summary the axial and tangential friction factor developed in this chapter can be stated in non-dimensional form.

$$f_{zgr,s} = a_1 \left[1 + \left(\frac{b_2 a_{2zgr,s}}{h} e^{-(a_{r,s}\sqrt{\frac{a_{2zgr,s}}{h}} + b_{r,s})} \right)^{\frac{1}{3}} \right] \tag{3.46}$$

$$f_{\theta gr,s} = a_1 \left[1 + \left(\frac{a_{2\theta gr,s}}{h} + \frac{b_3}{h u_{r,s}} \right)^{\frac{1}{3}} \right] \tag{3.47}$$

Constants used:

$$a_{2zgr,s} = \frac{e_{gr,s}}{2\bar{C}_r} \tag{3.48}$$

$$a_{r,s} = 3.8 \cdot tanh(0.16 \cdot (L_{er,s} + 0.4)) + 0.25\sqrt{L_{er,s} + 0.4} \tag{3.49}$$

$$b_{r,s} = 10.6 \cdot e^{-0.35 \cdot L_{er,s}} + 0.57 L_{er,s}^{-0.8} + 1.37 L_{er,s}^{0.54} - 10 \tag{3.50}$$

$$L_{er,s} = \frac{L_{gr,s}}{e_{gr,s}} \tag{3.51}$$

$$a_{2\theta gr,s} = \left(\left(\frac{u_{r\infty}}{u_{s\infty}} \right) \frac{(1 - u_\infty)}{u_\infty} \cdot \left[1 + \left(a_{2gr,s} + \frac{a_3}{u_{r\infty}} \right)^{\frac{1}{3}} \right] - 1 \right)^3 - \frac{a_3}{u_{s\infty}} \tag{3.52}$$

$$a_{2gr,s} = \frac{b_2 e_{r,s}}{2\bar{C}_r} \tag{3.53}$$

$$u_{r\infty} = \sqrt{1 + 4(u_\infty - 1)^2} \tag{3.54}$$

$$u_{s\infty} = \sqrt{1 + 4u_\infty^2} \tag{3.55}$$

$$u_\infty = 0.10(e^{-6L_{er,s}} - e^{-0.3L_{er,s}}) + 0.5 \tag{3.56}$$

$a_1 = 0.001375$, $b_2 = 2 \cdot 10^4$, and $b_3 = 10^6$ are as for the Moody friction factor. a_{2gr} and a_{2gs} are given from the machining roughnesses e_r and e_s in the grooves on the rotor and stator respectively. Note that the groove depths for rotor and stator are $e_{gr,s}$ while the machining roughnesses are $e_{r,s}$.

3.7 Friction factor for hole patterned seals

Based on the friction factor for grooved seal a friction factor for hole pattern seals was proposed based on the following assumptions:

- The friction factor can be split into two separate parts: One for the part of the seal area covered by the land portion and one for the radially projected hole area.

- The holes are placed in a uniform pattern so that the friction factor can be regarded as isotropic.
- A single hole with a given hole to diameter hole depth ratio represents an obstruction to the flow similar to a groove with the same groove width to depth ratio. The difference being that the groove extends the whole circumference of the seal while the hole only extends a small fraction of the circumference.

By means of these assumptions the axial and tangential friction factors for the holes take the same format as for the axial friction factor developed for the grooves by replacing the groove width to depth ratio by the hole diameter to depth ratio, and the groove clearance to minimum seal clearance ratio by the hole depth to minimum clearance ratio.

The weighting factors for the land and hole part friction factors are given in the expression for the total friction factor for holes on the stator and/or rotor:

$$f_{r,s} = \chi_{lr,s} f_{lr,s} + \chi_{hr,s} f_{hr,s} \tag{3.57}$$

The weighting factors are given by

$$\chi_{lr,s} = \frac{\bar{L}_{lr,s} - 4\bar{C}_r}{\bar{L}_{lr,s} + d_{hr,s}} \tag{3.58}$$

$$\chi_{hr,s} = \frac{d_{hr,s}}{\bar{L}_{lr,s} + d_{hr,s}} \tag{3.59}$$

$$\bar{L}_{lr,s} = d_{hr,s}\left(\frac{1-\gamma_{r,s}}{\gamma_{r,s}}\right) \tag{3.60}$$

$$\gamma_{r,s} = \frac{hole\ area_{r,s}}{total\ area_{r,s}} \tag{3.61}$$

$d_{hr,s}$ are the diameters of holes on rotor and/or stator surface respectively. If $\chi_{lr,s} \leq 0$ it is set equal to zero.

The hole pattern friction model for both tangential and axial direction is given by

$$f_{hr,s} = a_1 \left[1 + \left(\frac{b_2 a_{2hr,s}}{h} e^{-(a_{r,s}\sqrt{\frac{a_{2hr,s}}{h}} + b_{r,s})}\right)^{\frac{1}{3}}\right] \tag{3.62}$$

$$a_{2hr,s} = \frac{e_{hr,s}}{2\bar{C}_r} \tag{3.63}$$

$$a_{r,s} = 3.8 \cdot tanh(0.16 \cdot (L_{er,s} + 0.4)) + 0.25\sqrt{L_{er,s} + 0.4} \tag{3.64}$$

$$b_{r,s} = 10.6 \cdot e^{-0.35 \cdot L_{er,s}} + 0.57 L_{er,s}^{-0.8} + 1.37 L_{er,s}^{0.54} - 10 \tag{3.65}$$

$$L_{er,s} = \frac{d_{hr,s}}{e_{hr,s}} \tag{3.66}$$

a_1 and b_2 are as for the Moody friction factor. h is the non-dimensional film thickness, $e_{hr,s}$ are hole depths for rotor and stator, $d_{hr,s}$ are the hole diameters. $\bar{C}_r$ is the minimum clearance for straight seals and average minimum clearance for tapered seals. For the land portion $f_{lr,s}$ was modelled by the Moody friction factor.

In Chapter 4 the above formulation will be compared to experimental friction factors previously published and comparisons to theoretically predicted dynamic characteristics for hole pattern seal based on the proposed friction factor and experimental results will be given.

3.8 Concluding remarks

Many assumptions have been made in this development of analytic friction factors for groove and hole patterned seals. Still the theoretical results have a good enough agreement with experimental values by other authors to make the approach useful for leakage predictions in industrial seals. One should, however, be aware of some known limitations for the friction factor for the grooves:

- It is intended for turbulent flow in the Reynolds number range $4000 - 10^6$
- It was developed for groove depth to clearance ratios between 0.2 and 25.8 so one might expect larger deviations if it is used outside this range.
- The development was made for seals having a dominant axial flow. Inaccuracies may increase as the mean tangential flow exceeds the axial.
- The seal radius to clearance ratios used for CFD calculations were 125 or greater. For smaller ratios the accuracy in results may decrease.
- It is developed for sharp grooves, while grooves in practice will become rounded off due to wear. This can have significant influence on the friction factor as discussed by (H.Möbius, 1940).

Similar limitations also apply to the friction factor for hole pattern seals.

Although a number of restrictions have been pointed out, the proposed friction factors provide the tools needed to predict rotordynamic coefficients for seals with a wide range roughness patterns and operating conditions. Rotordynamic coefficients for liquid seals is the topic for Chapter 4. Final conclusions regarding the applicability of the friction factors proposed for predicting seal leakage performance and dynamic characteristics are given in Chapter 6.

Chapter 4

Dynamic characteristics of seals

4.1 Introduction

In this chapter the friction factors developed in Chapter 3 for circumferential rectangular grooves and hole patterns are used in a bulk flow theory for predicting rotordynamic coefficients of liquid annular seals. The bulk flow theory is based on the work by (Childs, 1993) and (Nordmann *et al.*, 1987).

New improvements to the theory outlined in this chapter are:

- Circumferential grooves or hole patterns on both rotor and stator can be modelled without calibration to experimental data.
- A transition to turbulence friction factor model (Zirkelback & San Andres, 1996) is included for seals with machining roughness.
- The derivation of the equations are such that other friction factors than presented in this thesis easily can be included in the theory.
- A seal taper either due to deliberate machining or deflection is taken into account for all surface treatments.
- Moment coefficients are included throughout. For seal taper geometries extra terms where added to the theory of (Childs, 1993) which excludes seal taper geometries for moment coefficients.

Certain surface treatments of the stator have been shown to improve margins against self excited vibrations in the past, while a roughened rotor / smooth stator configuration has proved to reduce these margins. The objective of this chapter was to develop a computer program for a pump designer to evaluate the total seal performance for seals with certain types of surface roughness.

In section 4.2 the equations governing incompressible bulk flow through a tapered annular seal with grooves on rotor and/or stator are derived. The approach is similar to the one by (Nordmann *et al.*, 1987) where the circumferential groove flow is included, but differs in the way shear stresses are treated. Numerous comparisons to experimental results will be made in section 4.3, and a parameter study for a seal with groove and hole patterns is included in section 4.7. The purpose of the parameter study was to find seal surface patterns that improve dynamic stability of the pump and to reduce leakage losses compared to smooth seals.

Figures 4.1 and 4.2 show the seal geometry and motion to be analyzed. The theoretical solution for seal leakage and swirl development in this chapter is for a concentric rotor, and it is referred to as the zeroth order solution.

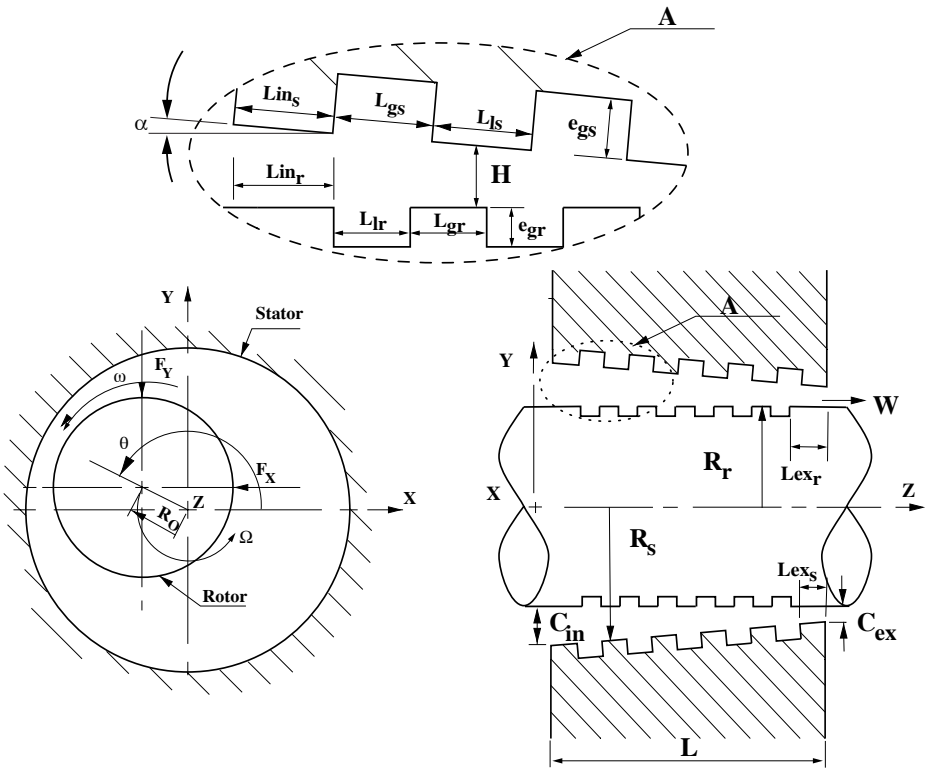

Figure 4.1: Description of groove, rotor, and stator geometry.

By perturbing the seal from its concentric position as shown in Fig. 4.2, the first order solution gives the pressure field needed to describe the relationship between the reaction force on the rotor and the described rotor motion:

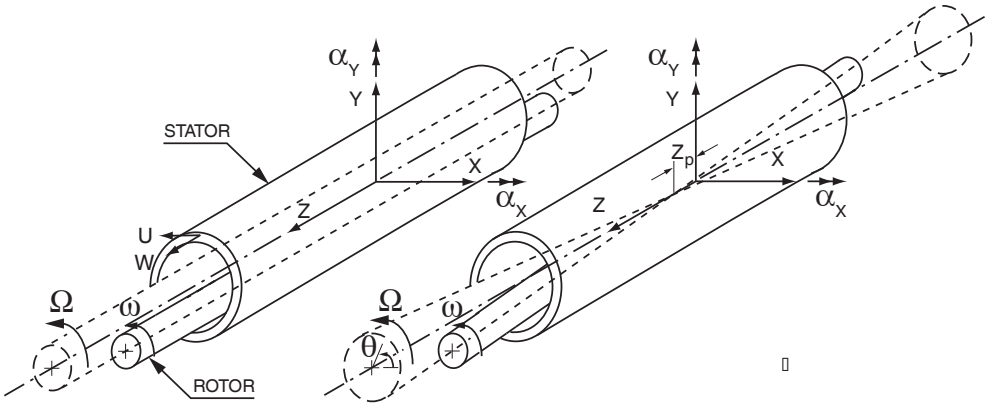

Figure 4.2: Rotor orbits for perturbation analysis.

$$
-\begin{Bmatrix} F_X \\ F_Y \\ M_Y \\ M_X \end{Bmatrix} = \begin{bmatrix} K & k & K_{\epsilon\alpha} & -k_{\epsilon\alpha} \\ -k & K & -k_{\epsilon\alpha} & -K_{\epsilon\alpha} \\ K_{\alpha\epsilon} & k_{\alpha\epsilon} & K_\alpha & -k_\alpha \\ k_{\alpha\epsilon} & -K_{\epsilon\alpha} & k_\alpha & K_\alpha \end{bmatrix} \begin{Bmatrix} X \\ Y \\ \alpha_Y \\ \alpha_X \end{Bmatrix}
$$
$$
+ \begin{bmatrix} C & c & C_{\epsilon\alpha} & -c_{\epsilon\alpha} \\ -c & C & -c_{\epsilon\alpha} & -C_{\epsilon\alpha} \\ C_{\alpha\epsilon} & c_{\alpha\epsilon} & C_\alpha & -c_\alpha \\ c_{\alpha\epsilon} & -C_{\epsilon\alpha} & c_\alpha & C_\alpha \end{bmatrix} \begin{Bmatrix} \dot{X} \\ \dot{Y} \\ \dot{\alpha}_Y \\ \dot{\alpha}_X \end{Bmatrix}
$$
$$
+ \begin{bmatrix} M & m & M_{\epsilon\alpha} & -m_{\epsilon\alpha} \\ -m & M & -m_{\epsilon\alpha} & -M_{\epsilon\alpha} \\ M_{\alpha\epsilon} & m_{\alpha\epsilon} & M_\alpha & -m_\alpha \\ m_{\alpha\epsilon} & -M_{\epsilon\alpha} & m_\alpha & M_\alpha \end{bmatrix} \begin{Bmatrix} \ddot{X} \\ \ddot{Y} \\ \ddot{\alpha}_Y \\ \ddot{\alpha}_X \end{Bmatrix} \tag{4.1}
$$

4.2 Bulk flow theory

The main purpose of the bulk flow theory in this chapter is to compute the stiffness- (K, k etc.), damping- (C, c etc.), and added mass coefficients (M, m etc.) in Eq. 4.1. From Fig. 4.3 one can derive the continuity and momentum equations as used by (Nordmann *et al.*, 1987), which includes the terms $H^+ = H_s^+ + H_r^+$ and $H^* = H + H^+$ (see Fig. 4.3) to take into account circumferential flow in the grooves. For hole pattern seals $H^+ = 0$ and $H^* = H$ as in the formulation by (Childs, 1993). Note that in the current formulation, friction factors are related to the minimum see through film thickness, H, so H^+ and H^* only appear in the first order solution of the equations below.

Assuming an incompressible fluid the continuity equation can be written as in (Nordmann *et al.*, 1987)

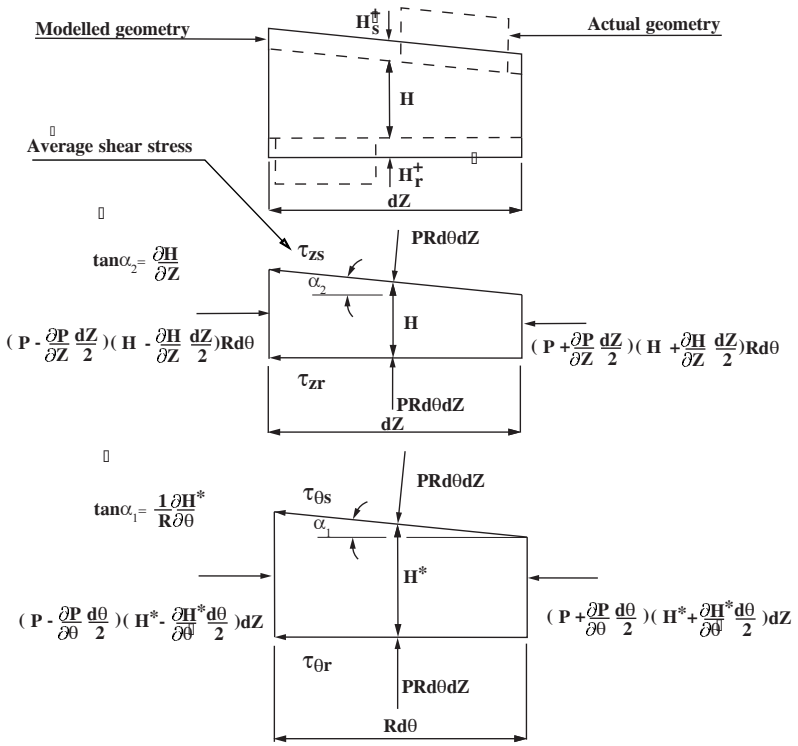

Figure 4.3: Forces acting on control volume. The shear stresses are averaged over the groove and land portion.

$$\frac{\partial H}{\partial t} + \frac{1}{R}\frac{\partial (HU)}{\partial \theta} + \frac{\partial (HW)}{\partial Z} + \frac{H^+}{R}\frac{\partial U}{\partial \theta} = 0 \tag{4.2}$$

H is the local film thickness (excluding groove depth), $R = R_r$ is the rotor radius, t is time, U the tangential bulk velocity, W the axial bulk velocity, and H^+ is the average added film thickness for the grooves ($H^+ = H_r^+ + H_s^+$).

Using the free body diagram of Fig. 4.3 the momentum equations may be written

$$-H\frac{\partial P}{\partial Z} - (\tau_{zr} + \tau_{zs}) = \rho H \left[\frac{\partial W}{\partial t} + \frac{U}{R}\frac{\partial W}{\partial \theta} + W\frac{\partial W}{\partial Z}\right] - \rho W \frac{H^+}{R}\frac{\partial U}{\partial \theta} \tag{4.3}$$

$$-\frac{H^*}{R}\frac{\partial P}{\partial \theta} - (\tau_{\theta r} + \tau_{\theta s}) = \rho H^* \left[\frac{\partial U}{\partial t} + \frac{U}{R}\frac{\partial U}{\partial \theta} + W\frac{\partial U}{\partial Z}\right] - \rho W H^+ \frac{\partial U}{\partial Z} \tag{4.4}$$

where

$$H = \left(\bar{C}_r + \frac{\alpha L}{2}\right) - \alpha Z \tag{4.5}$$

$$H^* = H + H^+ \tag{4.6}$$

$$H^+ = H_r^+ + H_s^+ \tag{4.7}$$

$$H_{r,s}^+ = \frac{e_{gr,s} L_{gr,s}}{\bar{L}_{lr,s} + L_{gr,s}} \tag{4.8}$$

$$\bar{L}_{lr,s} = \frac{Lin_{r,s} + (N_{gr,s} - 1) L_{lr,s} + Lex_{r,s}}{N_{gr,s}} \tag{4.9}$$

ρ is the fluid density, $H^* = H + H^+$ is the average film thickness, τ_{zr}, τ_{zs} are the average shear stresses in the axial direction and $\tau_{\theta r}$, $\tau_{\theta s}$ are the average shear stresses in the tangential direction for rotor and stator respectively, N_{gr} and N_{gs} are the number of grooves on the rotor and stator, and the other seal geometry parameters α, L, $Lin_{r,s}$, $Lex_{r,s}$ and $e_{gr,s}$ are shown in Fig. 4.1.

For the stator the shear stresses $\tau_{\theta s}$, τ_{zs}, and the relative bulk flow velocity U_s are given by

$$\tau_{\theta s} = \tau_{sa} \cdot \frac{U}{U_s} = \left(f_{\theta s} \rho \frac{U_s^2}{2}\right) \cdot \frac{U}{U_s} \tag{4.10}$$

$$\tau_{zs} = \tau_{sb} \cdot \frac{W}{U_s} = \left(f_{zs} \rho \frac{U_s^2}{2}\right) \cdot \frac{W}{U_s} \tag{4.11}$$

$$U_s = \sqrt{W^2 + U^2} \tag{4.12}$$

where $f_{\theta s}$ and f_{zs} are the friction factors.

Similarly for the rotor

$$\tau_{\theta r} = \tau_{ra} \cdot \frac{\omega R - U}{U_r} = \left(f_{\theta r} \rho \frac{U_r^2}{2}\right) \cdot \frac{U - \omega R}{U_r} \tag{4.13}$$

$$\tau_{zr} = \tau_{rb} \cdot \frac{W}{U_r} = \left(f_{zr} \rho \frac{U_r^2}{2}\right) \cdot \frac{W}{U_r} \tag{4.14}$$

$$U_r = \sqrt{W^2 + (U - \omega R)^2} \tag{4.15}$$

Note that the stresses $\tau_{r,sa}$ and $\tau_{r,sb}$ for the anisotropic case are pseudo stresses acting in the direction of the bulk flow vector. The pseudo stresses are used to calculate the tangential and axial shear stresses, and the actual shear force vector can have a different direction than the bulk flow.

All friction factors used in this thesis for groove, hole pattern, and transition to turbulence are given in Chapter 3 and Appendix B. The theory in this chapter is developed for a generic anisotropic friction factor for which isotropic friction factors

Table 4.1: Constants and dimensionless variables.

$\bar{W}$	=	$\frac{\dot{Q}}{2\pi R\bar{C}_r}$	b	=	$\frac{R\omega}{\bar{W}}$	w	=	$\frac{W}{\bar{W}}$
τ	=	$\frac{t}{T}$	T	=	$\frac{L}{\bar{W}}$	p	=	$\frac{P}{\rho\bar{W}^2}$
u	=	$\frac{U}{R\omega}$	h	=	$\frac{H}{\bar{C}_r}$			
α	=	$\frac{C_{in}-C_{ex}}{L}$	$\bar{C}_r$	=	$\frac{C_{in}+C_{ex}}{2}$	q	=	$\frac{\alpha L}{2C_r}$
h^+	=	$\frac{H^+}{\bar{C}_r}$	h^*	=	$\frac{H^*}{\bar{C}_r}$	z	=	$\frac{Z}{L}$

can be regarded as subsets. The expressions for the friction factors used in this thesis appear only in the coefficients given in Appendix B which are used in the differential equation to be solved.

To convert the continuity and momentum equations into non-dimensional form the constant and dimensionless variables of Table 4.1 are introduced. The dimensionless variables are u for tangential velocity, w axial velocity, p pressure, h film thickness, h^+ additional film thickness for grooves, h^* total film thickness including grooves, z axial coordinate, and τ is time. R is the rotor radius, L the seal length, C_{in} and C_{ex} the seal inlet and exit clearance, and α the seal taper angle (see Fig. 4.1). Q is the volumetric flow rate, $\bar{W}$ the average axial bulk velocity, and ω the rotational speed of the rotor.

The dimensionless film thickness and bulk velocities relative to stator and rotor become

$$h = [1 + q(1 - 2z)] \tag{4.16}$$

$$u_s = \sqrt{w^2 + b^2u^2} \tag{4.17}$$

$$u_r = \sqrt{w^2 + b^2\left(u - 1\right)^2} \tag{4.18}$$

Non-dimensional momentum equations:

Substituting shear stress expressions into the momentum equations and converting the continuity and momentum equations into non-dimensional form by means of Table 4.1 the non-dimensional momentum equations become

$$\begin{aligned} -h\frac{\partial p}{\partial z} &= \frac{w}{2}u_s f_{zs}\left(\frac{L}{\bar{C}_r}\right) + \frac{w}{2}u_r f_{zr}\left(\frac{L}{\bar{C}_r}\right) \\ &+ h\left[\frac{\partial w}{\partial \tau} + b\left(\frac{L}{R}\right)u\frac{\partial w}{\partial \theta} + w\frac{\partial w}{\partial z}\right] - h^+ b\left(\frac{L}{R}\right)w\frac{\partial u}{\partial \theta} \end{aligned} \tag{4.19}$$

$$\begin{aligned} -\frac{h^*}{b}\frac{L}{R}\frac{\partial p}{\partial \theta} &= \frac{u}{2}u_s f_{\theta s}\left(\frac{L}{\bar{C}_r}\right) + \frac{(u-1)}{2}u_r f_{\theta r}\left(\frac{L}{\bar{C}_r}\right) \\ &+ h^*\left[\frac{\partial u}{\partial \tau} + b\left(\frac{L}{R}\right)u\frac{\partial u}{\partial \theta} + w\frac{\partial u}{\partial z}\right] - h^+ w\frac{\partial u}{\partial z} \end{aligned} \tag{4.20}$$

Non-dimensional continuity equation:

$$\frac{\partial h}{\partial \tau} + \left(b\frac{L}{R}\right)\left(\frac{\partial\left(hu\right)}{\partial\theta} + \frac{\partial\left(h^{+}u\right)}{\partial\theta}\right) + \frac{\partial\left(hw\right)}{\partial z} = 0 \tag{4.21}$$

In order to separate the solution into a zeroth order solution for the concentric seal and a first order solution for the perturbed orbiting motion the following variables are introduced:

$$h = h_0 + h_1 \quad u = u_0 + u_1 \quad w = w_0 + w_1 \quad p = p_0 + p_1$$

Throughout this chapter an index for the variable ending with 1 means first order perturbed value for the variable, while 0 means zeroth order solution for the variable. By introducing the zeroth and first order variables and doing several manipulations the zeroth and first order equations can be given as shown below.

Zeroth order continuity and momentum equations:

$$h_0 w_0 = 1 \tag{4.22}$$

$$\frac{dp_0}{dz} = -\frac{1}{2h_0^2}\left(u_{s0}\sigma_{zs0} + u_{r0}\sigma_{zr0}\right) + \left[\frac{1}{h_0^3}\frac{dh_0}{dz}\right] \tag{4.23}$$

$$\frac{du_0}{dz} = -\frac{1}{2}\left[u_0 u_{s0}\sigma_{\theta s0} + \left(u_0 - 1\right)u_{r0}\sigma_{\theta r0}\right] \tag{4.24}$$

where $\sigma_{zs0} = f_{zs0}\left(\frac{L}{C_r}\right)$, $\sigma_{\theta s0} = f_{\theta s0}\left(\frac{L}{C_r}\right)$, $\sigma_{zr0} = f_{zr0}\left(\frac{L}{C_r}\right)$, and $\sigma_{\theta r0} = f_{\theta r0}\left(\frac{L}{C_r}\right)$

First order continuity, axial- and tangential momentum equations:

$$b\frac{L}{R}h_0^{*}\frac{\partial u_1}{\partial\theta} + \frac{\partial\left(h_0 w_1\right)}{\partial z} + \frac{\partial h_1}{\partial\tau} + \omega T u_0\frac{\partial h_1}{\partial\theta} + w_0\frac{\partial h_1}{\partial z} - \frac{h_1}{h_0^2}\frac{\partial h_0}{\partial z} = 0 \tag{4.25}$$

$$\frac{\partial p_1}{\partial z} + A_{2z}u_1 + A_{3z}w_1 + \left[\frac{\partial w_1}{\partial\tau} + b\left(\frac{L}{R}\right)u_0\frac{\partial w_1}{\partial\theta} + w_0\frac{\partial w_1}{\partial z}\right] = A_{1z}h_1 + \frac{h^{+}}{h_0^2}b\left(\frac{L}{R}\right)\frac{\partial u_1}{\partial\theta} \tag{4.26}$$

$$\frac{L}{R}\frac{1}{b}\left(\frac{\partial p_1}{\partial\theta}\right) + A_{2\theta}u_1 + A_{3\theta}w_1 + \left[\frac{\partial u_1}{\partial\tau} + b\left(\frac{L}{R}\right)u_0\frac{\partial u_1}{\partial\theta} + \frac{1}{h_0^{*}}\frac{\partial u_1}{\partial z}\right] = A_{1\theta}h_1 \tag{4.27}$$

The expressions for $A_{1\theta}$, $A_{2\theta}$, $A_{3\theta}$, A_{1z}, A_{2z}, A_{3z} are given in Appendix B. They contain the friction factors which are given by the zeroth order solution. The format of the above equations is similar to that of (Nordmann *et al.*, 1987) apart from the term $\frac{\partial(h_0 w_1)}{\partial z}$ in Eq. 4.25, which is due to the angular whirling motion used for moment coefficients.

The clearance function for lateral and angular perturbations (see Fig. 4.2) is given by

$$h = h_0 - \left[x + \alpha_y\left(z - z_p\right)\right]cos\theta - \left[y - \alpha_x\left(z - z_p\right)\right]sin\theta \tag{4.28}$$

where the dimensionless perturbation angles are $\alpha_y = \alpha_Y \left(\frac{L}{C_r}\right)$, $\alpha_x = \alpha_X \left(\frac{L}{C_r}\right)$. z_p is the dimensionless axial coordinate of the pivot point, and θ is the angular position around the rotor circumference.

With reference to Fig. 4.2 seal perturbed motion as a function of time is given by

$$h_1 = -\left[x(\tau) + \alpha_y\left(\tau\right)\left(z - z_p\right)\right] cos\theta - \left[y(\tau) - \alpha_x\left(\tau\right)\left(z - z_p\right)\right] sin\theta \tag{4.29}$$

Assume a circular orbit and circular angular perturbation

$$x_{max} = y_{max} = r_O \qquad\qquad \alpha_{x_{max}} = \alpha_{y_{max}} = \alpha_O \tag{4.30}$$

To simplify the derivation of the solvable ordinary differential equations, the perturbed film thickness is the real part of $\mathbf{h}_1$

$$\mathbf{h}_1 = -h_{1O} e^{j(\Omega T \tau - \theta)} \tag{4.31}$$

$$h_{1O} = r_O + \alpha_O (z - z_p) \tag{4.32}$$

$$r_O = \frac{R_O}{\bar{C}_r} \tag{4.33}$$

The assumed complex solutions are

$$\mathbf{u}_1 = \bar{u}_1 e^{j(\Omega T \tau - \theta)} \tag{4.34}$$

$$\mathbf{w}_1 = \bar{w}_1 e^{j(\Omega T \tau - \theta)} \tag{4.35}$$

$$\mathbf{p}_1 = \bar{p}_1 e^{j(\Omega T \tau - \theta)} \tag{4.36}$$

$\mathbf{u}_1, \mathbf{w}_1$, $\mathbf{p}_1$ are the complex first order tangential- and axial velocities and pressure relative to the stationary x, y, z coordinate system, and $\bar{u}_1, \bar{w}_1$, $\bar{p}_1$ are the complex solutions relative to the rotating frame of reference.

Note that the time T is the time it takes for a fluid particle to pass through the seal, Ω is the frequency of orbital motion, which is a fraction, F, of the rotational speed ω, and hence

$$T = \frac{L}{\bar{W}}, \qquad\qquad \Omega = F\omega, \qquad\qquad \Omega \neq \frac{1}{T}$$

By substituting the expression for the perturbed film thickness and the assumed form of the solution the complex equations to be solved are

$$\frac{d}{dz}\begin{Bmatrix} \bar{w}_1 \\ \bar{u}_1 \\ \bar{p}_1 \end{Bmatrix} + [A(z)] \begin{Bmatrix} \bar{w}_1 \\ \bar{u}_1 \\ \bar{p}_1 \end{Bmatrix} = r_O \begin{Bmatrix} g_1 \\ g_2 \\ g_3 \end{Bmatrix} + \alpha_O \begin{Bmatrix} g_4 \\ g_5 \\ g_6 \end{Bmatrix} \tag{4.37}$$

$$[A(z)] = \begin{bmatrix} \frac{1}{h_0}\frac{\partial h_0}{\partial z} & -j\omega T\frac{h_0^*}{h_0} & 0 \\ h_0^* A_{3\theta} & h_0^*\left(A_{2\theta} + j\Gamma T\right) & -jh_0^*\frac{1}{b}\left(\frac{L}{R}\right) \\ A_{3z} - \frac{1}{h_0^2}\frac{\partial h_0}{\partial z} + j\Gamma T & A_{2z} + j\frac{\omega T}{h_0^2}(h_0 + 2h^+) & 0 \end{bmatrix} \tag{4.38}$$

$$\begin{Bmatrix} g_1 \\ g_2 \\ g_3 \end{Bmatrix} = \begin{Bmatrix} \frac{1}{h_0} j\Gamma T - \frac{1}{h_0^3}\frac{\partial h_0}{\partial z} \\ -h_0^* A_{1\theta} \\ -\left(A_{1z} - \frac{1}{h_0^4}\frac{\partial h_0}{\partial z} + \frac{1}{h_0^2} j\Gamma T\right) \end{Bmatrix} \tag{4.39}$$

$$\begin{Bmatrix} g_4 \\ g_5 \\ g_6 \end{Bmatrix} = \begin{Bmatrix} \left(\frac{1}{h_0} jT\Gamma - \frac{1}{h_0^3}\frac{\partial h_0}{\partial z}\right)(z - z_p) + \frac{1}{h_0^2} \\ -h_0^* A_{1\theta}(z - z_p) \\ -\frac{1}{h_0^2} - \frac{1}{h_0^2} j\Gamma T(z - z_p) + \frac{1}{h_0^4}\frac{\partial h_0}{\partial z}(z - z_p) - A_{1z}(z - z_p) \end{Bmatrix} \tag{4.40}$$

where

$$\Gamma = \Omega - u_0(z)\omega \tag{4.41}$$

The additional terms in this development compared to the combined previous work of (Childs, 1993) and (Nordmann *et al.*, 1987) are found in g_4, g_5, g_6 since the seal taper is included for the moment coefficients. For a seal with no taper $h_0 = 1$ and the terms containing $\frac{\partial h_0}{\partial z}$ vanish.

Unknowns for zeroth order equations are

p_0	=	$p_0(z)$	pressure as a function of axial position
u_0	=	$u_0(z)$	tangential fluid velocity as a function of axial position
w_0	=	$w_0(z)$	axial fluid velocity as a function of axial position

There are 3 equations and 3 unknowns. Two boundary conditions can be derived from the Bernoulli equation and by assuming an inlet and outlet viscous pressure loss. The upstream pressure for the seal is P_s and the downstream pressure is P_e.

$$P_s - P(0,\theta,t) = \frac{\rho}{2}(1+\xi)\,W^2(0,\theta,t) \tag{4.42}$$

$$P(L,\theta,t) + \frac{\rho}{2}(1+\xi_e)\,W^2(L,\theta,t) = P_e \tag{4.43}$$

In dimensionless zeroth order form the Equations 4.42 and 4.43 become

$$p_s - p(0) = \frac{1}{2}(1+\xi)\,w_0^2(0) \tag{4.44}$$

$$p(1) - p_e = -\frac{1}{2}(1+\xi_e)\,w_0^2(1) \tag{4.45}$$

Note that $w_0 h_0 = 1$.

The third boundary condition is the inlet swirl, $u_0(z=0)$, which is determined from the flow conditions in the seal inlet chamber.

The boundary conditions for the first order solution become

$$\bar{p}_1(0) = -(1+\xi)\bar{w}_1(0)/h_0(0) \tag{4.46}$$
$$\bar{p}_1(1) = -(1-\xi_e)\bar{w}_1(1)/h_0(1) \tag{4.47}$$
$$\bar{u}_1(0) = 0 \tag{4.48}$$

The ordinary differential equation 4.22 was solved by a fourth order Runge Kutta method (see for example (Press *et al.*, 1992)), and a similar solution procedure was chosen for the complex equation 4.37. Since the boundary conditions are specified at both inlet and outlet, the linear shooting procedure described in Appendix B was used.

Applying the radial and angular perturbation separately, the numerical solution is of the form

$$\left\{ \begin{array}{c} \bar{w}_1 \\ \bar{u}_1 \\ \bar{p}_1 \end{array} \right\} = r_O \left\{ \begin{array}{c} s_{1c} + j s_{1s} \\ s_{2c} + j s_{2s} \\ s_{3c} + j s_{3s} \end{array} \right\}, \left\{ \begin{array}{c} \bar{w}_1 \\ \bar{u}_1 \\ \bar{p}_1 \end{array} \right\} = \alpha_O \left\{ \begin{array}{c} s_{4c} + j s_{4s} \\ s_{5c} + j s_{5s} \\ s_{6c} + j s_{6s} \end{array} \right\} \tag{4.49}$$

where s_1 is the magnitude of the complex axial velocity vector $\bar{w}_1$ relative to the rotating frame of reference, s_{1c} and s_{1s} means $s_1 cos(\theta_1)$, $s_1 sin(\theta_1)$ respectively, and $tan(\theta_1) = \frac{s_{1s}}{s_{1c}}$. θ_1 is the angle between the radial rotating axis and the vector $\bar{w}_1$.

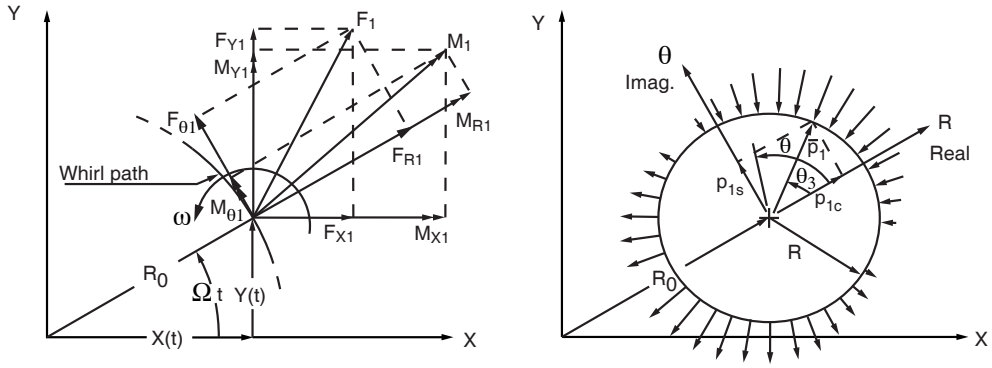

Figure 4.4: Coordinate systems for reaction forces and moments, and perturbed pressure distribution.

From the first order solution the forces acting on the rotor are derived in the same manner as in (Childs, 1993), and by perturbing the rotor with five different whirling speeds the desired dynamic coefficients are found. The final steps are given in short for perturbed translational motion.

Perturbation reaction force-components are given by

$$F_{X1} = -\int_0^L \int_0^{2\pi} P_1 cos\theta R d\theta dZ \tag{4.50}$$

$$F_{Y1} = -\int_0^L \int_0^{2\pi} P_1 sin\theta R d\theta dZ \tag{4.51}$$

where P_1 is the perturbed pressure at the rotor surface of the seal.

By introducing

$$P_1 = p_1 \rho \bar{W}^2, \quad F_0 = 2LR\Delta P, \quad z = \frac{Z}{L}, \quad \Delta P = C_d \frac{\rho \bar{W}^2}{2}$$

where C_d is the total pressure drop coefficient given by the zeroth order solution, the non-dimensional reaction force in the x-direction can be written:

$$\frac{F_{X1}}{2\Delta PRL} = -\frac{1}{C_d} \int_0^1 \int_0^{2\pi} p_1(\theta, z, t) cos\theta d\theta dz \tag{4.52}$$

$$\frac{F_{X1}}{F_0} = -\frac{\pi}{C_d} \int_0^1 p_{1c}(z,t) dz \tag{4.53}$$

Similarly

$$\frac{F_{Y1}}{F_0} = -\frac{\pi}{C_d} \int_0^1 p_{1s}(z,t) dz \tag{4.54}$$

Transforming the reaction forces to the cylindrical $r-\theta$ coordinate system which is precessing with whirling speed Ω the sum of radial and tangential force becomes

$$\frac{F_{r1} + jF_{\theta 1}}{F_0} = \frac{(F_{X1} + jF_{Y1})\, e^{-j(\Omega t)}}{F_0} \tag{4.55}$$

$$= -\frac{\pi}{C_d} \int_0^1 (p_{1c} + jp_{1s})\, e^{-j(\Omega t)} dz \tag{4.56}$$

Hence at $t = 0$

$$\frac{F_{r1} + jF_{\theta 1}}{F_0} = -\frac{\pi}{C_d} \int_0^1 \bar{p}_1 dz \tag{4.57}$$

$$\frac{F_{r1}}{F_0} = -\frac{\pi r_O}{C_d} \int_0^1 s_{3c} dz \tag{4.58}$$

$$\frac{jF_{\theta 1}}{F_0} = -\frac{\pi r_O}{C_d} \int_0^1 s_{3s} dz \tag{4.59}$$

Now introduce the non-dimensional form of the dynamic coefficients.

$$\tilde{K} = K\frac{\bar{C}_r}{F_0} \quad \tilde{C} = \frac{C\bar{C}_r\omega}{F_0} \quad \tilde{M} = \frac{M\bar{C}_r\omega^2}{F_0} \quad \tilde{k} = \frac{k\bar{C}_r}{F_0} \quad \tilde{c} = \frac{c\bar{C}_r\omega}{F_0} \quad \tilde{m} = \frac{m\bar{C}_r\omega^2}{F_0}$$

and six of the coefficients given in Eq. 4.1 can be related to the non-dimensional reaction force in the radial and tangential direction.

$$F_r(\Gamma)/R_O = -\left(\tilde{K} + \Gamma\tilde{c} - \Gamma^2\tilde{M}\right) \tag{4.60}$$

$$F_\theta(\Gamma)/R_O = \tilde{k} - \Gamma\tilde{C} - \Gamma^2\tilde{m} \tag{4.61}$$

A least square fit of the data was performed to solve for the six coefficients. Five frequency ratios, $\Gamma = \frac{\Omega}{\omega} = 0, .5, 1.0, 1.5, 2.0$ were used.

Moment coefficients are calculated similarly based on the procedure by (Childs, 1982).

4.3 Overview of results

The results presented and discussed in the following sections are for the extensions to the theory of (Childs, 1993) and (Nordmann *et al.*, 1987). The results are presented as follows:

- A comparison is made to the two dimensional transition to turbulence solution by (San Andres, 1991) and the experimental results for the transition regime by (Iwatsubo & Sheng, 1990).
- Solutions based on the developed friction factors for grooved and hole pattern seals are compared to a range of previously published experimental results and other theoretical solutions.
- Finally a parameter study is made for groove and hole pattern seals.

Results for plain and tapered seals with machining roughness and fully turbulent flow were not included in this thesis since they are based on the same theory as (Childs, 1993). However, comparisons were made for program verification. The references used were (Childs, 1993) for plain seals, (San Andres, 1993) for moment coefficients, and (Linsey, 1993) for tapered seals. No significant deviations in results were found.

4.4 Transition to turbulence results

4.4.1 Comparison to theoretical results by Zirkelback

(Zirkelback & San Andres, 1996) solve a two-dimensional zeroth order bulk flow equation based on the transition friction factor given in Appendix B, Eq. B.14. The purpose of this is to model the friction factor for the range of Reynolds numbers

Table 4.2: Seal parameters.

ρ	$= 900$ kg$/m^3$	C_r	$=$	0.2 to 1.1 mm
μ	$= 13 \cdot 10^{-3} Pa \cdot s$	ϵ_s	$=$	$\epsilon_r = 0.0$
$u(0)$	$= 0.5$	R	$=$	76.2 mm
ξ	$= 0.1$	L	$=$	50.8 mm
ξ_e	$= 1.0$	ω	$=$	3000 rpm
ΔP	$=$ 1.72 and 3.5 MPa			

$2000 < R_{r,s} < 6000$ for which the Moody friction factor may be inaccurate. One should note here that both the Moody and the transition friction factors are based on experiments for pipe flow for fully developed flow with no swirl or wall disturbances. This 2D approach by (Zirkelback & San Andres, 1996) differs from the theory presented in this chapter since it allows eccentricity effects to be studied. However, for the concentric seal results presented here, one should expect very similar results between the results by (Zirkelback & San Andres, 1996) and those based on the theory of this chapter. Seal parameters are given in Table 4.2.

Comparisons to the theoretical results of (Zirkelback & San Andres, 1996) are shown in Figures 4.5 to 4.7. The Reynolds number range for both pressures goes from laminar to fully turbulent. Since the non-dimensional swirl is 0.5 the Reynolds numbers relative to rotor and stator surfaces are equal ($Re_s = Re_r$). For the 3.50MPa pressure difference laminar flow is found for a clearance up to 350 microns, transition to turbulence for a clearance between 350 and 750 microns, and fully turbulent flow for a clearance greater than 750 microns (see Fig. 4.5). For the 1.72MPa pressure difference the corresponding ranges are $C < 440\mu m$ for laminar, $440\mu m < C < 980\mu m$ for transition to turbulence, and $980\mu m < C$ for fully turbulent flow.

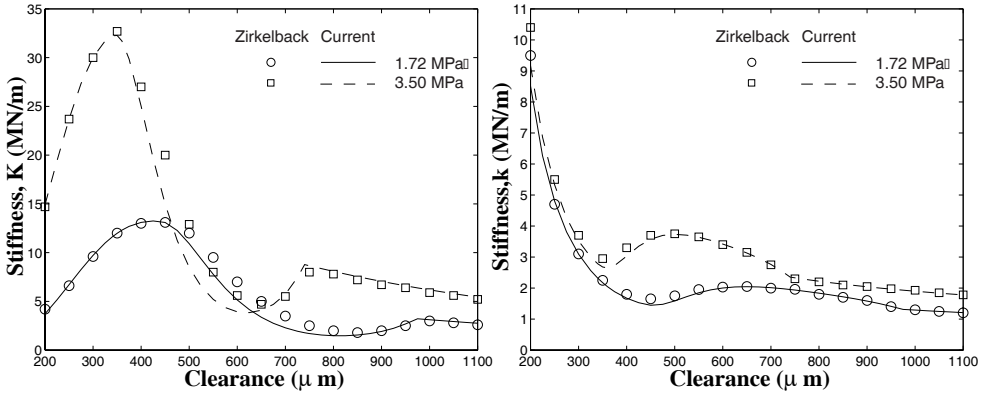

Figure 4.5: Direct stiffness (left) and cross-coupled stiffness (right). Transition turbulence friction factor. Comparison between the current bulk flow solution and the 2D solution by Zirkelback.

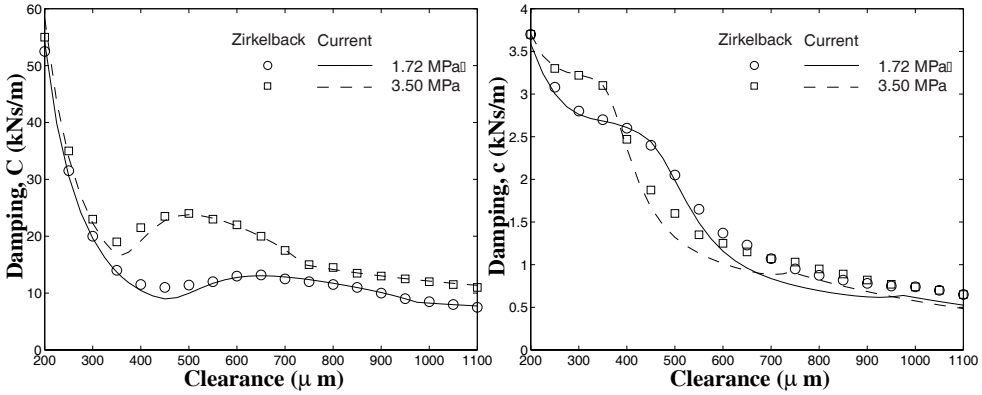

Figure 4.6: Direct damping (left) and cross-coupled damping (right). Transition turbulence friction factor. Comparison between the current bulk flow solution and the 2D solution by Zirkelback.

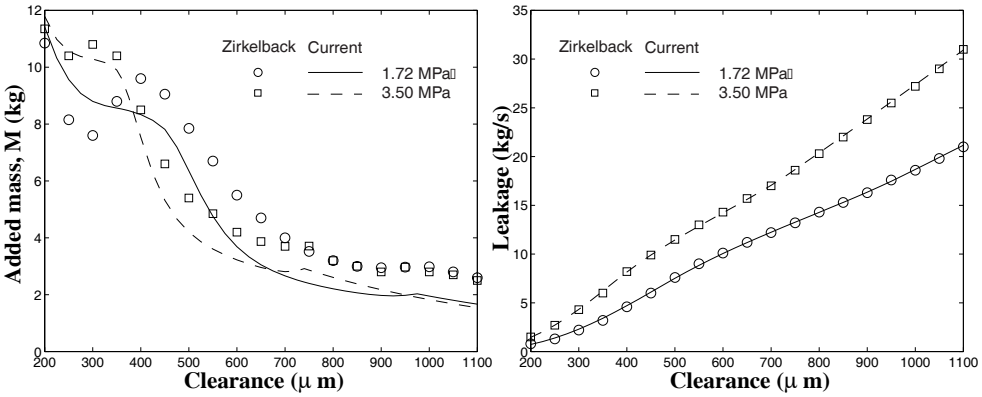

Figure 4.7: Added mass and leakage. Transition turbulence friction factor. Comparison between the current bulk flow solution and the 2D solution by Zirkelback.

Discussion of comparison to Zirkelback's results

For a pressure difference of 1.72 MPa Figures 4.5 and 4.6 show very similar results for direct-, cross-coupled stiffness and direct damping for laminar-, and fully turbulent flow. Laminar flow corresponds a clearance less than 400 μm and fully turbulent flow corresponds to a clearance greater than 750 μm at the 1.72 MPa pressure difference. In the transition zone the results deviate more, which is a little disturbing from a theoretical viewpoint. However, the deviations in results has little significance in a practical application. For cross-coupled damping and added mass in Fig. 4.6 and 4.7 there are discrepancies over the entire range, but generally deviations are not greater than 30%. A possible explanation for the differences is that cross-coupled damping and added mass are more sensitive to the numerical procedure used than the other coefficients.

4.4.2 Comparison to experimental results by Kanemori

(Kanemori & Iwatsubo, 1992) document dynamic coefficients for a seal operating in the laminar, transition-, and fully turbulent flow regime. The seal specification is given in Table 4.3.

Table 4.3: Seal specifications by Kanemori and Iwatsubo.

ρ	$= 999.0$ kg$/m^3$	C_{in}	$=$	$C_{ex} = 0.394$ mm
μ	$= 1.04 \cdot 10^{-3} Pa \cdot s$	ϵ_s	$=$	$\epsilon_r = 0.0$
ΔP	= Variable	R	$=$	39.656 mm
ξ	$= 0.5$	ω	$=$	Variable
ξ_e	$= 1.0$	$u(0)$	$=$	Variable
L	$= 240.0$ mm			

Variables used for the theoretical analysis are given in Table 4.4.

Table 4.4: Variables used for theoretical predictions.

rpm	ΔP	$u(0)$
600	5. to 2000 kPa	0.43 to 0.21
1080	8. to 2000 kPa	0.50 to 0.23
1980	20 to 2000 kPa	0.50 to 0.33
3000	40 to 2000 kPa	0.50 to 0.38

Inlet swirl was retrieved from the graphical representation in (Kanemori & Iwatsubo, 1992), but linear interpolation in the above table (swirl vs pressure for each speed) may be a reasonable approximation. Results are shown in Figures 4.8 to 4.11.

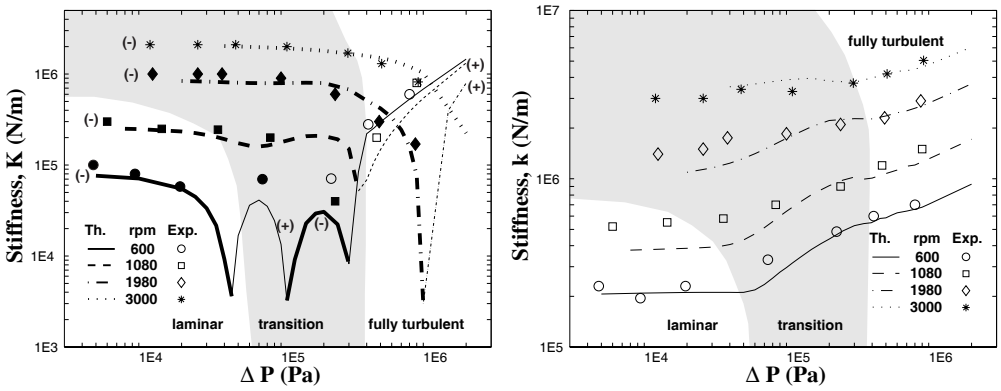

Figure 4.8: Direct and cross-coupled stiffness. Transition to turbulence friction factor. Comparison to experiment by Kanemori. Negative direct stiffness is indicated by filled markers and thick lines.

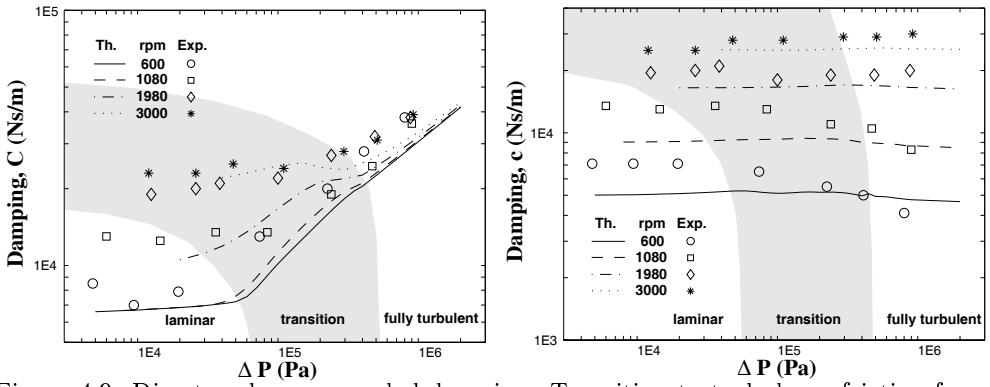

Figure 4.9: Direct and cross-coupled damping. Transition to turbulence friction factor. Comparison to experiment by Kanemori.

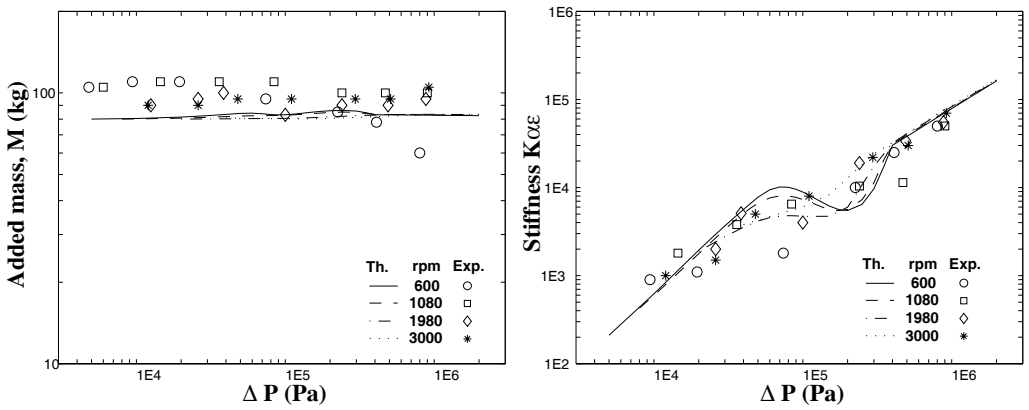

Figure 4.10: Direct added mass and cross-coupled stiffness. Transition to turbulence friction factor. Comparison to experiment by Kanemori.

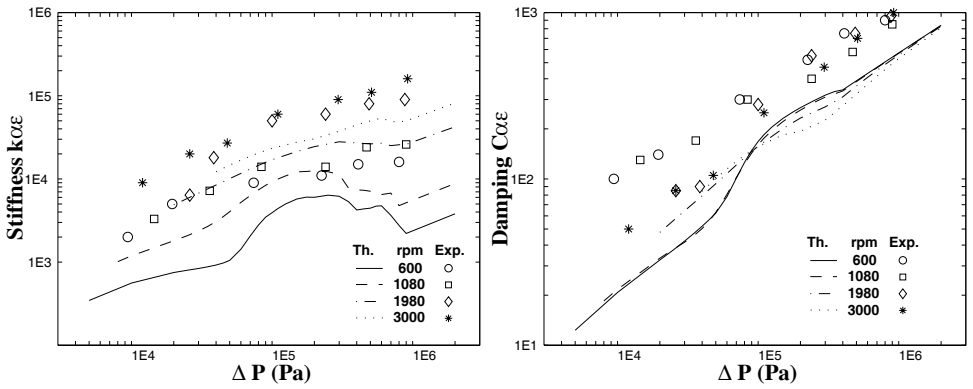

Figure 4.11: Cross-coupled stiffness and damping. Transition to turbulence friction factor. Comparison to experiment by Kanemori.

Discussion of comparison to Kanemori's results

Fig. 4.8 shows how the experimental direct stiffness varies from negative values for low pressures and positive for high pressures. Good agreement between predicted and experimental direct stiffness is found in the laminar and fully turbulent ranges. However, in the transition turbulence zone the discrepancies are rather large for some cases.

At 600 rpm the predictions based on the transition to turbulence factor give a negative stiffness at low pressures followed by positive valuez, then negative and finally positive values of stiffness for high pressures. Experimentally the resolution may not be great enough to accurately capture the trends in the transition to turbulence zone. However, looking at the discrete point at $8 \cdot 10^4$ Pa the experimental stiffness is $-7 \cdot 10^4$ N/m while the theoretical value is $+4 \cdot 10^4$ N/m. For this point the theoretical prediction by (Kanemori & Iwatsubo, 1992) is $-3 \cdot 10^4$ N/m based on the Hirs friction factor. The Hirs friction factor is very similar to the Moody friction factor for hydraulically smooth surfaces used here. It appears to predict the direct stiffness better than transition to turbulence friction factor for the $8 \cdot 10^4$ Pa pressure difference for which the Reynolds number relative to the rotor and stator is approximately 2800.

The cross-coupled stiffness in Fig. 4.8 and direct damping in Fig. 4.9 are under-predicted by as much as 50% by the current theory in the laminar and transition zone, while the Hirs solution by (Kanemori & Iwatsubo, 1992) fits better in the entire range.

Finally the predicted moment coefficients in Fig. 4.11 compare well qualitatively to experimental results. Such qualitative correspondence was also found for the thory by (Kanemori & Iwatsubo, 1992).

In summary the comparison between experimental and theoretical results indicates no gain in agreement with experimental dynamic coefficients by introducing the transition turbulence friction factor instead of a Hirs or Moody friction factor. The comparison to the results of (Kanemori & Iwatsubo, 1992) indicate that for the case studied it is better to use the Hirs or Moody friction factor alone for the entire range of results. Possible reasons for this may be that the actual friction is influenced by:

- Inlet conditions which may be highly turbulent.
- The orbiting motion of the rotor.

These are factors that are not accounted for in experiments of pipe flow, from which the proposed transition to turbulence friction factor was derived.

4.5 Results for grooved seals

In this section comparison will be made between results from the current theory, which includes the friction factors developed in Chapter 3, and results available in

the literature from experimental work and other theoretical approaches. Since the current theory supposedly cover a wide range of geometries and Reynolds numbers, comparisons are made to several references. Figure 4.12 shows the groove friction factor for the range tested in Chapter 3, and the values for the groove width to depth ratios $\frac{L_{gs}}{e_{gs}}$ and groove depth to hydraulic diameter ratios $\frac{e_{gs}}{2\bar{C}_r}$ which are covered by the references in this section.

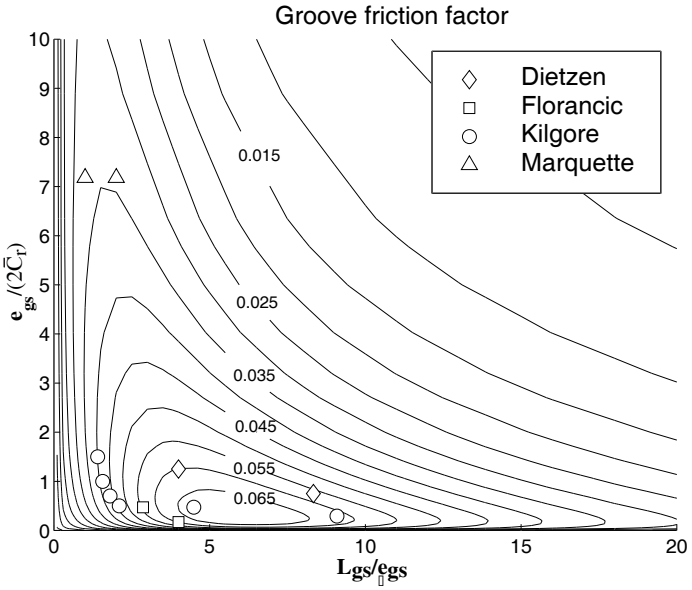

Figure 4.12: Overview of calculated groove friction factor for the stator from (Dietzen, 1987), (Florancic, 1990), (Kilgore & Childs, 1990), and (Marquette *et al.*, 1997)
.

An overview of seal parameters studied in this section is given in Table 4.5.

Table 4.5: Overview of seal length to diameter ratios, seal length to clearance ratios, and tangential Reynolds number ranges covered.

Author	L/D	$\frac{L}{2\bar{C}_r}$	$Re_z = \frac{2\rho W C_r}{\mu}$	$Re_\omega = \frac{\omega R \bar{C}_r}{\mu}$
(Dietzen, 1987)	0.500	58.75	9368	2801
(Florancic, 1990)	0.114	54.05	6500 - 176900	10950 - 137500
	0.114	27.03	12300 - 340700	20650 - 272200
(Kilgore & Childs, 1990)	0.504	54.04	89800 - 287000	25300 - 177100
	0.504	53.81	89500 - 289000	25300 - 177100
	0.504	66.67	90000 - 251000	25300 - 177100
	0.504	51.61	119000 - 351000	25300 - 177100
	0.504	40.00	129000 - 429000	25300 - 177100
	0.504	33.33	159000 - 508000	25300 - 177100
(Marquette *et al.*, 1997)	0.45	158.03	11000 - 15200	8400 - 19500

Detailed comparisons to each reference are given in turn.

4.5.1 Comparison to experimental and CFD results by Dietzen

(Dietzen, 1987) studied six seals with different groove depths experimentally and theoretically with a two-dimensional finite difference CFD-solution. The same case has also been studied theoretically by (Arghir & Frêne, 1997c). Seal parameters used for theoretical predictions are given in Table 4.6.

Table 4.6: Common parameters for all seals.

ρ	$= 996$ kg/m^3	C_{in}	$=$	$C_{ex} = 0.2$ mm
μ	$= 0.70 \cdot 10^{-3} Pa \cdot s$	e_s	$=$	e_r =0.0
Re_z	$= 9368$	R	$=$	23.5 mm
ξ	$= 0.38$	ω	$=$	4000 rpm
ξ_e	$= 1.0$	$u(0)$	$=$	0.2
L	$= 240.0$ mm	L_{gs}	$=$	2.5 mm
Lin_s	$= 3$ mm	Lex_s	$=$	3 mm
N_{gs}	$= 10$	h_s^+	$=$	1

The seals only differ in groove depth, $e_{gs} = 0.0$, 0.1, 0.2, 0.3, 0.4, 0.5 respectively.

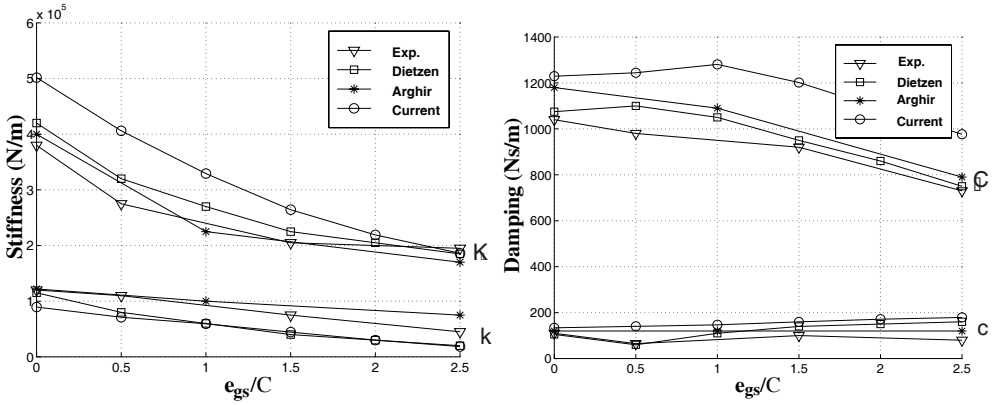

Figure 4.13: Stiffness and damping coefficients. Comparison between experimental results and the current bulk flow solution. CFD Solutions by (Arghir & Frêne, 1997c) and (Dietzen, 1987) are also shown.

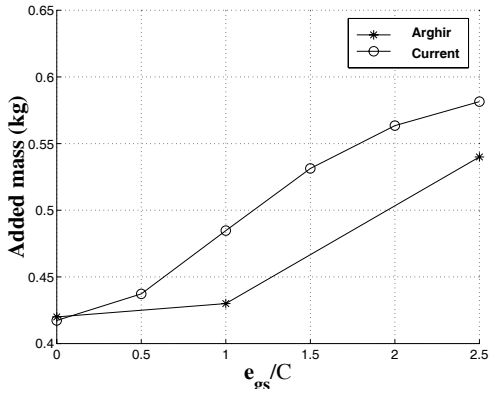

Figure 4.14: Added mass. Comparison between the current bulk flow solution and the CFD Solution by (Arghir & Frêne, 1997c).

Discussion of comparison to Dietzen's results

Fig. 4.13 shows that the predictions based on CFD-methods generally predict the dynamic coefficients with slightly better agreement with experimental results than the current bulk flow model. However, the bulk flow model does predict coefficients with an accuracy which probably is adequate for most practical applications, and the analysis time and complexity to the user are much less than required to use the CFD-methods which solve the detailed two-dimensional flow field by the Reynolds Averaged Navier-Stokes equations. (Arghir & Frêne, 1997c) document grooved seal solutions that take up to 40000 CPU seconds to run on a 233 MHz workstation while the solutions based on the theory in this chapter spends about 2 CPU seconds for any grooved seal on a 133 MHz PC.

4.5.2 Comparison to experimental and theoretical results by Florancic

(Florancic, 1990) studied one plain and two grooved seals and implemented a three volume bulk flow solution to calculate dynamic coefficients. Comparisons will be made between the current theory and Florancic's experimental and theoretical results. The water temperature in the seal was varied between 20 to 160 deg C to allow a large Reynolds number range to be studied. Seal parameters are given in Table 4.7.

Seal parameters used for the current theory are listed in Table 4.7.

Individual parameters:

Seal 1, no grooves: $C_{in} = C_{ex} = 0.37$mm, $\xi = 0.25$, $e_{gs} = 0.0$

Seal 2, with grooves: $C_{in} = C_{ex} = 0.37$mm, $\xi = 0.25$, $e_{gs} = 0.35$ mm

Seal 3, with grooves: $C_{in} = C_{ex} = 0.74$mm, $\xi = 0.40$, $e_{gs} = 0.25$ mm

Table 4.7: Seal parameters used for the current theory.

ρ	= Variable	C_{in}	=	C_{ex} = Variable
μ	= Variable	e_s	=	$e_r = 8 \cdot 10^{-6} m$
ΔP	= Variable	R	=	175 mm
ξ	= Variable	ω	=	Variable
ξ_e	= 1.0	$u(0)$	=	Variable
L	= 40.0 mm	L_{gs}	=	1 mm
Lin_s	= 1.5 mm	Lex_s	=	1.5 mm
L_{ls}	= 1.0 mm	N_{gs}	=	19

For the current model two sets of results are tabulated, one where the dimensionless additional circumferential height, $h_s^+ = 1$ and one where $h_s^+ = 0$. The rationale for this is that for very shallow grooves relative to the clearance one may assume no perturbed flow in grooves, which means $h_s^+ = 0$, while at very deep grooves one may expect that all the groove flow is perturbed and hence $h_s^+ = 1$. The results are given in Tables 4.8 to 4.8. At the bottom of tables 4.11 and 4.13 the average ratio and standard deviation between theoretical results from the current theory and experimental results are given. Below Tables 4.11 and 4.13 the average ratio and standard deviation obtained by (Florancic, 1990) between theoretical predictions using a three-control-volume method and the experimental results are included for comparison.

Table 4.8: **Seal 1:** Theoretical results based on the Moody friction factor and Childs' model.

#	$\frac{\Delta P}{10^5}$ Pa	ω rpm	$u(0)$	ρ $[\frac{kg}{m^3}]$	$\frac{\mu}{10^{-3}}$ $[\frac{Ns}{m^2}]$	$\frac{Re_z}{1000}$	$\frac{K}{1e6}$ $[\frac{N}{m}]$	$\frac{k}{1e6}$ $[\frac{N}{m}]$	$\frac{C}{1e4}$ $[\frac{Ns}{m}]$	$\frac{c}{1e4}$ $[\frac{Ns}{m}]$	M $[kg]$
1	1.98	1500	0.12	998	1.000	6.16	1.79	0.29	0.97	0.12	9.07
2	6.20	1500	0.22	998	1.000	12.82	5.71	0.62	1.94	0.12	8.59
3	15.1	1500	0.25	998	1.000	21.11	13.6	1.18	3.20	0.12	8.32
4	1.72	1500	0.11	979	0.407	14.04	1.56	0.26	0.89	0.12	8.92
5	5.75	1500	0.21	979	0.407	30.36	5.30	0.57	1.86	0.12	8.40
6	13.7	1500	0.24	979	0.407	49.34	12.4	1.07	3.04	0.11	8.14
7	4.68	2500	0.14	973	0.357	26.54	4.28	0.79	1.47	0.20	8.86
8	16.6	2500	0.25	973	0.357	59.30	15.4	1.95	3.17	0.20	8.32
9	35.5	2500	0.24	973	0.357	90.32	32.1	2.85	4.87	0.19	8.09
10	2.21	2000	0.12	908	0.172	34.91	1.96	0.45	0.95	0.15	8.29
11	8.09	2000	0.25	908	0.172	81.71	7.53	1.04	2.10	0.15	7.83
12	18.7	2000	0.25	908	0.172	130.9	16.9	1.66	3.39	0.14	7.57
13	5.07	3000	0.14	908	0.172	53.20	4.51	1.06	1.44	0.23	8.28
14	19.6	3000	0.25	908	0.172	127.6	18.1	2.43	3.28	0.22	7.80
15	9.58	4000	0.15	908	0.172	74.31	8.62	1.94	2.00	0.30	8.28

Table 4.9: **Seal 1:** Comparison to experimental results for the plain seal of Florancic and the current theory based on the Moody friction factor. Experimental values reported equal to zero are not included when calculating average and standard deviation values.

Case #	Q $\frac{Th}{Exp}$	K $\frac{Th}{Exp}$	k $\frac{Th}{Exp}$	C $\frac{Th}{Exp}$	c $\frac{Th}{Exp}$	M $\frac{Th}{Exp}$
1	1.03	0.88	0.51	0.65	1.04	0.60
2	1.07	0.92	0.44	0.67	Inf	0.90
3	1.13	0.96	0.52	0.84	-0.65	0.36
4	0.95	1.17	0.72	0.80	1.45	1.35
5	1.03	1.02	0.47	0.71	Inf	Inf
6	1.10	1.04	0.59	0.92	-Inf	0.26
7	0.96	1.05	0.60	0.67	0.75	0.98
8	1.07	1.06	0.48	0.78	1.63	0.91
9	1.08	1.04	0.61	0.79	0.74	0.28
10	0.81	1.06	0.89	0.82	1.49	1.08
11	0.96	1.09	0.52	0.87	Inf	1.12
12	1.03	1.04	0.67	1.01	Inf	0.19
13	0.84	1.07	0.79	0.83	1.06	0.95
14	0.99	1.12	0.51	0.88	0.95	0.70
15	0.87	1.13	0.71	0.85	1.00	1.00
Avg.	0.99	1.04	0.60	0.80	0.95	0.82
Std.	0.10	0.08	0.13	0.10	0.64	0.33

Table 4.10: **Seal 2:** Theoretical results based on the current grooved seal friction factor model with $h_s^+ = 0$.

#	$\frac{\Delta P}{10^5}$ Pa	ω rpm	$u(0)$	ρ $[\frac{kg}{m^3}]$	$\frac{\mu}{10^{-3}}$ $[\frac{Ns}{m^2}]$	$\frac{Re_z}{1000}$	$\frac{K}{1e6}$ $[\frac{N}{m}]$	$\frac{k}{1e6}$ $[\frac{N}{m}]$	$\frac{C}{1e4}$ $[\frac{Ns}{m}]$	$\frac{c}{1e4}$ $[\frac{Ns}{m}]$	M $[kg]$
1	2.77	1500	0.15	998	1.000	6.76	2.03	0.39	1.21	0.12	9.05
2	9.53	1500	0.15	998	1.000	13.36	6.50	0.55	2.57	0.10	8.52
3	20.8	1500	0.15	998	1.000	20.17	13.2	0.80	4.01	0.09	8.27
4	1.86	1500	0.16	979	0.407	13.22	1.35	0.36	0.94	0.12	8.93
5	6.71	1500	0.15	979	0.407	27.08	4.74	0.45	2.07	0.10	8.50
6	15.6	1500	0.11	979	0.407	42.27	10.1	0.46	3.39	0.09	8.18
7	5.25	2500	0.15	973	0.357	25.40	3.83	0.96	1.59	0.20	8.89
8	19.7	2500	0.15	973	0.357	52.95	13.8	1.23	3.56	0.17	8.42
9	44.7	2500	0.14	973	0.357	81.62	28.8	1.68	5.73	0.15	8.11
10	2.33	2000	0.15	908	0.172	33.12	1.66	0.55	1.00	0.15	8.29
11	9.83	2000	0.13	908	0.172	74.45	7.05	0.61	2.38	0.13	7.95
12	24.6	2000	0.15	908	0.172	121.3	16.0	1.10	4.09	0.11	7.58
13	5.47	3000	0.15	908	0.172	50.98	3.90	1.23	1.53	0.22	8.30
14	23.7	3000	0.12	908	0.172	116.0	16.9	1.30	3.73	0.19	7.92
15	50.7	3000	0.12	908	0.172	173.7	33.2	1.73	5.84	0.17	7.62
16	10.1	4000	0.14	908	0.172	69.71	7.28	2.17	2.09	0.29	8.31
17	46.2	4000	0.11	908	0.172	162.3	32.6	2.03	5.26	0.25	7.89

Table 4.11: **Seal 2:** Comparison between experimental results by Florancic and the current theory with $h_s^+ = 0$ (the five first coefficients) and $h_s^+ = 1$ for the remaining.

#	$\frac{Q_{Th}}{Q_{Exp}}$	K $\frac{K_{Th}}{K_{Exp}}$	k $\frac{k_{Th}}{k_{Exp}}$	C $\frac{C_{Th}}{C_{Exp}}$	c $\frac{c_{Th}}{c_{Exp}}$	M $\frac{M_{Th}}{M_{Exp}}$	K $\frac{K_{Th}}{K_{Exp}}$	k $\frac{k_{Th}}{k_{Exp}}$	C $\frac{C_{Th}}{C_{Exp}}$	c $\frac{c_{Th}}{c_{Exp}}$	M $\frac{M_{Th}}{M_{Exp}}$
1	1.04	0.86	0.82	0.59	0.60	0.43	0.84	0.42	0.59	0.82	0.44
2	0.99	0.75	1.01	0.72	0.88	0.29	0.73	0.12	0.71	1.40	0.30
3	1.00	0.73	1.02	0.61	0.36	0.52	0.71	0.14	0.60	0.59	0.54
4	0.89	0.80	1.45	0.83	1.32	0.52	0.77	0.93	0.83	1.71	0.54
5	0.92	0.76	1.19	0.67	1.29	0.83	0.74	0.15	0.66	2.02	0.86
6	0.95	0.76	0.78	0.79	Inf	Inf	0.74	-0.34	0.77	Inf	Inf
7	0.90	0.80	1.38	0.65	0.74	0.47	0.78	0.84	0.65	0.97	0.49
8	0.93	0.81	0.82	0.66	0.60	0.39	0.79	0.05	0.65	0.95	0.40
9	0.97	0.83	0.99	0.77	0.23	0.22	0.81	-0.04	0.76	0.38	0.23
10	0.74	0.72	1.79	0.76	1.39	0.63	0.70	1.30	0.76	1.71	0.65
11	0.87	0.88	0.82	0.73	1.47	0.94	0.86	-0.05	0.72	2.34	0.98
12	0.94	0.93	0.79	0.88	Inf	0.36	0.91	0.10	0.86	Inf	0.37
13	0.78	0.77	1.49	0.75	1.11	0.57	0.75	1.04	0.75	1.39	0.58
14	0.88	0.97	0.73	0.75	0.45	0.35	0.94	-0.14	0.74	0.73	0.36
15	0.99	1.12	0.90	0.80	0.28	0.39	1.09	-0.28	0.78	0.47	0.41
16	0.80	0.84	1.41	0.74	0.71	0.58	0.81	0.95	0.74	0.90	0.60
17	0.92	0.96	1.16	0.74	0.40	0.26	0.93	-0.56	0.73	0.67	0.28
Avg.	0.91	0.84	1.09	0.73	0.79	0.49	0.82	0.27	0.72	1.14	0.51
Std.	0.08	0.10	0.31	0.07	0.43	0.20	0.10	0.55	0.07	0.59	0.21

Average values and standard deviation from (Florancic, 1990)

Avg.		0.96	0.91	0.86	0.61		
Std.		0.08	0.21	0.09	0.44		

Table 4.12: **Seal 3:** Theoretical results based on the current grooved seal friction factor model with $h_s^+ = 0$.

#	$\frac{\Delta P}{10^5}$ Pa	ω rpm	$u(0)$	ρ $[\frac{kg}{m^3}]$	$\frac{\mu}{10^{-3}}$ $[\frac{Ns}{m^2}]$	$\frac{Re_z}{1000}$	$\frac{K}{1e6}$ $[\frac{N}{m}]$	$\frac{k}{1e6}$ $[\frac{N}{m}]$	$\frac{C}{1e4}$ $[\frac{Ns}{m}]$	$\frac{c}{1e4}$ $[\frac{Ns}{m}]$	M $[kg]$
1	1.35	1500	0.14	998	1.000	11.88	0.73	0.03	0.40	0.07	5.04
2	5.02	1500	0.15	998	1.000	24.21	2.34	0.12	0.93	0.05	4.42
3	11.14	1500	0.14	998	1.000	36.72	4.83	0.21	1.45	0.04	4.24
4	1.30	1500	0.15	979	0.407	28.42	0.70	0.03	0.39	0.06	4.93
5	4.21	1500	0.14	979	0.407	53.82	1.99	0.09	0.83	0.05	4.38
6	10.29	1500	0.15	979	0.407	85.98	4.47	0.20	1.38	0.04	4.16
7	3.27	2500	0.15	973	0.357	51.13	1.76	0.09	0.61	0.11	4.93
8	12.25	2500	0.15	973	0.357	104.70	5.74	0.29	1.42	0.08	4.33
9	28.29	2500	0.15	973	0.357	162.17	12.29	0.58	2.28	0.06	4.14
10	1.70	2000	0.15	908	0.172	73.34	0.91	0.05	0.42	0.08	4.63
11	6.88	2000	0.15	908	0.172	157.04	3.25	0.16	1.02	0.06	4.06
12	15.90	2000	0.14	908	0.172	243.47	6.92	0.30	1.65	0.05	3.87
13	3.64	3000	0.15	908	0.172	107.11	1.96	0.11	0.61	0.12	4.64
14	15.73	3000	0.15	908	0.172	237.79	7.41	0.38	1.55	0.09	4.05
15	37.09	3000	0.16	908	0.172	372.45	16.14	0.84	2.52	0.07	3.86
16	7.33	4000	0.15	908	0.172	153.38	3.95	0.21	0.88	0.16	4.61
17	29.28	4000	0.15	908	0.172	324.85	13.71	0.69	2.12	0.11	4.04

Table 4.13: **Seal 3:** Comparison between experimental results by Florancic and the current theory with $h_s^+ = 0$ (the five first coefficients) and $h_s^+ = 1$ for the remaining.

#	Q $\frac{Th}{Exp}$	K $\frac{Th}{Exp}$	k $\frac{Th}{Exp}$	C $\frac{Th}{Exp}$	c $\frac{Th}{Exp}$	M $\frac{Th}{Exp}$	K $\frac{Th}{Exp}$	k $\frac{Th}{Exp}$	C $\frac{Th}{Exp}$	c $\frac{Th}{Exp}$	M $\frac{Th}{Exp}$
1	0.97	0.75	0.58	0.58	1.02	0.39	0.73	-0.27	0.58	1.23	0.40
2	0.97	0.70	2.48	0.80	1.53	0.19	0.70	1.04	0.80	1.84	0.19
3	0.97	0.69	1.96	0.80	0.20	0.20	0.69	1.13	0.80	0.24	0.20
4	0.96	0.73	0.33	0.56	1.04	0.38	0.72	-0.09	0.56	1.25	0.39
5	0.92	0.77	0.75	0.80	0.91	0.27	0.76	0.21	0.79	1.11	0.28
6	0.98	0.74	2.09	0.77	0.31	0.35	0.73	1.25	0.76	0.37	0.36
7	0.92	0.85	0.35	0.65	1.15	0.50	0.83	-0.09	0.65	1.39	0.51
8	0.96	0.81	0.84	0.82	0.57	0.21	0.80	0.33	0.82	0.69	0.22
9	0.98	0.78	1.09	0.89	0.21	0.15	0.77	0.67	0.89	0.25	0.15
10	0.86	0.76	0.31	0.60	1.54	0.51	0.74	-0.06	0.60	1.86	0.52
11	0.92	0.81	0.80	0.75	0.92	0.27	0.80	0.26	0.74	1.11	0.28
12	0.95	0.77	0.99	0.92	0.33	0.19	0.76	0.55	0.91	0.40	0.19
13	0.84	0.80	0.38	0.67	1.27	0.51	0.78	-0.09	0.68	1.53	0.53
14	0.93	0.83	0.64	0.86	0.45	0.22	0.82	0.24	0.86	0.54	0.23
15	0.97	0.81	1.20	0.87	0.16	0.16	0.80	0.78	0.86	0.19	0.16
16	0.90	0.88	0.24	0.66	0.99	0.56	0.86	-0.04	0.66	1.19	0.57
17	0.95	0.84	0.50	0.87	0.42	0.20	0.83	0.20	0.86	0.51	0.20
Avg.	0.94	0.78	0.91	0.76	0.77	0.31	0.77	0.35	0.75	0.93	0.32
Std.		0.05	0.67	0.12	0.47	0.14	0.05	0.47	0.11	0.56	0.14

Average values and standard deviation from (Florancic, 1990)

Avg.		0.92	1.66	1.19	0.94	0.27	
Std.		0.05	1.10	0.19	0.41	0.09	

Discussion of comparison to Florancic's results

Table 4.8 shows the comparison between the straight **Seal 1** solution based on the Moody friction factor and the experimental values. On average the theory predicts leakage very well, but it under-predicts leakage for cases 4, 7, 10, and 13 and over-predict leakage for cases 3, 6, 9, and 12 in Table 4.8. The under-prediction in leakage which is up to 19% for case 10 in the table occurs when the tangential Reynolds number is approximately twice the axial and over-prediction occurs for the inverse ratio. This indicates that there is a greater swirl dependency on leakage than predicted by the Moody friction factor.

Regarding stiffness coefficients direct stiffness is well predicted with little deviation, while the predicted cross-coupled stiffness is on average just 60% of the measured values. Predicted direct damping and added mass are on average 80% of the experimental, and added mass has a significant standard deviation, which probably is due to experimental error.

Table 4.11 shows the comparison between Florancic's experimental and current theoretical results with no tangential flow in the grooves, $h_s^+ = 0$, and full contribution from tangential flow $h_s^+ = 1$ for the grooved **Seal 2**. On average leakage is under-predicted by the theory by 9%. At large ratios of tangential to axial flow leakage is

under-predicted while better correspondence is found when the axial flow is greater than the tangential. So there is a greater swirl dependency on leakage than accounted for by the current axial friction factor. This trend is similar to that for the straight seal for which the Moody friction factor was used.

Regarding dynamic coefficients for **Seal 2** h_s^+ has little influence on direct stiffness, direct damping, and added mass, and these coefficients are on average 0.84, 0.73, and 0.49 times the experimental values respectively. This is a reduced agreement with experimental result compared to the straight seal solution for which the corresponding ratios were 1.04, 0.80, and 0.82.

For **Seal 2** where the clearance is approximately the same as the dimensionless groove depth, h_s^+ does have a significant influence on cross-coupled stiffness and damping. With $h_s^+ = 0$, the average values and standard deviations are similar to the ones obtained by the three-control-volume code by (Florancic, 1990), while at $h_s^+ = 1$ the cross-coupled stiffness for this seal is on average significantly under-predicted. In the previous comparison to the experimental results of (Dietzen, 1987), h_s^+ did not have the same influence on cross-coupled stiffness and damping although similar groove depth to clearance ratios were studied. Hence, no general conclusion could be made regarding the appropriate choice of h_s^+ based on the groove depth to clearance ratio alone.

For the results of **Seal 3**, shown in Table 4.13, both the average and standard deviations from experimental values predicted by (Florancic, 1990) (results below the table) using a three-control-volume method and the current predictions show poor agreement with experimental results. However, the absolute values are very small and experimental inaccuracies are large in comparison.

4.5.3 Comparison to Kilgore's experimental results

(Kilgore & Childs, 1990) studied the dynamic characteristics of two seals with triangular grooves and four with rectangular grooves. The axial Reynolds numberRe_z ranges from $9 \cdot 10^4$ to $5 \cdot 10^5$ The current model which is developed for rectangular grooves was used to approximate the behaviour of triangular grooves, by setting $h_s^+ = 0.5$ and using the maximum groove depth for friction factor calculations. Seal parameters are given in Tables 4.14 and 4.15. The rotational speeds used for each seal are ω= 1000, 2000, 3000, 5300, 7200 rpm.

Table 4.14: Parameters used for all seals.

ρ	$= 1570\ kg/m^3$	C_{in}	$= C_{ex}$ = Variable
μ	$= 1.54 \cdot 10^{-4}\ Pa \cdot s$	e_s	$= e_r = 0.76 \cdot 10^{-6} m$
Re_z	= Variable	R	= 50.42 mm
ξ	= 0.15	ω	= Variable
ξ_e	= 1.0	$u(0)$	= 0.1
L	= 50.8 mm	Lex_s	= 1.4 mm
Lin_s	= 1.4 mm	L_{ls}	= 1.0 mm
L_{ls}	= 1.0 mm		

Table 4.15: Dimensions for grooved seals in Kilgore's test. Seal 1 and 2 have triangular grooves.

Stator	C_r (mm)	e_{gs} (mm)	L_{ls}(mm)	L_{gs} (mm)	h_s^+ (mm)
1	0.470	0.445	2.00	2.00	0.5
2	0.472	0.275	1.50	2.50	0.5
3	0.381	1.143	1.60	1.60	1.0
4	0.508	1.016	1.60	1.60	1.0
5	0.635	0.889	1.60	1.60	1.0
6	0.762	0.762	1.60	1.60	1.0

Figure 4.15 shows the combined rotor/stator friction factor, f=$f_r + f_s$ for Stator 1 and 2 which have triangular grooves.

Kilgore's test rig did not identify the individual coefficients since the orbital speed Ω had to be the same as the rotational speed ω. Hence the effective stiffness, -damping, and -mass shown in Eq. 4.63 was used.

$$F_\theta/R_O = C_{ef}\omega \tag{4.62}$$

$$F_r/R_O = K_{ef} + M_{ef}\omega^2 \tag{4.63}$$

R_O=radial perturbation and it is assumed that k and c vary linearly with ω.

Table 4.16 shows a comparison between the experimental effective dynamic coefficients and theory. The theoretical values were obtained in the following manner for each stator and axial Reynolds number: The slope of the tangential force curve, $C_{ef} = \frac{k}{\omega} - C$, is retrieved for each rotational speed. This value was close to being constant like the experiment predicts, and the average C_{ef} slope for the six rotational speeds was reported. K_{ef} is the value of F_r/R_0 for zero velocity for the rotor. Its value was obtained by a quadratic curve fit through the values of F_r/R_0 at six rotational speeds, and extrapolation to zero rotational speed.

The effective mass, M_{ef}, can be found by the following formulas based on (Kilgore & Childs, 1990):

$$M_{ef} = \frac{F_r/R_O + K_{ef}}{\omega^2} \tag{4.64}$$

$$M_{ef} = \frac{K_{ef} - K}{\omega^2} - \frac{c}{\omega} + M \tag{4.65}$$

M_{ef}, should according to theory, remain near constant for all speeds tested. Theoretically, however, there is a significant variation in M_{ef} with ω. The reported value of M_{ef} is based on the single value M as ω goes to zero.

Table 4.16: Comparison between current theoretical results and experimental results by Kilgore.

Re_z	K_{ef} Exp	C_{ef} Exp	M_{ef} Exp	K_{ef} Exp/Th	C_{ef} Exp/Th	M_{ef} Exp/Th
Stator 1						
89803	271000	3160	4.85	0.84	0.63	0.74
130040	495000	5210	6.33	0.73	0.71	0.95
160000	741000	6450	7.57	0.73	0.72	1.14
220000	1470000	9300	10.00	0.77	0.75	1.50
287000	2280000	12700	11.60	0.70	0.79	1.73
Stator 2						
89502	264000	3590	4.89	0.83	0.69	0.75
130000	620000	5530	6.29	0.92	0.73	0.95
160000	930000	7040	7.21	0.92	0.75	1.09
220000	1620000	10100	9.38	0.85	0.78	1.41
289000	2690000	14000	11.40	0.82	0.82	1.71
Stator 3						
89997	409000	5540	4.46	1.42	1.17	0.46
130000	852000	7800	5.94	1.44	1.16	0.62
170000	1310000	10200	7.10	1.30	1.17	0.74
219000	2240000	12100	9.17	1.35	1.07	0.95
251000	3270000	13400	11.30	1.50	1.03	1.17
Stator 4						
118990	281000	3840	4.04	1.05	1.05	0.59
189000	488000	6880	5.73	0.73	1.21	0.83
220000	747000	8000	6.73	0.83	1.22	0.98
279000	1100000	10600	7.44	0.76	1.27	1.08
351000	1790000	12500	8.27	0.78	1.18	1.20
Stator 5						
129000	277000	3060	2.99	1.49	1.17	0.57
199000	592000	5020	4.76	1.35	1.27	0.91
278010	976000	7700	5.78	1.15	1.42	1.10
348000	1550000	10300	7.75	1.17	1.51	1.48
429000	1680000	11500	5.71	0.83	1.36	1.09
Stator 6						
159000	162000	2300	2.22	0.91	1.02	0.54
258010	444000	4260	3.24	0.95	1.18	0.78
336990	791000	6190	3.80	1.00	1.32	0.91
377000	869000	6640	3.96	0.88	1.26	0.95
507990	2250000	9260	4.74	1.26	1.30	1.13
Avg.				1.01	1.06	1.00
Std.				0.26	0.25	0.33

Average values and standard deviations from (Kilgore & Childs, 1990) where the theory used was based on the Hirs friction factor.

Avg.				1.31	1.01	2.93
Std.				0.46	0.09	0.71

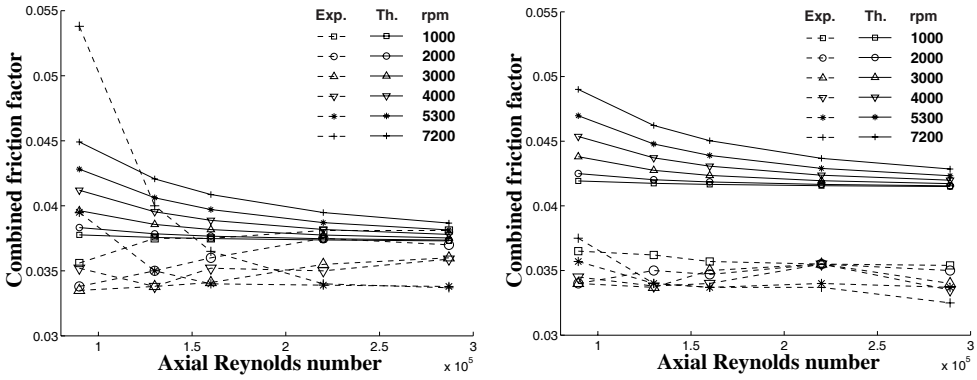

Figure 4.15: Combined friction factor for grooved stator 1 and 2.

Discussion of comparison to Kilgore's results

The theoretical predictions of leakage in Fig. 4.15 are about 20% greater than the Kilgore's experimental values, which means that theoretical leakage is approximately 10% under-predicted in this case. The theoretical friction factor predicts a small increase with rotational speed while the experimental results show a mixed trend.

However, the result for dynamic coefficients in Table 4.16 compares well to the Hirs friction factor solution presented by Kilgore where the Hirs friction factor is calibrated to experiment. Possible reasons for the good agreement in results may be that the partial derivative of the current groove friction factor with respect to the film thickness, $\frac{\partial f_{zgs}}{\partial h}$, is better accounted than in the Hirs based solution and that the Reynolds number dependency for the friction factor is not very strong.

From the comparison in Table 4.16 one can see that the effective stiffness K_{ef} is predicted with less standard deviation by the current friction factor than by the calibrated Hirs friction factor, while the effective damping is somewhat under-predicted for the rectangular grooves and over-predicted for the triangular grooves. The Hirs solution is more consistent, and the reason may be that the rectangular groove friction factor model does not apply directly to the triangular-grooves for Stator 1 and 2.

Partially the deviations in Table 4.16 may be due to parameters that are assumed to be constant like inlet/exit loss and inlet swirl. By setting inlet swirl to zero, the effective damping gets reduced by about 12%, while inlet/exit loss has greatest influence on direct stiffness.

4.5.4 Comparison to Marquette's deep groove experimental results

The grooved seals used for comparison in the previous sections have had grooves with depths up to three times the clearance. (Marquette *et al.*, 1997) studied two grooved seals that had grooves with depths about 14.4 times the clearance. Seal parameters needed for the comparison are given in Tables 4.17 and 4.18.

Table 4.17: Parameters for both seals.

ρ	$= 985.7\ kg/m^3$	C_{in}	$= C_{ex} =$ Variable
μ	$= 5.13 \cdot 10^{-4}\ Pa \cdot s$	ϵ_s	$= \epsilon_r = 0.0$
R_O	= Variable	R	= 38.252 mm
ξ	= 0.10	ω	= Variable
ξ_e	= 1.0	$u(0)$	= 0.25
L	= 34.925 mm	L_{ls}	= 1.587 mm

Individual parameters

The smooth seal results, which are documented for comparison, are based on the same minimum clearance and length the results for the grooved seals.

Table 4.18: Dimensions used for grooved seals in Marquette's test.

Seal 1	C_r (mm)	e_{gs} (mm)	L_{gs}(mm)	Lin_s mm	Lex_s (mm)
rpm 10200	0.1074	1.587	1.587	2.381	2.381
rpm 17400	0.1052	1.587	1.587	2.381	2.381
rpm 24600	0.1029	1.587	1.587	2.381	2.381
Seal 2					
rpm 10200	0.1074	3.175	3.175	1.587	1.587
rpm 17400	0.1052	3.175	3.175	1.587	1.587
rpm 24600	0.1029	3.175	3.175	1.587	1.587

Figures 4.16 to 4.22 show a comparison between experimental and theoretical result for leakage, dynamic coefficients, and whirl frequency ratio for the two grooved seals. Two pressures differences across the seal, 4.14 and 6.45 MPa, and three rotational speeds, 10200, 17400, and 24600 rpm were considered. The smooth seals results included for comparison are theoretical and based on the theory by (Childs, 1993).

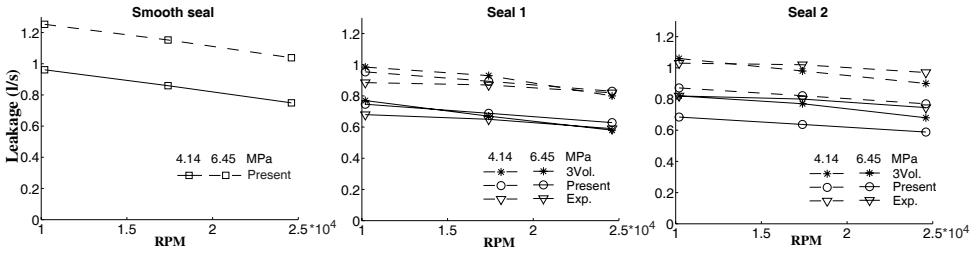

Figure 4.16: Leakage from experiment, three volume theory by Marquette, and comparison to the current results and smooth seal theory.

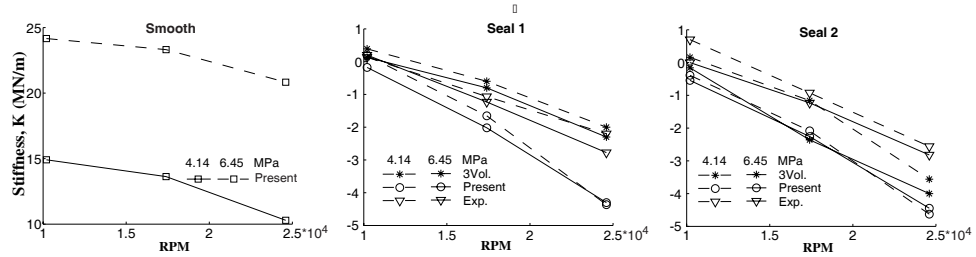

Figure 4.17: Direct stiffness from experiment and three volume theory by Marquette and comparison to the current results and smooth seal theory.

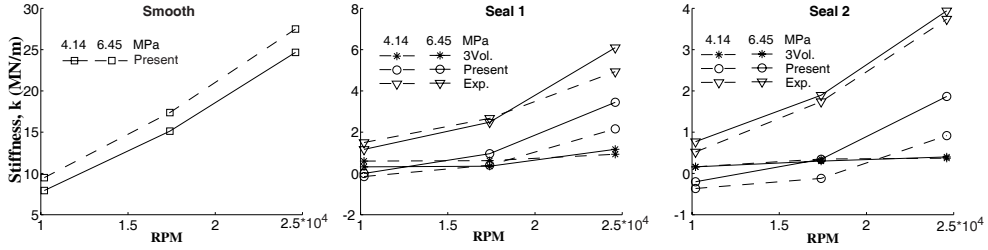

Figure 4.18: Cross-coupled stiffness from experiment and three volume theory by Marquette and comparison to the current results and smooth seal theory.

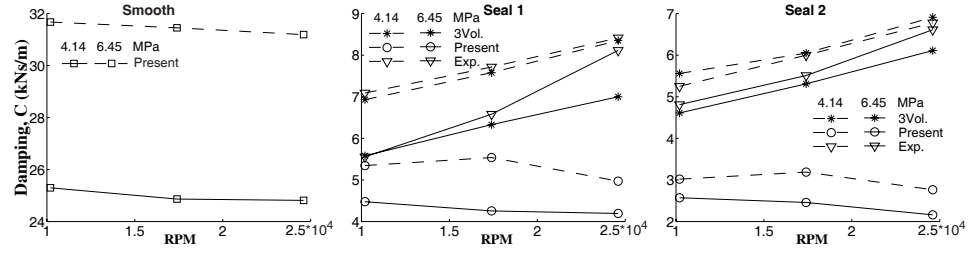

Figure 4.19: Direct damping from experiment and three volume theory by Marquette and comparison to the current results and smooth seal theory.

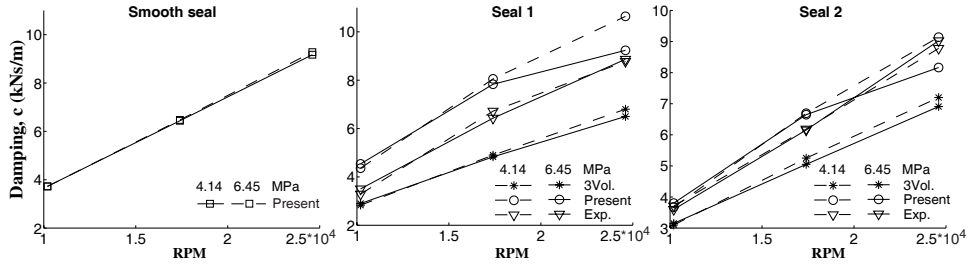

Figure 4.20: Cross-coupled damping from experiment and three volume theory by Marquette and comparison to the current results and smooth seal theory.

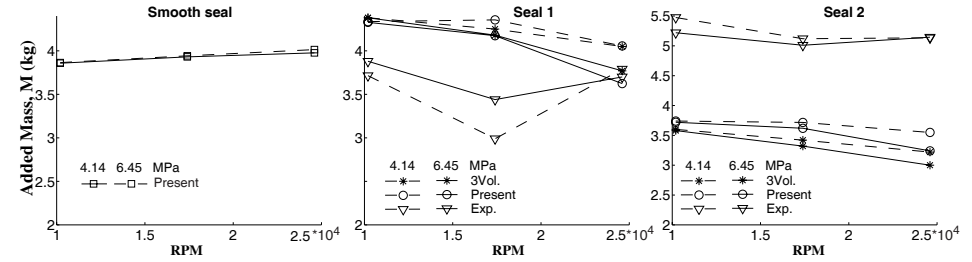

Figure 4.21: Direct added mass from experiment and three volume theory by Marquette and comparison to the current results and smooth seal theory.

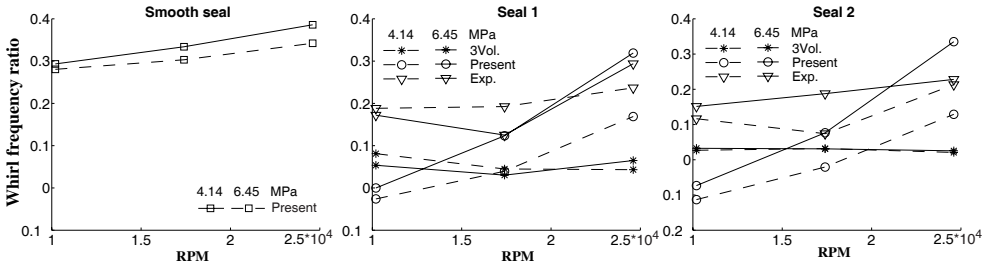

Figure 4.22: Whirl frequency ratio from experiment and three volume theory by Marquette and comparison to the current results and smooth seal theory.

Discussion of comparison to Marquette's results

From Fig. 4.16 it can be seen that the current code predicts slightly less leakage for the deeply grooved seals than for the equivalent smooth seal. Compared to Marquette's xperimental results the leakage is over-predicted by about 5% for Seal 1 and under-predicted by about 15% for Seal 2 respectively. The leakage predictions by Marquette have about the same agreement with experimental for Seal 1 and better agreement for Seal 2.

Figures 4.17 to 4.19 show that there is a very significant drop in direct, cross-coupled stiffness, and direct damping for the grooved seals compared to the smooth. The direct stiffness becomes negative and hence acts to increase rotor eccentricity at 17400 and 24600 rpm. Cross-coupled stiffness drops more in percent than damping, and this has a positive effect on the whirl frequency ratio which is reduced compared to the smooth seal.

Cross-coupled damping and added mass change less when the grooves are introduced. Figures 4.20 and 4.21 show that both coefficients are predicted with reasonable accuracy compared to the experimental results.

4.6 Results for hole pattern seals

Strictly speaking, the friction factor developed for grooved seals might not be applicable to hole pattern seals. However, a hypothesis was established, suggesting that:

- The hole pattern will yield an isotropic friction factor
- The axial friction factor developed for grooved seals can be used in an arbitrary direction for hole pattern seals. In practice, one needs to calculate equivalent length for the land zone based on the ratio of hole area to total surface area.
- There is no net tangential or radial flow for fluid within the holes, hence $h^+ = 0$.

In order to test the above hypothesis a comparison was made to two references that both document experimental results and theoretical results based on the Hirs friction factor which was calibrated to experiment.

Figure 4.23 gives an overview of how the geometries tested are located in the range for the current hole friction factor. Table 4.19 gives an overview of approximate seal length to diameter ratios, length to minimum clearance ratios, and tangential Reynolds number ranges covered.

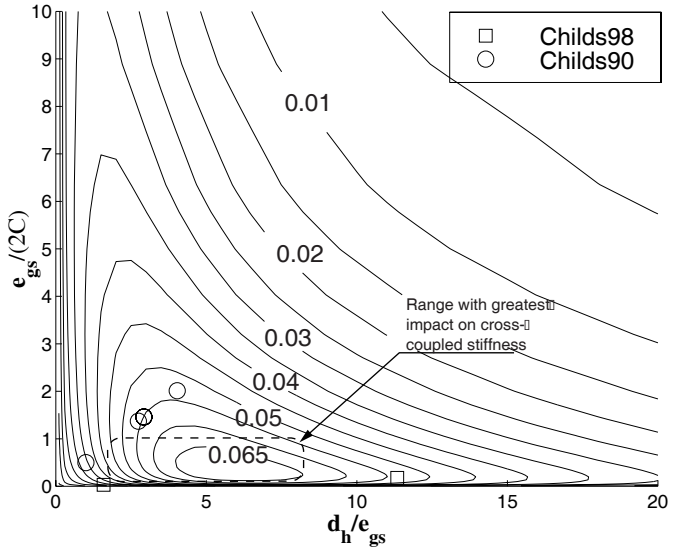

Figure 4.23: Overview of the hole patterns studied experimentally and the current theoretical friction factor. The dashed line indicates the range of hole patterns that was found to have greatest influence on cross-coupled stiffness in a parameter study at the end of this section.

Table 4.19: Seal parameters.

Author	L/D	$\frac{L}{2\bar{C}_r}$	$Re_z = \frac{2\rho W C_r}{\mu}$	$Re_\omega = \frac{\omega R \bar{C}_r}{\mu}$
(Childs *et al.*, 1990)	0.49	133	90000-258110	20400- 143000
(Childs & Fayolle, 1998)	0.46	176	10000-13500	7750-16100

4.6.1 Comparison to experimental results by Childs et al

The comparison here is to the experiment by (Childs *et al.*, 1990) on hole pattern seals.

Parameters used for all seals The inlet swirl was not measured, and hence it

Table 4.20: Seal geometry and fluid parameters

ρ	$= 1570\ kg/m^3$	C_{in}	$=$	C_{ex} = Variable
μ	$= 1.54 \cdot 10^{-4}\ Pa \cdot s$	e_s	$=$	$e_r = 0.74\ \mu$m
R_O	= Variable	R	$=$	50.08 mm
ξ	$= 0.15$	ω	$=$	Variable
ξ_e	$= 1.0$	$u(0)$	$=$	0.2
L	= 49.96 mm			

has to be estimated. As seen in the experiment of (Linsey, 1993) swirl is generally a function of rotational speed and leakage, but here an average value was chosen that may be to high for some cases and too low for others.

Individual parameters

Table 4.21: Individual seal geometries.

Stator	d_h (mm)	C_r (mm)	e_{hs} (mm)	γ
1	3.80	0.376	0.376	0.34
2	3.80	0.371	1.017	0.34
3	3.80	0.376	1.098	0.34
4	3.80	0.379	1.527	0.34
5	3.55	0.376	1.098	0.27
6	4.31	0.381	1.113	0.42

The rotational speeds used for each seal are, $\omega = 1000$, 2000, 3000, 4000, 5300, 7200, and the reported dynamic coefficients are as for Kilgore's grooved seal in the previous section based on effective stiffness, damping and added mass, defined by Eq. 4.63.

Figure 4.24 shows a comparison between the experimental friction factor for Stator 1 and 6 and the theoretical values. The friction factor shown is the combined friction factor for rotor and stator $f = f_r + f_s$

Table 4.22 shows a comparison between the experimental effective dynamic coefficients and theory. The theoretical values were obtained in the following manner for each stator and axial Reynolds number: For each rotational speed, $C_{ef} = \frac{k}{\omega} - C$ which is the slope of the tangential force curve, is retrieved. This value was close to being constant like the experiment predicts, and the average C_{ef} for the six rotational speeds was reported. K_{ef} describes the radial force per unit displacement F_r/R_O at an extrapolated zero velocity for the rotor. Its value was obtained by a quadratic curve fit through the six radial forces and extrapolation.

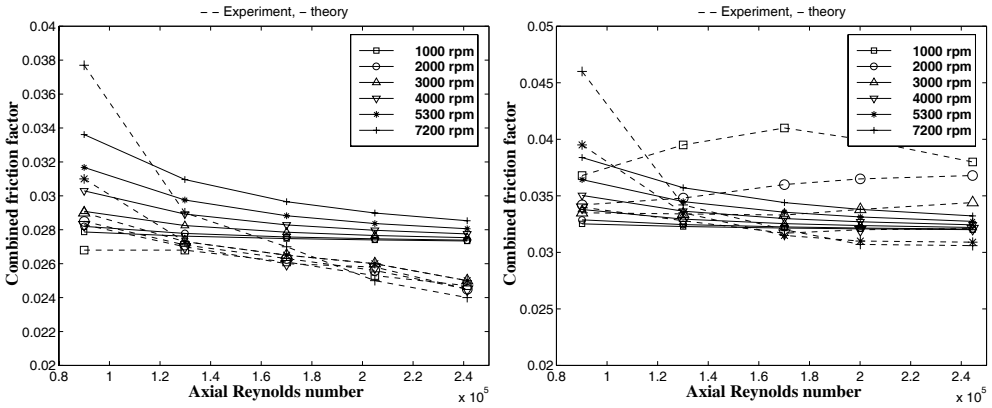

Figure 4.24: Left figure: Combined friction factor for Stator 1. Right figure: Combined friction factor for Stator 6.

The effective mass, M_{ef}, can be found by Equations 4.64 and 4.64:

M_{ef} should according to theory remain near constant for all speeds tested. Theoretically, however, there is a significant variation in M_{ef} with ω. The reported value of M_{ef} is based on the single value M as ω goes to zero.

Table 4.22: Comparison to the hole pattern seal of Childs et al.

Re_z	K_{ef} Exp	C_{ef} Exp	M_{ef} Exp	K_{ef} Exp/Th	C_{ef} Exp/Th	M_{ef} Exp/Th
Stator 1						
90005	635200	7737	8.30	0.89	0.87	1.17
129790	1267000	11640	8.51	0.84	0.91	1.20
170010	1848000	15200	7.95	0.73	0.92	1.12
204910	2590000	18190	7.53	0.71	0.91	1.06
241410	3643000	21680	12.24	0.72	0.93	1.72
Stator 2						
90018	950000	7378	8.94	1.28	0.78	1.24
129810	1823000	11330	9.15	1.17	0.83	1.26
160170	2537000	14910	10.40	1.09	0.89	1.44
190200	3312000	17670	12.17	1.02	0.89	1.68
232100	4892000	21990	14.12	1.02	0.91	1.95
Stator 3						
90005	948000	7135	8.51	1.33	0.79	1.20
129790	1772000	11290	9.23	1.18	0.87	1.30
160210	2474000	14640	9.17	1.10	0.91	1.29
195110	3765000	17310	9.33	1.14	0.89	1.31
241410	5251000	21270	12.77	1.05	0.89	1.79
Stator 4						
90723	1066000	5596	8.36	1.49	0.67	1.20
130830	1848000	10840	6.84	1.22	0.90	0.98
161480	2637000	13840	7.21	1.16	0.93	1.03
196670	3810000	18930	11.26	1.14	1.05	1.61
243340	4742000	22120	14.10	0.93	0.99	2.02
Stator 5						
90005	1049000	6217	11.28	1.46	0.76	1.61
129790	1736000	9934	8.72	1.14	0.85	1.25
179780	3211000	14830	11.09	1.11	0.92	1.59
220030	4371000	18400	11.68	1.02	0.94	1.67
258110	5479000	20880	8.74	0.94	0.91	1.25
Stator 6						
90114	987000	6551	2.45	1.47	0.69	0.34
130100	2111000	10060	2.37	1.50	0.74	0.33
170100	3393000	12670	4.83	1.45	0.71	0.68
200100	4462000	13740	10.31	1.40	0.66	1.44
244500	5621000	15320	9.46	1.19	0.61	1.32
Avg.				1.13	0.85	1.30
Std.				0.23	0.10	0.40

Average values and standard deviations from (Childs *et al.*, 1990) where the theory used was based on the Hirs friction factor.

Avg.				1.01	0.92	2.91
Std.				0.33	0.10	0.70

Discussion of comparison to results by Childs et al.

The current theory for hole pattern seals under-predicts the effective stiffness measured by (Childs *et al.*, 1990) by 12% on average (see Table 4.22), but has less standard deviation than the solution based on the Hirs friction factor which is calibrated to experiment. Table 4.22 also shows that effective damping is over-predicted by 12% on average compared to the experimental values and has approximately the same standard deviation as the Hirs method.

The effective added mass varied with ω, and the only value reported is the added mass M, at zero rotational speed. This value gives a reasonable estimate of the effective added mass M_{ef} although large deviations are found for Stator 6.

When ω is greater than zero, the theory rapidly predicts deviations in M_{ef} from experiment. In order to quantify how the different theoretical coefficients K, c, and M contribute to M_{ef}, a parameter study was performed for Stator 1. Fig. 4.25 shows the individual contribution from the terms $\frac{K_{ef}-K}{\omega^2}$, $-\frac{c}{\omega}$, and M. If one assumes that the theoretical prediction of relatively constant added mass term, M, is correct, then the term $\frac{K_{ef}-K}{\omega^2} - \frac{c}{\omega}$, has to cancel in order to keep a constant M_{ef}. From Fig. 4.25 it is clear that an over-predicted cross-coupled damping and direct stiffness term reduces the effective mass. This trend is confirmed in the comparison to results of (Childs & Fayolle, 1998) in the next section, where individual coefficients were identified. Comparison between the results based on the current theory and experimental values in (Childs & Fayolle, 1998) show that the current theory significantly over-predicts cross-coupled damping and direct stiffness. Since a sensitivity test on the results of Fig. 4.25 showed that cross-coupled damping was little influenced by inlet swirl or inlet/exit losses, one will have to look elsewhere for an explanation for this discrepancy.

The over-prediction in direct-stiffness, K, means that the Lomakin effect is over-estimated. This may may be due to several factors. For example, the assumed inlet loss may be too large, the friction factor for hole patterns may be inaccurate, or secondary flows may exist that are not accounted for in the current theory.

Other deviations in results may be due to the parameters the assumed inlet swirl. An inlet swirl of $u(0) = 0.2$ was assumed here since it was not specified. C_{ef} increases significantly as $u(0)$ increases. The reason for choosing $u(0) = 0.2$ was that there is no preswirl of the fluid before it enters the seal inlet chamber. Hence, one should expect a inlet swirl between 0.0 and 0.5 depending on the leakage rate.

4.6.2 Comparison to experimental results by Childs & Fayolle

In (Childs & Fayolle, 1998) the individual dynamic coefficients for two hole pattern seals are documented. Seal parameters are given in Table 4.23.

Individual parameters

Seal 1 is run at 10200, 17400, 24600 rpm. $e_{hs} = 0.28$ mm

Seal 2 at 10200, 15600, 21000 rpm. $e_{hs} = 2.0$ mm

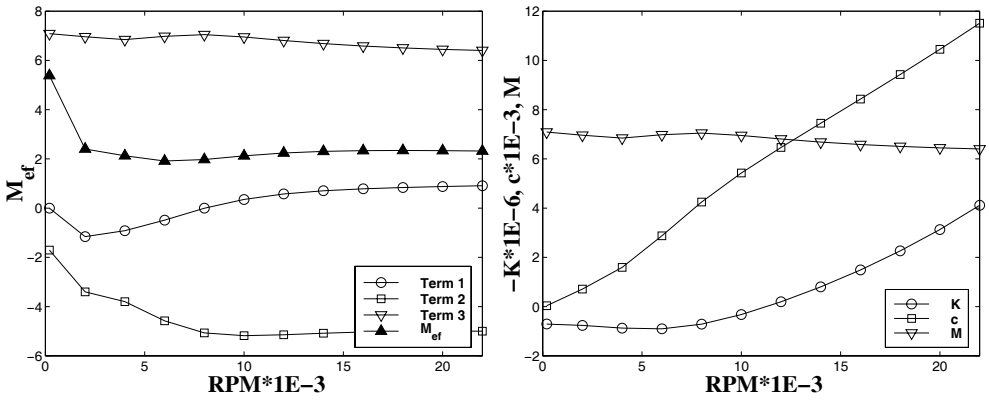

Figure 4.25: Left figure: Effective mass M_{ef}=Term 1 + Term 2 + Term 3, where Term 1= $\frac{K_e f - K}{\omega^2}$, Term 2= $-\frac{c}{\omega}$
, Term 3=M. Right figure: The individual coefficients which contribute to F_r/R_O.

Two pressure differences, 4.0 MPa, and 7.0 MPa are used for both seals at all speeds.

Seal 2 has theoretically very similar leakage since the hole-friction factors are so similar and the hole to total area ratio γ is the same for both seals. No direct comparison to (Childs & Fayolle, 1998) was available, but they report a leakage reduction of about 6% compared to the plain seals. From Fig. 4.26 the theoretical prediction gives slightly less leakage, but it is approximately within 10 to 15% of experimental values.

In Figures 4.27 to 4.31 the dynamic coefficients for the two hole pattern seals are compared to theoretical predictions. For comparison the theoretical coefficients for a plain seal are shown. The plain seal has the same dimensions and machining roughness as the two hole pattern seals but no holes. When studying these results one should bear in mind that the experimental uncertainties documented by (Childs & Fayolle, 1998) are in the order of

$K \approx 1$ MN/m, $k \approx 2$ MN/m, $C \approx 1$ kNs/m, $c \approx 1$ kNs/m, $M \approx 1.5$ kg

which means that the predictions for Seal 2 have reasonable accuracy while Seal 1 shows qualitative results for the direct stiffness, and added mass.

Table 4.23: Parameters used for both seals.

ρ	$= 985.7\ kg/m^3$	C_{in}	$=$	$C_{ex} = 0.1$ mm
μ	$= 5.13 \cdot 10^{-4}\ Pa \cdot s$	e_s	$=$	$e_r = 0.74\ \mu$m
ΔP	= Variable	R	$=$	38.129 mm
ξ	$= 0.10$	ω	$=$	Variable
ξ_e	$= 1.0$	$u(0)$	$=$	0.25
L	= 34.925 mm	d_h	$=$	3.175
γ	= 0.364 mm	h^+	$=$	0.0

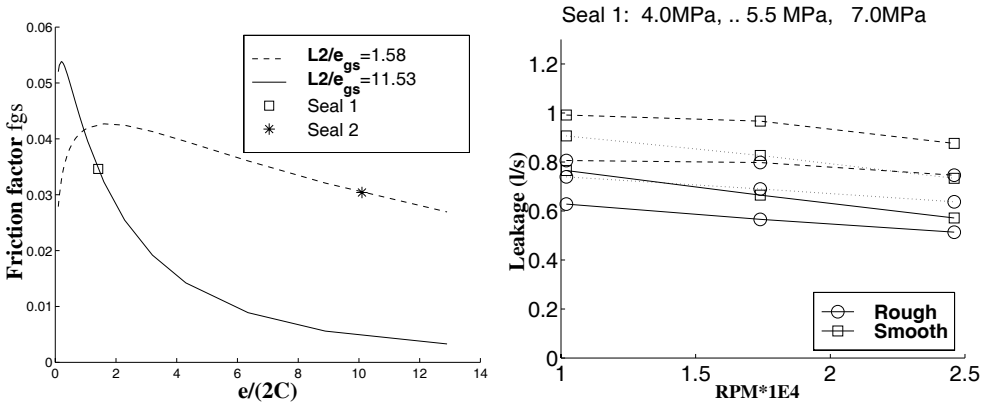

Figure 4.26: To the left: Friction factors for the holes of Seal 1 and 2 plotted together with the friction factor for the same holes at a range of clearances. To the right: Leakage for Seal 1 and a corresponding a hydraulically smooth seal with the same clearance.

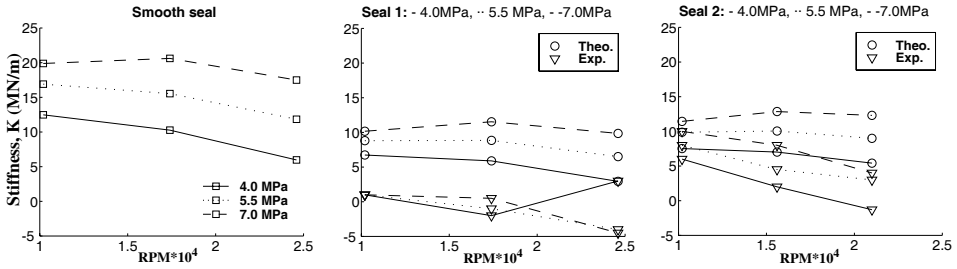

Figure 4.27: Direct stiffness for round hole pattern seals. Comparison between experimental, theoretical, and theoretical smooth seal results.

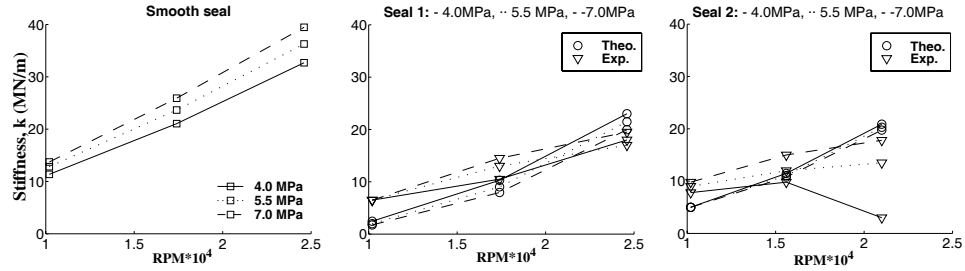

Figure 4.28: Cross-coupled stiffness for round hole pattern seals. Comparison between experimental, theoretical, and theoretical smooth seal results.

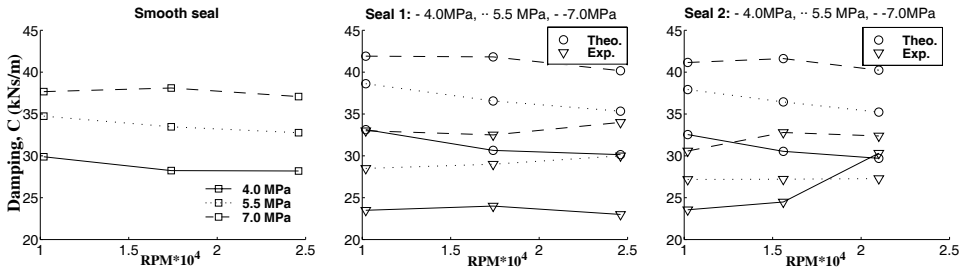

Figure 4.29: Direct damping for round hole pattern seals. Comparison between experimental, theoretical, and theoretical smooth seal results.

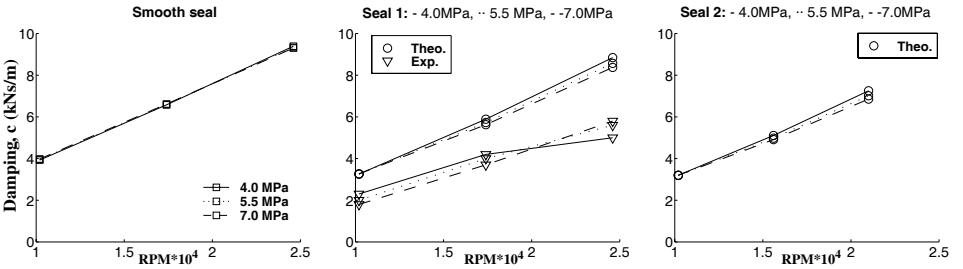

Figure 4.30: Cross-coupled damping for round hole pattern seals. Comparison between experimental, theoretical, and theoretical smooth seal results.

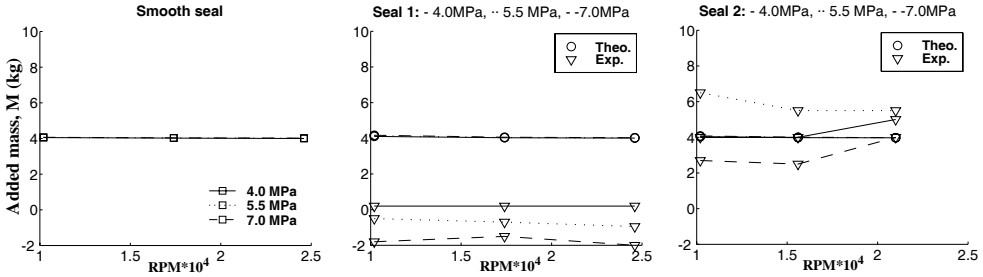

Figure 4.31: Direct added mass for round hole pattern seals. Comparison between experimental, theoretical, and theoretical smooth seal results.

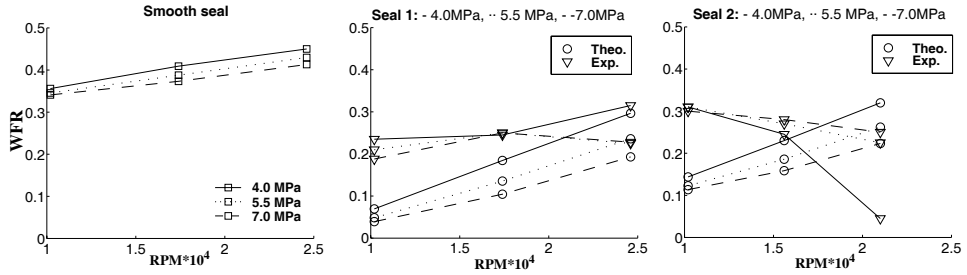

Figure 4.32: Whirl frequency ratio for round hole pattern seals. Comparison between experimental, theoretical, and theoretical smooth seal results.

Discussion of comparison to Childs' results

The theoretical prediction of cross-coupled stiffness (Fig. 4.28), direct damping (Fig. 4.29), and corresponding whirl frequency ratio (Fig. 4.32) is of a similar agreement to experimental results as the theoretical solution documented in (Childs & Fayolle, 1998). The theoretical method used by (Childs & Fayolle, 1998) is based on the Hirs friction factor which was calibrated and modified to fit experimental data. Their theoretical results shows comparable accuracy in the direct damping term and slightly poorer accuracy for cross-coupled stiffness. However, the Hirs based method over-predicts direct stiffness and cross-coupled damping to a great extent.

For Seal 2 in Figures 4.27 and 4.30 the current program predicts direct stiffness and cross-coupled damping with reasonable agreement to experiment at the lowest speed, but over-predicts stiffness as the speed is increased. This is consistent with the findings in the comparison to the results of (Childs *et al.*, 1990), where M_{ef} was under-predicted at high speeds.

For Seal 1 the experimental results are surprising in that direct stiffness and added mass drop to near zero which neither the current method nor the method of (Childs & Fayolle, 1998) are able to predict. As discussed in (Childs & Fayolle, 1998) there will be a loss in direct stiffness as the term $\frac{\partial f}{\partial h}$ becomes positive.

$$\frac{\partial f}{\partial h} = \frac{\partial f}{\partial \epsilon}\frac{\partial \epsilon}{\partial h} = -\frac{\epsilon}{h}\frac{\partial f}{\partial \epsilon} \tag{4.66}$$

f is the friction factor ϵ relative surface roughness and h the film thickness. The current friction factor has these properties as can be seen from Fig. 4.26 but in order to achieve a more accurate prediction of the direct stiffness the slope at the point for Seal 1 would have to be steeper. It might be that experiments on hole patterns may reveal such a behaviour, but it may also be due to other phenomena like recirculation in the seal tangential direction which is not accounted for in the current model.

4.7 Parameter study

Based on the results from the previous sections the friction factor developed in Chapter 3 has shown to be useful in predicting dynamic coefficients in grooved and hole-patterned annular liquid seals. Since the method does not require calibration to experiment it can be used to study the effect of changing various parameters.

To the designer the question will typically be: How can a seal design be improved? Can cross-coupled stiffness be eliminated? How much can leakage be reduced? How can direct stiffness be increased? How can maximum damping be achieved? The importance of the different questions will be vary between different pumps so no general optimal solution can be expected.

4.7.1 Grooved seal

In this section a liquid seal with operation conditions and geometry similar to seals used in an industrial application is studied. The focus for the parameter study is to see how different groove depths and widths will change the dynamic characteristics of the seal. Hence, the minimum clearance of the seal, pressure difference, and fluid properties are kept constant throughout. The ratio between the groove width, L_{gs}, and average land width, $\bar{L}_{ls}$, is equal to 2.0 for all stators. The rotor is kept smooth for all analyses. Seal parameters are given in Table 4.24.

Table 4.24: Common values for parameter study.

ρ	$= 1000$ kg/m^3	C_{in}	$=$	$C_{ex} = 0.15$ mm
μ	$= 10^{-3} Pa \cdot s$	e_s	$=$	$e_r = 0.0$
$u(0)$	$= 0.5$	R	$=$	72 mm
ξ	$= 0.25$	L	$=$	56 mm
ξ_e	$= 1.0$	ω	$=$	15000 rpm
ΔP	$= 10$ MPa	h^+	$=$	1

The leakage and exit swirl, rotordynamic coefficients, and whirl frequency ratios are shown in Figures 4.33 to 4.45.

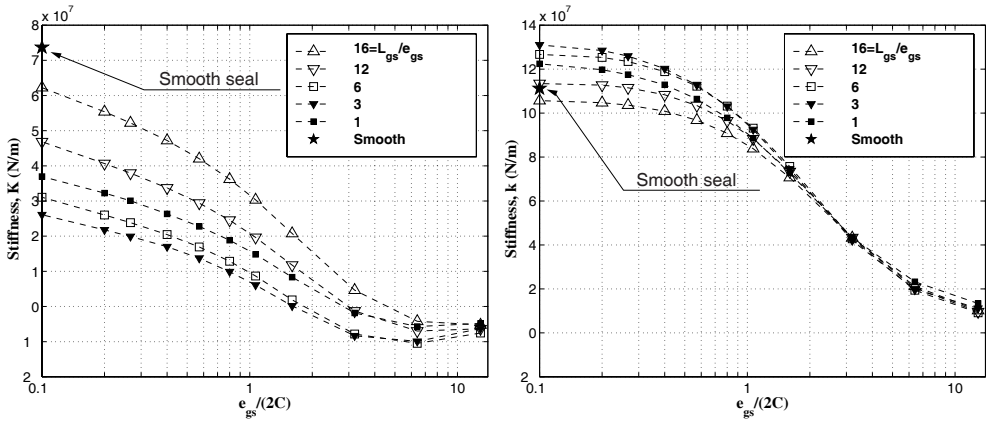

Figure 4.33: Grooved seal parameter study. Left figure: Direct stiffness. Right figure: Cross-coupled stiffness.

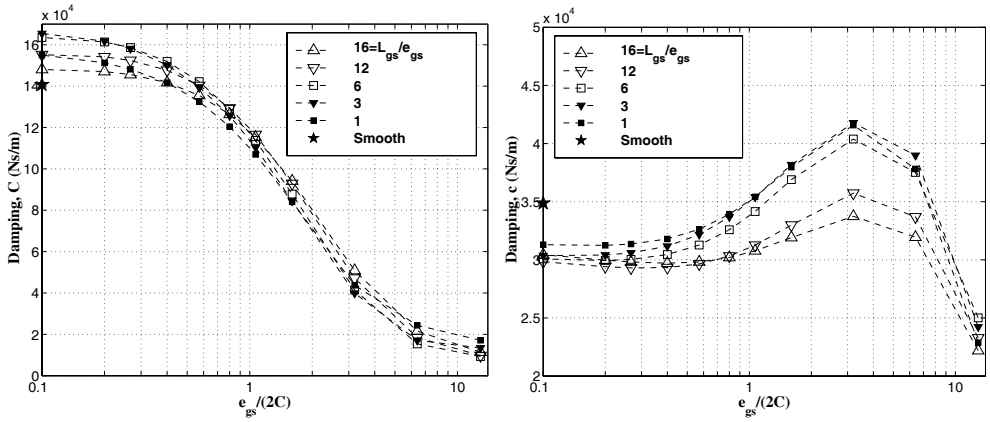

Figure 4.34: Grooved seal parameter study. Left figure: Direct damping. Right figure: Cross-coupled damping.

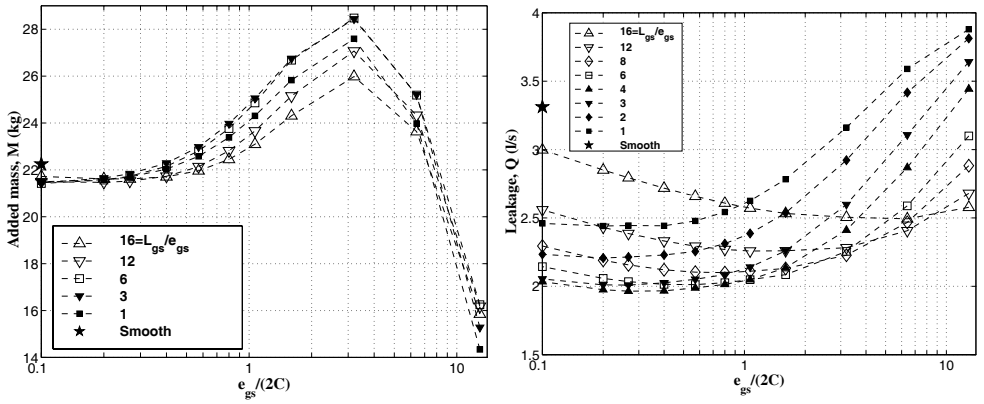

Figure 4.35: Grooved seal parameter study. Left figure: Added mass. Right figure: Leakage.

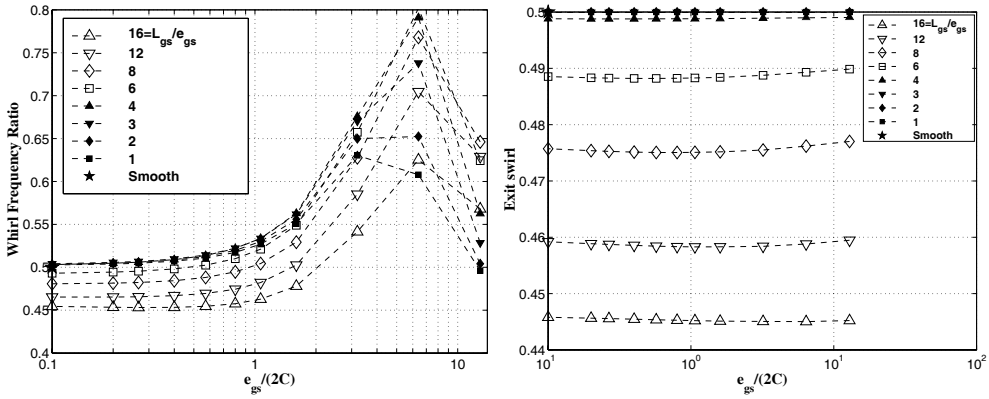

Figure 4.36: Grooved seal parameter study. Left figure: Whirl frequency ratio. Right figure: Non-dimensional exit swirl.

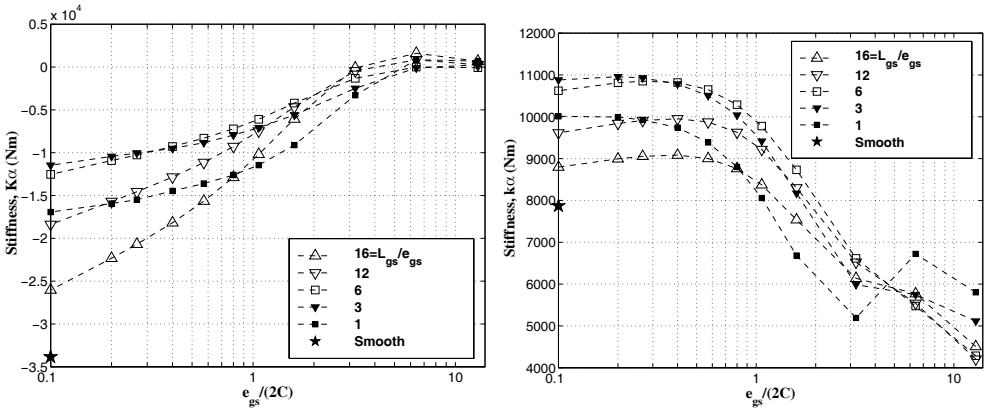

Figure 4.37: Grooved seal parameter study. Left figure: Direct angular stiffness. Right figure: Cross-coupled angular stiffness.

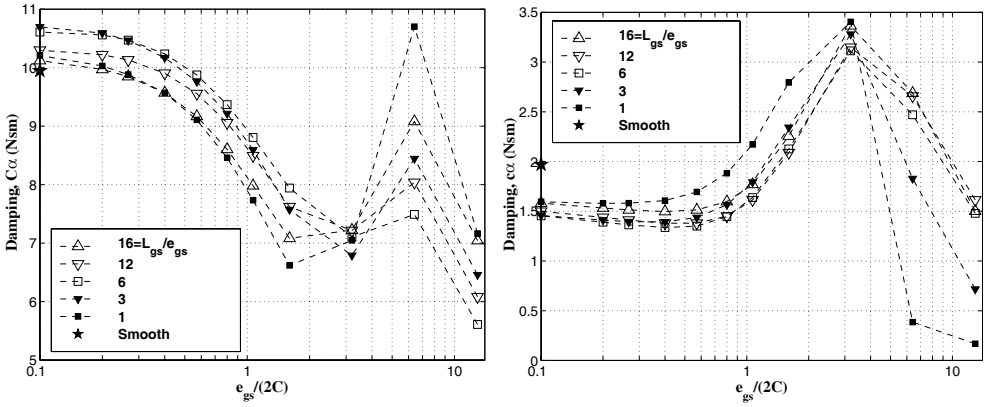

Figure 4.38: Grooved seal parameter study. Left figure: Direct angular damping. Right figure: Cross-coupled angular damping.

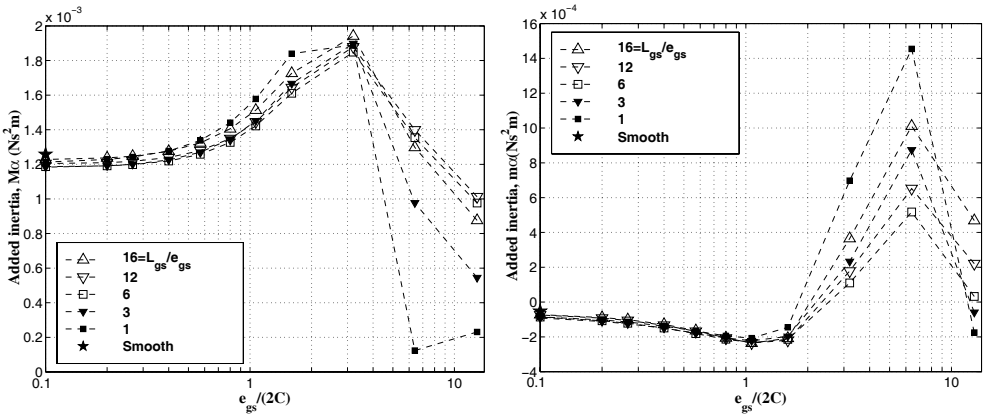

Figure 4.39: Grooved seal parameter study. Left figure: Direct angular mass moment of inertia. Right figure: Cross-coupled angular added mass moment of inertia.

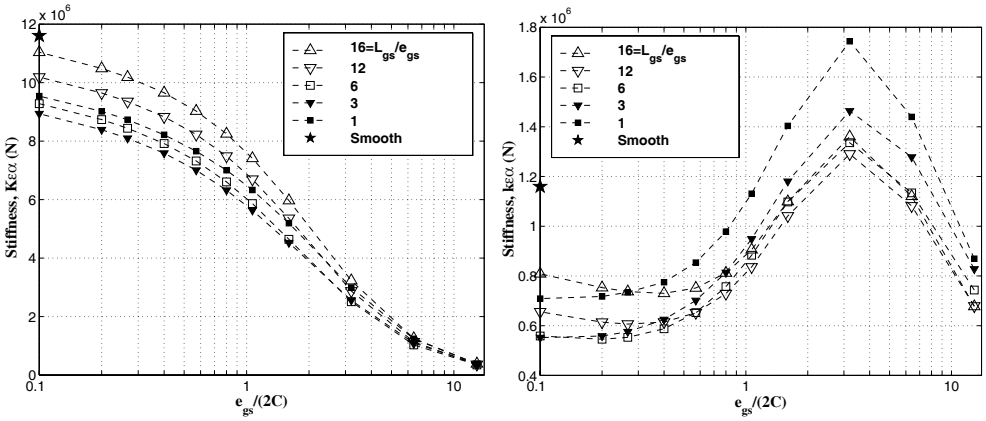

Figure 4.40: Grooved seal parameter study. Cross-coupled angular to translational stiffness.

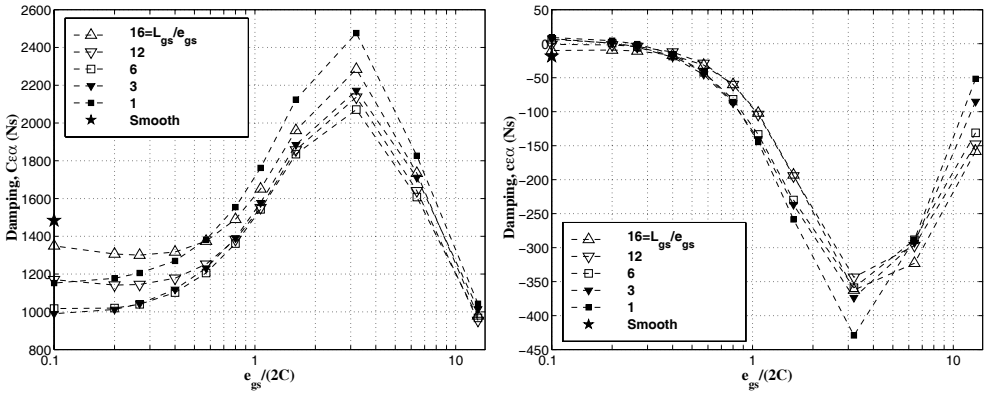

Figure 4.41: Grooved seal parameter study. Cross-coupled angular to translational damping.

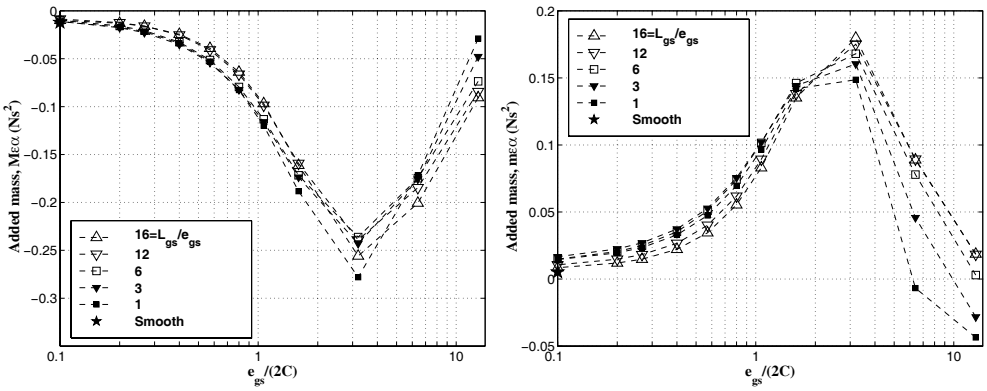

Figure 4.42: Grooved seal parameter study. Cross-coupled angular to translational added mass.

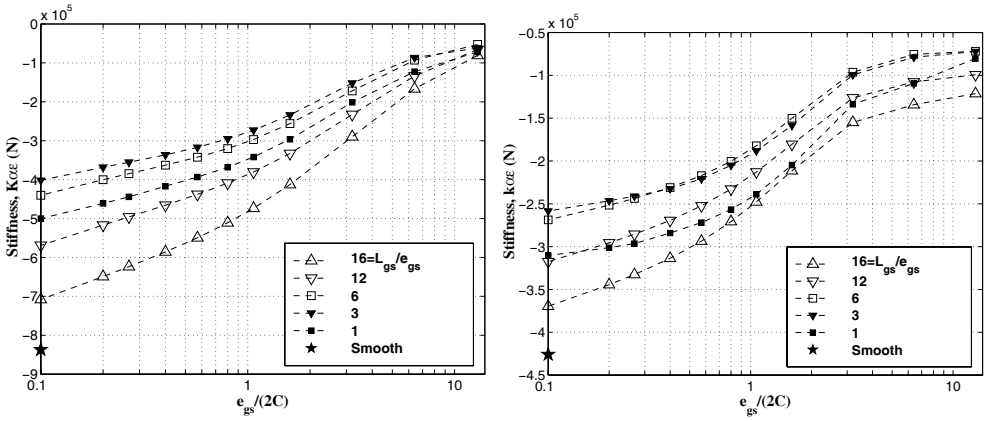

Figure 4.43: Grooved seal parameter study. Cross-coupled translational to angular stiffness.

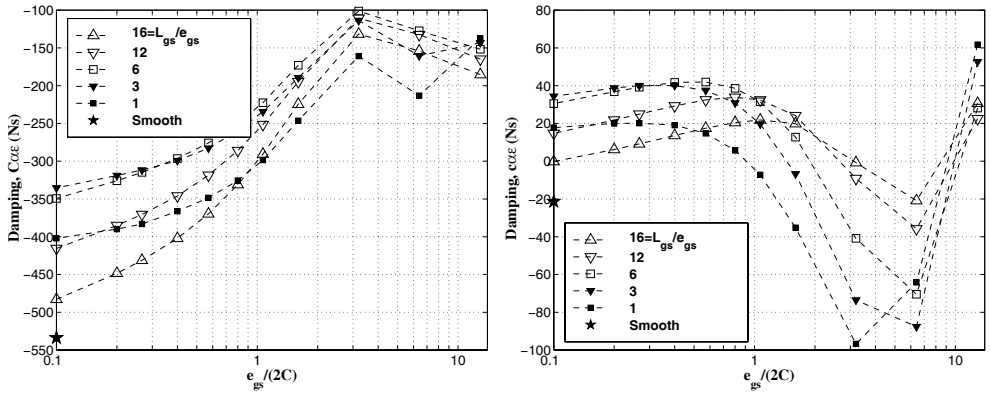

Figure 4.44: Grooved seal parameter study. Cross-coupled translational to angular damping.

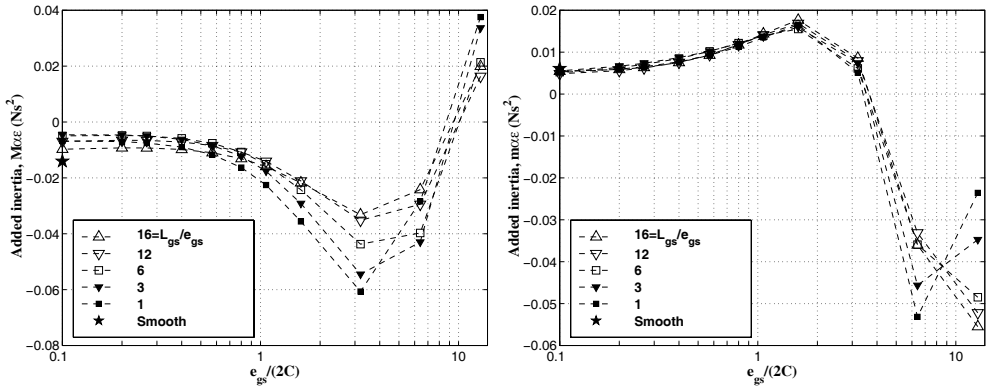

Figure 4.45: Grooved seal parameter study. Cross-coupled translational to angular added mass moment of inertia.

Discussion of parameter study for grooved seal

Figures 4.33 to 4.45 show a significant influence from the groove pattern on leakage, rotordynamic coefficients, and whirl frequency ratio.

Figure 4.35 shows that leakage can be reduced to about 0.6 times the corresponding smooth seal value. By using a shorter land zone and grooves on the rotor as well the leakage may be reduced further. Almost the whole test range shows leakage less than the smooth seal. Hence dynamic characteristics can be changed by introducing grooves in the whole range without introducing great leakage losses compared to a smooth seal.

For deep grooves there are substantial changes for several dynamic coefficients. The great reduction in direct stiffness K and direct damping C with increasing groove depth is supported by the experiment of (Marquette *et al.*, 1997). The main reason for this reduction is the circumferential flow in the grooves ($h^+ = 1$), but the loss in leakage and the friction factor also contribute to this effect. The reduction in stiffness may significantly reduce the first natural frequency of the system and the loss in direct damping may increase vibration levels. For groove depths in the same order of magnitude as the clearance or significantly smaller than the clearance, the loss in stiffness and damping are less dramatic, and it is more likely to find a solution with a compromise between leakage and dynamic characteristics.

At an inlet swirl of 0.5 the cross-coupled stiffness is reduced at a slightly slower rate than direct damping as the groove depth to clearance ratio is increased. This means that the whirl frequency increases. One would have to introduce swirl brakes at the inlet to reduce the WFR significantly as shown in the comparison to the result of (Marquette *et al.*, 1997).

Moment coefficients they have not been compared qualitatively to experimental values, so there is greater uncertainty about their accuracy. However, based on the great reduction in K, k, and C with the groove to clearance ratio it is not surprising that there will be a reduction in the magnitude in some of the coefficients like K_α, C_α, $K_{\epsilon\alpha}$ while others, such as c and M, change less.

4.7.2 Hole pattern seal

A seal of a similar geometry and operating conditions to the one studied for grooved seals was studied here. The only difference being that the grooves are replaced by hole patterns where the hole diameter, d_{hs}, is two times the equivalent land length, $\bar{L}_{ls}$. The reason for introducing hole pattern seals is that they can be used to reduce the cross-coupled stiffness, increase damping, and reduce the whirl frequency ratio. The non-dimensional added film thickness, $h^+ = 0$, is the only seal parameter which is different in this test compared to those for the grooved seal parameter study given in Table 4.24.

Cross-coupled stiffness influenced both by the swirl velocity and the friction factor and its derivatives. The zeroth order solution in Figures 4.48 and 4.49 show leakage and whirl frequency ratio and exit swirl from the seal, while the remaining figures in

this section show rotordynamic coefficients.

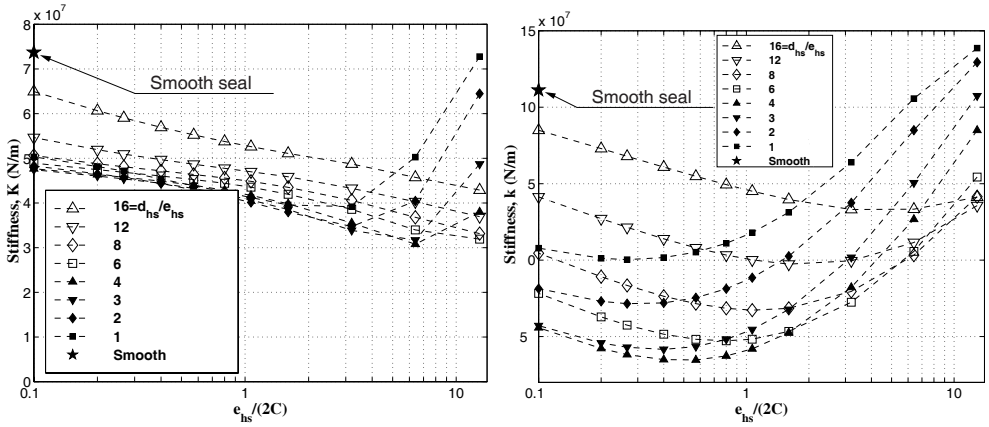

Figure 4.46: Parameter study of hole pattern seal. Left figure: Direct stiffness. Right figure: cross-coupled stiffness.

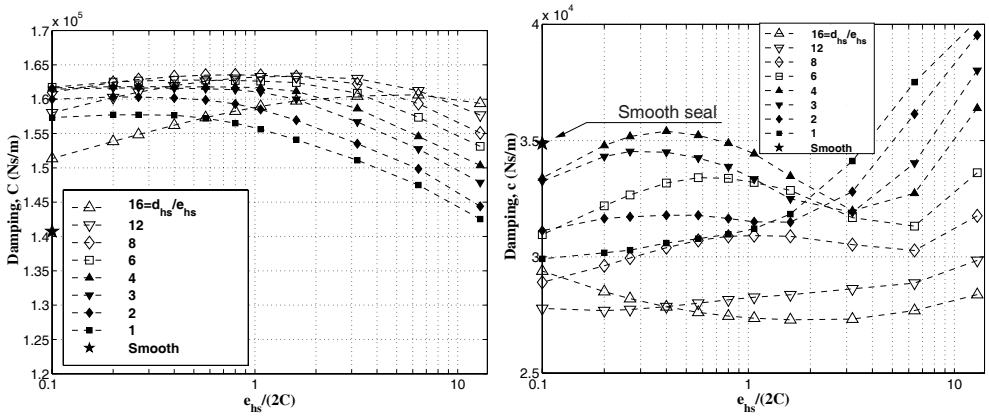

Figure 4.47: Parameter study of hole pattern seal. Left figure: Direct damping. Right figure: cross-coupled damping.

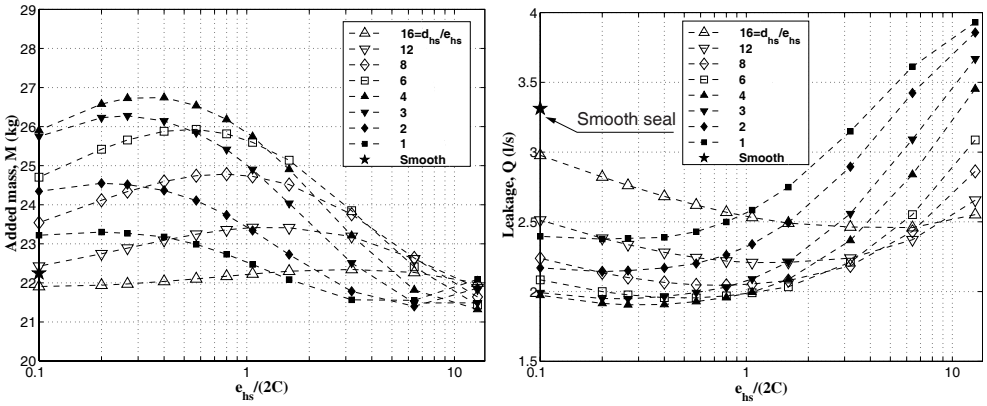

Figure 4.48: Parameter study of hole pattern seal. Left figure: Direct added mass. Right figure: leakage.

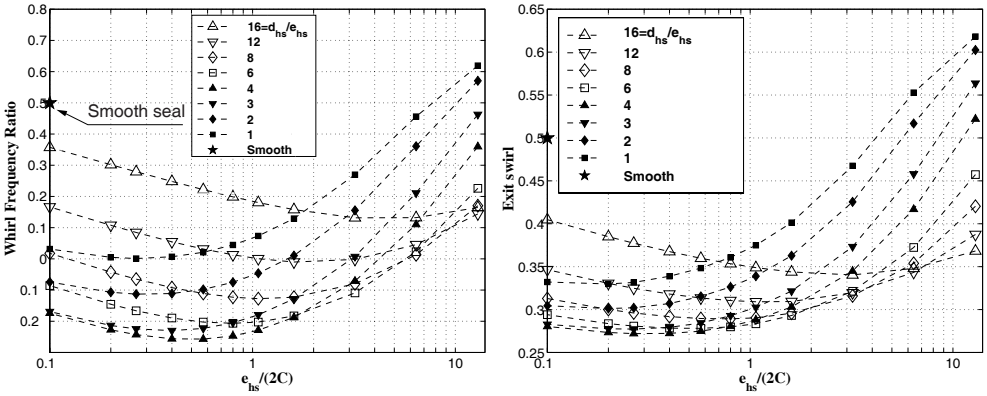

Figure 4.49: Parameter study of hole pattern seal. Left figure: Direct whirl frequency ratio. Right figure: Non-dimensional swirl at seal exit.

Discussion of parameter study for hole pattern seals

The most important trend in the above results is the large reduction in cross-coupled stiffness compared to that of a smooth seal. Fig. 4.46 actually indicates that the cross-coupled stiffness can be changed from a significant value of about 11 MN/m for a smooth seal to zero or negative values for a range of hole-patterns. Whether negative values can be obtained in practice will require more experimental results, but the trend in results is expected to hold. Direct damping values are relatively constant and a few percent greater than the corresponding smooth seal damping. Based on the comparison between the results from the theory in this chapter and the experimental results by (Childs & Fayolle, 1998) it may be expected that this value is slightly over-predicted.

Direct stiffness K, it is shown to decay for all choices of hole-patterns compared with a smooth seal. Based on the experimental results it is also likely that the decay in practice may be greater than predicted. Added mass and cross-coupled damping do not change significantly for the whole range of hole patterns. Compared to experimental values it may be expected that cross-coupled damping is somewhat over-predicted.

Fig. 4.48 indicate that good leakage performance can be obtained.

4.7.3 Seal design guidelines

Based on the parameter studies of groove and hole pattern seals and the friction factor study in Chapter 3 some guidelines for seal design with groove and hole patterns can be suggested.

For leakage reduction:

- For both groove and hole pattern seals a groove or hole depth to clearance ratio of 0.53 and a groove or hole width to depth ratio equal to six gives the best reduction in leakage.
- The land portion should be made as small as possible. Since an infinitesimal land portion probably would wear off too quickly one will have to consider wear aspects for the choice of land zone width.
- If possible one should apply the groove patterns to both rotor and stator for maximum leakage reduction. One could also apply the optimal hole pattern for leakage reduction to the rotor, but this may reduce dynamic stability and increase mechanical losses due to tangential friction.

For increased stability:

- Hole patterns should be placed on the stator only.
- For grooved seals one can use additional swirl breaking devices upstream of the seal since the circumferential grooves offer little reduction in swirl within the seal.

- For hole pattern seals one will have to analyse each particular seal and operating conditions. However, it is likely that the optimal pattern for reduction in cross-coupled stiffness can be found within the range of hole patterns studied in this thesis.

For combined leakage reduction and dynamic stability:

- Hole patterns should be placed on the stator combined with a near optimal groove pattern for leakage reduction on the rotor. What hole pattern and land zones one should use would require a study of rotordynamic coefficients and leakage for each particular seal.

Chapter 5

Experimental studies of viscous losses

5.1 Introduction

The seal inlet-, exit-, and friction losses have an influence both on leakage and dynamic characteristics.

The focus of this experimental study is on:

- The friction factor for turbulent and transition turbulent flow for plain and shallow groove rotor surfaces. The results of this study would help verify the theory presented in Chapter 3.
- The exit loss coefficient as a function of rotational speed, seal outlet, and exit chamber geometry. Results will be compared to numerical predictions in Appendix E.
- The inlet loss coefficient as a function of rotational speed, seal inlet, and inlet chamber geometry. Results will be compared to a formula by (Kündig, 1993) and numerical results from Appendix E.

A schematic overview of the seals studied is shown in Fig. 5.1.

It was discovered when comparing the typical industrial design for annular seals of a high speed water injection pump that both the inlet and exit seal edge were chamfered for handling purposes. For pipes, experiments have shown that an inlet edge of this type would reduce the inlet loss coefficient from 0.5 to approximately 0.2 compared to a 90 degree sharp inlet, while exit loss coefficients would remain approximately equal to 1.0, (White, 1994). Whether this would apply to seals with tangential flow was an open question so a preliminary numerical study using CFD was carried out. This study, which is included in Appendix E, indicated that the exit loss for a 45

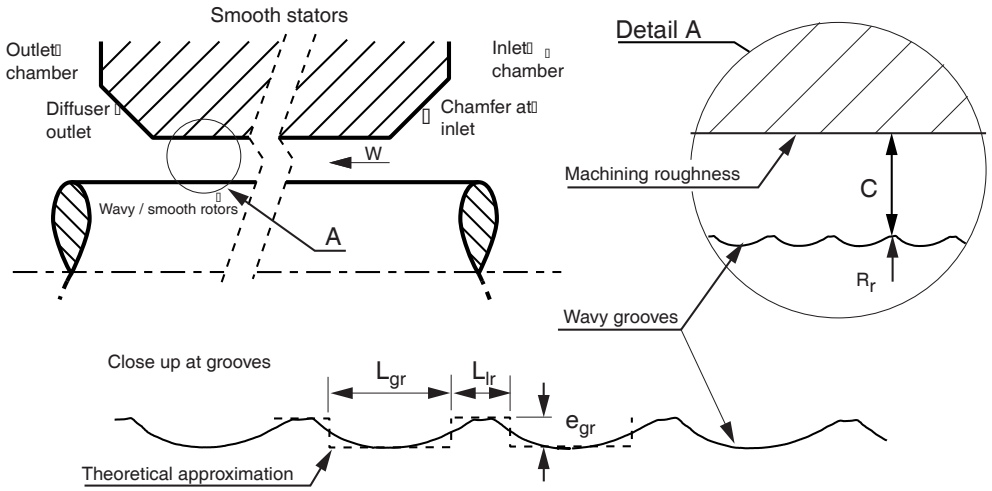

Figure 5.1: Schematic overview of test seals. Grooves were spiraled at such a small angle that the rotational direction was irrelevant to the results.

degree chamfer outlet would be reduced from 1.0 to approximately 0.6, which if correct would have a significant influence on the prediction of direct stiffness. To the author's knowledge studies of the exit coefficient as a function of seal exit geometry have not been carried out in the past. Thanks to the industrial partners in this project, a test rig was built, and the facility was made available for a limited period of time.

Operational conditions for a typical industrial seal were of main interest in this study. However, the pressures differences of $90 - 300$ bar across the liquid annular seals used by the industrial partners were not achievable in the test rig, so the radial seal clearance had to be increased from a typical range of $0.1 - 0.3$ mm for a 70 mm rotor to $0.5 - 1$ mm in order to have Reynolds numbers in the appropriate range for the seal. If and how the results in this chapter can be scaled to the typical industrial seals will be discussed.

Regarding the inlet loss coefficient (Kündig, 1993) studied how this varied with different inlet geometries and he also suggested a formula for how the inlet loss depends on the swirl velocity:

$$\xi = \xi_O 10^{\frac{U}{12W}} \tag{5.1}$$

where, ξ_O is the entrance loss at zero swirl and U, W are the tangential and axial bulk velocities. The formula indicates that if the swirl velocity is 4 and 12 times the axial, the inlet loss coefficient increases by a factor 2.15 and 10 respectively. One might then expect that seals with deep grooves which may be treated as a succession of inlet and exit losses for each groove would yield a similar increase in friction loss as the swirl velocity increases. However, both (Kilgore & Childs, 1990) and (Florancic, 1990) have found a decrease in the friction loss as the swirl velocity was increased. Therefore it was decided to investigate the inlet loss dependency on swirl.

For pipe entrance flow into an infinite reservoir (White, 1994) documents inlet loss factors of 0.2, 0.5, and 1.0 for a 45 degree chamfer, sharp corner, and a protruding edge (reentrant) inlet respectively. The author does not know any previous attempts to study the effect of reentrant inlets for seals. The three stator geometries proposed for experimental studies were a sharp inlet, a 45° chamfered entrance, and a protruding edge (see Fig. 5.6). Two clearances were studied for each stator.

Regarding transition to turbulence (Zirkelback & San Andres, 1996) used a friction factor based on experiments with transition to turbulence in pipe flow to predict dynamic characteristics theoretically. Although theoretical predictions of dynamic characteristics in this thesis were very close to those by (Zirkelback & San Andres, 1996), the comparison to experimental and theoretical results by (Iwatsubo & Sheng, 1990) were somewhat discouraging. In the experiment documented here comparisons between the transition to turbulence friction factor and experimental results will be made.

In order to study in detail the apparent discrepancies and unknowns in the literature mentioned above one would need a great number of experiments. The objective of this chapter was not to answer all questions in detail, but to find out which of the factors would have the greatest influence on seal design, so that suggestions for further studies and improvements could be made.

5.2 Description of experiment

5.2.1 Test loop

The test loop is shown in Fig. 5.2. Cold water is supplied into a 500 liter reservoir at a steady rate to keep the water temperature near constant throughout the experiment. Filtered fresh water is fed to the test unit by a constant speed boiler feed water pump of maximum capacity 90 m^3/h. The valve located upstream of the filter was used to control the flow rate, and the valve located downstream of the test unit was used to keep the test unit pressure well above atmospheric. The maximum pressure used in the test loop was approximately 10 bar.

By means of the gear system in Fig. 5.3 and an electric the rotor speed may be varied between 0 and 2250 rpm. Water enters the test unit inlet in Fig. 5.3 through a flexible hose and it is given a swirl velocity into the seal inlet chamber by a radial impeller. The swirl velocity in the chamber was measured by a pitot-tube connected to three water columns. Since the absolute pressure in the inlet chamber could get as high as 10 bar, the air pressure above the pitot water columns had to be adjusted for each leakage measurement. Since no rapidly fluctuating pressure measurements were to be made all pressure measurements were made by guiding water from the pressure tap through 6 mm flexible hoses either to a water column or pressure transducer located outside the test unit. The water columns were used simultaneously with the transducers which allowed for low pressure measurements and for calibration of the transducers. The water columns were connected by a manifold at the top which allowed a reference air pressure well above atmospheric. Two pressure taps were

located in the upstream chamber, three in the seal clearance, and two in the exit chamber (see Fig. 5.3). For each pressure tap in the seal clearance 4 holes of 0.3 mm diameter located with a 90° spacing around the circumference were drilled so that an average pressure could be measured for each axial location. Two differential and one absolute pressure transducers, were used for measurements in the seal, while absolute pressure transducers were used for the inlet and exit chambers. In the inlet and exit chamber the pressure tap holes had a diameter of 1.5 mm. The cannula located at the seal exit chamber allowed pressure to be measured at any radius along the exit chamber wall. In order to study different inlet and exit geometries three cylindrical stator inserts (see Fig. C.1) were made. Other dimensions of the test unit are given in Appendix C. Different rotor surface treatments were achieved by cylindrical rotor inserts (see Fig. C.2).

The water temperature was measured upstream and downstream of the test unit, and the average value was used to calculate fluid properties.

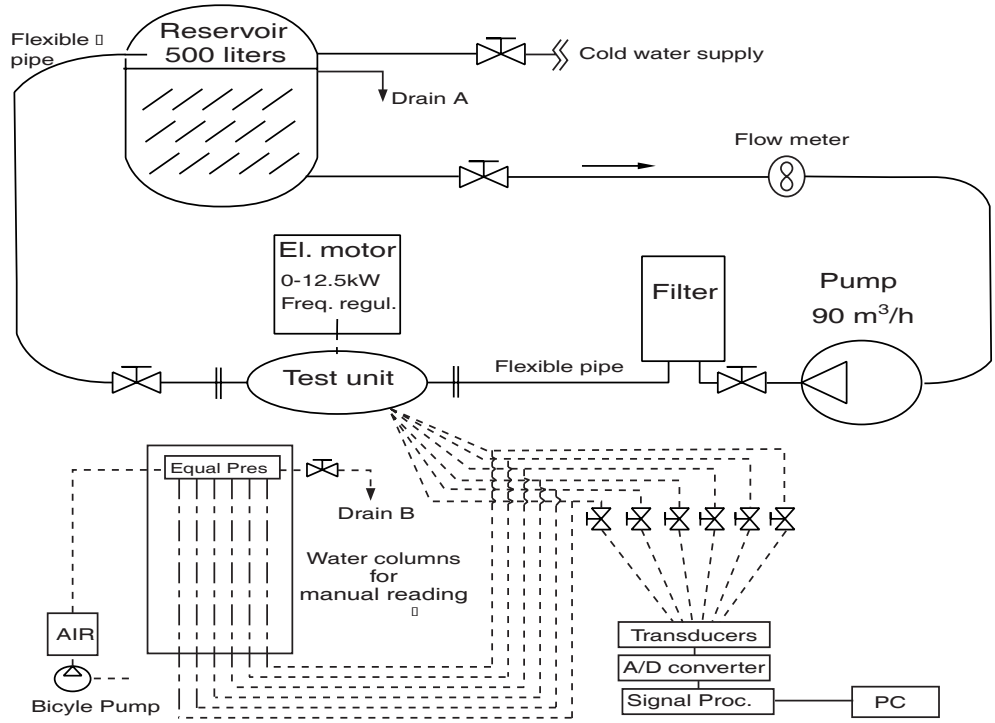

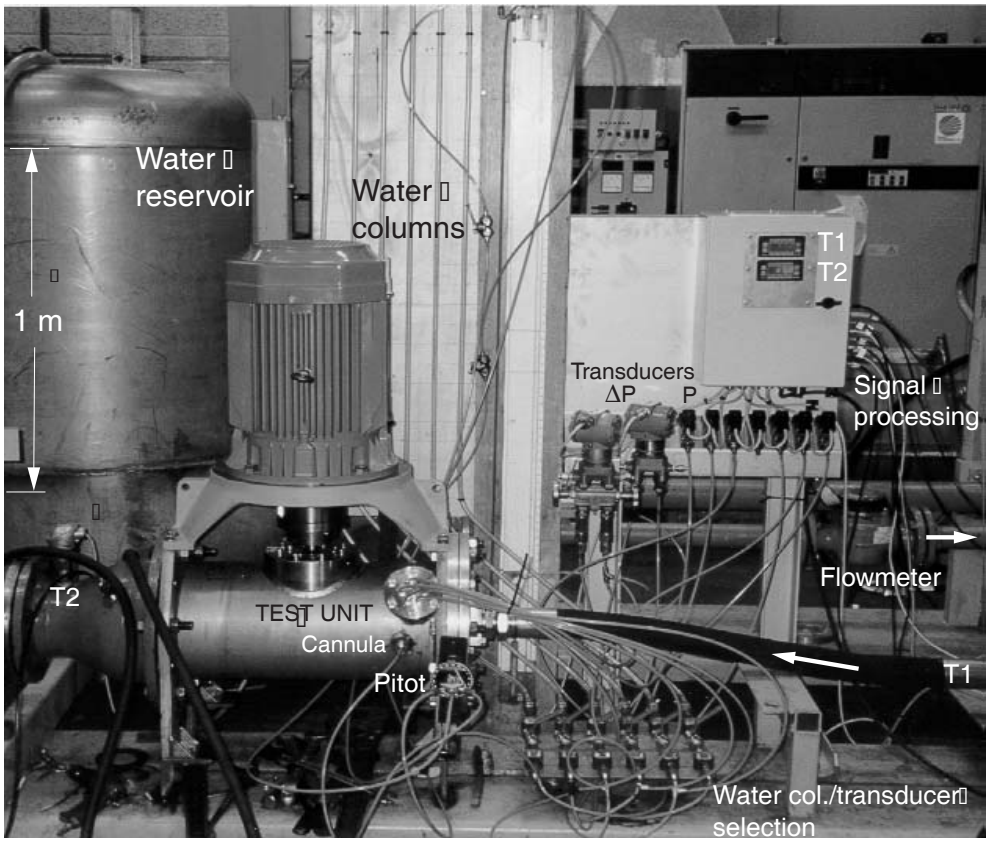

Figure 5.2: Test loop and test-rig photo.

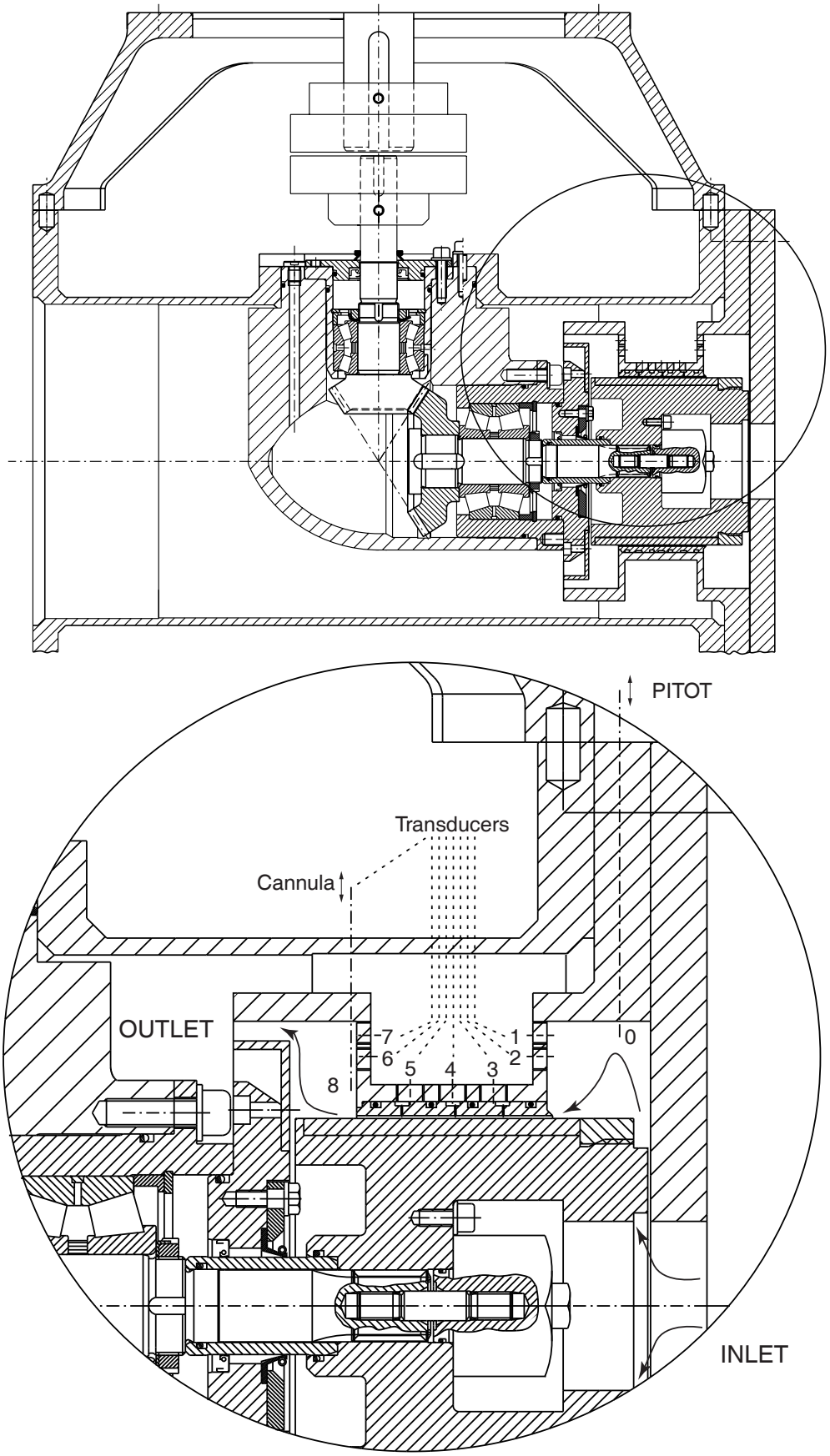

Figure 5.3: Assembly bucket.

5.2.2 Measurement details

In Table 5.1 the various sensor types used for measurements are listed together with the achievable accuracy.

Table 5.1: Instrumentation.

Quantity	Sensor type	Range	Uncertainty Manufacturer	Uncertainty Measured
Pressure	Abs. pressure	$10^4 - 10^6$	10^4	10^3
(Pa)	Rel. pressure	$10^3 - 2 \cdot 10^5$	$2 \cdot 10^3$	200
	Water column	$100 - 2.5 \cdot 10^4$	N/A	$10 - 100$
	Swirl stag.pres.	$100 - 2.5 \cdot 10^4$	N/A	$10 - 100$
Leakage	Flow meter	$25 - 500$	N/A	$0.5 - 10$
(l/min.)	In bucket/time	$10 - 100$	N/A	$0.2 - 2$
Temp.($^\circ C$)	El.thermometer	$0 - 100$	0.1	N/A
Dimensions	Micrometer	$125 - 135$	0.005	0.005
(mm)	Profilometer	$1 \cdot 10^{-4} - 0.2$	$1 \cdot 10^{-5} - 0.01$	N/A
Rot. speed (rpm)	Rpm-meter	0-10000	2.5%	N/A

Pressures measured by transducers and temperature were measured over a 30 second period. The time average value was used throughout. For low leakage pressure measurements by vertical water columns were used, and the column height was measured manually. Although the pressure could be measured to an accuracy of 1 mm water column, this was achievable only when the total pressure drop across the test unit was in the order of 30 cm. As the pressure difference becomes equivalent to 2.5 m water column the inlet pressure fluctuated so that the accuracy in measurements were in the order of ± 2.5 cm. For each series of results measured by the pressure transducers water column measurements were also made at low leakage so that calibration of transducers could be made for all test series. By using this procedure some of the inaccuracy of the transducers caused by changes in day to day temperature and atmospheric pressure was eliminated.

5.2.3 Rotor and stator surface treatment

An illustration of the shallow grooves on the rotors is shown to scale in Detail A in Fig. 5.1 for Rotor number 6, which had the deepest grooves. The grooves were machined in a spiral pattern with a pitch equal to the distance between the grooves. The pitch was so small that the rotor turning direction did not influence results. Two of the rotors, Rotor 1 and 4 and all the stators did not have grooves. They were polished to an average surface roughness shown in Table 5.2.

A profilometer was used to measure the surface roughness profiles on the rotor and stator. In Figures 5.4 and 5.5 the greatly magnified rotor surface profiles are shown

for an axial section. $y = 0$ corresponds to the rotor radius R_r. The tangential profiles for rotors and stators and the axial stator profiles do not show a repeated pattern. For theses surfaces the average roughness Ra_θ and Rt_θ values in Table 5.2 describe the roughness.

The grooved surfaces have a surface profile that may resemble worn seals of rectangular grooves. To compare friction factors for these seals to theoretical predictions by Eq. 3.46 the groove and land widths were calculated so that the rectangular profile area matched the wavy profile area (see Fig. 5.1). The depth of the rectangular profiles were set equal to the maximum groove depth. The calculated values for equivalent groove and land widths are shown in Table 5.3.

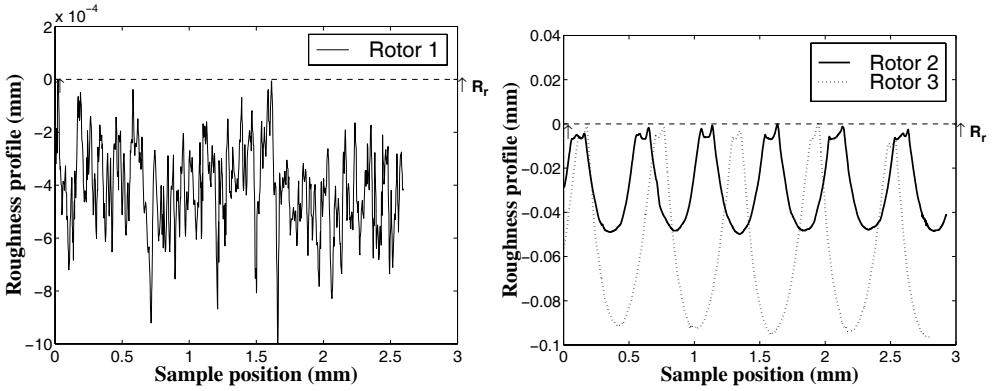

Figure 5.4: Measured rotor surface profiles for rotor R1, R2, and R3.

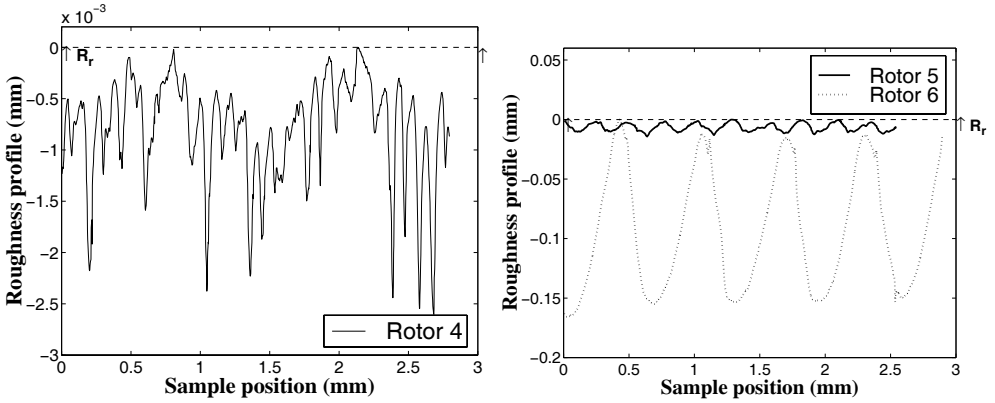

Figure 5.5: Measured rotor surface profiles for rotor R4, R5, and R6.

The radii in Table 5.2 are based on the average values of eight diameters measured at 22.5° intervals at both ends of the rotor and stator cylinders. There are two groups of radii, the first (R1, R2, and R3) have a specified radius of 66.5 mm which would yield an average clearance of 1.0 mm and the second (R4, R5, and R6) had a radius of 67 mm which would yield a 0.5 mm average clearance. It was important to measure

Table 5.2: Rotor and stator radii and roughness.

Rotor	R_r (mm)	ΔR_{rmax} (mm)	ΔR_{rmin} (mm)	Ra_z μm	Rt_z μm	Ra_θ μm	Rt_θ μm
R1	66.507	0.013	-0.012	0.13	1.00	0.16	1.27
R2	66.523	0.002	-0.003	15.56	49.79	0.39	2.56
R3	66.514	0.026	-0.024	28.07	96.49	1.30	12.00
R4	66.996	0.034	-0.026	0.38	2.61	0.49	4.14
R5	66.980	0.035	-0.030	2.90	14.27	0.77	6.92
R6	67.036	0.034	-0.031	44.86	165.69	1.58	14.16
Stator	R_s (mm)	ΔR_{smax} (mm)	ΔR_{smin} (mm)	Ra_x μm	Rt_z μm	Ra_θ μm	Rt_θ μm
S1	67.549	0.014	-0.014	0.62	4.36	0.18	2.52
S2	67.516	0.025	-0.037	0.62	3.82	0.15	1.76
S3	67.585	0.037	-0.061	0.67	4.59	0.51	2.95

the average radius since the profilometer showed that rotor and stator cylinders were deformed slightly during clamping for the machining process. A single measurement could yield significant deviations from the average as indicated in the table. The measured average dimensions are shown in Table 5.3. For an industrial pump the out of roundness achieved would most likely be less than what was achieved in this case since one normally would be machining a solid rotor and stator component.

One way to describe the roughness is to use the mean roughness, Ra which is:

$$Ra = \frac{1}{L_s} \int_0^{L_s} |y| dz \tag{5.2}$$

where L_s is the sampling length and y is the roughness height measured from the mean surface position. Another measure is the R_t value which is the maximum difference in y-values for the sampling length. Table 5.2 describes the mean and maximum roughness for the axial and circumferential directions z and θ, mean radii, and deviations from the mean radius for each rotor and stator.

The combinations of rotors and stators studied are shown in Table 5.3. In order to do comparisons to theoretical friction factor calculations an equivalent roughness of 8 μm was used in the Moody friction factor for surfaces without grooves. This value was found by graphically fitting the experimental and theoretical curves for the seals without grooves.

Three stators (S1, S2, and S3) are studied. S1 has a sharp 90° inlet and outlet, while the inlet and outlet geometries for S2 (45° chamfer) and S3 (45° protruding edge) are shown in Fig. 5.6. At the protruding edge of S3 there was a nose radius of approximately 0.15 mm which could be similar to a slightly worn inlet. Other details of the geometry are given in Appendix C.

Table 5.3: Rotor and stator combinations studied, groove dimensions and roughnesses used for theoretical calculations of the friction factor.

Rotor	C (mm)	e_s, e_r (μm)	L_{lr} (mm)	L_{gr} (mm)	e_{gr} (μm)	$\frac{e_{gr}}{2C}$	$\frac{L_{gr}}{e_{gr}}$
S2/R1	1.009	8	N/A	N/A	N/A	N/A	N/A
S1/R2	1.026	8	0.218	0.276	49.79	0.0243	5.54
S3/R3	1.071	8	0.236	0.353	96.49	0.0450	3.66
S1/R4	0.553	8	N/A	N/A	N/A	N/A	N/A
S2/R4	0.520	8	N/A	N/A	N/A	N/A	N/A
S3/R5	0.605	8	0.111	0.126	14.27	0.0118	8.79
S2/R5	0.536	8	0.111	0.126	14.27	0.0133	8.79
S3/R6	0.549	8	0.220	0.435	165.69	0.1509	2.63

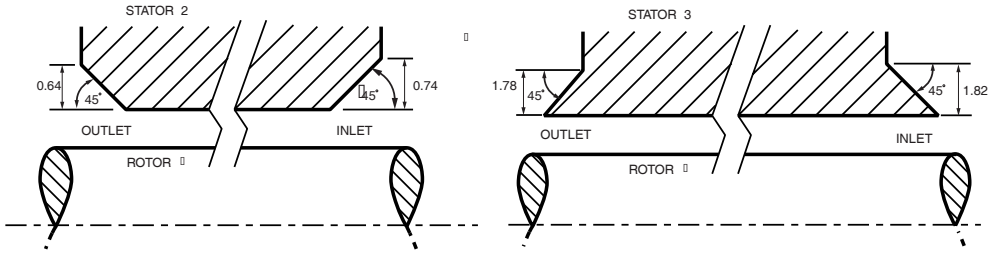

Figure 5.6: Seal inlet- and outlet-geometries.

5.3 Friction factor

5.3.1 Experimental and theoretical results

The friction factors f presented in Figures 5.7 to 5.10 are based on the equation

$$\Delta P = 4f\frac{L}{2C}\rho\frac{W^2}{2} \tag{5.3}$$

where $\Delta P = P_3 - P_5$ in Fig. 5.3, W is the axial velocity calculated from leakage measurements, L is the axial distance between pressure points 3 and 5 in Fig. 5.3, and C is the minimum clearance from Table 5.2. For the theoretical predictions the following fluid properties were used.

$$\rho \quad = 999.4\ kg/m^3 \qquad \mu \quad = \quad 1.37 \cdot 10^{-3}\ Pa \cdot s$$

The rotational speeds tested for each seal were ω= 0, 500, 1000, 1500, 2250 rpm. Figure 5.7 shows the experimental friction factor for two of the polished seals with

different clearances, and the Moody friction factor based on an 8 μm equivalent roughness. For comparison the Moody friction factor based on hydraulically smooth surfaces, and zero rotational speed is included in the graphs. The rotor stator combination S1/R1 gave essentially the same results as the combination S1/R4, and is hence not reported.

In Figure 5.8 a comparison is made between the experimental results which lie in the transition turbulence regime, and theoretical predictions both by the Moody friction factor and the combined Moody-laminar transition to turbulence friction factor, Eq. B.14, used by (Zirkelback & San Andres, 1996).

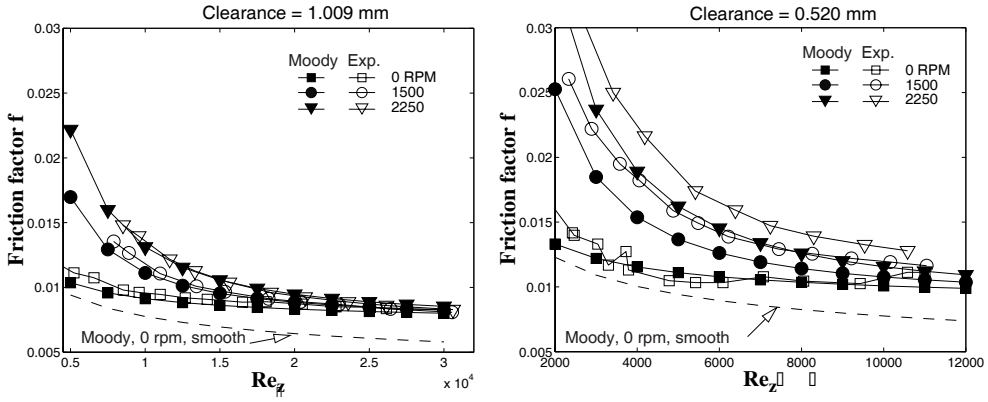

Figure 5.7: Left figure: Friction factor for stator rotor combination S2,R1. Right figure: Friction factor for S2/R4. All surfaces are polished.

In the Figures 5.9 and 5.9 comparison is made between the experimental results and the friction factor developed in Chapter 3, Eq. 3.46.

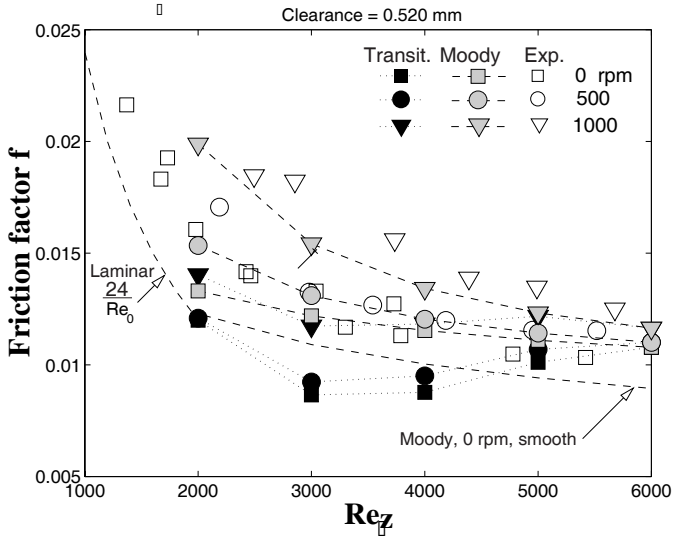

Figure 5.8: Transition turbulence: Friction factor for S2/R4 (polished surfaces).

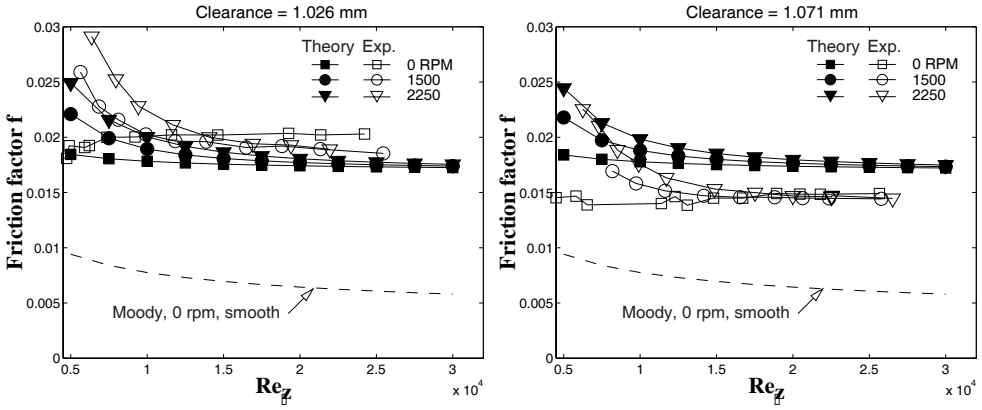

Figure 5.9: Left figure: Friction factor for S1/R2 Right figure: Friction factor for S3/R3: Both rotors have a wavy-surface profile.

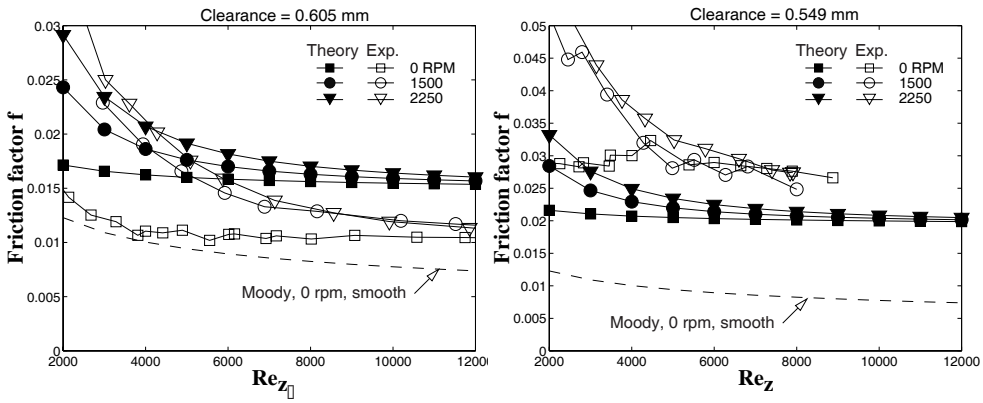

Figure 5.10: Left figure: Friction factor for S3/R5. Right figure: Friction factor for S3/R6. Both rotor surfaces have wavy profiles.

5.3.2 Discussion of friction factor results

For the polished surfaces the Moody friction factor shows a good correspondence to the experimental values for the surface roughness of $8\mu m$ chosen. One weakness of the Moody friction factor is that the measured mean surface roughness height does not alone provide a good estimate for the roughness that will give a best fit to experimental data. In this case the largest average roughness measured is $0.62\mu m$, which is less than one tenth of the roughness that gives best fit to the experiment. In comparison (Florancic, 1990) used an equivalent surface roughness of 2.5 times the specified mean surface roughness, which was a N8 surface finish with maximum $R_a = 3.2$.

The friction factor for the transition to turbulence regime did not provide a more accurate fit to the experimental results than the Moody friction factor. This is shown in Fig 5.10. The transition to turbulence friction factor predicts a dip in the Reynolds number range 2000-6000, and this dip is not found in the experiment. Similarly in Section 4.3 the same friction factor used for predicting dynamic coefficients produced qualitative trends in the coefficients that were not found in the experiment. In fact the Moody friction factor provides better qualitative and quantitative results in both cases. Possible reasons for the discrepancy between the pipe and seal flow transition friction factor may be the finite seal eccentricity and swirl flow.

The results on the eccentric seal friction factor from (Yamada *et al.*, 1969) show that eccentricity by itself has great influence on the friction factor near the laminar zone. At zero eccentricity and zero rotational speed some of the results of (Yamada *et al.*, 1969) indicate a significant dip in the friction factor near the laminar zone similar to the transition turbulence factor used by (Zirkelback & San Andres, 1996). However, at an eccentricity of 0.25 this dip disappears. At zero eccentricity and low rotational speed some results of (Yamada *et al.*, 1969) show a dip in the friction factor in the transition zone while others do not.

The shallow grooves applied to the rotor surface provide an increase in the overall friction coefficient of up to a factor three compared to that of a smooth seal (rotor stator combination S3/R6). By applying the roughness treatment of rotor R6 to the stator as well, one might expect an increase in this relative factor to 5 compared to a smooth seal, which would give a leakage less than half of that for the smooth seal. The theoretical friction factor is mostly within 25% of the experimental which means that leakage predictions would be within 12%. This is a slightly poorer match in results compared to results in Chapter 3 and 4. Still the results are surprisingly good because all the seals but one (S3,R6) have groove depth to clearance ratios less than the test-matrix used in Chapter 3. Also with reference to Fig. 3.13 the profiles have an $\frac{e_{gr}}{2C}$ ratio between 0.0118 and 0.15 which is in the region of the graph where small changes in the groove width to depth and groove depth to clearance have a large influence on the friction factor. Since there groove pattern is machined as a spiral, the rotor was run in both directions to check if this influenced the friction factor. However, no influence on rotational direction was observed. Looking at trends in the results, the theoretical predictions show less sensitivity to rotational speed than the experimental. This is a limitation of the current friction factor which was developed for tangential bulk velocities less than or equal to the axial bulk speed. To the author's knowledge there are no other procedures available for explicitly predicting friction losses of the wavy surfaces documented here, apart from numerical simulations using CFD.

5.4 Interpretation of exit and entrance loss results

Although the numerical study in Appendix E indicates that pressures measured at single points in the entrance and exit chambers makes the commonly used equations for entrance and exit loss invalid at large ratios of tangential to axial speed it was decided to use this formulation for the interpretation of experimental results. The reason being that for the current experiment for the results for elevated rotational speed Eq. 5.4 still gives an indication of trends in results. In order to evaluate the entrance and exit loss from experimental results the pressures a locations **b**, **c**, **d**, and **e** in Fig. 5.11 are needed.

The two equations used for evaluating inlet (ξ) and exit loss (ξ_e) coefficients for a concentric rotor and stator may then be given as follows:

$$P_b - P_c = \frac{\rho}{2}(1+\xi)\,W^2 \tag{5.4}$$

$$P_d + \frac{\rho}{2}(1+\xi_e)\,W^2 = P_e \tag{5.5}$$

where P_b, P_c, P_d, P_e are the pressures at the respective reference points in Fig. 5.11, and W, the axial velocity in the seal. This was the format used for evaluating inlet and exit losses from the experiments in this chapter. The pressures at points **c** and **d** where not used directly, but calculated by linear extrapolation from pressure points located 1/3 and 2/3 times the seal length from the entrance. The points P_b and P_e were chosen so that the radial pressure field due to swirling flow would not influence

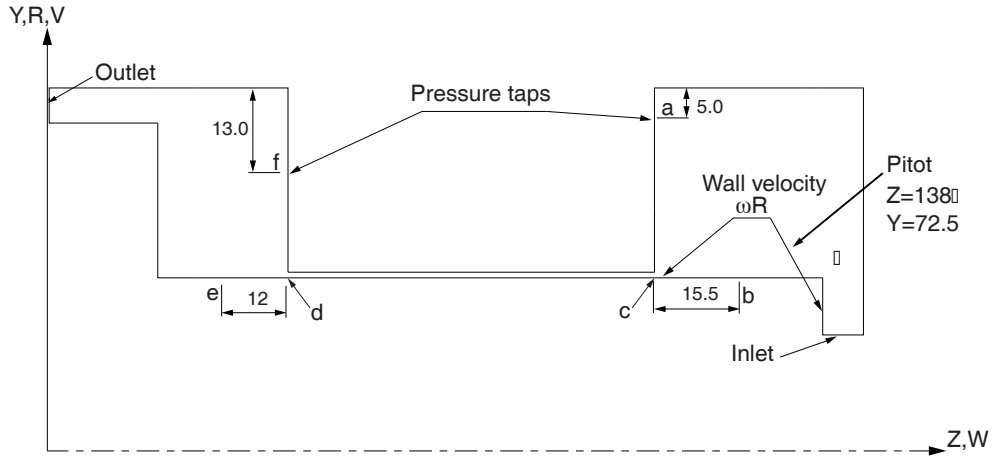

Figure 5.11: Boundary conditions and pressure point locations used for calculating inlet and exit loss.

the coefficients. In the experimental setup points P_b and P_e were not available, so some means of calculating these pressures was needed. Since the experimental pressures at P_a and P_f were known the problem was resolved by evaluating the pressure differences $P_a - P_b$ and $P_f - P_e$ as a function of leakage and rotational speed. The results for these pressure differences from Appendix E are shown in Fig. 5.12.

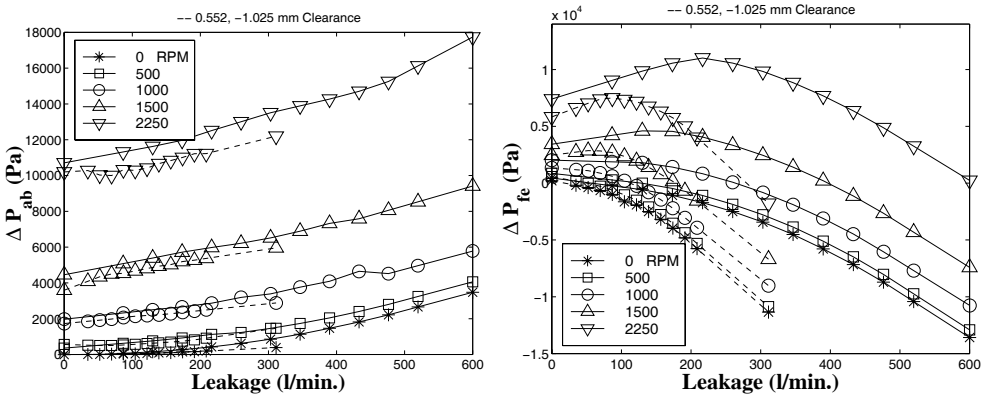

Figure 5.12: Pressure differences $P_a - P_b$ and $P_f - P_e$ as a function of leakage for the two clearances analyzed.

For a known experimental leakage the results of Fig. 5.12 was used to find the corresponding pressure difference from the measured pressure at locations **a** and **f** and the pressure at the desired locations **b** and **e** respectively. Interpolation was used when experimental leakage values did not correspond directly to one of the leakage values for the numerical simulation.

Although the other combinations of rotors and stators would yield slightly different

clearances than those used in the numerical simulations it was assumed that the results presented in Fig. 5.12 would be adequate for the whole test-series.

Inlet swirl, U, was measured at a single point with coordinates (138,72.5) in Fig. 5.11. A pitot tube was used for this purpose. Swirl was measured for rotor stator combinations S1/R2 and S1/R4. It was assumed that the swirl made by the impeller at the inlet of the inlet chamber would be a function of leakage only. The resulting swirl vs. leakage is shown in Fig. 5.13.

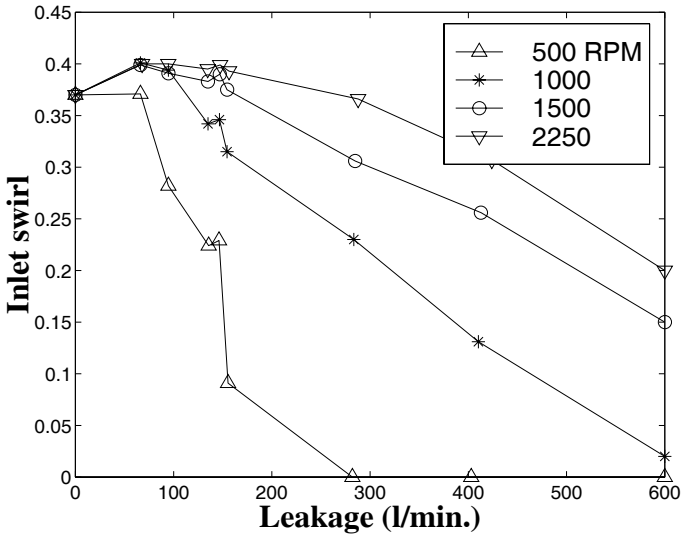

Figure 5.13: Measured dimensionless inlet swirl ($\frac{U}{\omega R}$).

For the theoretical calculations the inlet swirl was kept constant at $0.5\omega R$ at the 56 mm inlet radius. This gave a seal dimensionless inlet swirl as shown in Appendix E Fig. E.14. Although there are some discrepancies between measured and theoretical values, the discrepancies are within measurement accuracy at low leakages and high speeds, where the swirl influence is significant.

5.5 Exit loss results

In Figures 5.14 to 5.16 the experimental exit losses based on Eq. 5.5 are shown. Fig. 5.15 also shows the theoretical exit loss for a 90 degree sharp outlet at the two clearances 1.009 and 0.553.

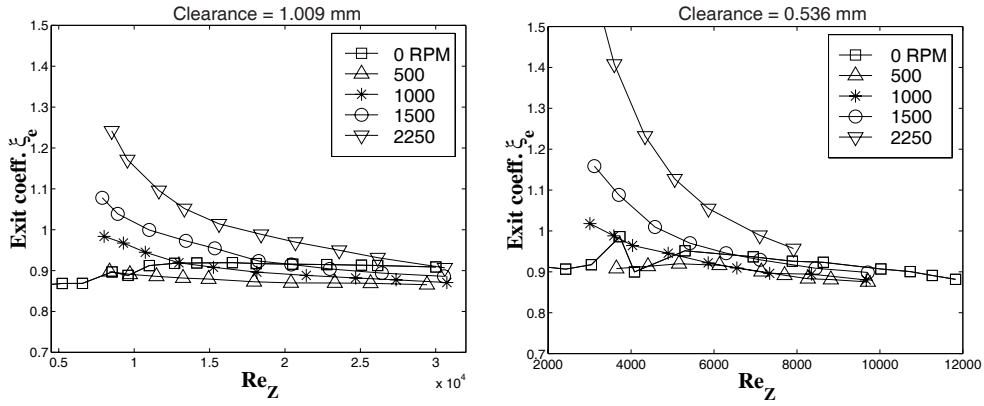

Figure 5.14: Exit coefficient, ξ_e, for the 45° chamfer. Left figure: Stator rotor combination S1/R2. Right figure: S2/R5.

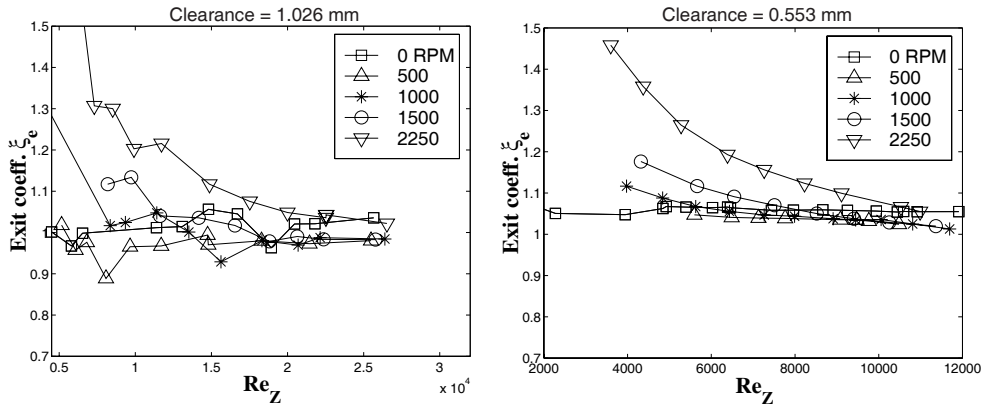

Figure 5.15: Exit coefficient, ξ_e, for the 90° sharp exit. Left figure: Stator rotor combination S1/R2. Right figure S1/R4.

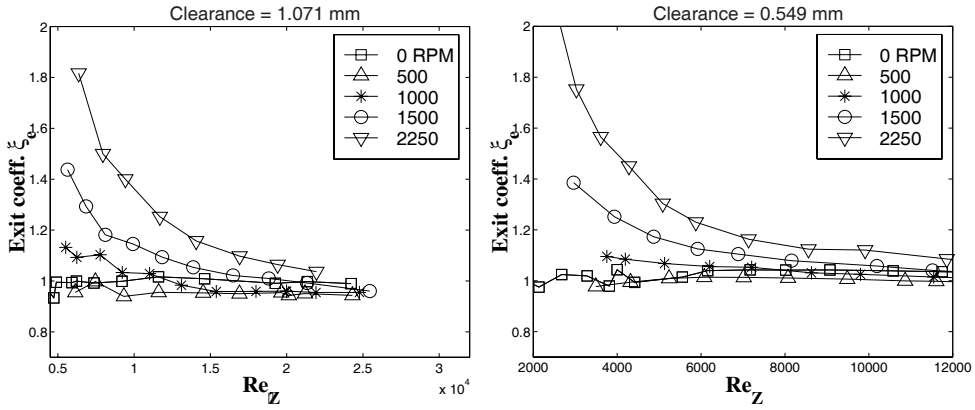

Figure 5.16: Exit coefficient, ξ_e, for the 45° protruding edge. Left figure: Stator rotor combination S3/R3. Right figure S3/R6.

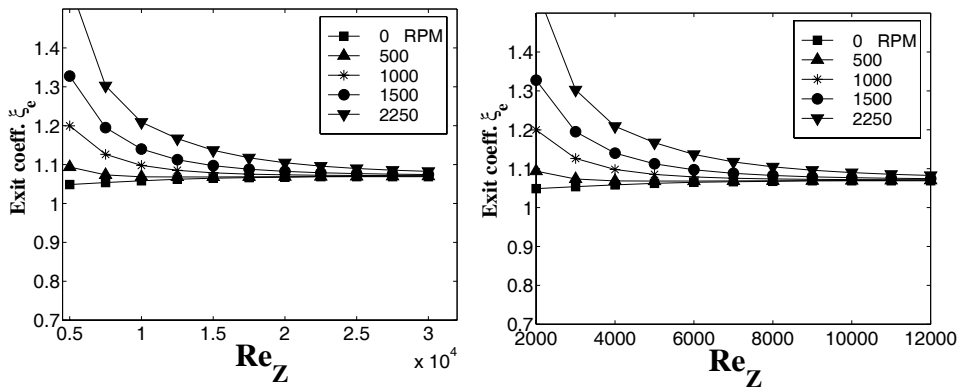

Figure 5.17: CFD predictions of the exit coefficient, ξ_e, for the 90° sharp exit. Left figure: Stator rotor combination S1/R1. Right figure: S1/R4.

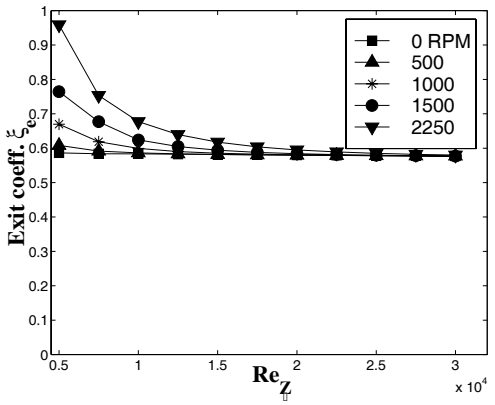

Figure 5.18: CFD predictions of the exit coefficient, ξ_e, for the 45° chamfer. The rotor stator combination is S2/R1.

5.5.1 Discussion of exit loss results

For the two clearances reported for each geometry there is little difference in this asymptotic value, which is approximately 1.0 for the 90° degree sharp and 45° protruding edge and 0.9 for the 45° protruding edge. Comparing this result to the values predicted by CFD, the 90 degree sharp exit (Fig. 5.17) fits the experimental results (Fig. 5.15) very well both in the asymptotic value and the trend in results as leakage is decreased. However, the theoretical results for the 45° chamfer do not fit experimental data well. With an asymptotic value of about 0.6, which indicates a very significant pressure recovery, the theoretical value is far off the experimental value of 0.9. As mentioned at the start of this chapter an exit coefficient of 0.6 compared to 1.0 for a 90° degree sharp exit would be advantageous since it would increase the direct stiffness of the seal significantly. So it was somewhat discouraging to find that the 45° chamfer only reduced the exit coefficient from 1.0 to 0.9.

A study described in Appendix E was carried out to find the reason for the greatly over-predicted pressure recovery by CFD. The main finding was that the $k-\epsilon$ model fails to predict separation at the concial exit, while a $k-\omega$ low Reynolds number turbulence model with a much refined computational grid gave results close to experimental.

For result at rotational speeds the main trend in the results is that the exit coefficient increases as the axial Reynolds number (and leakage) is reduced, and approaches an asymptotic value (as for 0 rpm) as the leakage is increased. The maximum value for the exit coefficient at 2250 rpm is in excess of 1.5 and clearly increasing with rotational speed.

Based on the experimental and theoretical results one could be tempted to make a functional relationship, like (Kündig, 1993), Eq. 5.1, did for the entrance coefficient, to describe the exit coefficient as a function of rotational speed.

However, there are several reasons why this was not done:

- The method used for obtaining the exit coefficient relies on pressure measurement at single points at the seal exit and exit chamber. Since the pressure varies in the exit chamber one may ask: Which point should one choose? Will one single pressure measurement be enough? As shown in the numerical study a single a single point measurement is not enough when the ratio between tangential to axial bulk flow gets large, and improved formulations are needed.
- Since the pressure variation in the exit chamber depends on the vortex speed and size, the exit coefficient ought to be a function of exit chamber geometry as well. Comparing dimensions used for typical industrial seals to the current experiment, the ratios between seal clearance and exit chamber depth and height will typically be one order of magnitude less for industrial seals. Hence, a functional relationship based on the current results would be of limited use.
- Eq. E.2 for the exit coefficient is based on an assumption that the velocity downstream of the seal exit is close to zero. Due to slow diffusion of the downstream jet this assumption does not hold if one considers a control volume near the seal exit.

5.6 Entrance loss results

The experimental results for the entrance coefficient based on Eq. 5.4 are shown in Figures 5.19 to 5.21. The results are based pressure entrance chamber pressure point **b** (see Fig. 5.11) at the rotor wall, and a linearly extrapolated pressure at point **c** just inside the seal.

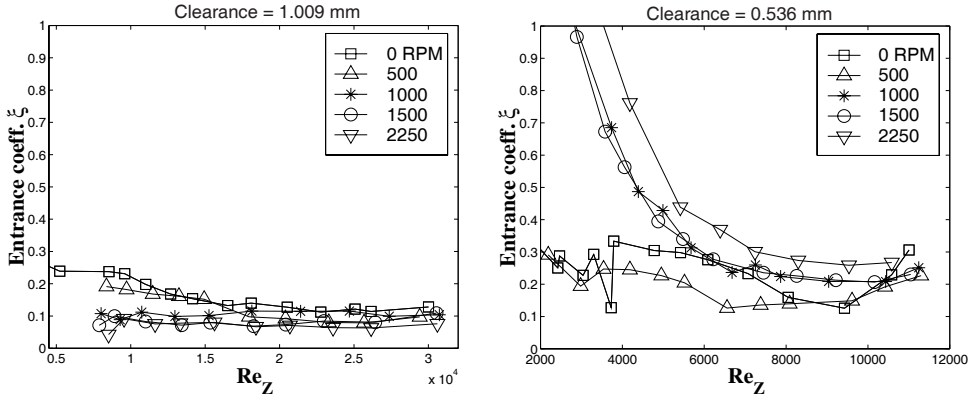

Figure 5.19: Entrance loss, ξ, for the 45° chamfer stator. Left figure: Stator rotor combination S2/R1. Right figure: S2/R4.

Theoretical results based on CFD and the Eq. 5.1 are shown in Figures 5.22 to 5.23.

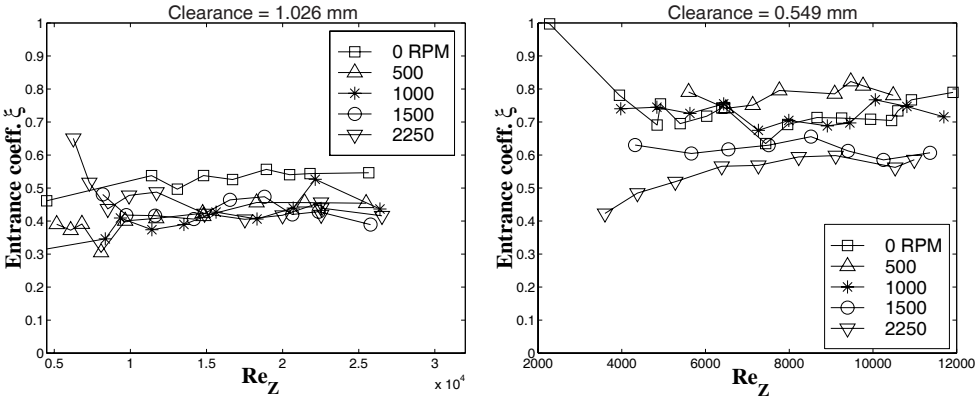

Figure 5.20: Entrance loss, ξ, for the 90° entrance. Left figure: Stator rotor combination S1/R2. Right figure: S1/R4.

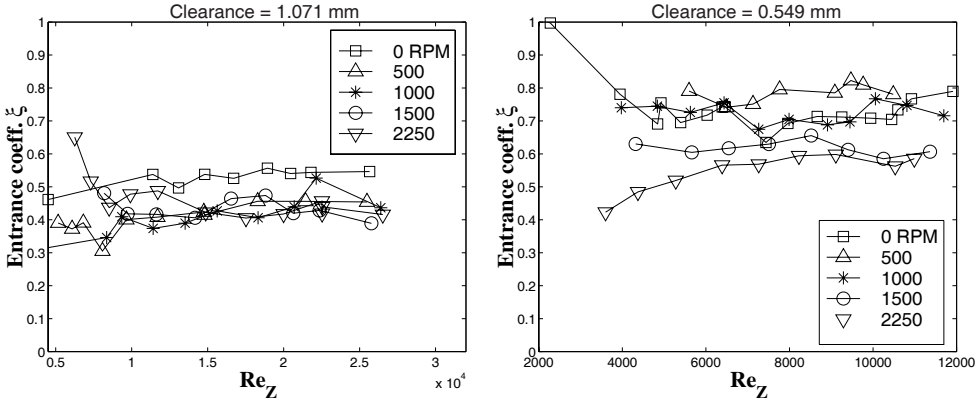

Figure 5.21: Entrance loss, ξ, for the 45° protruding edge. Left figure: Stator rotor combination S3/R3. Right figure: S3/R6.

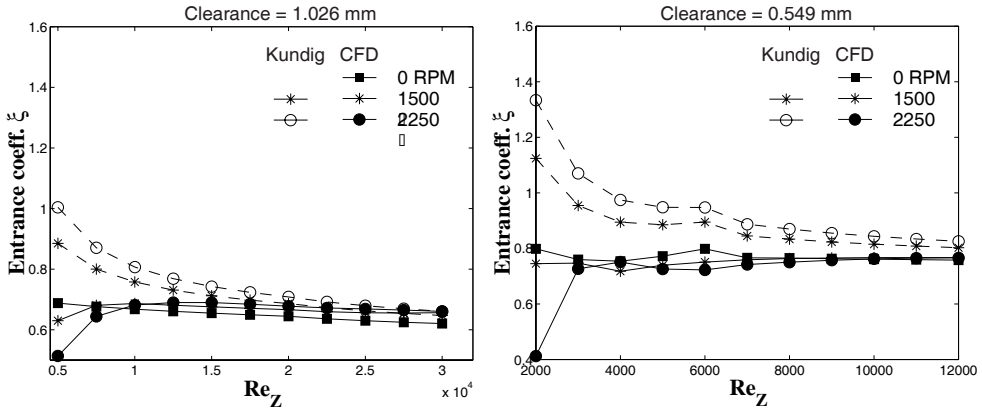

Figure 5.22: Entrance loss, ξ, for the 90° entrance. Left figure: Stator rotor combination S1/R1. Right figure: S1/R4.

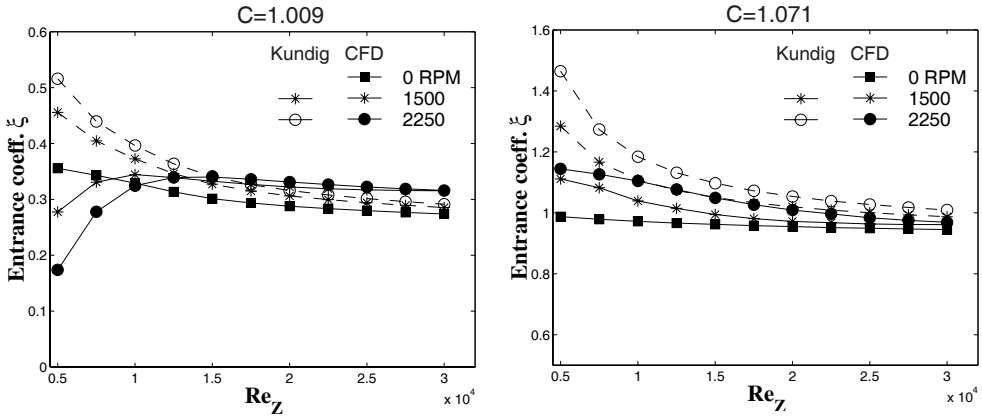

Figure 5.23: Left figure: ξ, for the 45° chamfer (S2/R1). Right figure: ξ, for the 45° protruding edge (S3/R3.

5.6.1 Discussion of entrance loss results

Some general trends are clear from the entrance loss coefficient results in Figures 5.19 to 5.21. In Fig. 5.19 both seal clearances for the 45 degree chamfer show an entrance coefficient between 0.1 and 0.3 at zero rotational speed. The corresponding values for both the 90 degree sharp inlet and the 45 degree protruding edge are between 0.5 and 0.7. If one scales the results of the chamfer for the exaggerated clearance of 1.0 mm to a seal with 0.1 mm clearance, one may expect an entrance loss coefficient near 0.1 for a chamfer of 0.074 mm. In practice it will probably be difficult to maintain an edge which is much sharper than this due to wear, so a 0.1 entrance coefficient may be a good conservative choice for practical designs.

It was surprising to find that the results for the protruding edge in Fig. 5.21 did not show any increase in the inlet loss coefficient compared to the sharp 90 degree inlet geometry (Fig. 5.20) as the numerical simulations indicate. Close inspection of the geometries showed that there was a blunt edge of approximately 0.15 mm radius at the protruding edge while the radius of the 90 degree edge was of the order 0.01 mm. This is likely to be a major reason for the discrepancy in results in addition to deficiencies in the numerical prediction.

Another trend in the results is that there is a greater spread in results for different rotational speeds at the maximum axial Reynolds number for the 0.5 mm clearance compared to the 1.0 mm clearance. A possible reason for this is that it was discovered that the rotor tilted at high pressure because of the knee like construction. In fact rub marks were discovered at the seal entrance for the smallest clearance. Hence there is a very significant eccentricity which may influence the results considerably. Clearly a different test-rig design would be needed if typical seal clearances between 0.1 and 0.2 mm were to be tested.

Regarding results at low axial Reynolds numbers and increasing rotational speed there is no common trend in the results. The chamfer inlet, Fig. 5.19, shows an increase in the inlet coefficient, while the other two inlet geometries show a decrease in the coefficient relative to zero rotational speed. In comparison the numerical results indicate that the inlet loss coefficient decreases at the lowest axial Reynolds numbers for the sharp and chamfer edge while a slight increase is found for the protruding edge. Hence, the numerical results are not consistent with the experimental. In Figures 5.22 and 5.23 the analytical formula suggested by (Kündig, 1993), Eq. 5.1, predicts a clear increase in the inlet loss as the ratio of tangential to axial velocity increases. This is contrary to most of the experimental and numerical predictions found in the current work. A possible explanation for this discrepancy may be found in the scaling of results. (Kündig, 1993) used a large clearance of 1.8 mm and a different inlet chamber than in the current experiment, so it might be that relative rotor radius to clearance ratios plays a significant role. One would need more experimental results, possibly in combination with improved numerical analyses, to determine how inlet loss varies with rotational speeds, inlet geometries and rotor radius. Also the simple formulation used here to predict the inlet loss ought to be replaced by a two-dimensional integral formulation, which takes radial velocity and pressure variations at the inlet into account.

Chapter 6

Conclusions

Important aspects in the design of centrifugal pumps, are pump efficiency, dynamic stability and compactness. Seal leakage contributes to a loss in pump efficiency and seal forces influence the range of stable operation for such pumps. In this thesis a friction factor for turbulent incompressible flow in grooved annular seals was developed by means of Computational Fluid Dynamics (CFD), and a friction factor for hole pattern seals was proposed. This friction factor has a key role for predicting leakage, the development of tangential flow in the seal, and dynamic characteristics which comprise the main topics of this thesis. Seal entrance and exit losses influence seal leakage and rotordynamic coefficients to some extent. Experiments were carried out to determine these losses as a function of geometry, axial and tangential flow, and comparisons to numerical predictions by CFD were made. Seal pressure drops for turbulent and transition to turbulent flow in seals with smooth and wavy surfaces was studied experimentally, and the results were compared to theoretical predictions.

Conclusions regarding seal leakage predictions, dynamic coefficients, and experimental work are presented in the following sections, followed by suggestions for further work.

6.1 Seal leakage

The friction factor developed for industrial seals with rectangular grooves assumes predominantly axial turbulent flow and a seal clearance to rotor radius ratio greater than 125. The groove geometries considered have width to depth ratios between 1 and 16 and groove depth to clearance ratios between 0.2 and 25.8.

The optimal groove geometry for leakage reduction calculated by CFD was for a groove depth to clearance ratio of 0.534 and a groove width to depth ratio equal to six and a minimal groove land zone. For this groove geometry tangential friction was hardly distinguishable from that of a smooth surface with the same minimum clearance as for the grooved seal, and the corresponding leakage was 25% of the smooth seal leakage at an axial Reynolds number of 100000 and 32% at an axial Reynolds number of =10000.

In general leakage predictions compared to experimental results where within ± 10%.

An extension to the friction factor model was suggested for hole pattern seals by an assumption of similar recirculating flows in the grooves and holes. Leakage predictions compared to the scarce experimental data available indicated that leakage for the hole pattern seals was predicted within ± 15%

6.2 Dynamic characteristics of seals

The turbulent flow friction factors for grooved and hole-pattern tapered seals were used in a bulk-flow theory for predicting rotordynamic coefficients. These friction factors make it possible to directly predict leakage and rotordynamic coefficients based on a given groove or hole geometry. This is a considerable advantage compared with previous models based on a Hirs friction factor where calibration to experimental data was needed. Although the intention of the proposed model was to deal primarily with groove depths less than the seal clearance good qualitative results were found for groove depths several times the clearance. Moment coefficients for tapered seals that may include groove or hole patterns on rotor or stator are accounted for. This is an extension of the bulk-flow theories previously published. A previously published transition to turbulent friction factor was also introduced for comparison to previously published results based on a different theoretical formulation for predicting seal rotordynamic coefficients. Conclusions will be presented below for each type of seal in turn.

6.2.1 Plain seals, transition to turbulence

In the transition to turbulence regime (Reynolds numbers between 2000 and 6000) the accuracy of the Moody friction deteriorates for leakage predictions in pipe flow. An improved friction factor for pipe flow was used to predict rotordynamic coefficients for seals operating in the transition to turbulence range. The dynamic coefficients calculated in this thesis compared well with previously published theoretical results but comparison to experimental results were discouraging. Theoretical results based on the standard Moody friction factor show better agreement with experimental results in this range.

6.2.2 Grooved seals

The current approach predicts rotordynamic coefficients with an agreement to experimental results similar to alternative models. There is a single free parameter $0 < h^+ < 1$ in the formulation which allows circumferential groove flow to be excluded or included in the rotordynamic calculation. Most results indicate that the circumferential groove flow should be included. Advantages of the current model compared to three-control-volume theories are that moment coefficients are calculated and that the current model covers a wide range of groove geometries.

A parameter study was carried out for a grooved stator seal with various groove width to depth ratios. The results show that a leakage reduction of about 60% was achievable compared to a smooth seal when groove depths were less than the seal clearance. For the same geometry the direct radial and moment stiffnesses were reduced by approximately 60% and there was little change in all other coefficients. This indicates that significant improvements in overall pump efficiency may be achieved for some pumps with little change in the pump's dynamic characteristics.

For groove depths greater than the seal clearance, there is less leakage reduction. However, direct stiffness, cross-coupled stiffness, and direct damping can be reduced by one order of magnitude. The results indicate that the direct stiffness becomes negative for very deep grooves. A negative direct stiffness acts to increase the eccentricity of the rotor, and this may be detrimental to the seal. The results for a non-dimensional inlet swirl of 0.5 also indicate that the whirl frequency ratio increases from about 0.5 for shallow grooves to a maximum value as high as 0.8 for a seal with deep grooves. If this effect can be confirmed by experiment, such a deep groove seal may limit the range of safe operation for a pump significantly.

6.2.3 Hole pattern seals

Based on the numerical calculations of pressure drops in grooved annular seals, a friction factor for turbulent flow in hole pattern seals was proposed for hole diameter to hole depth ratios between 1 and 16 and hole depth to seal clearance ratios between 0.2 and 25.8. Based on experimental dynamic characteristics published by other authors the current theory predicts effective stiffness and damping with a standard deviation of 13% and 12% from the experimental values. Effective mass based on zero rotational speed gave results on average within 30% of the predicted value, but radial force at high rotational speed is less accurately predicted. The current theory predicts cross-coupled stiffness, direct damping and hence whirl frequency ratio with a reasonable agreement to experimental results. Direct seal stiffness is predicted to drop significantly for hole pattern seals compared to smooth seals with the same minimum clearance, but the experimental results show a larger drop in direct stiffness than that predicted.

The major advantage of the current model is that it allows studies of hole pattern seal leakage, dynamics, and mechanical loss without calibration to experiment. Since the model appears to predict whirl frequency ratio well it may prove to be useful for suggesting what hole pattern would be optimal for reducing the whirl frequency for a given seal and operating condition, possibly to the extent of eliminating self induced vibrations from the seal.

A parameter study carried out for a given seal with a number of hole patterns on the stator suggests that the positive cross-coupled stiffness obtained for a smooth seal with inlet swirl of half the rotor speed may be reversed, yielding a negative cross-coupled stiffness for hole patterns with hole depths less than the seal clearance and a hole depth to diameter ratio between 2 and 8. This range of hole patterns has not been studied experimentally in the open literature. For the same range of hole patterns, a leakage reduction of up to 60% was predicted relative to that of a smooth

seal and an approximate halving of direct stiffness was found. The predictions for the hole pattern seal gave an increase in direct damping by about 15%, a reduction in cross-coupled damping by about 30%, and small deviations in direct added mass relative to the smooth seal.

6.3 Experimental and CFD results

6.3.1 Seal friction factor

The circumferential wavy rotor grooves with depths of approximately one order less than the seal clearance gave a friction factor up to three times that of a polished rotor. The friction factor developed in this thesis for rectangular grooves predicted leakage within 12% of the experimental values for the wavy grooves. This indicates that the groove friction factor is useful for a wide range of grooved surfaces.

For the Reynolds number range $2000 - 6000$ the transition to turbulence factor developed for pipe flow showed no improvement in the correlation to results compared to the Moody friction factor. The main discrepancy was found as the Reynolds number approaches the laminar zone. The transition to turbulence friction factor predicts that there will be a significant friction drop while the experimental results show a gradual increase. Comparison to other experimental results indicated that the discrepancy between the seal and pipe transition friction factor may be due to the finite eccentricity and a rotational speed of the seal.

6.3.2 Seal entrance loss

A change of the entrance loss coefficient from approximately 0.5 to 0.1 was found at zero rotational speed when the entrance geometry changed from a sharp 90° inlet to a 45° chamfer. The chamfer size was in the same order as the clearance. Assuming that the results for a 1.0 mm clearance can be scaled to that of a 0.1 mm clearance this means that a chamfer as small as 0.075 mm will give an inlet coefficient of 0.1. In practice one may expect that a sharp seal inlet will be worn to this extent, so in design one should consider both cases when calculating dynamic characteristics of the seal in order to be conservative.

An attempt to increase the seal inlet loss coefficient compared to a sharp inlet by introducing a 45° protruding edge was not successful. The purpose of this attempt was to increase direct seal stiffness. However, an entrance loss of 0.5 was measured, and the numerically predicted value was close to 1.0. It is possible that the unintended nose radius of about 0.15 mm at the protruding edge could explain some of the discrepancy in results.

One of the seal-stator configurations showed an increase in the inlet loss coefficient with rotational speed while all others showed an approximately constant or decreasing coefficient. Numerical predictions indicated that the inlet loss remained constant or slightly decreasing tangential- to axial bulk velocity ratios up to 5. Hence, this finding

supports the commonly used assumption that the entrance coefficient does not vary significantly with rotational speed.

From numerical and experimental results at high rotational speeds the inlet chamber flow field and pressure distribution is such that the validity of the equation used for inlet coefficient predictions is questionable for the large clearances used. There is a radial pressure variations along the seal inlet that make the constant pressure assumption inaccurate. The apparent inlet loss coefficient measured may no longer be a frictional loss alone, since it may include pressure gradient effects caused by the flow field itself.

For the numerical predictions both the standard $k-\epsilon$ turbulence model and the low Reynolds number $k-\omega$ model over-predict the inlet loss significantly for all inlet geometries considered. The standard model gave a good prediction of the decrease in the entrance loss coefficient for the chamfered seal inlet, but over-predicts the increase in the entrance loss for a protruding edge. For the experimental results presented in this thesis there was very little change in inlet loss as a function of swirl. The theoretical predictions follow the same trend as the experimental for most cases.

6.3.3 Seal exit loss

For zero rotational speed the exit geometries of 45° chamfer, 90° sharp corner, and 45° protruding edge gave exit coefficients of approximately 0.9, 1.0 and 1.0 respectively. Numerical predictions by CFD utilizing the standard $k-\epsilon$ model correspond well with the experimental results for the 90° sharp corner, but grossly over-predict pressure recovery in the exit chamber (exit coefficient of 0.6) for the 45° chamfer. The main reason for this discrepancy was that the $k-\epsilon$ model did not predict separation in the expanding exit correctly. This was discovered by using a low-Reynolds number $k-\omega$ turbulence model with a dense grid so that the boundary layer was calculated numerically from a non-dimensional wall distance of $y^+ = 1$ or less. With this model the exit coefficient results changed to 0.96 which is close to the average experimental exit coefficient of approximately 0.9.

As rotational speed is increased both experimental and theoretical predictions indicate that the exit loss coefficient increases, and there is good correspondence between experimental and theoretical results for a sharp corner exit. A strong vortex in the seal exit chamber due to the swirling flow creates a pressure field in the chamber which is close to constant for a given leakage and rotational speed. For a rotational speed of 10000 rpm, an axial Reynolds number of 5000 and two different clearances of 1.009 and 0.553 mm gave apparent exit coefficients of 8.37 and 3.13 respectively while the corresponding exit coefficient for a 0.1 mm clearance seal would be 1.07. The term apparent exit coefficient is used since the formula used for predicting the exit coefficient does not separate the exit chamber flow field contribution and frictional loss effects on the pressure downstream of the seal exit.

6.4 Suggestions for further work

- **Experimental validation:** The friction factor developed in this thesis for predicting friction loss in hole and groove pattern seals covers a wide range of geometries that have not been experimentally verified. Studies around the predicted optimal patterns for leakage reduction would be of great interest. For hole pattern seals it is predicted in this thesis that a certain range of hole patterns will provide a great reduction in positive cross-coupled stiffness. Experimental data are needed to verify if the theory holds.

- **Extension of current friction factor model:** A known weakness of the current groove and hole friction factor model is that it is limited to seals with predominantly axial flow. Further studies are needed to extend the current models to cover seals with a greater range of tangential and axial flows. One may divert to the promising three-control-volume methods for grooved seals and possibly extend these to deal with hole pattern seals.

- **Transition to turbulence:** A friction factors for transition to turbulent flow in seals based on pipe flow did not compare well to experimental results for smooth or machine roughened seal surfaces. A transition to turbulence model is lacking for groove and hole patterns. Further experimental work, possibly combined with numerical CFD calculations, may improve friction factor models in this regime in the future.

- **Entrance and exit coefficients:** For seal entrance and exit coefficients the dependency on tangential flow has not been studied in great detail. Two-dimensional integral pressure and kinetic energy effects may have to be considered for high rotational speeds in order to achieve a more refined model for viscous losses and local pressure gradients at the seal inlet and exit. A range of clearance to radius ratios needs to be considered to derive a general formulation. Seal exits designed as a diffuser with a smaller cone angle than used in this thesis may prove to increase direct seal stiffness. For both entrance- and exit coefficients the inlet- and exit chamber geometry influence results. Future studies may determine which geometries are preferable.

- **CFD turbulence models for swirling flow:** The standard $k-\epsilon$ and low Reynolds number $k-\omega$ turbulence models used in this thesis over-predicted inlet loss significantly. Some modifications of these models that improve predictions have been published, but still their accuracy is limited, and improved turbulence models are needed.

References

Anderson Jr., John D. 1995. *Computational Fluid Dynamics. The Basics With Application.* International edn. Mechanical Engineering Series. McGRAW-HILL.

Arghir, Mihai, & Frêne, Jean. 1995. Entrance Effects in Annular Seal Flows. *Pages 1149–1156 of: Proceedings of the ASME 1995 Design Engineering Technical Conferences.* DE-Vol. 84-2, vol. 3 - part B.

Arghir, Mihai, & Frêne, Jean. 1997a. Forces and Moments Due to Misalignment Vibrations in Annular Liquid Seals Using the Averaged Navier-Stokes Equations. *Journal of Tribology*, **119**(Apr.), 279–290.

Arghir, Mihai, & Frêne, Jean. 1997b. Inclusion of Roughness Effects in Perturbed Navier-Stokes Rotordynamic Methods. *Journal of Tribology*, **119**(Apr.), 358–360.

Arghir, Mihai, & Frêne, Jean. 1997c. Rotordynamic Coefficients of Circumferentially-Grooved Liquid Seals Using the Averaged Navier-Stokes Equations. *Journal of Tribology*, **119**(July), 556–567.

Athavale, M. M., Przekwas, A. J., & Hendricks, R. C. 1993. A 3D-CFD Code for Accurate Predicition of Fluid Flows and Fluid Forces in Seals. *Pages 137–147 of: Proceedings of the workshop: Rotordynamic Instability Problems in High-Performance Turbomachinery.* NASA CP-3239.

Athavale, M. M., Przekwas, A. J., & Liang, A. 1994. SCISEAL A 3D CFD Code for Accurate Analysis of Fluid Flow and Forces in Seals. *In: Proceedings of the Advanced ETO Propulsion Conference, May 1994.*

Athavale, M. M., Hendricks, R. C., & Steinetz, B. M. 1995. *Numerical Simulation of Flow in a Whirling Annular Seal and Comparison to Experiments.* Tech. rept. NASA TM-106961. American Institute of Aeronautics and Astronautics, National Aeronautics and Space Administration, Lewis Research Center, Cleveland, Ohio 44135-3191.

Barbin, A. R., & Jones, J. B. 1963. Turbulent Flow in the Inlet Region of a Smooth Pipe. *ASME Journal of Basic Engineering*, **85**(1), 29–34.

Baskharone, E. A. 1994. Perturbed Flow Structure in an Annular Seal due to Synchronous Whirl. *Journal of Fluids Engineering*, **116**(Sept.), 564–569.

Baskharone, E. A., & Hensel, S. J. 1991a. A Finite-Element Perturbation Approach to Fluid/Rotor Interaction in Turbomachinery Elements. Part 1: Theory. *Journal of Fluids Engineering*, **113**(Sept.), 353–361.

Baskharone, E. A., & Hensel, S. J. 1991b. A Finite-Element Perturbation Approach to Fluid/Rotor Interaction in Turbomachinery Elements. Part 2: Application. *Journal of Fluids Engineering*, **113**(Sept.), 362–367.

Beatty, P. A., & Hughes, W. F. 1987. Turbulent Two-Phase Flow in Face Shaft Seals. *Journal of Tribology*, **109**(Jan.), 91–99.

Beatty, P. A., & Hughes, W. F. 1990. Stratified Two-Phase Flow in Annular Seals. *Journal of Tribology*, **112**(Apr.), 372–381.

Beeler, Richard Maxwell. 1985 (May). *Effects of Two-Phase Flow in Shaft Seals.* Ph.D. Dissertation, Carnegie Mellon University, Pittsburgh Pennsylvania.

Black, H. F. 1969. Effects of Hydraulic Forces in Annular Pressure Seals on the Vibrations of Centrifugal Pump Rotors. *Journal of Mechanical Engineering Science*, **11**(2), 206–213.

Black, H. F., & Cochrane, E. A. 1973 (Feb.). Leakage and Hybrid Bearing Properties of Serrated Seals in Centrifugal Pumps. *Pages 61–70 of: 6th International Conference on Fluid Sealing.* BHRA Fluid Engineering, Cranfield, Bedford, England.

Black, H. F., & Murray, J. L. 1969. The Hydrostatic and Hybrid Bearing Properties of Annular Pressure Seals in Centrifugal Pumps. *The British Hydromechanics Research Association*, Oct. Report RR 1026.

Black, H. F., Allaire, P.E., & Barret, L.E. 1981 (Apr.). Inlet Flow Swirl in Short Turbulent Annular Seal Dynamics. *Pages 141–152 of: Proceedings of the Ninth International Conference in Fluid Sealing.*

Braun, M. J., Hendricks, R. C., Wheeler III, R. L., & Mullen, R. L. 1987. Finite Difference Solution for a Generalized Reynolds Equation with Homogeneous Two-Phase Flow. *Pages 424–439 of: Conference Paper: ISBN:0-89116-572-X.* Hemisphere Publishing Corp. Washington D.C., U.S.A.

CFX. 1996 (Nov.). *Using CFX 4 With CFX-Build Lecture Notes.* CFX International, 8.19 Harwell, Didcot, Oxfordshire, United Kingdom.

CFX. 1997 (Dec.). *CFX 4.2 Solver.* CFX International, 8.19 Harwell, Didcot, Oxfordshire, United Kingdom.

Childs, Dara W. 1982. Rotordynamic Moment Coefficients for Finite-Length Turbulent Seals. *Proceedings of the IFToMM Conference on Rotordynamic Problems in Power Plants*, 371–378. Rome, Italy.

Childs, Dara W. 1983. Dynamic Analysis of Turbulent Annular Seals Based on Hirs' Lubrication Equation. *Journal of Lubrication Technology*, **105**(July), 429–436.

Childs, Dara W. 1993. *Turbomachinery Rotordynamics; Phenomena, Modeling, and Analysis.* John Wiley & Sons, New York.

Childs, Dara W., & Dressman, J. B. 1985. Convergent-Tapered Annular Seals: Analysis and Testing for Rotordynamic Coefficients. *Journal of Tribology*, **107**(July), 307–317.

Childs, Dara W., & Fayolle, Patrice. 1998. Test Results for Liquid Damper Seals Using a Round-Hole Roughness Pattern for the Stators. *In: Submitted for the ASME-STLE Joint Tribology Conference.*

Childs, Dara W., Nolan, S., & Nunez, D. 1988. Clearance effects on leakage and rotordynamic coefficients of smooth, liquid annular seals. *Pages 371–378 of: Proceeding of the IMechE International Conference Proceedings, Vibrations in Rotating Machinery.*

Childs, Dara W., Nolan, S., & Kilgore, J. J. 1990. Additional Test Results for Round-Hole-Pattern Damper Seals: Leakage, Friction Factors, and Rotordynamic Force Coefficients. *Journal of Tribology*, **112**(Apr.), 365–371.

Clarke, Diane S., & Wilkes, Nigel S. 1989. *The calculation of turbulent flow in complex geometries using a Differential Stress Model.* AERE-R 13428. AEA Technology, Library Information Services, Building 465, AEA Technology, Harwell, Oxfordshire, OX11 0RA, England.

Clarke, Diane S., & Wilkes, Nigel S. 1991. *The calculation of turbulent flow in complex geometries using a Differential Flux Model.* AEA-InTec 0216. AEA Technology, Library Information Services, Building 465, AEA Technology, Harwell, Oxfordshire, OX11 0RA, England.

Colebrook, Cyril Frank. 1939. Turbulent Flow in Pipes, with particular reference to the Transition Region between the Smooth and Rough Pipe Laws. *J. Inst. Civ. Eng. Lond.*, **11**(Paper No. 5204), 133–156.

Dietzen, F. J., & Nordmann, R. 1986. Calculating Rotordynamic Coefficients of Seals by Finite-Difference Techniques. *Pages 77–96 of: Proceedings of the workshop: Rotordynamic Instability Problems in High-Performance Turbomachinery.* NASA CP-2443.

Dietzen, F. J., & Nordmann, R. 1987. Calculating Rotordynamic Coefficients of Seals by Finite-Difference Techniques. *Journal of Tribology*, **109**(July), 388–394.

Dietzen, F. J., & Nordmann, R. 1988. A 3-Dimensional Finite-Difference Method for Calculating The Dynamic Coefficients of Seals. *Pages 211–227 of: Proceedings of the workshop: Rotordynamic Instability Problems in High-Performance Turbomachinery.* NASA CP-3026.

Dietzen, Josef. 1987 (Dec.). *Bestimmung der dynamischen Koeffizienten von Dichtspalten mit Finite - Difference - Verfahren.* Ph.D. Dissertation, Universität Kaiserslautern.

Doormal, J. P. Van, & Raithby, G. D. 1984. Enhancements of the SIMPLE method for predicting incompressible fluid flows. *Numerical Heat Transfer*, **7**, 147–163.

Elrod, David A. 1988 (Aug.). *Entrance and Exit Region Friction Factor Models for Annular Seal Analysis.* Ph.D. Dissertation, Texas A&M University.

Florancic, Stefan. 1990 (May). *Annular Seals of High Energy Centrifugal Pumps: A New Theory and Full Scale Measurements of Rotordynamic Coefficients and Hydraulic Friction Factors.* Ph.D. Dissertation, Swiss Federal Institute of Technology Zürich.

Hirs, G. G. 1973. A Bulk-Flow Theory for Turbulence in Lubricant Films. *Journal of Lubrication Technology*, 137–146.

Hirsch, C. 1988. *Numerical Computation of Internal and External Flows, Volume 1-2.* Wiley.

Hirschel, E. H., Thiede, P., & Monnoyer, F. 1988. Turbulence Management - Application Aspects. *Pages 23–1 to 23–12 of: Fluid Dynamics of Three Dimensional Turbulent Shear Flows and Transition, Cesme, Turkey, 3-6 October.* AGARD-CP-438.

H.Möbius. 1940. Experimentelle Untersuchungen des Wiederstandes und der Geschwindigkeitsverteilung in Rohren mit regelmässig angeordneten Rauhigkeiten bei turbulenter Strömung. *Phys. Z.*, **41**, 202–225.

Holman, Jack P. 1994. *Experimental Methods for Engineers.* 6 edn. McGraw-Hill, Inc.

Iwatsubo, T., & Nishino, T. 1994. The Dynamic Forces of Pump Annular Seals through Two Phase Flow. *Pages 191–196 of: Proceedings of the Fourth IFToMM International Conference on Rotor Dynamics.*

Iwatsubo, T., & Sheng, B. C. 1990. An Experimental Study on the Static and Dynamic Characteristics of Damper Seals. *Pages 307–312 of: Proceedings of the Third IFToMM International Conference on Rotor Dynamics.*

Iwatsubo, Takuzo. 1980. Evaluation of Instability Forces of Labyrinth Seals in Turbines or Compressors. *Pages 139–167 of: Proceedings of the workshop: Rotordynamic Instability Problems in High-Performance Turbomachinery.* NASA CP-2133.

Iwatsubo, Takuzo, Motooka, N., & Kawai, R. 1982. Flow Induced Force and Flow Pattern of Labyrinth Seal. *Pages 205–222 of: Proceedings of the workshop: Rotordynamic Instability Problems in High-Performance Turbomachinery.* NASA CP-2250.

Kanemori, Yuji, & Iwatsubo, Takuzo. 1992. Experimental Study of Dynamic Fluid Forces and Moments for a Long Annular Seal. *Journal of Tribology*, **114**(Oct.), 773–778.

Kaye, Joseph, & Elgar, E. C. 1958. Modes of Adiabatic and Diabatic Fluid Flow in an Annulus With an Inner Rotating Cylinder. *Transactions of the ASME*, Apr., 753–765.

Kilgore, J. J., & Childs, D. W. 1990. Rotordynamic Coefficients and Leakage Flow of Circumferentially Grooved Liquid-Seals. *Journal of Fluids Engineering*, **112**(sep), 250–256.

Kim, Chang-Ho. 1985 (Aug.). *Analysis and Testing for Rotordynamic Coefficients of Grooved Turbulent Annular Seals.* Ph.D. Dissertation, Texas A & M University.

Koh, Yang-Moon. 1992. Turbulent Flow Near a Rough Wall. *Journal of Fluids Engineering*, **114**, 537–542.

Kreyzig, Erwin. 1983. *Advanced Engineering Mathematics.* 5 edn. Library of Congress Cataloging in Publication Data. John Wiley & Sons, Inc.

Kündig, Peter. 1993. *Gestufte Labyrinthdichtungen hydraulischer Maschinen Experimentelle Untersuchung der Leckage, der Reibung und der stationäre Kräfte.* Ph.D. Dissertation, Swiss Federal Institute of Technology Zürich, ETH, Zürich,Switzerland.

Launder, B. E., & Spalding, D. B. 1974. The Numerical Computation of Turbulent Flow. *Computer Methods in Applied Mechanics and Engineering*, **3**, 269–289.

Linsey, William Todd. 1993 (Aug.). *Experimental Versus Theoretical Comparison of The Effects of Taper and Static Eccentricity of the Rotordynamic Coefficients of Short, Smooth, High-speed, Liquid Annular Seals.* TL-SEAL-9-93 360. The Texas A&M University System, College Station, Texas, 77843-3254.

Lomakin, A. A. 1958. Calculation of Critical Speed and Securing of the Dynamic Stability of the Rotor of Hydraulic High Pressure Machines with Reference to Forces Arising in Seal Gaps. *Energomashinostroenie*, **4**.

Lucas, Victor, Danaila, Sterian, Bonneau, Olivier, & Frêne, Jean. 1994. Roughness Influence on Turbulent Flow Through Annular Seals. *Journal of Tribology*, **116**(Apr.), 321–329.

Lucas, Victor, Bonneau, Olivier, & Frêne, Jean. 1996. Roughness Influence on Turbulent Flow Through Annular Seals Including Inertia Effects. *Journal of Tribology*, **118**(Jan.), 175–182.

Lund, J. 1966. *Self-Excited, Stationary Whirl Orbits of Journal in a Sleeve Bearing.* Ph.D. Thesis, Rensselaer Polytechnic Institute, Troy, NY.

Marquette, O. R., Childs, D. W., & Phillips, S. G. 1997. Theory Versus Experiment for Leakage and Rotordynamic Coefficients of Circumferentially - Grooved Liquid Annular Seals With L/D of 0.45. *In: 1997 ASME Fluids Engineering Division Summer Meeting FEDSM'97 June 22-26, 1997.* FEDSM97-3333. ASME.

McDonald, A. T., Fox, R. W., & Van DeWostine, R. V. 1971. Effects of Swirling Inlet Flow on Pressure Recovery in Conical Diffusers. *AIAA Journal*, **9**(10), 2014.

Moody, Lewis F. 1944. Friction Factors for Pipe Flow. *ASME Transactions*, Nov., 671–684.

Morrison, G. L., Johnson, M. C., & Tatterson, G. B. 1988. 3-D Laser Anemometer Measurements in Annular Seals. *In: ASME Paper No. 88-GT-64.*

Morrison, Gerald L., & Johnson, Mark C. 1996. Upstream Swirl Effects on the Flow Inside a Labyrinth Seal. *Pages 145–160 of: Proceedings of the workshop: Rotordynamic Instability Problems in High-Performance Turbomachinery.* NASA CP-3344.

Morrison, Gerald L., DeOtte Jr., Robert E., & Thames, H. D. 1992. Turbulence Measurements of High Shear Flow Fields in a Turbomachine Seal Configuration. *In: Proceedings of the Advanced Earth-To-Orbit Propulsion Technology Conference.*

Muszynska, A. 1986a. Whirl and Whip- Rotor/Bearing/Seal Instabillity Problems. *Journal of Sound and Vibration*, **110**(3).

Muszynska, Agnes. 1986b. *Fluid-Related Rotor/Bearing/Seal Instabillity Problems.* Tech. rept. Bently Rotor Dynamics Research Corporation, Minden, Nevada.

Nelson, C. 1985. Rotordynamic Coefficients for Compressible Flow in Tapered Annular Seals. *Journal of Tribology*, **107**, 318–325.

Nelson, Clayton C., & Nguyen, Dung T. 1986. Comparison of Hirs' Equation with Moody's Equation for Determining Rotordynamic Coefficients of Annular Pressure Seals. *Pages 189–203 of: Proceedings of the workshop: Rotordynamic Instability Problems in High-Performance Turbomachinery.* NASA CP-2443.

Nikuradse, J. 1933. Strömungsgesetze in rauhen Rohren. *VDI-Verlag*, **Forschungsheft 361**, 1–22.

Nordmann, R., & Weiser, P. 1988. Rotordynamic Coefficients for Labyrinth Seals Calculated by means of a Finite-Difference Technique. *Pages 211–227 of: Proceedings of the workshop: Rotordynamic Instability Problems in High-Performance Turbomachinery.* NASA CP-3026.

Nordmann, R., & Weiser, P. 1990. Evaluation of Rotordynamic Coefficients of Look-Through Labyrinths by Means of a Three Volume Bulk Model. *Pages 141–157 of: Proceedings of the workshop: Rotordynamic Instability Problems in High-Performance Turbomachinery.* NASA CP-3122.

Nordmann, R., Dietzen, F. J., Janson, W., Frei, A., & Florancic, S. 1987. Rotordynamic Coefficients and Leakage Flow of Parallel Grooved Seals and Smooth Seals. *Pages 129–153 of: Proceedings of the workshop: Rotordynamic Instability Problems in High-Performance Turbomachinery - 1986.* NASA CP-2443.

Patankar, Suhas V. 1980. *Numerical Heat Transfer and Fluid Flow.* Taylor & Francis.

Press, William H., Teukolsky, Saul A., Vetterling, William T., & Flannery, Brian P. 1992. *Numerical Recipes in FORTRAN.* 2. edn. Cambridge University Press.

Rhie, C. M. 1981. *Numerical study of the flow past an isolated airfoil with separation.* Ph.D. Dissertation, University of Illinois at Urbana-Champaign.

Rhie, C. M., & Chow, W. L. 1983. Numerical study of the turbulent flow past an airfoil with trailing edge separation. *AIAA J1*, **21**, 1527–1532.

Rodi, Wolfgang. 1993. *Turbulence Models and Their Applicability in Hydraulics.* A state-of-the-art review Third Edition. IAHR/AIRH Monograph Series.

San Andres, Luis A. 1991. Analysis of Variable Fluid Properties, Turbulent Annular Seals. *Journal of Tribology*, **113**(Oct.), 694–702.

San Andres, Luis A. 1993. Dynamic Force and Moment Coefficients for Short Length Annular Seals. *Journal of Tribology*, **115**(jan), 61–70.

Scharrer, J. K., & Nelson, C. C. 1991. Rotordynamic Coefficients for Partially Roughened Pump Annular Seals. *Journal of Vibration and Acoustics*, **113**(Apr.), 240–244.

Schetz, Joseph A., & Fuhs, Allen E. 1996. *Handbook of Fluid Dynamics and Fluid Machinery.* 1. edn. Vol. 3. John Wiley & Sons, Inc.

Schlichting, Hermann. 1936. *Experimentelle Untersuchungen zum Rauhigkeitsproblem.* Ingenieur-Archiv 7, pages 1-34.

Schlichting, Hermann. 1979. *Boundary-Layer Theory, 7th ed.* McGraw Hill.

Stampa, Burkhard. 1971. *Experimentelle Untersuchungen an axial durchströmten Ringspalten.* Ph.D. Dissertation, Ub8-8774, Technischen Universität Braunschweig, Braunschweig, Germany. In German.

Tam, L.T., Przekwas, A. J., Muszynska, A., Hendricks, R. C., Braun, M. J., & Mullen, R. L. 1988. Numerical and Analytical Study of Fluid Dynamic Forces in Seals and Bearings. *Journal of Vibration, Acoustics, Stress, and Reliability in Design*, **110**(July), 315–325.

Taylor, G. I. 1923. Stability of a Viscous Fluid Contained Between Two Rotating Cylinders. *Philosophical Transactions of the Royal Society of London*, **223**(series A), 289–343.

Tennekes, H., & Lumley, J. L. 1972. *A First Course in Turbulence.* MIT Press.

Thames III, H.D. 1992 (May). *Mean Flow and Turbulence Characteristics in Whirling Annular Seals.* M.S. Thesis, Texas A & M University.

von Pragenau, G. 1982. *Damping Seals for Turbomachinery.* NASA Technical Paper No. 1987. NASA.

Wakes, S. J., & Holdœ, Arne Erik. 1997. Wall functions used with current turbulence models. *ASME FEDSM97-3147*, jun.

Weber, D. 1971. *Experimentelle Untersuchungen an axial durchströmten kreisringfömingen Spaltdichtungen für Kreiselpumpen.* Ph.D. Dissertation, Technischen Universität Braunschweig, Braunschweig, Germany. In German.

Weiss, Marvin H. 1993 (Sept.). *Drag Reduction with Riblets in Pipe Flow.* Ph.D. Dissertation, The University of Calgary.

White, Frank M. 1994. *Fluid Mechanics, Third Edition.* McGraw Hill.

Wiederhold, Wilhelm. 1949 (Dec.). *Über den Einfluss von Rohrablagerungen auf den hydraulischen Druckabfall.* Heft 24 Volume 99 no. 634. Gas und Wasserfach.

Wilcox, D. C. 1993. *Turbulence Modeling for CFD.* DCW Industries, Inc.

Wyssman, H., Pham, T., & Jenny, R. 1984. Prediction of Stiffness and Damping Coefficients for Centrifugal Compressor Labyrinth Seals. *Journal of Engineering for Gas Turbines and Power*, **106**(Apr.), 920–926.

Yamada, Y. 1962a. On the Pressure Loss of Flow between Rotating Co-Axial Cylinders with Rectangular Grooves. *Bulletin of JSME*, **5**(20), 642–651.

Yamada, Y. 1962b. Resistance of a Flow through an Annulus with an Inner Rotating Cylinder. *Bulletin of JSME*, **5**(18), 302–310.

Yamada, Yutaka, Nakabayashi, Kouichi, & Maeda, Kozo. 1969. Pressure Drop Measurements of the Flow through Eccentric Cylinders with Rotating Inner Cylinders. *Bulletin of JSME*, **12**(53), 1032–1040.

Zirkelback, Nicole, & San Andres, Louis. 1996. Bulk-Flow Model for the transition to Turbulence Regime in Annular Pressure Seals. *STLE Tribology Transactions*, **39**(4), 835–842.

Appendix A

CFD-software description

A.1 Description of the CFX program

CFX version 4.2, by CFX International, is a computer program used for predicting incompressible, weakly compressible or fully compressible transient and stationary flows with heat transfer in three dimensional geometries. It has a wide range of features which are thoroughly described in (CFX, 1997). CFX is based on a non-staggered Finite Volume method technique and it uses body-fitted coordinates to treat arbitrary two- and three-dimensional geometries. The Finite Volume method is described in many text books, see for example (Hirsch, 1988) and (Patankar, 1980). In CFX cartesian-, polar- and rotating- coordinates are available as well as moving grid. Details on the coordinate transforms used is described in (CFX, 1997) with reference to (Rhie, 1981) and (Rhie & Chow, 1983). The program offers algebraic- and differential stress turbulence models (Clarke & Wilkes, 1991) and (Clarke & Wilkes, 1989), two equation k-ϵ model by (Launder & Spalding, 1974) and low Reynolds number k-ω model by (Wilcox, 1993).

Appendix B

Details of the bulk flow model

B.1 First order perturbation coefficients

The coefficients listed below are used in Chapter 4, Eq. 4.38.

$$A_{1_z} = \frac{u_{s0}}{2h_0^2}\left(\frac{\sigma_{zs0}}{h_0} - \frac{\partial \sigma_{zs0}}{\partial h_0}\right) + \frac{u_{r0}}{2h_0^2}\left(\frac{\sigma_{zr0}}{h_0} - \frac{\partial \sigma_{zr0}}{\partial h_0}\right) \tag{B.1}$$

$$A_{2_z} = \frac{b^2}{2h_0^2}\left[u_0\left(\frac{\partial \sigma_{zs0}}{\partial u_{s0}} + \frac{\sigma_{zs0}}{u_{s0}}\right) + (u_0 - 1)\left(\frac{\partial \sigma_{zr0}}{\partial u_{r0}} + \frac{\sigma_{zr0}}{u_{r0}}\right)\right] \tag{B.2}$$

$$\begin{aligned} A_{3_z} &= \frac{1}{2h_0^3}\left(\frac{\partial \sigma_{zs0}}{\partial u_{s0}} + \frac{\sigma_{zs0}}{u_{s0}} + \frac{\partial \sigma_{zr0}}{\partial u_{r0}} + \frac{\sigma_{zr0}}{u_{r0}}\right) - \frac{1}{h_0^2}\frac{\partial h_0}{\partial z} \\ &+ \frac{u_{s0}\sigma_{zs0}}{2h_0} + \frac{u_{r0}\sigma_{zr0}}{2h_0} \end{aligned} \tag{B.3}$$

$$A_{1_\theta} = \frac{u_0 u_{s0}}{2h_0^*}\left(\frac{\sigma_{\theta s0}}{h_0} - \frac{\partial \sigma_{\theta s0}}{\partial h_0}\right) + \frac{u_{r0}\,(u_0 - 1)}{2h_0^*}\left(\frac{\sigma_{\theta r0}}{h_0} - \frac{\partial \sigma_{\theta r0}}{\partial h_0}\right) \tag{B.4}$$

$$\begin{aligned} A_{2_\theta} &= \frac{b^2 u_0^2}{2h_0^*}\left(\frac{\partial \sigma_{\theta s0}}{\partial u_{s0}} + \frac{\sigma_{\theta s0}}{u_{s0}}\right) + \frac{b^2\,(u_0 - 1)^2}{2h_0^*}\left(\frac{\partial \sigma_{\theta r0}}{\partial u_{r0}} + \frac{\sigma_{\theta r0}}{u_{r0}}\right) \\ &+ \frac{u_{s0}\sigma_{\theta s0}}{2h_0^*} + \frac{u_{r0}\sigma_{\theta r0}}{2h_0^*} \end{aligned} \tag{B.5}$$

$$\begin{aligned} A_{3_\theta} &= \frac{u_0}{2h_0 h_0^*}\left(\frac{\partial \sigma_{\theta s0}}{\partial u_{s0}} - \frac{\sigma_{\theta s0}}{u_{s0}}\frac{b^2 u_0^2}{w_0^2}\right) \\ &+ \frac{(u_0 - 1)}{2h_0 h_0^*}\left(\frac{\partial \sigma_{\theta r0}}{\partial u_{r0}} - \frac{\sigma_{\theta r0}}{u_{r0}}\frac{b^2 (u_0 - 1)^2}{w_0^2}\right) \end{aligned} \tag{B.6}$$

where $\sigma_{zs0} = f_{zs0}\left(\frac{L}{C_r}\right)$, $\sigma_{\theta s0} = f_{\theta s0}\left(\frac{L}{C_r}\right)$, $\sigma_{zr0} = f_{zr0}\left(\frac{L}{C_r}\right)$, $\sigma_{\theta r0} = f_{\theta r0}\left(\frac{L}{C_r}\right)$. In order to determine the above coefficients for the different seals studied in this thesis, the friction factors and their partial derivatives for each type of surface roughness are needed.

B.2 Friction factors

Friction factors for the following types of seals are documented in this appendix:

- Plain seals with surface roughness from hydraulically smooth up to an absolute roughness one order of magnitude less than the clearance. Fully turbulent flow is modelled with the Moody friction factor, laminar flow is modelled with a laminar friction factor, and the transition friction factor is a combination of the Moody and laminar friction factors.
- Serrated/Grooved seals. Intended for seals with circumferential grooves with a depth ranging from one order of magnitude less than the minimum clearance to one order of magnitude greater than the minimum clearance. The groove depth to clearance ratio should be in the range 0.2 to 25.8, and groove width to depth ratio should be in the range 1 to 16. Only fully turbulent flow is considered.
- Hole pattern seals. Intended for seals with holes with a depth ranging from one order of magnitude less than the minimum clearance to one order of magnitude greater than the minimum clearance. The hole depth to clearance ratio should be in the range 0.2 to 25.8, and the hole diameter to depth ratio should be in the range 1 to 16. Only fully turbulent flow is considered.

Details on the various friction factors are shown in the following sections.

B.2.1 Smooth and machine roughness seals

For isotropic roughness Moody's friction formula is used

$$f_{\theta r} = f_{zr} = f_r \tag{B.7}$$

$$f_{\theta s} = f_{zs} = f_s \tag{B.8}$$

$$f_{r,s} = a_1 \left[1 + \left(\frac{b_2 e_{r,s}}{2H} + \frac{b_3}{Re_{r,s}} \right)^{\frac{1}{3}} \right] \tag{B.9}$$

where $Re_{r,s} = \frac{2U_{r,s}H\rho}{\mu}$, $a_1 = 1.375 \cdot 10^{-3}$, $b_2 = 20000$, $b_3 = 10^6$, and H is the local film thickness. This formula gives values that are within 5% of the Moody diagram for

$$4000 < Re_{r,s} < 10^7 \tag{B.10}$$

Moody's friction factor is used for the land portion of the groove and hole pattern seals.

For the laminar regime

$$f_{r,s} = \frac{24}{Re_{r,s}} \tag{B.11}$$

where $Re_{r,s} \leq 2000$. The laminar flow friction factor was used for plain seals only.

Subscript convention used

The subscripts denote direction, groove or land, rotor and/or stator, zeroth or first order solution. So for the friction factor $f_{\theta gr,s0}$. θ means angular direction, g indicates grooved portion of seal, r, s indicates two equations one for rotor and stator respectively, and 0 means zeroth order variables.

For example Eq. B.11 actually means two equations:

$$f_r = \frac{24}{Re_r} \tag{B.12}$$

$$f_s = \frac{24}{Re_s} \tag{B.13}$$

For the transition regime, $2000 < Re_{r,s} < 6000$, in plain seals a formulation by (Zirkelback & San Andres, 1996) was used.

$$f_{r,s} = \frac{24}{Re_{r,s}}\left(1 - 3\xi_{r,s}^2 + 2\xi_{r,s}^3\right) + f_{r,s}^{moody}(3\xi_{r,s}^2 - 2\xi_{r,s}^3) \tag{B.14}$$

$$= f_{r,s}^{lamin} + \left(3\xi_{r,s}^2 - 2\xi_{r,s}^3\right)\left(f_{r,s}^{moody} - f_{r,s}^{lamin}\right) \tag{B.15}$$

where $\xi_{r,s} = \frac{Re_{r,s} - A_3}{A_4}$, $A_3 = 2000$, and $A_4 = 4000$.

Introduce the dimensionless variables

$$\begin{array}{llllllllllll} \bar{W} & = & \frac{\dot{Q}}{2\pi R\bar{C}_r} & b & = & \frac{R\omega}{\bar{W}} & w & = & \frac{W}{\bar{W}} & a_{2r,s} & = & b_2\epsilon_{r,s} \\ u & = & \frac{U}{R\omega} & h & = & \frac{H}{\bar{C}_r} & Re_z & = & \frac{2\bar{C}_r\bar{W}\rho}{\mu} & \epsilon_{r,s} & = & \frac{e_{r,s}}{2\bar{C}_r} \\ \alpha & = & \frac{C_{in} - C_{ex}}{L} & \bar{C}_r & = & \frac{C_{in} + C_{ex}}{2} & q & = & \frac{\alpha L}{2\bar{C}_r} & z & = & \frac{Z}{L} \\ a_3 & = & \frac{b_3}{Re_z} & & & & & & & & & \end{array}$$

The dimensionless velocities and film thickness are

$$u_s = \sqrt{w^2 + b^2u^2} \tag{B.16}$$

$$u_r = \sqrt{w^2 + b^2\left(u - 1\right)^2} \tag{B.17}$$

$$h = [1 + q(1 - 2z)] \tag{B.18}$$

Dimensionless Moody, laminar, and transition friction factor formulas for rotor and stator become:

$$f_{r,s}^{moody} = a_1\left[1 + \left(\frac{a_{2s}}{h} + \frac{a_3}{hu_{r,s}}\right)^{\frac{1}{3}}\right] \tag{B.19}$$

$$f_{r,s}^{lamin} = \frac{24}{Re_z h u_{r,s}} \tag{B.20}$$

$$f_{r,s} = f_{r,s}^{lamin} + \left(3\xi_{r,s}^2 - 2\xi_{r,s}^3\right)\left(f_{r,s}^{moody} - f_{r,s}^{lamin}\right) \tag{B.21}$$

B.2.2 Grooved seal friction factor

For grooved rotor and stator the friction factor consists of one part from the land portion and one from the grooved portion.

$$f_{\theta r,s} = \chi_{\theta lr,s} f_{lr,s} + \chi_{gr,s} f_{\theta gr,s} \tag{B.22}$$

$$f_{zr,s} = \chi_{zlr,s} f_{lr,s} + \chi_{gr,s} \frac{w}{u_{r,s}} f_{zgr,s} \tag{B.23}$$

χ_{lr} and χ_{gr} are the relative land and groove portions of the rotor respectively. χ_{lr} is split in to parts $\chi_{\theta lr}$ and χ_{zlr} since a better fit to the CFD solution was found when the fully developed land friction factor for the z-direction does not act over the whole land surface. However, setting $\chi_{\theta lr}$ equal to χ_{lr} gave the best correlation for the tangential friction factor calculations. The reason for the terms $w/u_{r,s}$ in Eq. B.23 is that the axial friction factor for the grooves is related to the axial flow only, while the other friction factors are related to the total velocity relative to the rotor and stator.

$$\chi_{zlr,s} = \frac{\bar{L}_{lr,s} - 4\bar{C}_r}{\bar{L}_{lr,s} + L_{gr,s}} \tag{B.24}$$

$$\chi_{\theta lr,s} = \frac{\bar{L}_{lr,s}}{\bar{L}_{lr,s} + L_{gr,s}} \tag{B.25}$$

$$\chi_{gr,s} = \frac{N_{gr,s} L_{gr,s}}{L} \tag{B.26}$$

$$\bar{L}_{lr,s} = \frac{Lin_{r,s} + (N_{gr,s} - 1) L_{lr,s} + Lex_{r,s}}{N_{gr,s}} \tag{B.27}$$

where $N_{gr,s}$ is the number of grooves on the rotor and stator, $Lin_{r,s}$ is the inlet land zone length, $Lex_{r,s}$ the exit land zone length, $L_{lr,s}$ the land zone length between grooves. If $\chi_{zlr,s} < 0$ it is set equal to zero, so that all friction loss is due to the grooves. The relative portions of the seal $\chi_{zlr,s}$ and $\chi_{gr,s}$ covered by the land and groove zone are calculated based on the assumption that the same groove width and depth are used for all grooves on each surface and that the groove spacing is constant.

The details of the friction factors $f_{\theta gr,s}$ and $f_{zgr,s}$ for circumferential grooves are given in Chapter 3, Eq. 3.46. For the land portion Moody's friction factor is used.

B.2.3 Hole pattern seal friction factor

$$f_{\theta r} = \chi_{lr} f_{lr} + \chi_{hr} \frac{u-1}{u_r} f_{hr} \tag{B.28}$$

$$f_{\theta s} = \chi_{ls} f_{ls} + \chi_{hs} \frac{u}{u_s} f_{hs} \tag{B.29}$$

$$f_{zr,s} = \chi_{lr,s} f_{lr,s} + \chi_{hr,s} \frac{w}{u_{r,s}} f_{hr,s} \tag{B.30}$$

The weighting factors, mean land length and hole area fraction are given by

$$\chi_{lr,s} = \frac{\bar{L}_{lr,s} - 4\bar{C}_r}{\bar{L}_{lr,s} + d_{hr,s}} \tag{B.31}$$

$$\chi_{hr,s} = \frac{d_{hr,s}}{\bar{L}_{lr,s} + d_{hr,s}} \tag{B.32}$$

$$\bar{L}_{lr,s} = d_{hr,s}\left(\frac{1-\gamma_{r,s}}{\gamma_{r,s}}\right) \tag{B.33}$$

$$\gamma_{r,s} = \frac{hole\ area_{r,s}}{total\ area_{r,s}} \tag{B.34}$$

If $\chi_{lr,s} \leq 0$ it is set equal to zero.

The details of the friction factors, $f_{hr,s}$, for hole patterns are given in Chapter 3, Eq. 3.62. For the land portion Moody's friction factor is used. The terms $\frac{u-1}{u_r}$, $\frac{u}{u_s}$, and $\frac{w}{u_{r,}}$, in Equations B.28 to B.30 are needed since the friction factor for the holes in the tangential direction is related to the tangential flow only and the hole friction factor for the axial direction is related only to the axial flow.

B.2.4 Partial differentiation of friction factors

Moody

$$\frac{\partial f_{r,s0}}{\partial h_0} = \frac{1}{h_0}\frac{1}{3}\left(a_1 - f_{r,s0}\right) \tag{B.35}$$

$$\frac{\partial f_{r,s0}}{\partial u_{r,s0}} = \frac{1}{u_{r,s0}} f_{r,s0} b_{r,s} \tag{B.36}$$

where

$$b_{r,s} = \left[-\frac{1}{3}\frac{1}{\left(\frac{a_{2r,s}}{h_0} + \frac{a_3}{h_0 u_{r,s0}}\right)}\left(1 - \frac{a_1}{f_{r,s0}}\right)\left(\frac{a_3}{u_{r,s0} h_0}\right)\right] \tag{B.37}$$

and $f_{r,s0}$ is Moody's friction factor.

Laminar

$$\frac{\partial f_{r,s0}}{\partial h_0} = -f_{r,s0}\frac{1}{h_0} \tag{B.38}$$

$$\frac{\partial f_{r,s0}}{\partial u_{r,s0}} = -f_{r,s0}\frac{1}{u_{r,s0}} \tag{B.39}$$

where $f_{r,s0}$ is the laminar friction factor.

Transition to turbulence

$$\xi_{r,s0} = \frac{R_{r,s0} - A_3}{A_4} \tag{B.40}$$

$$A_3 = 2000 \tag{B.41}$$

$$A_4 = 4000 \tag{B.42}$$

$$\frac{\partial f_{r,s0}}{\partial h} = \frac{1}{h_0}\left[\begin{array}{c} -f_{r,s0}^{lamin} + 6\xi_{r,s0}\frac{24}{A_4}\frac{1}{f_{r,s0}^{lamin}}\left(1-\xi_{r,s0}\right)\left(f_{r,s0}^{moody} - f_{r,s0}^{lamin}\right) \\ +\left(3\xi_{r,s0}^2 - 2\xi_{r,s0}^3\right)\left(\frac{1}{3}\left(a_1 - f_{r,s0}^{moody}\right) + f_{r,s0}^{lamin}\right) \end{array}\right] \tag{B.43}$$

$$\frac{\partial f_{r,s0}}{\partial u_{r,s0}} = \frac{1}{u_{r,s0}}\left[\begin{array}{c} -f_{r,s0}^{lamin} + 6\xi_{r,s0}\frac{24}{A_4}\frac{1}{f_{r,s0}^{lamin}}\left(1-\xi_{r,s0}\right)\left(f_{r,s0}^{moody} - f_{r,s0}^{lamin}\right) \\ +\left(3\xi_{r,s0}^2 - 2\xi_{r,s0}^3\right)\left(b_{r,s}f_{r,s0}^{moody} + f_{r,s0}^{lamin}\right) \end{array}\right] \tag{B.44}$$

Grooved surface, both on rotor and stator, fully turbulent $Re_{r,s} > 4000$

Angular friction factor:

$$\frac{\partial f_{\theta r,s0}}{\partial h_0} = \chi_{\theta lr,s}\frac{\partial f_{lr,s0}}{\partial h_0} + \chi_{gr,s}\frac{\partial f_{\theta gr,s0}}{\partial h_0} \tag{B.45}$$

$$\frac{\partial f_{\theta r,s0}}{\partial u_{r,s0}} = \chi_{\theta lr,s}\frac{\partial f_{lr,s0}}{\partial u_{lr,s0}} + \chi_{gr,s}\frac{\partial f_{\theta gr,s0}}{\partial u_{r,s0}} \tag{B.46}$$

For the land section $\frac{\partial f_{lr,s0}}{\partial h_0}$ and $\frac{\partial f_{lr,s0}}{\partial u_{lr,s0}}$ are the same as for Moody above. For the grooved part it is very similar, except that the equivalent roughness $a_{2\theta gr,s}$ is different.

$$\frac{\partial f_{\theta gr,s0}}{\partial h_0} = \frac{1}{h_0}\frac{1}{3}\left(a_1 - f_{\theta gr,s0}\right) \tag{B.47}$$

$$\frac{\partial f_{\theta gr,s0}}{\partial u_{r,s0}} = \frac{1}{u_{r,s0}} f_{\theta gr,s0} b_{\theta gr,s0} \tag{B.48}$$

where

$$b_{\theta gr,s0} = \left[-\frac{1}{3} \frac{1}{\left(\frac{a_{2\theta gr,s}}{h_0} + \frac{a_3}{h_0 u_{r,s0}} \right)} \left(1 - \frac{a_1}{f_{\theta gr,s0}} \right) \left(\frac{a_3}{u_{r,s0} h_0} \right) \right] \tag{B.49}$$

Axial direction:

$$\frac{\partial f_{zr,s0}}{\partial h_0} = \chi_{zlr,s} \frac{\partial f_{lr,s0}}{\partial h_0} + \chi_{zgr,s} \frac{w_0}{u_{r,s0}} \frac{\partial f_{zgr,s0}}{\partial h_0} \tag{B.50}$$

$$\frac{\partial f_{zr,s0}}{\partial u_{r,s0}} = \chi_{zlr,s} \frac{\partial f_{lr,s0}}{\partial u_{lr,s0}} + 0 \tag{B.51}$$

where

$$\frac{\partial f_{zgr,s0}}{\partial h_0} = \left[\frac{1}{3h_0} \left(\frac{a_{r,s}}{2h_0} \sqrt{\frac{a_{2zgr,s0}}{h_0}} - 1 \right) \right] \left(f_{zgr,s0} - \frac{a_1}{h_0 u_{r,s0}} \right) \tag{B.52}$$

$$\frac{\partial f_{zgr,s0}}{\partial u_{r,s0}} = 0 \tag{B.53}$$

Hole pattern, fully turbulent flow, $Re_{r,s} > 4000$

For holes on rotor and stator the friction factor is assumed to be isotropic.

$$\frac{\partial f_{zr,s0}}{\partial h_0} = \chi_{lr,s} \frac{\partial f_{lr,s0}}{\partial h_0} + \chi_{hr,s} \frac{w_0}{u_{r,s0}} \frac{\partial f_{hr,s0}}{\partial h_0} \tag{B.54}$$

$$\frac{\partial f_{\theta r0}}{\partial h_0} = \chi_{lr} \frac{\partial f_{lr0}}{\partial h_0} + \chi_{hr} \frac{(u_0 - 1)}{u_{r0}} \frac{\partial f_{hr0}}{\partial h_0} \tag{B.55}$$

$$\frac{\partial f_{\theta s0}}{\partial h_0} = \chi_{ls} \frac{\partial f_{ls0}}{\partial h_0} + \chi_{hs} \frac{u_0}{u_{s0}} \frac{\partial f_{hs0}}{\partial h_0} \tag{B.56}$$

$$\frac{\partial f_{zr,s0}}{\partial u_{r,s0}} = \chi_{lr,s} \frac{\partial f_{lr,s0}}{\partial u_{lr,s0}} + 0 \tag{B.57}$$

$$\frac{\partial f_{\theta r,s0}}{\partial u_{r,s0}} = \chi_{lr,s} \frac{\partial f_{lr,s0}}{\partial u_{lr,s0}} + 0 \tag{B.58}$$

where

$$\frac{w_0}{u_{r,s0}}\frac{\partial f_{hr,s0}}{\partial h_0} = c_{r,s}\left(f_{hr,s0} - \frac{a_1}{h_0 u_{r,s0}}\right) \quad \text{(B.59)}$$

$$\frac{(u_0-1)}{u_{r0}}\frac{\partial f_{hr0}}{\partial h_0} = c_r\left(f_{hr0} - \frac{a_1(u_0-1)}{u_r}\right) \quad \text{(B.60)}$$

$$\frac{u_0}{u_{s0}}\frac{\partial f_{hs0}}{\partial h_0} = c_s\left(f_{hs0} - \frac{a_1 u_0}{u_{s0}}\right) \quad \text{(B.61)}$$

$$\frac{\partial f_{hr,s0}}{\partial u_{r,s0}} = 0 \quad \text{(B.62)}$$

and

$$c_{r,s} = \left[\frac{1}{3h_0}\left(\frac{a_{r,s}}{2h_0}\sqrt{\frac{a_{2hr,s0}}{h_0}} - 1\right)\right] \quad \text{(B.63)}$$

B.3 Solution to first order differential equations

The solution procedure for Eq. 4.38 is outlined in this section. For the first order equations a combination of inlet and outlet conditions must be specified. This means that the first order equations fall into a class of problems called boundary value problems. Boundary value problems can be solved in many different ways. Note that the method adopted below is for linear ordinary differential equations only. It involves solving the equations for three different initial conditions and then combining the solutions so that all boundary conditions are fulfilled.

The equation to be solved is

$$\frac{d\vec{Z}}{dz} + A(z)\vec{Z} + g(z) = 0 \quad \text{(B.64)}$$

where z=Z/L and

$$\vec{Z}(z) = \left\{ \begin{array}{c} \bar{w}_1(z) \\ \bar{u}_1(z) \\ \bar{p}_1(z) \end{array} \right\} \quad \text{(B.65)}$$

Although both inlet and exit conditions should be fulfilled one can solve the problem for three initial values first where exit conditions will not be fulfilled.

$$\frac{d\vec{Z}}{dz} + A(z)\vec{Z} + g(z) = 0, \vec{Z}(0) = \begin{Bmatrix} 0 \\ u_1(0) \\ 0 \end{Bmatrix} \tag{B.66}$$

$$\frac{d\vec{Z}}{dz} + A(z)\vec{Z} = 0, \vec{Z}(0) = \begin{Bmatrix} 1 \\ 0 \\ 0 \end{Bmatrix} \tag{B.67}$$

$$\frac{d\vec{Z}}{dz} + A(z)\vec{Z} = 0, \vec{Z}(0) = \begin{Bmatrix} 0 \\ 0 \\ 1 \end{Bmatrix} \tag{B.68}$$

These give solutions $\vec{Z}_3(z), \vec{Z}_1(z), \vec{Z}_2(z)$ which can be combined to get the actual solution which fulfills all boundary conditions.

Now determine λ_1, λ_2 to fulfill boundary conditions

$$\vec{Z}(0) = \vec{Z}_3(0) + \lambda_1 \vec{Z}_1(0) + \lambda_2 \vec{Z}_2(0) \tag{B.69}$$

$$\vec{Z}(1) = \vec{Z}_3(0) + \lambda_1 \vec{Z}_1(0) + \lambda_2 \vec{Z}_2(0) \tag{B.70}$$

$$\vec{Z}(0) = \begin{Bmatrix} \bar{w}_1(0) \\ \bar{u}_1(0) \\ \bar{p}_1(0) \end{Bmatrix} = \begin{Bmatrix} 0 \\ \bar{u}_1(0) \\ 0 \end{Bmatrix} + \lambda_1 \begin{Bmatrix} 1 \\ 0 \\ 0 \end{Bmatrix} + \lambda_2 \begin{Bmatrix} 0 \\ 0 \\ 1 \end{Bmatrix} \tag{B.71}$$

This gives λ_1, $\bar{w}_1(0)$, $\lambda_2 = p_1(0)$, and $u_1(0) = u_1(0)$.

Setting

$$\vec{Z}_3(z) = \begin{Bmatrix} \psi_3(z) \\ \gamma_3(z) \\ \phi_3(z) \end{Bmatrix} \quad \vec{Z}_1(z) = \begin{Bmatrix} \psi_1(z) \\ \gamma_1(z) \\ \phi_1(z) \end{Bmatrix} \quad \vec{Z}_2(z) = \begin{Bmatrix} \psi_2(z) \\ \gamma_2(z) \\ \phi_2(z) \end{Bmatrix}$$

$$\vec{Z}(1) = \begin{Bmatrix} \bar{w}_1(1) \\ \bar{u}_1(1) \\ \bar{p}_1(1) \end{Bmatrix} = \begin{Bmatrix} \psi_3(1) \\ \gamma_3(1) \\ \phi_3(1) \end{Bmatrix} + \lambda_1 \begin{Bmatrix} \psi_1(1) \\ \gamma_1(1) \\ \phi_1(1) \end{Bmatrix} + \lambda_2 \begin{Bmatrix} \psi_2(1) \\ \gamma_2(1) \\ \phi_2(1) \end{Bmatrix} \tag{B.72}$$

gives

$$\bar{w}_1(1) = \psi_3(1) + \bar{w}_1(0)_1\psi_1(1) + \bar{p}_1(0)\psi_2(1) \tag{B.73}$$

$$\bar{u}_1(1) = \gamma_3(1) + \bar{w}_1(0)_1\gamma_1(1) + \bar{p}_1(0)\gamma_2(1) \tag{B.74}$$

$$\bar{p}_1(1) = \phi_3(1) + \bar{w}_1(0)_1\phi_1(1) + \bar{p}_1(0)\phi_2(1) \tag{B.75}$$

$$\lambda_1 = \bar{w}_1(0) = \frac{\bar{p}_1(1) - \phi_3(1) - \bar{p}_1(0)\phi_2(1)}{\phi_1(1)} \tag{B.76}$$

Introducing the boundary conditions

$$\left\{ \begin{array}{c} \bar{u}_1(0) = 0 \\ \bar{p}_1(0) = -(1+\xi)\bar{w}_1(0)/h_0(0) = k_1\bar{w}_1(0) \\ \bar{p}_1(1) = -(1-\xi_e)\bar{w}_1(1)/h_0(1) = k_2\bar{w}_1(1) \end{array} \right\} \tag{B.77}$$

where

$$h_0(0) = (1+q) \tag{B.78}$$

$$h_0(1) = (1-q) \tag{B.79}$$

$$k1 = \frac{(1+\xi)}{(1+q)} \tag{B.80}$$

$$k2 = \frac{(1-\xi_e)}{(1-q)} \tag{B.81}$$

one can solve for $\bar{w}_1(0)$.

$$\bar{w}_1(0) = \frac{k2\psi_3(1) + \phi_3(1)}{(k1k2\psi_2(1) + k1\phi_2(1) - \phi_1(1) - k2\psi_1(1))} \tag{B.82}$$

Finally the solution for the perturbed pressure field is

$$\bar{p}_1(z) = \bar{w}_1(0)\phi_1(z) + \bar{p}_1(0)\phi_2(z) + \phi_3(z) \tag{B.83}$$

$\phi_3(z)$ is determined by he type of whirling motion and it will have one solution for the radial- and one for the angular perturbed motion.

Appendix C

Test rig details

C.1 Geometry

In Figures C.1 to C.5 geometry details are shown for the main components of the test unit described in Chapter 5. O-rings were used between the stator bucket and insert in Fig. C.1 to separate the pressures measured in the 0.3 mm holes in the stator surface. Between the front plate and the bucket a gasket was fitted, and the thickness after mounting was approximately 1.5 mm.

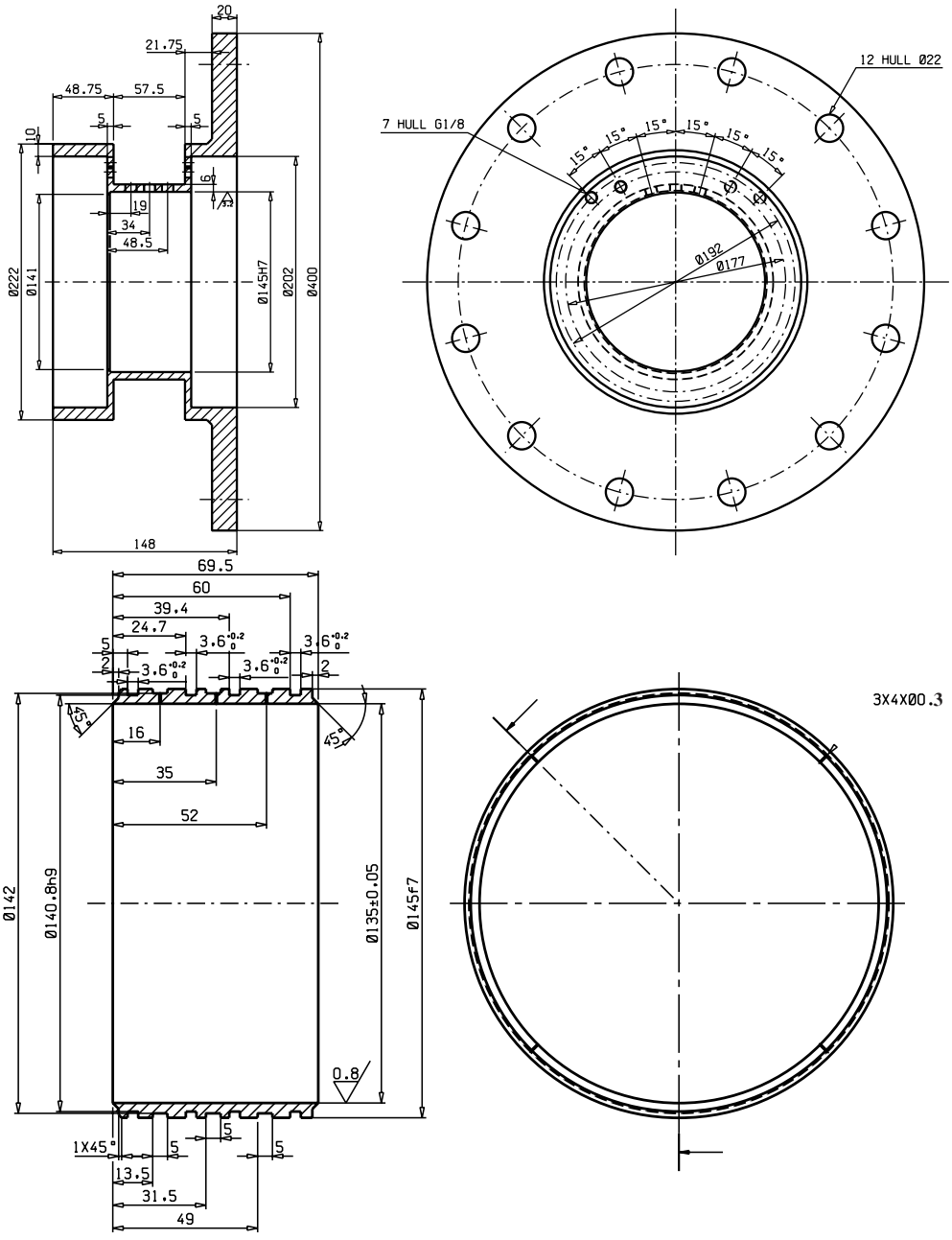

Figure C.1: Stator- bucket and insert.

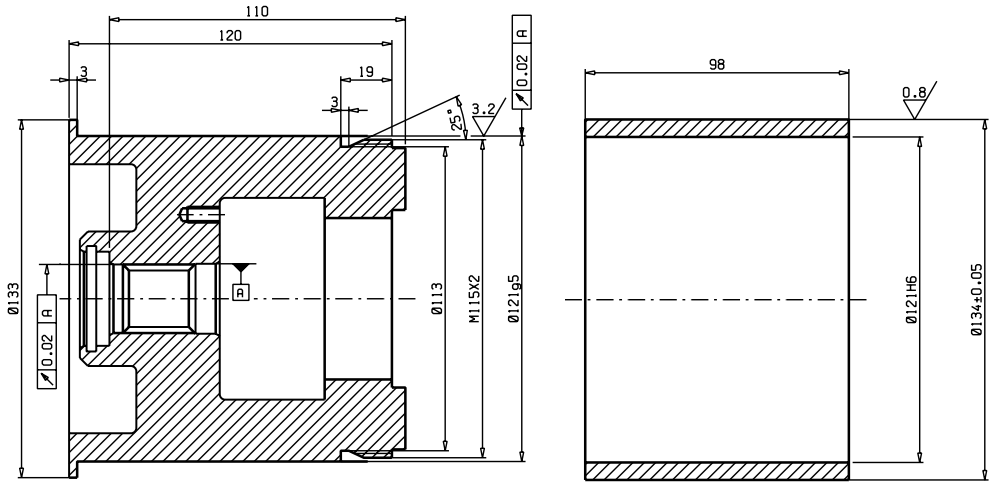

Figure C.2: Rotor.

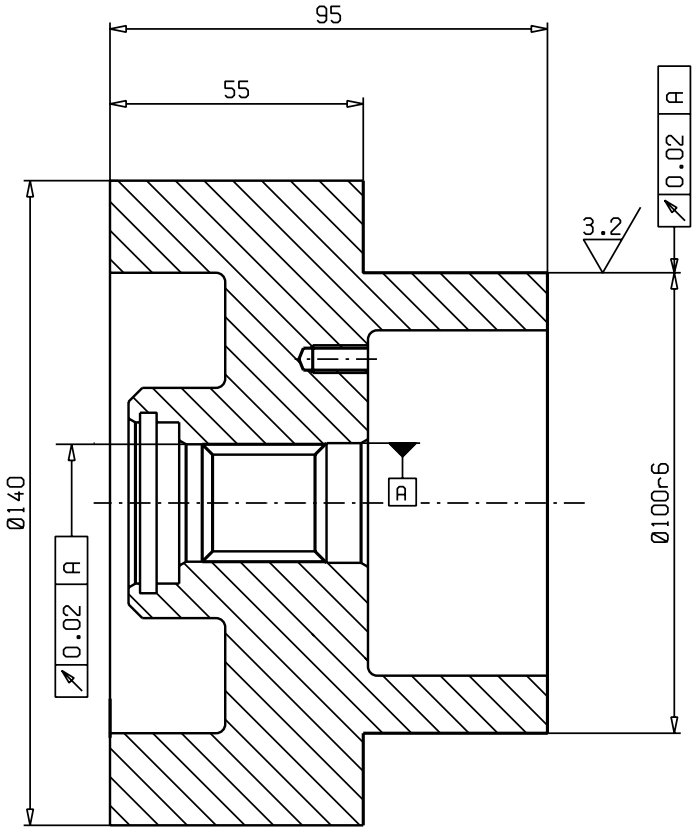

Figure C.3: Boss.

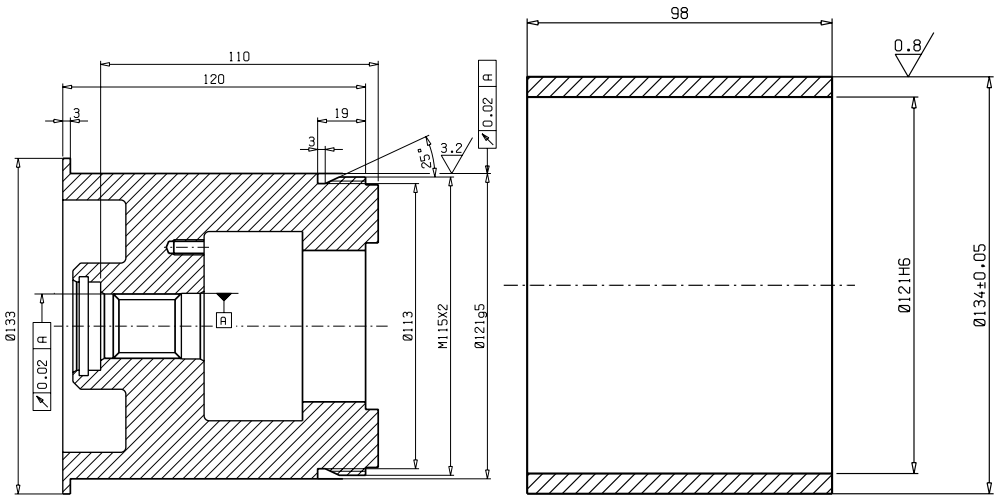

Figure C.4: Rotor.

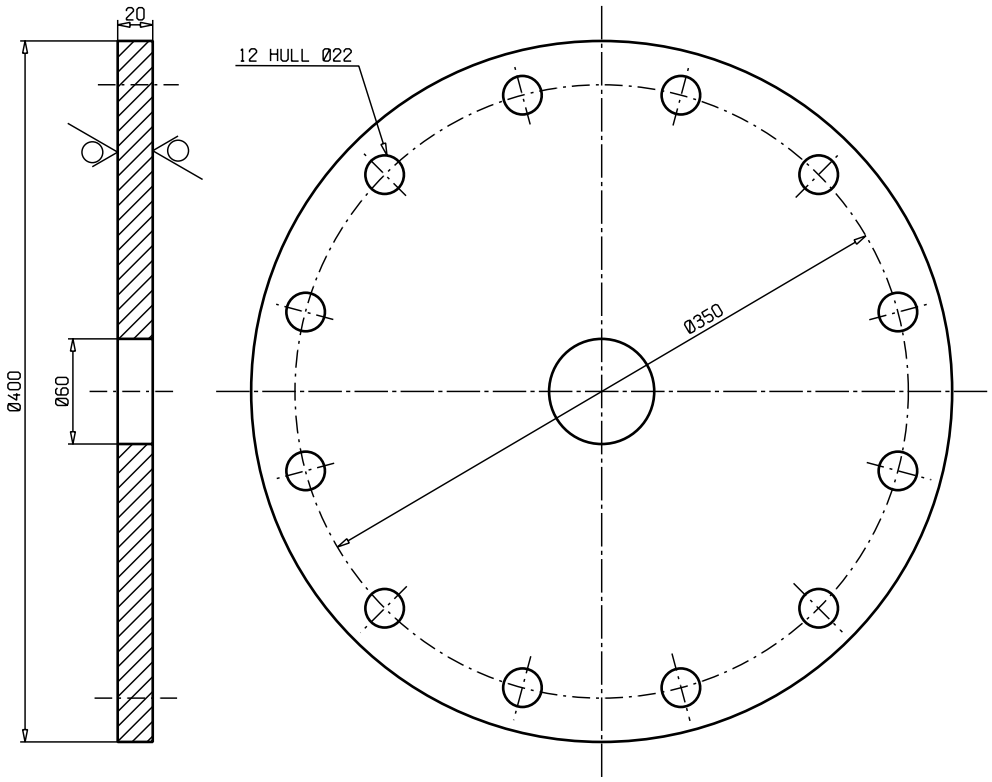

Figure C.5: Front plate.

Appendix D

Friction factor conversions

For a given rough annular seal with a known axial flowrate the average axial velocity depends on the related seal clearance. The literature survey in Chapter 2 showed that many researchers use an average clearance, $\bar{C}$, for bulk flow calculations instead of the minimum clearance, C, used in this thesis. The average clearance is measured from the location of the average surface profile at one surface to the next. When comparing friction factors one needs to convert between the two approaches. Variables related to the average clearance are denoted by a bar above the variable.

Volume flowrate

$$\bar{Q} = \bar{U}\bar{A} = 2\bar{U}\pi\bar{R}\bar{C} \tag{D.1}$$

$$Q = UA = 2U\pi RC \tag{D.2}$$

where the average radii are $\bar{R} = R_r + \bar{C}/2$ and $R = R_r + C/2$ and $\bar{Q} = Q = Q$ The two different bulk flow velocities become:

$$\bar{U} = \frac{Q}{2\pi\bar{R}\bar{C}} \tag{D.3}$$

$$U = \frac{Q}{2\pi RC} \tag{D.4}$$

The pressure drop can then be calculated as follows:

$$\Delta P_{tot} = \bar{f}\frac{2L}{\bar{C}}\frac{\rho}{2}\bar{U}^2 \tag{D.5}$$

$$\Delta P_{tot} = f\frac{2L}{C}\frac{\rho}{2}U^2 \tag{D.6}$$

or

$$\Delta P_{tot} = \bar{f}\frac{2L}{\bar{C}}\frac{\rho}{2}\left(\frac{Q}{2\pi\bar{R}\bar{C}}\right)^2 \tag{D.7}$$

$$\Delta P_{tot} = f\frac{2L}{C}\frac{\rho}{2}\left(\frac{Q}{2\pi RC}\right)^2 \tag{D.8}$$

which gives

$$\frac{\bar{f}}{f} = \frac{\bar{R}^2\bar{C}^3}{R^2C^3} \tag{D.9}$$

For annular seals the approximation

$$\frac{\bar{f}}{f} = \left(\frac{\bar{C}}{C}\right)^3 \tag{D.10}$$

holds well for most practical purposes when $\bar{R}$ and R are nearly the same. Similarly for the axial Reynolds number

$$\bar{Re} = \frac{\rho\bar{U}\bar{C}}{\mu} \tag{D.11}$$

$$Re = \frac{\rho UC}{\mu} \tag{D.12}$$

$$\frac{\bar{Re}}{Re} = \frac{\bar{U}\bar{C}}{UC} = \frac{\frac{Q}{2\pi\bar{R}}}{\frac{Q}{2\pi R}} = \frac{R}{\bar{R}} \approx 1 \tag{D.13}$$

For pipe flow it can similarly be shown that the ratio of friction factors evaluated at different radii $\bar{R}$ and R is given by

$$\frac{f}{\bar{f}} = \left(\frac{R}{\bar{R}}\right)^5 \tag{D.14}$$

Appendix E

Numerical study of seal inlet and exit losses

This numerical study was carried out to compare numerical predictions to the experimental results presented in Chapter 5. The geometries studied are described in detail in Appendix C and Chapter 5.

E.1 CFD-study with the $k-\epsilon$ turbulence model

The widely used formula for inlet (ξ) and exit loss (ξ_e) for concentric liquid annular seals is given in for example (Childs, 1993) as follows:

$$P_s - P_{in} = \frac{\rho}{2}(1+\xi)W^2 \tag{E.1}$$

$$P_{ex} + \frac{\rho}{2}(1+\xi_e)W^2 = P_e \tag{E.2}$$

where W is the bulk axial velocity in the seal, P_s, P_e are the entrance and exit chamber pressures respectively. P_{in} and P_{ex} are the pressures just inside the seal at the entrance and the exit respectively (see Fig. E.5). The two formulas are not only important for determining the pressure drop across the seal, but also for calculating the pressure gradient at the entrance and exit, which is important for dynamic coefficient calculations.

Assumptions used in this formulation are that:

- The entrance and exit chamber pressures at the control volume surfaces are constant
- The mean axial velocity at the inlet of the inlet control volume surfaces and at the exit of the exit control volume is zero.

- The bulk swirl velocity remains constant through the inlet and exit control volumes.

One objective of this study was to test the validity of these assumptions. Since the test rig only allowed a very limited number of pressure sampling points, numerical predictions using CFD were chosen to try and discover the qualitative trends in results, and to see if the experimental results would help to verify the numerical predictions.

Two models of different radial seal clearance were generated for this purpose, both with a 90 degree inlet and exit geometry. The program and options used for numerical simulations were the same as described in Chapter 3. The boundary conditions used are shown in Fig. E.1, and the computational grid and dimensions used are shown in Fig. E.2. The only difference in geometry for the two models used was the radial clearance C which was 1.025 and 0.553 mm for the two models respectively. For each model the flow and pressure field were solved for 11 leakages and 5 rotational speeds (0, 500, 1000, 1500, and 2250 rpm).

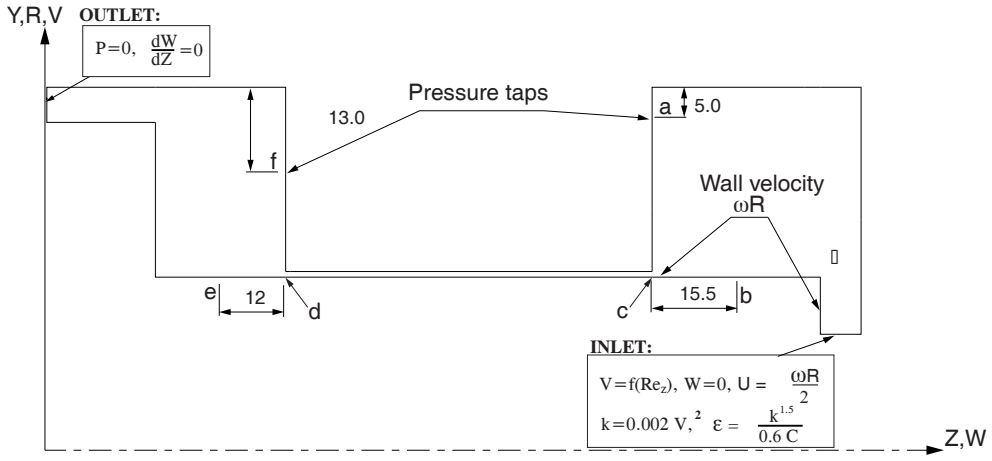

Figure E.1: Boundary conditions and pressure point locations used for calculating inlet and exit loss.

Velocity contours for the clearance, $C = 1.025$, are illustrated in Fig. E.3, and a typical pressure distribution along the mean clearance radius (from point A to B in Fig. E.3) is shown in Fig. E.4 for $C = 0.552$. One important feature of the flow field in the exit chamber is the strong jet at the seal exit. The jet dissipates slowly sideways, and sets up a vortex with much greater peripheral velocity than in the inlet chamber and this in turn influences the pressure field. This can be seen in Fig. E.4 which shows a marked pressure increase at point B due to the stagnation of the jet.

Regarding the assumption of negligible axial velocity at the inlet chamber this assumption holds well for a radial distance of 2 to 3 times the seal clearance from the seal entrance. A small control volume (CV1 Fig. E.5) may be formed for which the zero axial velocity assumption holds. Hence, the first assumption in the list holds well for the entrance coefficient. At the seal exit the situation is totally different since the

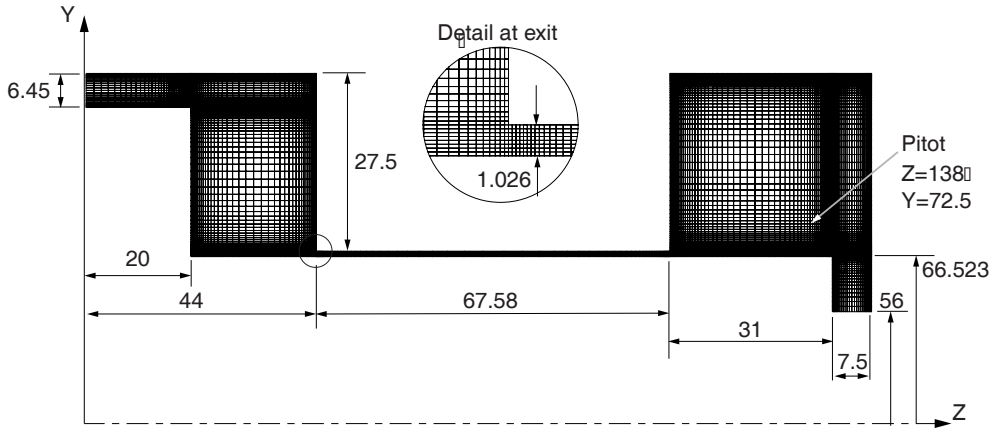

Figure E.2: Computational grid and dimensions used for CFD calculations for stator rotor combination S1/R2.

axial velocity does not slow down significantly before the jet impinges on the back wall. In order for the exit loss equation to hold one would have to use the whole exit chamber as a control volume, and one may lose significant information regarding pressure gradients at the seal exit. One may ask: Why has the current formulation of Eq. E.2 worked so well in the past?

It should first be noted that the most commonly used exit coefficient for dynamic coefficient calculations is 1.0 which gives a zero pressure gradient at the exit.

If one creates a control volume near the seal exit as shown in Fig. E.5 and studies the velocity field at zero rotational speed in this volume it is clear that if the exit cone angle, ϕ, defined by the streamline from the seal exit, is close to zero. By assuming that it is zero the inlet and exit axial bulk velocity does not change over the control volume. By further assuming that there is no frictional loss across the short control volume and no change in the swirl velocity the pressure gradient will be zero which matches the commonly used assumption of an exit coefficient of 1.0. In practice the

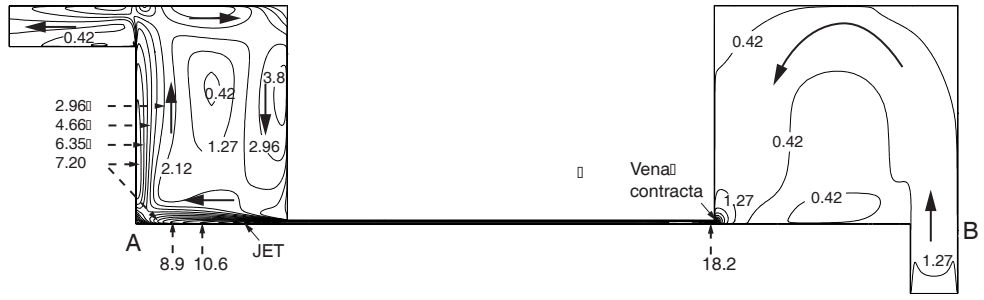

Figure E.3: Velocity contours at 0 rpm, axial Reynolds number of 12000 and clearance 0.552.

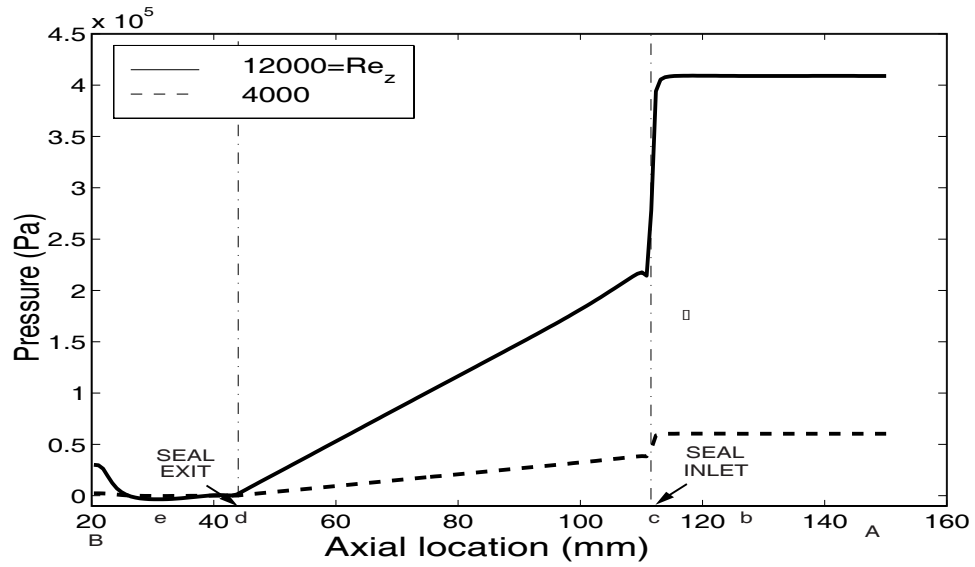

Figure E.4: Pressure distribution along rotor radius for zero rotational speed and axial Reynolds numbers 4000 and 12000.

cone angle will depend on the seal outlet geometry as well as the chamber geometry and there will be a frictional loss present. In the case with a 90° degree angle the numerical simulation indicates a small positive $\phi-$angle which would contribute to a positive pressure gradient. The friction loss in the control volume would contribute to a negative pressure gradient. Fig. E.4 indicates that the combined effect of an expanding flow and a friction drop gives a pressure gradient close to zero in this case. So it may be argued that although the formulation of Eq. E.2 does not hold when applied to a control volume near the seal exit it captures the combined effect of the frictional loss and the expanding jet at the seal exit for the case studied in Fig. E.4.

To test the validity of the constant pressure assumption at inlet and exit chambers

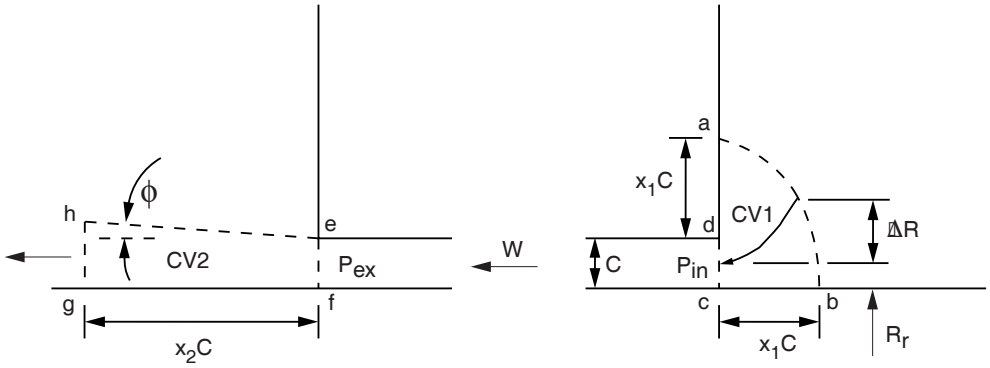

Figure E.5: Control volumes at seal inlet and exit.

the following procedure was followed to visualize loss coefficients depending on where the entrance and exit chamber pressures are measured:

- Calculate the pressures P_{in} and P_{ex} just inside the seal entrance and exit by extrapolating the linear pressure variation inside the seal.
- For each cell in the inlet chamber calculate the inlet loss coefficient, ξ, based on Eq. E.1 by setting $P_s = P_{cell}$
- For each cell in the outlet chamber calculate the outlet loss coefficient, ξ_e, based on Eq. E.2 by setting $P_e = P_{cell}$
- Plot the contours for entrance and exit loss on the same figure.

For the assumption to be correct there should be no variations in the contours at the inlet or exit chambers. The results at high leakage combined with zero rotational speed and low leakage combined with maximum rotational speeds illustrate the trend in results. Fig. E.6 and E.7 show the results at zero rotational speed for the two clearances, $C = 1.026$ and $C = 0.553$ and axial Reynolds numbers in the seal of 25000 and 12000 respectively. Fig. E.8 and E.9 show the results for the same seals at 2250 rpm and axial Reynolds numbers of 7500 and 4000.

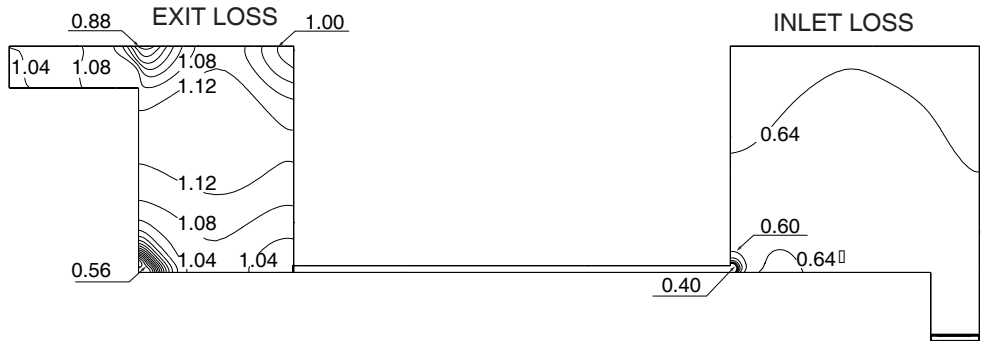

Figure E.6: Entrance and exit loss based on static pressure. 0 rpm, $Re_z = 25000$, S1/R2.

Fig. E.6 indicates that the inlet loss coefficient varies between 0.60 and 0.64 outside the small control volume in Fig. E.5 when $x_1 > 2.5$. For the half clearance the variation is even less. Very similar results were found for low leakage and zero rotational speed, and it can be concluded that the constant pressure assumption holds well for practical purposes for the range of Reynolds numbers tested and zero rotational speed. For the exit coefficient the strong vortex set up in the exit chamber makes the exit coefficient vary considerably between the sides and corner of the chamber. However, the stagnation corner is not close enough to the exit to have a significant influence on the pressure gradient at the exit of the seal. The exit coefficient contour is approximately 1.04 across a control volume where $x_2 = 4$ and at the exit of the chamber. Since the purpose of the exit coefficient is both to establish the pressure loss

Figure E.7: Entrance and exit loss based on static pressure. 0 rpm, $Re_z = 12000$, S1/R4.

and gradient across the exit an exit loss coefficient of 1.04 should be a very reasonable estimate for both clearances and zero rotational speed. This is also very close to the commonly assumed exit coefficient of 1.0 for an infinite chamber.

So far only the results for zero rotational speed have been discussed, and no major flaws in the commonly used formulas for entrance and exit loss coefficients have been found. In Figures E.8 and E.9 the variation of the entrance and exit loss coefficients with respect to location of the pressure reference point in the inlet and exit chamber are shown at a rotor velocity of 2250 rpm. From these figures it is clear that that there is a radial pressure distribution in both chambers which makes the loss coefficients a function of radial position. Since the entrance and exit loss should only represent viscous losses near the entrance it is no longer possible to choose any point in the entrance and exit chamber to evaluate the losses. A possible approach is consider control volumes at entrance and exit in Fig. E.5. The detail in Fig. E.8 shows that the entrance coefficient is between 0.7 and 0.8 along the line from point a to b in Fig. E.5 when $x1 \approx 2$. The exit coefficient based on the exit control volume line e,h,g, is between 1.0 and 1.2 for $x2 \approx 2$. Since the radial variations are small for the rotational speeds considered in the current experiment it was decided to use the single points **b** and **e** at the rotor (see Fig. E.1) to estimate theoretical and experimental exit and entrance coefficients respectively. Figure E.2 shows the pressure distribution along the rotor surface from point A to B in Fig. E.3, and the axial location of the reference points **b** and **e**. The pressure is normalized with respect to $\rho W^2/2$, where W is the axial bulk velocity in the seal. For the axial Reynolds numbers 5000, 7500, 10000, 12500, 30000 the respective ratios between inlet bulk tangential and axial velocity are 1.73, 1.20, 0.91, 0.74, 0.32. From this figure it can be seen that the axial location of the reference point for entrance and exit exit chamber pressures will influence the entrance and exit loss calculation. However, the chosen reference points will give a useful estimate.

As rotational speed is increased further the variations along the control volume lines a,b and e,h,g in Fig. E.5 are expected to increase.

To study pressure distributions at higher speeds it was decided to analyze the stator rotor combinations S1/R2 and S1/R4 at an axial Reynolds number of 5000, at ro-

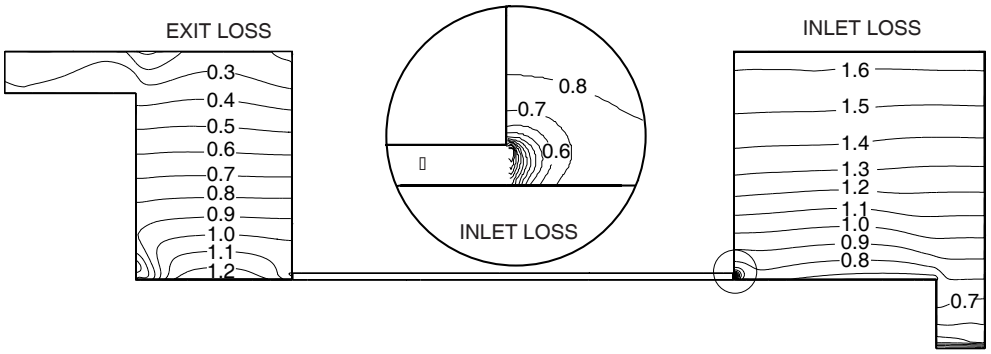

Figure E.8: Entrance and exit loss based on static pressure. 2250 rpm, $Re_z = 7500$, S1/R2.

tational speeds (rpm), 5000, 7500 and 10000. The difference in leakage between the two models is less than 0.5%. Figure E.11 shows the inlet and exit loss variation at a rotational speed of 10000 rpm which gives a ratio of tangential to axial bulk flow of approximately 10. For the control volume line a,b in Fig. E.5 at x1 = 2 the inlet loss coefficient varies between 0.4 and 1.0 approximately, and for the control volume line e,h,g at x2=2 the exit loss coefficient is between 1.0 and 2.0. Clearly the coefficients are no longer constant which means that Equations E.1 and E.2 no longer hold.

Figure E.9: Entrance and exit loss based on static pressure. 2250 rpm, $Re_z = 4000$, S1/R2.

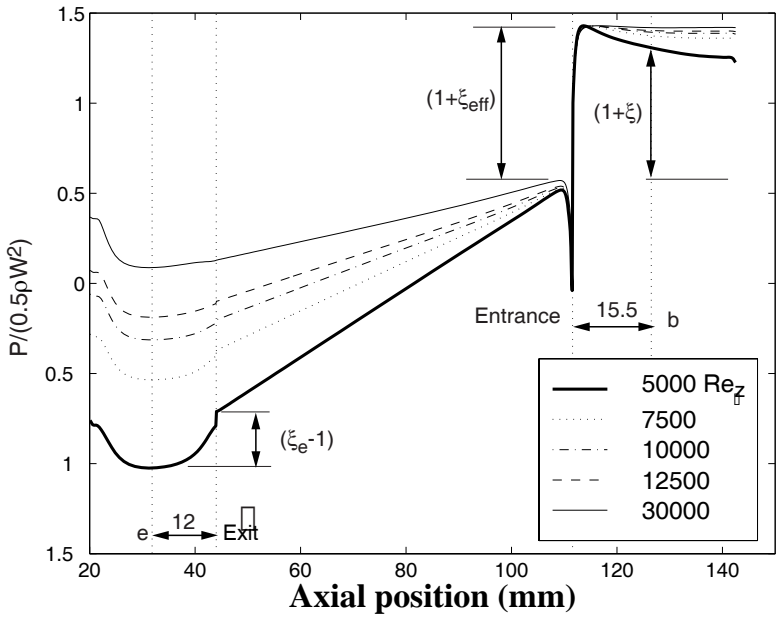

Figure E.10: CFD-predictions of normalized pressure at 2250 rpm, stator rotor combination S1/R2.

Figure E.11: Entrance and exit loss based on static pressure. 10000 rpm, $Re_z = 5000$, S1/R2.

Fig. E.12 shows the normalized pressure along the rotor. By inspection the entrance pressure drop is approximately constant for the entire range of rotational speeds for both clearances, while the pressure drop at the exit increases with rotational speed. Another important feature of the results is that the axial pressure gradient at the inlet is approximately constant from the maximum pressure to the inlet, while the exit gradient varies with axial position. The pressure gradient is an important boundary condition when calculating dynamic characteristics. The axial variation of the pressure gradient at the outlet indicates that in order to formulate an exit loss expression which predicts the pressure gradient accurately one will have to consider the limit when x2 in Fig. E.5 goes to zero.

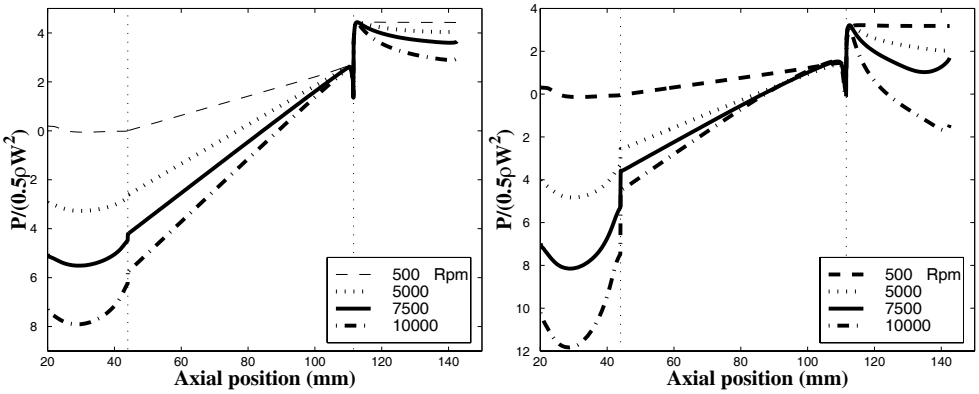

Figure E.12: Normalized pressure along rotor. Left figure: stator rotor combination S1/R4. Right figure: S1/R2.

Fig. E.13 shows the absolute pressure along the rotor. It shows that the pressure distribution upstream of the maximum pressure and downstream of the seal exit is very similar for both clearances when the rotational speed and leakage are the same. This again indicates that the pressure distribution in the entrance and exit chambers varies little as a function of clearance and that it is mainly due to the strong vortex caused by the swirling flow. The consequence of this is that any functional relationship developed for the exit loss coefficient in this case, could only be used for this specific exit chamber geometry, and the exit coefficient would no longer contain only viscous losses when calculated by

$$\xi_e = \frac{2(P_e - P_{ex})}{\rho W^2} \tag{E.3}$$

Consider the results for clearances 1.026 mm for S1/R2 and 0.553 mm for S1/R4 where both seals operate at 10000 rpm and $Re_z = 5000$, and the reference points **b** and **e** in Fig. E.1 is used for P_e. The pressure difference between the seal exit and the minimum exit chamber pressure is almost identical for the two cases, $P_{ex} - P_e = 4.11 \cdot 10^4$. By assuming that the same pressure difference would hold for a 0.1 mm clearance the corresponding exit coefficients are give in Table E.1.

W	U/W	ξ_e
3.34	5.07	8.37
6.20	2.73	3.13
33.7	0.50	1.07

The tangential velocity bulk velocity U is the average bulk flow at the seal exit. Table E.1 indicates that the pressure field in the exit chamber caused by the vortex influences the calculated exit coefficient to a great extent. As the ratio between tangential to radial velocity gets smaller than 0.5, the commonly used assumption of an exit coefficient equal to 1.0 for the given geometry appears to be a good choice.

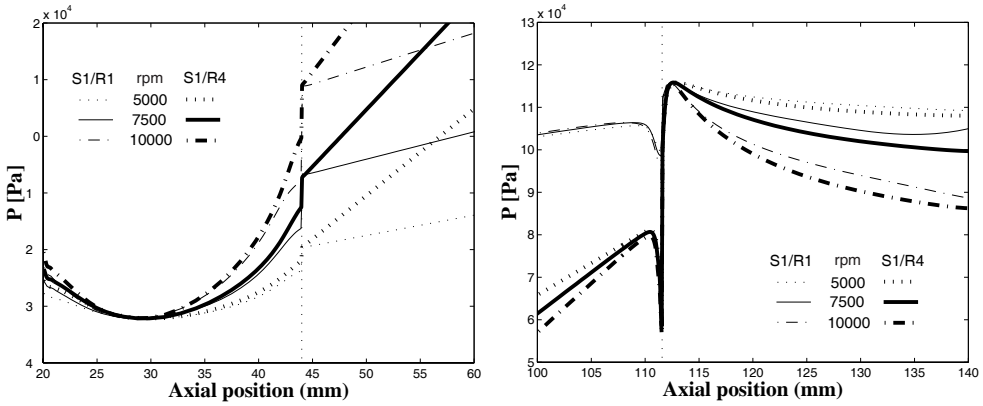

Figure E.13: Absolute pressure along rotor. Left figure: Exit chamber pressure with maximum pressure as reference. Right figure: Entrance chamber pressure with minimum pressure as reference point.

To test the assumption for Eq. E.1 that swirl velocity does not change significantly across the inlet and exit control volumes one solution at 2250 rpm, axial Reynolds number 5000, and clearance $C = 1.026$ was studied in more detail. This test case was chosen since the axial velocity is small compared to the tangential and any weakness in the assumption should be most pronounced in this case. The average swirl velocity was calculated at the entrance of the seal and along a straight line from point **a** to point **b** in Fig. E.5 where $x_1 C = 3mm$. The difference in average swirl was less than 3% between the inlet and exit of the control volume. Hence, it was assumed that there is no significant change in swirl across this control volume. Fig. E.14 shows the non-dimensional seal inlet swirl from the numerical simulations of stator rotor combinations S1/R2 and S1/R4. Since the average inlet swirl does not change across the control volume it appears that this assumption can be made also to a two-dimensional control volume formulation for the entrance loss. However, one should be aware that the average inlet swirl at the inlet a,b in Fig. E.5 is at a different average radius than the seal inlet. Hence, there will be a pressure gradient due to centrifugal forces associated with the change in radial location of the average swirl which has to be accounted for.

Further discussions and comparisons to experimental results are given in Chapter 5.

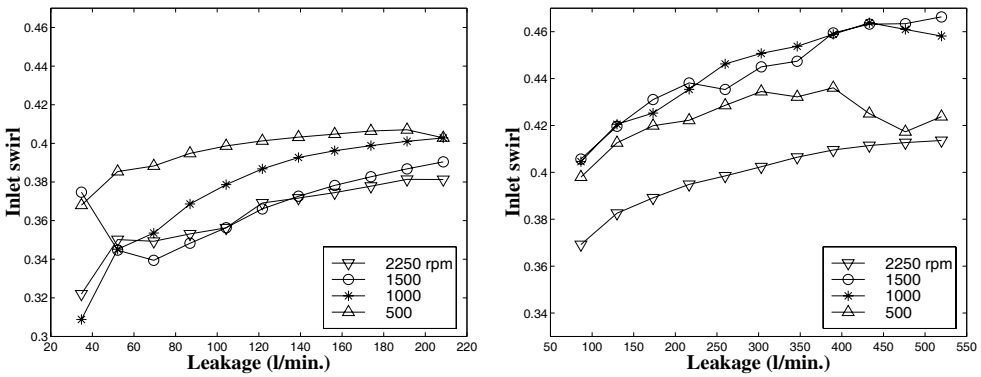

Figure E.14: CFD-predictions of non-dimensional inlet swirl ($\frac{U}{\omega R_r}$) as a function of leakage for sharp entrance. Left figure: Stator rotor combination S1/R4. Right figure: S1/R2.

E.2 CFD study of conical seal exit with $k-\omega$ turbulence model

The purpose of this study was to find out why the theoretical exit loss results in Chapter 5, Fig. 5.18 based on the $k-\epsilon$ turbulence model under-predicted the exit loss coefficient compared to experimental results shown in Fig. 5.14.

Close examination of the velocity profile at the seal exit revealed that the exit appeared to behave like an efficient diffuser with no flow separation in the conical outlet. This was unexpected since diffuser theory (see for example (White, 1994)) predicts separation for a diffuser angle above a 10°. One intuitive approach to a better numerical solution would be to refine the grid at the exit in order to resolve the flow field more accurately. However, at the Reynolds numbers and grid used for the results in Fig. 5.18, the non-dimensional wall distance, y^+, for the near wall cell was close to the lower limit of 11 for the standard $k-\epsilon$ turbulence model. Hence, it was decided to change to a low-Reynolds number turbulence model to resolve the boundary layer flow more accurately. With the $k-\omega$ model available in CFX (based on the theory by (Wilcox, 1993)) the boundary layer has to be solved down to y^+ values of about 1.0 or less to achieve useful results. To do so the solution was restricted to zero rotational speed and an axial Reynolds number of 5000. To achive the $y^+ < 1$ target the total number of computational cells was changed from 7150 to 125300. The resulting flow field and is shown in Fig. E.15. A close up at the exit of the two different models is shown in Fig. E.16. The corresponding axial pressure distributions along the rotor surface are shown in Fig. E.17.

Clearly the low Reynolds number solution completely changes the picture. Separation is predicted close to the start of the conical outlet, pressure recovery is significantly less, and the exit coefficient is 0.96 which is close to the experimental value of approximately 0.9. So this is good news, apart from the fact that the solution time changed from approximately one hour to two days on a HP 180 C workstation. It is expected

that the grid would have to be refined further for greater axial Reynolds numbers and much further for swirling flows due to large tangential Reynolds numbers in the inlet- and exit chambers.

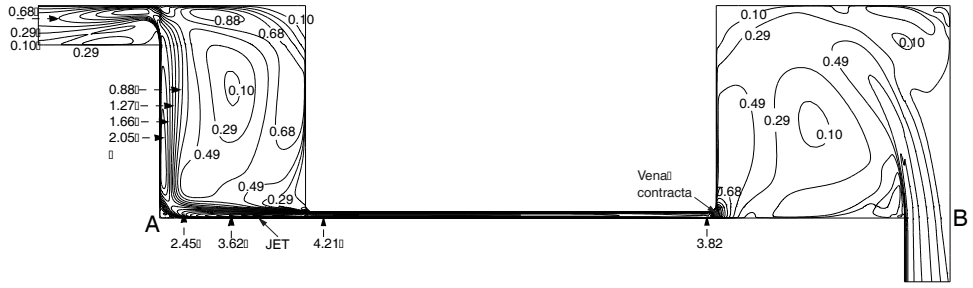

Figure E.15: Speed contours for the low-Reynolds number $k-\omega$ turbulence model, $Re_z = 5000$, 0 rpm, C=1.009 for the 45° chamfer.

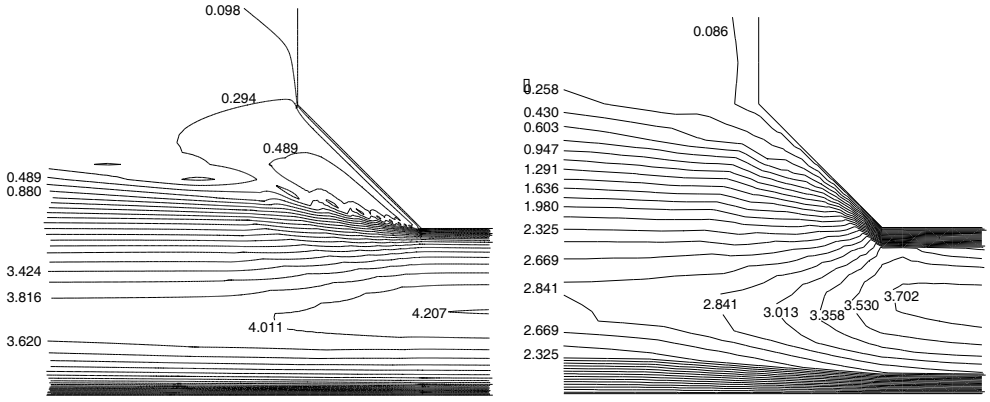

Figure E.16: Left figure: Speed contours close up at seal exit for the low-Reynolds number $k-\omega$ turbulence model, $Re_z = 5000$, 0 rpm, C=1.009 for the 45° chamfer. Right figure: Corresponding contours for the standard $k-\epsilon$ turbulence model.

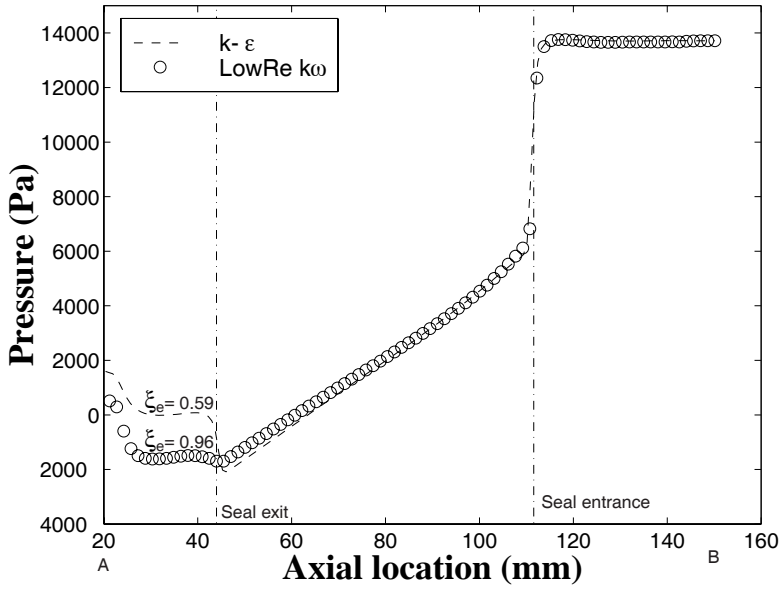

Figure E.17: Pressure distribution along middle seal radius for the standard k-ϵ and the low Reynolds number k-ω turbulence models.

Previous Dr.Ing theses

Department of Marine Engineering

Kviteng, Olav	Torsional Vibration Systems with non-linear Elements. 1972. (In Norwegian).
Mathiesen, Tor Chr.	Reliability Engineering in Ship Machinery Plant Design. 1973.
Bøe, Carsten	The Hydrodynamic Lubrication Problem for Engine Sleeve Bearing. 1975.
Rasmussen, Magnus	Evaluation of Structural Properties in Connection with Vibration Analysis for Condition Monitoring of Machinery. 1976. (In Norwegian).
Valland, Harald	Simulation of the Internal Combustion Engine Cycle. 1976. (In Norwegian).
Sandsmark, Nils	Analysis of Stationary and Transient Heat Conduction by the Finite Element Method. 1977. (In Norwegian).
Oldervik, Ole	The Hydrodynamically Lubricated Journal Bearing Subjected to Periodically Varying Load. 1979.
Saugerud, Odd Tore	Fatigue Life Prediction of Thermally Loaded Engine Components. 1981.
Haugslett, Åge	Mathematical Modelling of Hydraulic Systems using Bond-Graphs. 1981. (In Norwegian).
Strand, Kurt	A System Dynamic Approach to One-Dimensional Fluid Flow. 1986.
Småvik, Magnus	Thermal Load and Process Characteristics in a Two-Stroke Diesel Engine with Thermal Barriers. 1987. (In Norwegian).
Haagensen, Sven	Fuel Dependent Cyclic Variability in a Spark Ignition Engine – An Optical Approach. 1991.

Molteberg, Gunnar A.	The Application of System Identification Techniques to Performance Monitoring of Four Stroke Turbocharged Diesel Engines. 1991.
Chan Siu Hung	Nonlinear Analysis of Rotordynamic Instabilities in High-speed Turbomachinery. 1992.
Ask, Tor Øyvind	Ignition and Flame Growth in Lean Gas-Air Mixtures. An Experimental Study with a Schlieren System. 1992.
Steinebach, Christian	Knowledge Based Systems for Diagnosis of Rotating Machinery. 1993.
Nordrik, Rune	Investigation of Spark Ignition and Autoignition in Methane and Air using Computational Fluid Dynamics and Chemical Reaction Kinetics. 1993.
Paulsen, Hallvard	A Study of Transient Jet and Spray using a Schlieren method and Digital Image Processing. 1995.
Æsøy, Vilmar	Hot Surface Assisted Compression Ignition in a Direct Injection Natural Gas Engine. 1996.
Moksnes, Paul O.	Modeling Two-Phase Thermo-Fluid Systems Using Bond Graphs. 1997.
Torbergsen, Erik	Impeller/Diffuser interaction forces in centrifugal pumps. 1998.
Andersen, Trond	Short term maintenance planning. 1999.